Clumped and Traditional Stable Isotope Proxy Innovations for Paleoclimatic and Paleoceanographic Reconstructions

by

Alex A. Quizon

A dissertation submitted in partial fulfillment
of the requirements for the degree of
Doctor of Philosophy
(Earth and Environmental Sciences)
in the University of Michigan
2026

Doctoral Committee:

Associate Professor Sierra V. Petersen, Chair
Professor Rose M. Cory
Professor Thomas F. Duda Jr.
Professor Benjamin H. Passey
Assistant Professor Ian Z. Winkelstern, Grand Valley State University

Alex A. Quizon

aquizon@umich.edu

ORCID iD: 0009-0002-6349-8259

© Alex A. Quizon 2026

Dedication

To my parents, who have sacrificed so much and always supported me along the way.

Acknowledgements

To my advisor, Sierra, first and foremost – thank you so much for your incredible guidance and mentorship throughout my time here at the University of Michigan, from the get-go. You helped me grow and evolve in so many ways – as a researcher, a critical thinker, a logician, a writer, an educator, a science communicator, and so much more. Thank you for always pushing me, encouraging me to do better, and being proud and confident in my work. Even when I make mistakes, you see the best in me and have always helped me improve at every stage along the way. I am forever grateful for everything you have done for me, for the lab, for the UM EARTH community, and beyond.

To my former advisors at Williams College, both formal and informal within the Chemistry and Geosciences departments: Mea, Lisa, Anthony, Chris – thank you for having inspired me to do the work and research I have the privilege of doing today. From my introductory courses in chemistry, environmental science, and oceanography to my senior course in environmental organic chemistry to my paleoclimate and paleoceanography research thesis, I'm so grateful to have been taught by such enthusiastic, passionate educators who bring out the best in their students, inspiring us to pursue our interests to the fullest.

To my other committee members: Rose, Ben, Tom, and Ian – thank you for your continued support and advice throughout the years during my committee meetings and progressing my career as a geoscientist and climate scientist.

To the various collaborators I've gotten the opportunity to work with over the years – thank you for your continued guidance throughout the years as I developed and progressed each

of my projects. Thank you for filling in my knowledge gaps where they existed, enlightening me with all your insights after having done research for so many years in the field.

To the staff and faculty of the UM EARTH department – thank you for fostering a welcoming environment and constantly working to strive for better. Thank you to the staff who help to make things run smoothly in this department and thank you to all the faculty I've been able to interact and work with that have passed along their wisdom to us. Thank you in particular to Michela, Sydney, and the other members of the Center for Research on Learning and Teaching for inspiring and teaching me ways to be a more grounded and more compassionate teacher in this education landscape. Thank you to Udo and Jenna for being incredible co-instructors during a difficult time at Camp Davis. And thank you to Mark – a true master of his craft whose positivity and enthusiasm for teaching geology was absolutely contagious; thank you for not only inspiring me through your instruction of geology fundamentals to the students, but also for teaching these same concepts to me as I had never taken Intro to Geology before – for which I am eternally grateful. We all miss you dearly.

To my fellow members of the SCIPP Lab – thank you for being just the best lab group. To Ashling and Justin – thank you so much for all the work and management you've done behind the scenes to move our lab group's research forward. To Jade and Allison – thank you for being exemplary role models and mentors throughout my time here. To Cecilie – thank you for being a wonderful mentee and bearing with me as we learned all about clams during our four years here together. To Lucas, Adriana, Erin, Eric (and Nick, Cam, Elena) – thank you all for traversing the chaotic world of mollusk geochemistry with me, for all the midday lunch breaks for delicious sushi and fritas and Korean fried chicken, and for all the NUB 3021 shenanigans.

To all the friends I've made in the UM EARTH department (far too many to name and count) – thank you for being such a supportive group of peers, co-workers, and fellow travelers on the arduous journey of graduate school. Thank you for all the relaxed study sessions and reading group sessions, the 2+ hour-long GeoClub virtual EBoard meetings (yes I'm looking at you, Mack), the assorted departmental social outings to Bill's Beer Garden, and everything in between – it all ultimately adds a breath of levity to our experiences, however difficult they may be. Our paths haven't been easy, but I'm so glad to have gotten to know so many different types of eager geoscientists with a fervor to make this world better through our work.

To all the friends I've made in the larger Michigan community – thank you all for making me feel at home away from home. Thank you to the wonderful choir I've created music with at St. Mary's and friends in the parish I've gotten to know better – Devon, Mike, Ryan, Brendan, Meghan, Kevin, Lucy, Johanna, Jenny, Zach, David, Jeremy, and many others. Thank you to all the amazing people I've gotten to share experiences with locally – the Dexter Community Orchestra, the Michigan and Ann Arbor Super Smash Bros. Melee communities, the Station 300 Saline bowling league, the Spike and Adobo volleyball team – for making my time here worth it.

To all my other friends from past experiences who have stuck with me throughout the years from middle school through college, which are too many to count – thank you for always providing words of encouragement and being friends I can always count on. Words alone cannot express how incredibly grateful I am for *every single one* of you.

To my family – thank you for always supporting me along the way. Thank you to Mom, Dad, Kuya Albert, and Allen for always welcoming me back home during breaks, nourishing me with good food and company.

To Lucas and Cam – thank you for being my boys since day one. Both of you know how much I truly appreciate you.

And lastly, to Tara – thank you for being just the best partner. Thank you for wanting to live life together with me and appreciating novel experiences – as isotopic geochemists, as students in art classes, as a bowling league duo, as travel companions, as movie and literature critics, as Taylor Swift fans, as museum appreciators, as trivia enjoyers, as non-judgmental Planet Fitness workout buddies, and so much more. Thank you for all the care, kindness, and compassion you show each and every day – you are truly the best partner I could ever ask for.

Table of Contents

Dedication ii

Acknowledgements iii

List of Tables xiv

List of Figures xvi

Abstract xx

Chapter 1 Introduction 1

1.1 Overview and motivation 1

1.2 Sampling methods 4

1.3 Research questions and outline of the dissertation chapters 5

1.3.1 Do marine gastropods precipitate in 'clumped' isotope equilibrium and faithfully record environmental temperatures (Chapter 2)? 5

1.3.2 Do all turritellid gastropods exhibit vital (disequilibrium) effects, and can these biases be corrected for in the fossil record (Chapter 3)? 6

1.3.3 Is there a latitudinal $\delta^{18}O_w$ gradient that aligns with the latitudinal salinity gradient along the U.S. Eastern Seaboard, and can $\delta^{18}O_w$ signatures distinguish the Labrador Current and Gulf Stream (Chapter 4)? 7

1.3.4 What were paleoclimate and paleoceanographic conditions along the Atlantic Coastal Plain during Marine Isotope Stage 5, and can we use Δ_{47}-derived paleo- $\delta^{18}O_w$ values to distinguish the Labrador Current and Gulf Stream (Chapter 5)? 8

1.3.5 How did paleoclimate and paleoceanographic conditions evolve over the Last Interglacial at Nantucket, Massachusetts (Chapter 6)? 9

1.4 Summary 9

1.5 References 12

Chapter 2 Clumped Isotope Thermometry (Δ_{47}) Measurements in Marine Gastropods Suggest Equilibrium Precipitation 15

2.1 Abstract 15

2.2 Introduction 16

2.3 Materials and methods 22

2.3.1 Sample selection 22

2.3.2 Subannual oxygen and carbon isotope sclerochronology 23

2.3.3 Seasonally targeted clumped isotope measurements (Nu) 24

2.3.4 Seasonally targeted clumped isotope measurements (MAT 253) 28

2.3.5 Previously published Δ_{47} data from marine gastropods 29

2.3.6 Assigning calibration temperatures and $\delta^{18}O_w$ values 29

2.3.7 Statistical analysis of Δ_{47} residuals from the Anderson et al., 2021 calibration 30

2.3.8 Eocene Campanile data and processing 31

2.4 Results 32

2.4.1 Δ_{48} – gas-based vs. carbonate-based reference frames & acid fractionation factor calculation 32

2.4.2 Δ_{47} – gas-based vs. carbonate-based reference frames 33

2.4.3 $\delta^{18}O$ sclerochronology 34

2.4.4 Reconstructed Δ_{47}-temperatures 35

2.4.5 Reconstructed $\delta^{18}O_w$ values 36

2.4.6 Paired Δ_{47}/Δ_{48} 37

2.4.7 Fossil Δ_{47} data 37

2.5 Discussion 38

2.5.1 Δ_{48} Acid Fractionation Factors (AFFs) and 'true' Δ_{48} values 38

2.5.2 Interlaboratory differences in GU1 values 40

2.5.3 Clear equilibrium precipitation signatures 41

2.5.4 Possible disequilibrium precipitation signatures 42

2.5.5 Preliminary insights into disequilibrium precipitation 45

2.5.6 Unclear signatures 47
2.5.7 Application to paleoclimate 48
2.6 Conclusions 49
2.7 Acknowledgments 50
2.8 Appendices 50
2.8.1 Calibration window and Δ_{48} standards 50
2.9 References 82
Chapter 3 'Vital' (Disequilibrium) Effects in Turritellid Gastropods – A Case Study With Colombian Mid-Miocene Fossils 92
3.1 Abstract 92
3.2 Introduction 93
3.3 Materials and Methods 94
3.3.1 Site selection 94
3.3.2 Samples and sampling methods 94
3.4 Results 95
3.4.1 Modern turritellids 95
3.4.2 Fossil (Mid-Miocene) turritellids 96
3.5 Discussion 96
3.5.1 Presence of vital effects in modern turritellids 96
3.5.2 Mid-Miocene paleoclimate 98
3.5.3 Mid-Miocene Climatic Optimum (MMCO) at the Guajira Peninsula 99
3.6 Conclusions 100
3.7 Acknowledgments 100
3.8 Appendices 101
3.8.1 Modern climatology and hydrology 101
3.8.2 Fossil Δ_{47} sampling, data processing procedures, and temperature calculations 101

3.9 References 117

Chapter 4 Seawater Salinity and Oxygen Isotopes Along the U.S. East Coast From 24°N to 44°N 120

4.1 Abstract 120

4.2 Background & Summary 120

4.3 Methods 125

4.3.1 Sample localities 125

4.3.2 Sample collection procedures 126

4.3.3 Salinity measurements 126

4.3.4 $\delta^{18}O$ measurements 127

4.4 Results 127

4.4.1 Regional $\delta^{18}O_w$ and salinity variability 127

4.4.2 $\delta^{18}O_w$ covariance with salinity across latitudes 128

4.5 Discussion 128

4.5.1 Uncertainties in $\delta^{18}O$-based temperature reconstructions 128

4.5.2 Distinct $\delta^{18}O_w$ signatures for the Labrador Current and Gulf Stream 129

4.6 Data Records 130

4.7 Technical Validation 131

4.8 Acknowledgments 132

4.9 References 142

Chapter 5 MIS5 Paleoclimate and Paleoceanography Along the Atlantic Coastal Plain 148

5.1 Abstract 148

5.2 Introduction 149

5.3 Study Sites & Stratigraphy 153

5.3.1 Gomez Pit, Virginia (GPVA) – UDAMS 06076 154

5.3.2 Moyock Pit, North Carolina (MPNC) – UDAMS 07800, 07000 155

5.3.3 Forbes Pit, North Carolina (FPNC) – UDAMS 07730, 07731 156
5.3.4 East Lake Pit, North Carolina (ELPNC) – UDAMS 07556 156
5.3.5 RP3 Site (ICWSC) – UDAMS 08306 157
5.3.6 Berkeley Pit, SC (BPSC) – UDAMS 08136 158
5.3.7 Jones Pit, Georgia (JPGA) – UDAMS 09007 158
5.3.8 WCQ Site (WCQFL) – UDAMS 10185 159
5.3.9 Daytona Beach Site (DBPFL) – UDAMS 10100 159
5.4 Methods 160
5.4.1 Screening for preservation (Raman spectroscopy) 160
5.4.2 Amino Acid Racemization (AAR) 160
5.4.3 Isotopic Measurements ($\delta^{18}O$, Δ_{47}, $\delta^{18}O_{sw}$) 161
5.4.4 Modern climatology and hydrology 162
5.5 Results 163
5.5.1 AAR data 163
5.5.2 Isotopic temperature and $\delta^{18}O_{rsw}$ data 163
5.6 Discussion 165
5.6.1 MIS 5e paleoclimate 165
5.6.2 MIS 5a paleoclimate 167
5.6.3 Mid-coastal MIS 5e vs. MIS 5a comparison 167
5.6.4 Paleo-$\delta^{18}O_w$ as a water mass tracer 169
5.7 Conclusions 170
5.8 Acknowledgments 171
5.9 Appendices 171
5.9.1 Modern climatology and hydrology 171
5.9.2 Isotopic sampling and data processing 172

5.10 References 194

Chapter 6 End-Last Interglacial Transition and Substantial Ice Sheet Melt Detected at Sankaty Head, Massachusetts 205

6.1 Abstract 205

6.2 Introduction 205

6.3 Materials & Methods 209

6.3.1 Dating (AAR) 209

6.3.2 Isotopic Measurements ($\delta^{18}O$, $\delta^{13}C$, Δ_{47}) 209

6.4 Results 209

6.4.1 Dating (AAR) 209

6.4.2 Sclerochronology 210

6.4.3 Temperature & $\delta^{18}O_{sw}$ 210

6.5 Discussion 211

6.5.1 Age Interpretations 211

6.5.2 Paleoenvironment Interpretations 211

6.5.3 Comparison to Previous MIS5e Findings 213

6.6 Conclusions 213

6.7 Acknowledgments 214

6.8 Appendices 215

6.8.1 Specimens & sampling methods 215

6.8.2 Screening for preservation 217

6.8.3 Amino acid racemization (AAR) 217

6.9 References 231

Chapter 7 Conclusions 235

7.1 Do marine gastropods precipitate in ‘clumped’ isotope equilibrium and faithfully record environmental temperatures (Chapter 2)? 235

7.2 Do all turritellid gastropods exhibit vital (disequilibrium) effects, and can these biases be corrected for in the fossil record (Chapter 3)? 236

7.3 Is there a latitudinal $\delta^{18}O_w$ gradient that aligns with the latitudinal salinity gradient along the U.S. Eastern Seaboard, and can $\delta^{18}O_w$ signatures distinguish the Labrador Current and Gulf Stream (Chapter 4)? 237

7.4 What were paleoclimate and paleoceanographic conditions along the Atlantic Coastal Plain during Marine Isotope Stage 5, and can we use Δ_{47}-derived paleo- $\delta^{18}O_w$ values to distinguish the Labrador Current and Gulf Stream (Chapter 5)? 238

7.5 How did paleoclimate and paleoceanographic conditions evolve over the Last Interglacial at Nantucket, Massachusetts (Chapter 6)? 239

7.6 Future Directions 240

List of Tables

Table 2.1. Calculation of $\Delta_{48}{}^{*}{}_{70\text{-}90}$ using ETH standards within the calibration window..... 62

Table 2.2. Comparison of standards performance reported in gas-based and carbonate-based references frames within the calibration window. 63

Table S2.1. Table of climatological data for each sampling site, mostly obtained from the World Ocean Atlas 2018 database. 74

Table S2.2. Table of instrumental and modeled $\delta^{18}O_w$ data for each sampling site. 75

Table S2.3. Theoretical equilibrium Δ_{47} and Δ_{48} values for calibration standards used in this study. 76

Table S2.4. Calculation of $\Delta_{48}{}^{*}{}_{70\text{-}90}$ using ETH standards within the calibration window. 77

Table S2.5. Comparison of standards performance reported in gas-based and carbonate-based references frames within the calibration window. 78

Table S2.6. Table of statistics of genus-averaged Δ_{47} residuals from the Anderson et al. (2021) calibration line. 79

Table S2.7. Table of statistics of genus-averaged Δ_{47} residuals from the Fiebig et al. (2021) calibration line. 80

Table S2.8. Table of statistics of genus-averaged Δ_{48} residuals from the Fiebig et al. (2021) calibration line. 81

Table S3.1. Instrumental temperature data for the latitude/longitude information roughly corresponding to Guajira Peninsula, Colombia. 107

Table S3.2. Instrumental and modeled $\delta^{18}O_{sw}$ data for the latitude/longitude information roughly corresponding to the sample collection sites in Guajira Peninsula, Colombia..... 108

Table S3.3. Names of samples measured in this study and how they were sampled for Δ_{47}..... 109

Table 4.1. Sample collection campaigns for this study. 138

Table 4.2. Salinity thresholds for designations of collected water samples, reported in units of parts per thousand (ppt). 139

Table 4.3. WICO 2024 Intercomparison test results for the University of Michigan Stable Isotope Lab..... 140

Table 5.1. Summary of sample sites and brief descriptions of previous geochronology efforts. 182

Table 5.2. Summary of shell samples across sites, with descriptions of sampling strategies employed. 183

Table 5.3. Unit-averaged Δ_{47}-temperature and reconstructed $\delta^{18}O_w$ data for each sample locality in this study. 184

Table S5.1. Modern temperature data for sample sites in this study obtained from the World Ocean Atlas database (Locarnini et al., 2019). 185

Table S5.2. Proximal instrumental $\delta^{18}O_w$ values for the sample sites in this study. 186

Table S5.3. Summary of reconstructed isotopic temperatures and $\delta^{18}O_w$ values for all samples analyzed in this study. 189

Table S6.1. Instrumental temperature data for the latitude/longitude information corresponding to Sankaty Head Cliff on Nantucket Island, Massachusetts. 223

List of Figures

Figure 1.1. Schematic of isotopic methods applied to mollusk samples throughout this dissertation. 11

Figure 2.1. Phylogenetic relationships within class Gastropoda and relevant physiological characteristics of modern marine gastropods measured in this study or previously measured by Zhang et al. (2021) (C. pica) and Henkes et al. (2013) (C. ermineus). 54

Figure 2.2. Map of sample localities for marine gastropods analyzed in this study. 55

Figure 2.3. $\delta^{18}O$ sclerochronology and reconstructed $\delta^{18}O$-temperatures (colored) and seasonally targeted Δ_{47}-temperatures (black) for marine gastropods analyzed in this study..... 56

Figure 2.4. $1/T^2$-Δ_{47} calibration plots for marine gastropods analyzed in this study. 57

Figure 2.5. Shell-averaged reconstructed $\delta^{18}O_w$ values for marine gastropods analyzed in this study. 58

Figure 2.6. Δ_{47}/Δ_{48} data for all marine gastropods analyzed in this study. 59

Figure 2.7. Δ_{47}/Δ_{48} offsets from equilibrium as defined in Fiebig et al. (2021) for marine gastropods analyzed in this study. 60

Figure 2.8. Previously reported and new Δ_{47}-paleotemperatures from (A) Late Cretaceous, and (B) Eocene fossil gastropods. 61

Figure S2.1. Pictures of shells of marine gastropods analyzed in this study. 64

Figure S2.2. $\delta^{18}O$ sclerochronology and seasonally targeted Δ_{47}-temperatures from sample BM2 (Cittarium pica). 65

Figure S2.3. $1/T^2$ calibration plot for sample C2 (Campanile symbolicum), using assigned calibration temperatures reported from a local Geographe Bay temperature cited in de Winter et al. (2020). 66

Figure S2.4. Shell-averaged reconstructed $\delta^{18}O_w$ values for marine gastropods analyzed in this study 67

Figure S2.5. $\delta^{18}O_w$ residuals averaged by genus. 68

Figure S2.6. Δ_{47}/Δ_{48} offsets from equilibrium as defined in Fiebig et al. (2021) for marine gastropods analyzed in this study. 69

Figure S2.7. Δ_{48} residuals averaged by genus from compared to the Fiebig et al. (2021) (A) and Swart et al. (2021) (B) calibration lines. 70

Figure S2.8. Δ_{47}/Δ_{48} offsets from equilibrium as defined in Fiebig et al. (2021) for marine gastropods analyzed in this study. 71

Figure S2.9. Δ_{47}/Δ_{48} data for the 2 Eocene *Campanile giganteum* shells measured in this study. 72

Figure S2.10. $\delta^{18}O$-reconstructed vs. instrumental seasonality (World Ocean Atlas) cross plot for marine gastropods analyzed in this study. 73

Figure 3.1. Map of sample sites and simplified composite stratigraphic cross-section of the Cocinetas Basin deposits (Jimol and Castilletes Formations) spanning the Mid-Miocene Climatic Optimum (MMCO), adapted from Moreno et al. (2015) and Scholz et al. (2020). 103

Figure 3.2. Δ_{47}-temperatures (A) and reconstructed $\delta^{18}O_{sw}$ ('$\delta^{18}O_{rsw}$') values (B) for the modern turritellids measured in this study, with Δ_{47} and $\delta^{18}O_{rsw}$ offsets (i.e., measured minus predicted) from both this study and Quizon et al. (2025) displayed in (C). 104

Figure 3.3. Isotopic data from the seven fossil turritellids measured in this study. 105

Figure 3.4. Adjusted Mid-Miocene turritellid Δ_{47}-temperatures calculated by adding the 6°C offset observed from modern turritellids in Quizon et al. (2025) (A); average $\delta^{13}C$ values (B) and intra-shell $\delta^{18}O$ ranges (C) from all Miocene turritellid sclerochronology profiles reported in Scholz et al. (2020). 106

Figure S3.1. Photos of the modern specimens (628A, 628B) and the locations on the shells where samples were collected. 110

Figure S3.2. Δ_{47}-temperatures (A) and reconstructed $\delta^{18}O_{sw}$ ('$\delta^{18}O_{rsw}$') values for the modern turritellids measured in this study, with Δ_{47}-temperatures calculated using the 'UNICAL' equation from Petersen et al. (2019). Average Δ_{47}-temperature offsets from modern SSTs and upwelling temperatures are 3.2 +/- 7.9°C and -1.2 +/- 7.9°C, respectively. 111

Figure S3.3. Isotopic data from the seven fossil turritellids measured in this study. 112

Figure S3.4. Adjusted Mid-Miocene turritellid Δ_{47}-temperatures calculated by adding the 6°C offset observed from modern turritellids in Quizon et al. (2025), with Δ_{47}-temperatures calculated using the 'UNICAL' equation from Petersen et al. (2019). 113

Figure S3.5. Disequilibrium plots (i.e., offsets of measured values from predicted values) for turritellids measured in this study (purple) and previously by Quizon et al. (2025) (green). 114

Figure S3.6. Δ_{47}-temperature calibration from Anderson et al., 2021 overlain with modern turritellid data from this study and Quizon et al. (2025). 115

Figure S3.7. $\delta^{18}O$ sclerochronology (grey circles) and Δ_{47} measurements (black squares) for modern turritellid samples 628A (top) and 628B (bottom). 116

Figure 4.1. Sample locations. 133

Figure 4.2. Stacked histogram distributions of water sample (a) salinity and (b) $\delta^{18}O_w$ values. 134

Figure 4.3. Box plots of (A) $\delta^{18}O_w$ and (B) salinity from the SeaSOx dataset, separated by geographic region. 135

Figure 4.4. $\delta^{18}O_w$ (A) and salinity (B) measurements versus latitude along the U.S. Eastern Seaboard, excluding samples in the SeaSOx dataset collected from West Florida. 136

Figure 4.5. $\delta^{18}O_w$-salinity data for samples collected in the SeaSOx dataset. 137

Figure S4.1. $\delta^{18}O_w$ (A) and salinity (B) measurements versus latitude along the U.S. Eastern Seaboard, colored by year of sampling campaign. 141

Figure 5.1. Map of localities from which fossil samples were obtained and analyzed, colored by apparent ages of deposits. Abbreviations for site names can be found in Table 5.1. 175

Figure 5.2. Layer-averaged AAR data for *Mercenaria* sp. analyzed in this study. 176

Figure 5.3. Reconstructed isotopic temperatures and $\delta^{18}O_w$ values for all samples analyzed in this study 177

Figure 5.4. Reconstructed isotopic temperatures and $\delta^{18}O_w$ values for MIS5e-dated fossils in this study. 178

Figure 5.5. Reconstructed isotopic temperatures and $\delta^{18}O_w$ values for MIS5e-dated fossils in this study. 179

Figure 5.6. Reconstructed isotopic temperatures and $\delta^{18}O_w$ values for MIS5e- and MIS5a-dated fossils from the mid-coastal region (i.e., Virginia to South Carolina). 180

Figure S5.1. Raman spectra for all seven shells measured in this study and calcite and aragonite RRUFF standards. 190

Figure S5.2. $\delta^{18}O$ sclerochronology profiles for select *Mercenaria* sp. in this study. 191

Figure S5.3. $\delta^{13}C$ sclerochronology profiles for select *Mercenaria* sp. in this study. 192

Figure S5.4. Δ_{47} sclerochronology profiles for select *Mercenaria* sp. in this study. 193

Figure 6.1. Map and simplified cross-section of the Sankaty Head Cliff deposits at Nantucket Island, Massachusetts (41.28°N, 69.96°W), adapted from Oldale et al. (1982). 219

Figure 6.2. Average amino acid racemization (AAR) data from *Mercenaria mercenaria* from the Upper (blue) and Lower (red) Sands analyzed in this study. 220

Figure 6.3. $\delta^{18}O_{carb}$ (A) and $\delta^{13}C_{carb}$ (B) sclerochronology data for four shells: two from the Lower Sand, and two from the Upper Sand. 221

Figure 6.4. Bulk Δ_{47} and high-resolution (HR) Δ_{47} sclerochronology temperature (A) and reconstructed seawater $\delta^{18}O$ ('$\delta^{18}O_{rsw}$') (B) data from both the Lower and Upper Sands of the Sankaty Head Cliff deposits. 222

Figure S6.1. Map of water samples measured for salinity and $\delta^{18}O_{sw}$ measurements collected from the Boston and Cape Cod regions in Massachusetts in the SeaSOx dataset (Quizon et al., in prep). 224

Figure S6.2. Pictures of all seven shells measured in this study and corresponding sampling methods applied to each shell. 225

Figure S6.3. Raman spectra for all seven shells measured in this study and calcite and aragonite RRUFF standards. 226

Figure S6.4. Amino acid racemization (AAR) data and corresponding table from all *Mercenaria* sp. samples analyzed in this study (A), including the JW-83-69 (Upper Sand) and JW-83-96 (Lower Sand) colored in grey which are likely contaminated as evident in higher than expected L-Ser/L-Asp values (>0.2) (B). 227

Figure S6.5. $\delta^{18}O_{carb}$ -temperature data (A), 3-point averaged Δ_{47}-temperature data (B), and 3-point averaged reconstructed $\delta^{18}O_{sw}$ ($\delta^{18}O_{rsw}$) data (C) for samples JW-83-88 and JW-83-69.. 228

Figure S6.6. $\delta^{18}O$-temperature sclerochronology data for four shells: two from the Lower Sand and two from the Upper Sand. 229

Figure S6.7. $\delta^{13}C_{carb}$ versus $\delta^{18}O_{carb}$ data for samples measured for $\delta^{18}O$ and Δ_{47} sclerochronology. 230

Abstract

Stable oxygen isotope measurements ($\delta^{18}O$) are important tools in studies of climate, oceanography, and hydrology of today and the past. $\delta^{18}O$ in fossil marine carbonates ($\delta^{18}O_{carb}$) is used to reconstruct past ocean temperatures, and seawater $\delta^{18}O$ ($\delta^{18}O_w$) tracks with salinity and is used to interpret hydrological variability. However, $\delta^{18}O_{carb}$-temperature estimates rely on assumptions of how $\delta^{18}O_w$ varied in the past, which remains uncertain. 'Clumped' isotope thermometry (Δ_{47}) measurements are independent of $\delta^{18}O_w$, allowing us to circumvent this uncertainty and reconstruct past ocean temperatures and $\delta^{18}O_w$ when combined with $\delta^{18}O_{carb}$. This dissertation explores innovations in the utility of these isotopic tools and enhances our knowledge of modern analogs against which we can better interpret new data.

Chapter 2 investigates the viability of Δ_{47} in marine gastropods – an archive largely unexplored for Δ_{47}-paleotemperature reconstructions. These findings suggest that many gastropods precipitate their shells in isotopic equilibrium and accurately record environmental temperatures. However, several gastropods abundant in the fossil record appear to exhibit vital (disequilibrium) effects, resulting in Δ_{47}-temperatures cooler or warmer than actual environmental temperatures. Therefore, caution should be used before using these genera for Δ_{47}-paleotemperature reconstructions.

Chapter 3 expands on the finding from Chapter 2 that turritellids appear to exhibit a vital effect-induced cold bias, reporting Δ_{47}-temperatures from 2 modern and 7 fossil (Mid-Miocene, ~18-14 Ma) turritellids from Colombia. The Δ_{47} data from the modern turritellids support the previous finding of a ~6°C cold bias. After a +6°C adjustment is applied to Mid-Miocene Δ_{47}-

temperatures, adjusted Δ_{47}-temperatures align with previously published estimates in the region, highlighting the potential to use turritellids for paleoclimate reconstructions with the vital effect-based corrections.

Chapter 4 explores the utility of $\delta^{18}O_w$ as a tracer for the Labrador and Gulf Stream boundary currents in the North Atlantic. 358 new salinity and $\delta^{18}O_w$ measurements are reported from along the Eastern Seaboard, nearly tripling the number of existing data in the region. Paired $\delta^{18}O_w$-salinity data show distinct signatures for the Labrador Current and Gulf Stream roughly separated at Cape Hatteras, North Carolina. These data support the application of $\delta^{18}O_w$ as a tracer of these currents and increase our knowledge of spatial and temporal variability that will inform interpretations of Δ_{47}-derived paleo-$\delta^{18}O_w$.

Chapter 5 expands on the findings from Chapter 4 through exploration of the ability of Δ_{47}-derived paleo-$\delta^{18}O_w$ to track the Labrador Current and Gulf Stream in the past. Fossil quahogs (*Mercenaria* sp., ~130-115 ka and ~80 ka) from 9 localities along the Eastern Seaboard were analyzed and showed that paleo-$\delta^{18}O_w$ latitudinal trends generally align with the modern $\delta^{18}O_w$ latitudinal gradient. These findings showcase the potential of Δ_{47}-derived paleo-$\delta^{18}O_w$ to track water masses in the past.

Chapter 6 uses Δ_{47}-derived paleotemperatures and paleo-$\delta^{18}O_w$ to interpret paleoclimatological and paleohydrological variability in Nantucket, Massachusetts during the Last Interglacial (~130-115 ka). 7 *Mercenaria* across 2 Last Interglacial shell beds document paleotemperatures warmer than today and paleo-$\delta^{18}O_w$ values significantly depleted relative to modern, with paleo-$\delta^{18}O_w$ values increasing over time. This is consistent with substantial freshwater input (i.e., ice sheet melt) and subsequent ice sheet retreat over the interglacial.

Altogether, this dissertation builds on the existing framework of Δ_{47} and $\delta^{18}O_w$ as paleoclimatic and paleoceanographic tools by expanding their application to new carbonate archives (i.e., marine gastropods) and proposing new ways to interpret paleo-$\delta^{18}O_w$ data (i.e., paleocirculation, past ice sheet melt).

Chapter 1 Introduction

1.1 Overview and motivation

Since the industrial revolution, global temperatures on Earth have been rising steadily. Most recently, global temperatures from 2014-2023 increased by 0.26°C, resulting in a temperature anomaly of +1.81°C with respect to preindustrial levels (Forster et al., 2024); these trends are largely attributed to rapidly increasing emissions of greenhouse gases such as CO_2. Now more than ever, it has become necessary to investigate the processes and feedbacks that shape climate variability. In particular, our oceans play an important role in regulating global climate via processes such ocean circulation, ice volume changes and albedo feedbacks, and carbon cycling. Climate scientists and oceanographers have looked to the geologic past (i.e., paleoclimate and paleoceanography) during times when temperatures were warmer than today to find analogs for our future climate (Tierney et al., 2020). To do so, researchers utilize a variety of archives such as ice cores, sediment cores, tree rings, and fossils to reconstruct environmental conditions from the past.

One longstanding proxy measurement in the fields of paleoclimate and paleoceanography is that of stable oxygen isotopes ($\delta^{18}O$). Long-term $\delta^{18}O$ records from marine carbonate fossils are fundamental to our understanding of Earth's temperature evolution throughout history (Zachos et al., 2001; Lisiecki and Raymo, 2005). $\delta^{18}O$ describes the ratio of heavier ^{18}O atoms (i.e., isotopes) to the lighter ^{16}O isotopes in a sample, all relative to the same ratio in a community standard, as shown in the following expression:

$$\delta^{18}O_{samp} = (([^{18}O/^{16}O]_{samp}/[^{18}O/^{16}O]_{standard}) - 1) \times 1000 \qquad \text{Eqn. 1.1}$$

In the 1940s, researchers discovered an inverse relationship between the $\delta^{18}O$ of calcium carbonate formed ($\delta^{18}O_{carb}$) and the temperature at which that carbonate formed, caused by temperature-dependent fractionation of the isotopes (Urey, 1947). Paleoclimatologists applied this principle to the carbonate precipitation processes of biogenic calcifiers (e.g., foraminifera, corals, mollusks) (e.g., Epstein et al., 1953; Emiliani, 1955; Shackleton, 1967; Weber and Woodhead, 1972; Grossman and Ku, 1986) and other naturally occurring carbonates (e.g., speleothems, soil carbonates) (e.g., Gascoyne, 1992; Cerling, 1984), creating the framework for $\delta^{18}O$-based paleothermometry (i.e., past temperature reconstruction) in a variety of environments.

However, paleoclimatologists have long-recognized the uncertainties associated with $\delta^{18}O$-based temperature reconstructions – specifically, uncertainties in assumed values of the $\delta^{18}O$ of the precipitating fluid. For marine calcifiers, their carbonate exoskeletons are formed from naturally occurring Ca^{2+} and CO_3^{2-} ions in seawater, meaning that the $\delta^{18}O_{carb}$ signature recorded in the carbonate is a function of not only seawater temperature but also seawater $\delta^{18}O$ ($\delta^{18}O_w$). To correctly apply $\delta^{18}O_{carb}$ paleothermometry in the past, assumptions of past $\delta^{18}O_w$ must be made in order to calculate paleotemperatures. As $\delta^{18}O_w$ and salinity are governed by similar hydrological processes (Sharp, 2007) and are thus correlated, many studies have assumed $\delta^{18}O_w$ values based on paleohydrological interpretations (i.e., ice volume changes), sometimes anchoring estimates of past $\delta^{18}O_w$ with modern instrumental $\delta^{18}O_w$ values from nearby the study region. However, these methods of obtaining $\delta^{18}O_w$ often do not take into account spatial or temporal variability.

In recent years, paleoclimatologists have turned to other paleothermometry proxies independent of $\delta^{18}O_w$ to circumvent these uncertainties. One notable advancement over the past

two decades is 'clumped' isotope thermometry (Δ_{47}). 'Clumped' isotopes refer to bonds between two heavy isotopes (i.e., ^{18}O-^{13}C in carbonates), and the abundance of carbonate molecules containing these 'clumped' isotope bonds has been shown to be inversely correlated with carbonate formation temperature (Ghosh et al., 2006; Schauble et al., 2006; Eiler, 2007). Δ_{47} measurements are calculated with the following expression:

$$\Delta_{47} = (R_{47} / R_{47}^* - 1) \times 1000 \quad \text{Eqn. 1.2}$$

where R_{47} is the abundance ratio of heavier mass-47 CO_2 (primarily $^{13}C^{18}O^{16}O$) to the lighter and much more abundant mass-44 CO_2 (primarily $^{12}C^{16}O^{16}O$). R_{47}^* reflects this same ratio, but the distribution of heavy isotopes is defined from a stochastic, or random, distribution (Eiler, 2007). The advantage of Δ_{47}-based paleothermometry over $\delta^{18}O_{carb}$-based paleothermometry is that Δ_{47} measurements are independent of variations in $\delta^{18}O_w$. By combining Δ_{47} with $\delta^{18}O_{carb}$ measurements – which are inherently measured as part of Δ_{47} calculations – this enables reconstructions of past $\delta^{18}O_w$ in addition to more accurate paleotemperatures.

Mollusks are frequently used in paleoclimate studies that report Δ_{47}-temperatures, as they are fairly abundant in the fossil record. Most modern mollusks have been shown to exhibit Δ_{47} equilibrium signatures (e.g., Henkes et al., 2013; Caldarescu et al., 2021; Huyghe et al., 2022; Schlidt et al., 2025), making these measured species viable for Δ_{47}-temperature reconstruction. Previous studies have measured Δ_{47} in mollusks to reconstruct paleotemperatures and paleo-$\delta^{18}O_w$ values from periods such as the Cretaceous (e.g., Jones et al., 2022; deWinter et al., 2025), the Eocene (e.g., Kniest et al., 2024; Schlidt et al., 2025), and the Pleistocene (e.g., Zhang et al., 2021; Winkelstern et al., 2025), among others.

In this dissertation, I present new Δ_{47} data from several species of modern and fossil marine gastropods – a class of mollusks largely unexplored for this geochemical proxy. I also present new modern instrumental $\delta^{18}O_w$ and Δ_{47}-derived paleo-$\delta^{18}O_w$ measurements from the U.S. Eastern Seaboard, filling in data gaps in the region and advancing the viability of reconstructed $\delta^{18}O_w$ as a tool to track ocean circulation and ice sheet melt in the past. Altogether, this thesis advances the utility of Δ_{47} and $\delta^{18}O_w$ as tools for paleoclimate and paleoceanography research.

1.2 Sampling methods

Isotopic measurements from mollusk shells can be obtained from an assortment of methods (Fig. 1.1), all of which consist of using a dental drill at a low speed to extract calcium powder from the shell. The first isotopic sampling method applied to mollusks used in this dissertation is a bulk, or 'life-average', Δ_{47} measurement. This consists of drilling a transect along the growth axis of the shell – or a drill hole on the underside of the shell – to extract a single powder, effectively capturing growth conditions over a major portion of the organism's lifespan (typically ~1-2 years in the mollusks measured for this dissertation). Life-average Δ_{47}-temperatures are compared to mean annual temperature (MAT) conditions.

The second sampling method is a high-resolution method broadly referred to in the community as sclerochronology (e.g., Johnson et al., 2025). This consists of serially drilling along the growth axis of the mollusk for sequential carbonate powder samples, effectively capturing growth conditions over the organism's lifespan at a seasonal scale. $\delta^{18}O$ sclerochronology is quite common in the field for seasonal-scale paleotemperature reconstructions, though recent studies (e.g., Zhang et al., 2023) have proposed the use of Δ_{47}

sclerochronology, as it allows for simultaneous reconstruction of seasonal-scale paleotemperatures and paleo-$\delta^{18}O_w$ values.

The final mollusk isotopic sampling method used in this dissertation is a seasonally targeted Δ_{47} measurement, which is treated as an intermediate measurement between the two sampling approaches mentioned above. Δ_{47} sclerochronology provides captures seasonal-scale variations in detail but is time-intensive, as Δ_{47} measurements require far more instrument time than traditional $\delta^{18}O$ measurements. Instead, one can obtain a seasonal-scale temperature profile from $\delta^{18}O$ sclerochronology and re-drill powders at the apparent winter and summertime positions for seasonally targeted Δ_{47} measurements.

In addition to these mollusk isotopic sampling methods, this dissertation also includes measurements from modern water isotope sampling methods. This consists of collecting modern ocean water samples in Nalgene vials sealed airtight and later measuring these samples for $\delta^{18}O_w$ in the lab. These modern $\delta^{18}O_w$ measurements are compared to Δ_{47}-derived paleo-$\delta^{18}O_w$ throughout the dissertation.

1.3 Research questions and outline of the dissertation chapters

1.3.1 Do marine gastropods precipitate in 'clumped' isotope equilibrium and faithfully record environmental temperatures (Chapter 2)?

One factor all marine paleoclimatologists working on fossil marine archives must consider is that the measured carbonates are biogenic in origin, meaning that biologic controls can influence geochemical signatures in addition to chemical and environmental controls. These biological factors are broadly referred to in the paleoclimate community as vital effects or disequilibrium effects, or – with respect to isotope geochemistry – "biologically driven isotopic fractionations" (BioDIFs; Curley et al., 2023). Various carbonate archives such as corals (e.g.,

Davies et al., 2022) and speleothems (e.g., Bajnai et al., 2020) have been shown to exhibit disequilibrium effects, biasing their Δ_{47} signatures and thus reconstructed isotopic temperatures.

Marine gastropods are a relatively unexplored archive for Δ_{47} paleothermometry, despite having tremendous potential as a paleoclimate archive. Before this study, it was unclear if marine gastropods tended to precipitate their shells in or out of isotopic equilibrium and thus if they faithfully record environmental temperatures. Chapter 2 reports Δ_{47} (and another 'clumped' isotope measurement, Δ_{48}) data from a suite of marine gastropods across the phylogenetic tree with sample localities spanning the globe to investigate these questions.

Chapter 2 was published in *Geochimica et Cosmochimica Acta* (Quizon et al., 2025).

1.3.2 Do all turritellid gastropods exhibit vital (disequilibrium) effects, and can these biases be corrected for in the fossil record (Chapter 3)?

Chapter 2 demonstrated the likely presence of vital (disequilibrium) effects during turritellid carbonate precipitation, as turritellid Δ_{47}-temperatures were cooler than not only sea surface temperatures but also local upwelling temperatures. However, some of these samples have vague documentation about their collection sites, and these conclusions come from a limited number (4) of modern turritellids. Furthermore, due to a general paucity of fossil turritellid Δ_{47} data in the literature it remained unclear if the cold bias could be corrected for in the fossil record to reconstruct more accurate paleotemperatures.

Chapter 3 expands on these previous findings by introducing Δ_{47} data from two (2) more modern turritellids and seven (7) Mid-Miocene fossil turritellids from the Guajira Peninsula and Colombia. These data were originally collected on a different instrument than those from Chapter 2 and were thus used to determine the presence of an instrument-specific bias. Pulling

data across both studies together, these data tell a clearer story about vital effects in turritellids and the potential for vital effect-based adjustments to correct for the cold bias.

Chapter 3 is in preparation for submission to *Geology*.

1.3.3 Is there a latitudinal $\delta^{18}O_w$ gradient that aligns with the latitudinal salinity gradient along the U.S. Eastern Seaboard, and can $\delta^{18}O_w$ signatures distinguish the Labrador Current and Gulf Stream (Chapter 4)?

As previously stated, oceans play an integral role in regulating global climate, especially through global ocean circulation patterns. Deep water masses are known to exhibit distinct temperature and salinity signatures, mostly due to density gradients; surface currents also exhibit distinct temperature and salinity signatures, though these trends are driven by regional surface processes (e.g., ice sheet melt, evaporation). The surface boundary currents along the U.S. Eastern Seaboard – the Labrador Current and the Gulf Stream – play a huge role in regulating regional climate, with intensifying Gulf Stream waters contributing to more frequent and more intense hurricanes in recent years (e.g., Baluguru et al., 2022). The aforementioned regional surface processes produce a latitudinal salinity gradient in this region, and the positioning of these boundary currents results in a sharp, distinct boundary in salinity between these two water masses. Therefore, salinity can be used as a tracer for these water masses.

Paleoceanographers have attempted to use various proxies to reconstruct ocean circulation patterns and track water masses. Salinity is not readily recorded in the fossil record, but $\delta^{18}O_w$ – which has been demonstrated to be regionally correlated with salinity (e.g., Sharp, 2007) – is. However, existing modern instrumental $\delta^{18}O_w$ data in the North Atlantic are sparse, were sporadically collected, and were measured using outdated analysis procedures and standardization practices. These existing data do not fully capture a latitudinal $\delta^{18}O_w$ gradient

and are incapable of distinguishing between the Labrador Current and the Gulf Stream. Chapter 4 reports a comprehensive, high-resolution dataset of 358 new salinity and $\delta^{18}O_w$ measurements along the U.S. Eastern Seaboard to fill in these data gaps and to investigate these research questions.

Chapter 4 is in review at *(Nature) Scientific Data*.

1.3.4 What were paleoclimate and paleoceanographic conditions along the Atlantic Coastal Plain during Marine Isotope Stage 5, and can we use Δ_{47}-derived paleo- $\delta^{18}O_w$ values to distinguish the Labrador Current and Gulf Stream (Chapter 5)?

Marine Isotope Stage 5 (MIS5) is thought to have been a dynamic Pleistocene interglacial period, beginning with peak warmth during substage MIS 5e (~130-115 ka) – largely thought to be a potential 'analog' for future climate, given that it was the most recent time the Earth was as warm as it is today – and terminating with substantial cooling and ice sheet growth during substage MIS 5a (~80 ka). Numerous studies have reported global paleotemperature estimates from MIS 5e (e.g., Turney et al., 2020); MIS 5a estimates are much scarcer. However, data from both periods of time are generally lacking along the Atlantic Coastal Plain – a climatologically relevant region, as highlighted in Chapter 4. Furthermore, Chapter 4 highlights the potential of $\delta^{18}O_w$ as a regional water mass tracer (i.e., distinguishing between the Labrador Current and Gulf Stream), and in turn there is potential for Δ_{47}-derived paleo-$\delta^{18}O_w$ to be used as a paleo-water mass tracer.

Chapter 5 reports Δ_{47}-derived paleotemperature and paleo-$\delta^{18}O_w$ estimates from fossil mollusks (*Mercenaria* spp.) collected from various MIS 5e- and MIS 5a-dated sites along the Atlantic Coastal Plain. These data fill in the large data gap that exists in MIS 5 literature, especially at the regional level. This chapter outlines the climatological and oceanographic trends

from these data during both MIS 5e and MIS 5a and details the potential of Δ_{47}-derived paleo-$\delta^{18}O_w$ to track the Labrador Current and Gulf Stream during these time intervals.

Chapter 5 is in preparation for submission to *Paleoceanography and Paleoclimatology*.

1.3.5 How did paleoclimate and paleoceanographic conditions evolve over the Last Interglacial at Nantucket, Massachusetts (Chapter 6)?

The Sankaty Sand deposits located on the southeastern end of Nantucket, Massachuetts have tremendous potential to shed light on Pleistocene glacial-interglacial climate and ocean dynamics, as this site is located on what was the terminal moraine of the Laurentide Ice Sheet during the Last Interglacial (i.e., MIS 5e) (e.g., Verrill, 1875; Wilson, 1906). Previous studies have reported qualitative climate histories for the two layers contained within these deposits based on faunal evidence; however, there are no quantitative paleotemperature estimates from this site. Chapter 6 reports Δ_{47}-derived paleotemperature and paleo-$\delta^{18}O_w$ from these Sankaty Sand deposits and contextualizes these data within the existing framework of climate change and oceanographic processes over the course of the Last Interglacial.

Chapter 6 is in preparation for submission to *Geology*.

1.4 Summary

The five content chapters presented here build and improve on existing efforts to advance the utility of Δ_{47} and $\delta^{18}O_w$ as isotopic tools. The viability of Δ_{47} thermometry is explored in marine gastropods (Chapter 2) and specifically turritellids (Chapter 3), as they have largely been overlooked as an archive for this proxy. The applications of modern $\delta^{18}O_w$ and Δ_{47} paleo-$\delta^{18}O_w$ measurements as tracers of ocean circulation (Chapters 4 and 5) and ice sheet melt (Chapter 6) are investigated and discussed in the context of Pleistocene paleoenvironmental reconstructions.

Altogether, this work advances these relatively novel geochemical tools for future paleoclimate and paleoceanography research endeavors.

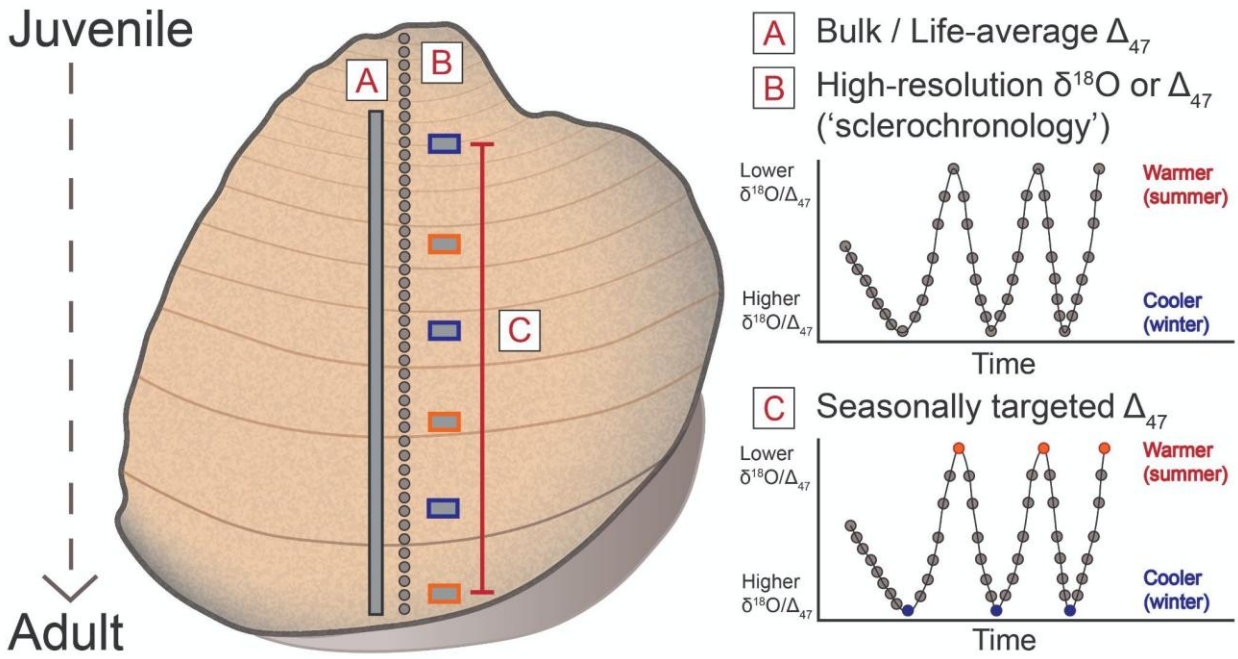

Figure 1.1. Schematic of isotopic methods applied to mollusk samples throughout this dissertation.

1.5 References

Bajnai, D., Guo, W., Spötl, C., Coplen, T. B., Methner, K., Löffler, N., Krsnik, E., Gischler, E., Hansen, M., Henkel, D., Price, G. D., Raddatz, J., Scholz, D., Fiebig, J., 2020. Dual clumped isotope thermometry resolves kinetic biases in carbonate formation temperatures. Nature Communications 11, 4005.

Baluguru, K., Foltz, G.R., Leung, L.R., Xu, W., Kim, D., Lopez, H., West, R., 2022. Increasing Hurricane Intensification Rate Near the US Atlantic Coast. Geophysical Research Letters 49(20), e2022GL099793.

Caldarescu, D.E., Sadatzki, H., Andersson, C., Schäfer, P., Fortunato, H., Meckler, A.N., 2021. Clumped isotope thermometry in bivalve shells: A tool for reconstructing seasonal upwelling. Geochimica et Cosmochimica Acta 294, 174-191.

Cerling, T.E., 1984. The stable isotopic composition of modern soil carbonate and its relationship to climate. Earth and Planetary Science Letters 71(2), 229-240.

Curley, A.N., Petersen, S.V., Edie, S.M., Guo, W., 2023. Biologically driven isotopic fractionations in bivalves: from palaeoenvironmental problem to palaeophysiological proxy. Biological Reviews 98(4), 1016-1032.

Davies, A.J., Guo, W., Bernecker, M., Tagliavento, M., Raddatz, J., Gischler, E., Flögel, Fiebig, J., 2022. Dual clumped isotope thermometry of coral carbonate. Geochimica et Cosmochimica Acta 338, 66-78.

de Winter, N.J., al Fudhaili, N., Arndt, I., Claeys, P., Fraaije, R., Goderis, S., Jagt, J., López Correa, M., Munnecke, A., Stolarski, J., Ziegler, M., 2025. Living on the edge: Response of Late Cretaceous rudist bivalves (Hippuritida) to hot and highly seasonal climate in the low-latitude Saiwan site, Oman. Climate of the Past 21(11), 2361-2387.

Eiler, J.M., 2007. “Clumped-isotope” geochemistry – The study of naturally-occurring, multiply-substituted isotopologues. Earth and Planetary Science Letters 262(3-4), 309-327.

Emiliani, C., 1955. Pleistocene Temperatures. The Journal of Geology 63(6), 538-578.

Epstein, S., Buchsbaum, R., Lowenstam, H.A., Urey, H.C., 1953. Revised Carbonate-Water Isotopic Temperature Scale. GSA Bulletin 64(11), 1315-1326.

Forster, P..M., Smith, C., Walsh, T., et al., 2024. Indicators of Global Climate Change 2023: annual update of key indicators of the state of the climate system and human influence. Earth System Science Data 16(6), 2625-2658.

Gascoyne, M., 1992. Palaeoclimate determination from cave calcite deposits. Quaternary Science Reviews 11(6), 609-632.

Ghosh, P., Adkins, J., Affek, H., Balta, B., Guo, W., Schauble, E.A., Schrag, D., Eiler, J.M., 2006. ^{13}C-^{18}O bonds in carbonate minerals: A new kind of paleothermometer. Geochimica et Cosmochimica Acta 70(6), 1439-1456.

Grossman, E.L., Ku, T.-L., 1986. Oxygen and carbon isotope fractionation in biogenic aragonite: Temperature effects. Chemical Geology: Isotope Geoscience section 59, 59-74.

Henkes, G.A., Passey, B.H., Wanamaker Jr., A.D., Grossman, E.L., Ambrose Jr., W.G., Carroll, M.L., 2013. Carbonate clumped isotope compositions of modern marine mollusk and brachiopod shells. Geochimica et Cosmochimica Acta 106, 307-325.

Huyghe, D., Daëron, M., de Rafelis, M., Blamart, D., Sébilo, M., Paulet, Y.-M., Lartaud, F., 2022. Clumped isotopes in modern marine bivalves. Geochimica et Cosmochimica Acta 316, 41-58.

Jones, M.M., Petersen, S.V., Curley, A.N., 2022. A tropically hot mid-Cretaceous North American Western Interior Seaway. Geology 50(8), 954-958.

Kniest, J.F., Davies, A.J., Brugger, J., Fiebig, J., Bernecker, M., Todd, J.A., Hickler, T., Voigt, S., Woodland, A., Raddatz, J., 2024. Dual clumped isotopes from Mid-Eocene bivalve shell reveal a hot and summer wet climate of the Paris Basin. Communications Earth & Environment 5, 330.

Lisiecki, L.E., Raymo, M.E., 2005. A Pliocene-Pleistocene stack of 57 globally distributed benthic $\delta^{18}O$ records. Paleoceanography 20(1), PA1003.

Quizon, A.A., Petersen, S.V., de Winter, N.J., Vellekoop, J., 2025. Clumped isotope thermometry (Δ_{47}) measurements in marine gastropods suggest equilibrium precipitation. Geochimica et Cosmochimica Acta 410, 234-249.

Schauble, E.A., Ghosh, P., Eiler, J.M., 2006. Preferential formation of ^{13}C-^{18}O bonds in carbonate minerals, estimated using first-principles lattice dynamics. Geochimica et Cosmochimica Acta 70(10), 2510-2529.

Schlidt, V., Evans, D., de Winter, N.J., Bernecker, M., Arndt, I., Staudigel, P.T., Davies, A.J., Brand, U., Müller, W., Fiebig, J., 2025. Most bivalves and gastropods calcify indistinguishably from dual clumped isotope equilibrium. Geochimica et Cosmochimica Acta 410, 174-187.

Shcakleton, N., 1967. Oxygen Isotope Analyses and Pleistocene Temperatures Re-assessed. Nature 215, 15-17.

Sharp, Z., 2007. Principles of Stable Isotope Geochemistry. Pearson Prentice Hall, Upper Saddle River, NJ.

Tierney, J.E., Poulsen, C.J., Montañez, et al., 2020. Past climates inform our future. Science 370(6517), eaay3701.

Turney, C.S.M., Jones, R.T., McKay, N.P., van Sebille, E., Thomas, Z.A., Hillenbrand, C.-D., Fogwill, C.J., 2020. A global mean sea surface temperature dataset for the Last Interglacial (129-116 ka) and contribution of thermal expansion to sea level change. Earth System Science Data 12(4), 3341-3356.

Urey, H.C., 1947. The Thermodynamic Properties of Isotopic Substances. Liversidge Lecture, Delivered before the Chemical Society in the Royal Institution on December 1st, 1946, 562-581.

Verrill, A.E., 1875. On the post-Pliocene fossils of Sankaty Head, Nantucket Island, with a note on the geology by S.H. Scudder. American Journal of Science 10, 364-375.

Weber, J.N., Woodhead, P.M.J., 1972. Temperature dependence of oxygen-18 concentration in reef coral carbonates. Journal of Geophysical Research 77(3), 463-473.

Wilson, J.H., 1906. The glacial history of Nantucket and Cape Cod with an argument for a fourth center of glacial dispersion in North America: New York, Columbia University Press, 90p.

Winkelstern, I., Petersen, S., Curran, H.A,. Phillips, C., Quizon, A., Glumac, B., Griffing, D., 2025. Cooling climate across last interglacial high stands on San Salvador and Great Inagua, The Bahamas. The Depositional Record 12(1), e70038.

Zachos, J., Pagani, M., Sloan, L., Thomas, E., Billups, K., 2001. Trends, Rhythms, and Aberrations in Global Climate 65 Ma to Present. Science 292(5517), 686-693.

Zhang, J.Z., Petersen, S.V., Winkelstern, I.Z., Lohmann, K.C., 2021. Seasonally Variable Aquifer Discharge and Cooler Climate in Bermuda During the Last Interglacial Revealed by Subannual Clumped Isotope Analysis. Paleoceanography and Paleoclimatology 36(6), e2020PA004145.

Zhang, J.Z., Petersen, S.V., 2023. Clumped and oxygen isotope sclerochronology methods tested in the bivalve *Lucina pensylvanica*. Chemical Geology 620, 121346.

Chapter 2 Clumped Isotope Thermometry (Δ_{47}) Measurements in Marine Gastropods Suggest Equilibrium Precipitation

2.1 Abstract

The clumped isotope paleothermometer (Δ_{47}) has been used to reconstruct temperatures from various biogenic carbonate archives. Calibration studies demonstrate that some biogenic carbonates precipitate in Δ_{47} equilibrium and record growth temperatures accurately (e.g., many bivalve mollusks), while others appear to exhibit disequilibrium, or 'vital', effects and yield isotopically reconstructed temperatures that are biased (e.g., shallow-water corals). These studies have largely excluded marine gastropods, so it is not known whether they tend to precipitate their shells in or out of isotopic equilibrium. In this study, we present seasonal-scale $\delta^{18}O$ and seasonally targeted Δ_{47} and Δ_{48} measurements from modern marine gastropods representing 8 genera and 10 species, reconstructing apparent growth temperatures and screening for equilibrium precipitation. We find that most marine gastropods appear to precipitate in Δ_{47} and Δ_{48} equilibrium and faithfully record environmental temperatures, making them suitable for Δ_{47}-paleothermometry. A few gastropods (*Caviturritella/Turritella* sp., *Campanile symbolicum*, *Megastraea undosa*) appear to precipitate out of Δ_{47} equilibrium, though these disequilibrium signatures may partially be explained by differences between actual growth temperatures and instrumental calibration temperatures (*Caviturritella/Turritella* sp., *M. undosa*) or differences between inner and outer layer precipitation (*C. symbolicum*). We present new Δ_{47}-temperature data for 2 Middle Eocene *Campanile giganteum* fossils collected from the Paris Basin and discuss how to interpret the results in the context of our modern samples. Finally, in

conducting this calibration we demonstrate paired Δ_{47}/Δ_{48} as an effective tool to screen for disequilibrium precipitation in marine gastropods.

2.2 Introduction

Ocean temperature is a fundamental parameter of Earth's climate system, impacting other climatological factors such as air temperature, heat transport, humidity, and cloud formation. Paleotemperature proxies allow us to obtain quantitative paleotemperature estimates from geologic periods representing vastly different climate states, thereby allowing us to investigate the limits of Earth's climate system. However, these proxies must be properly and rigorously calibrated to accurately reconstruct ocean paleotemperatures. One such proxy is the carbonate 'clumped' isotope paleothermometer (Δ_{47}) that has seen increased use over the past decade, where 'clumped' isotopologues refer to molecules containing two or more heavy isotopes (e.g., between ^{13}C and ^{18}O in $CaCO_3$). The formation of clumped isotopologues is thermodynamically favored over formation of singly-substituted isotopologues due to a greater reduction in zero-point-energy (Urey, 1947, Bigeleisen and Mayer, 2004, Eiler, 2007). The authors who proposed the proxy (Ghosh et al., 2006, Schauble et al., 2006, Eiler, 2007) suggest that the excess abundance of 'clumped' isotopologues relative to a stochastic distribution of isotopologues in the carbonate mineral lattice is directly related to formation temperature, with the important caveat that precipitation must occur in chemical, single-phase clumped isotopic and solid–fluid $\delta^{18}O/\delta^{13}C$ equilibrium. Development of this paleothermometer has thus far focused on the isotopologues of mass-47 CO_2 derived from various carbonates (primarily $^{13}C^{18}O^{16}O$), denoted by Δ_{47}, although the theory applies equally to all multiply substituted isotopologues. The community has recently developed and calibrated clumped isotope thermometry using higher mass isotopologues, expanding to include mass-48 CO_2, denoted by Δ_{48} (i.e., CO_2 derived from

$CaCO_3$ with a composition of mainly $^{12}C^{18}O_2$) (Fiebig et al., 2019, Fiebig et al., 2021), and even mass-49 CO_2, denoted by Δ_{49} (Bernecker et al., 2023).

The relationship between Δ_{47} and temperature is well-defined by molecular theory and corroborated through empirical calibrations of many types of carbonates. Benchmark calibrations of the Δ_{47} paleothermometer have been based on synthetic carbonates (e.g., Ghosh et al., 2006, Kluge et al., 2015, Kelson et al., 2017, Petersen et al., 2019, Anderson et al., 2021). Further calibrations focusing on several types of biogenic carbonates including coccolithophores (e.g., Tripati et al., 2010, Katz et al., 2017; Clark et al., 2024), foraminifera (e.g., Breitenbach et al., 2018, Meinicke et al., 2020, Peral et al., 2018, Piasecki et al., 2019, Tripati et al., 2010), eggshells (e.g., Eagle et al., 2015, Wacker et al., 2014), otoliths (e.g., Ghosh et al., 2007, Prasanna et al., 2021), and bivalve mollusks (e.g., Henkes et al., 2013, Eagle et al., 2013, Petrizzo et al., 2014, Huyghe et al., 2022, de Winter et al., 2022) compare well to data from synthetic carbonates. These 'well-behaved' biogenic carbonates follow the same Δ_{47}-temperature relationship as synthetic carbonates, with the minor variations between recent 'unifying' calibration studies (Bernasconi et al., 2018, Petersen et al., 2019, Jautzy et al., 2020, Anderson et al., 2021) shown to be within uncertainty of each other when errors are fully propagated (Daëron and Vermeesch, 2023). This consistency in the Δ_{47}-temperature relationship across such a wide range of carbonates gives us confidence in reconstructed paleotemperatures derived from applying Δ_{47} paleothermometry to fossil biogenic carbonates.

Absent from the biogenic carbonates listed above are gastropods – an underexplored fossil archive for Δ_{47} paleothermometry with substantial potential to expand our paleoclimate records. Gastropods are the most diverse class in the mollusk phylum, as there are hundreds of fossil gastropod families, some of which existed as early as the late Cambrian (Bouchet et al.,

2017). They live in diverse habitats, from mudflats to the subtidal zone to even deep-sea hydrothermal vents (e.g., Dyer, 1998, Underwood, 1979), opening up possibilities of paleoenvironmental reconstruction in more varied past environments. While over 10 terrestrial gastropod genera have been measured for Δ_{47} (e.g., Wang et al., 2016, Zhai et al., 2019, Bricker et al., 2023, Bao et al., 2023, Guo et al., 2024), only 2 marine (Henkes et al., 2013, Winkelstern et al., 2017, Zhang et al., 2021) and no freshwater gastropods have been measured for Δ_{47} to date.

Previous Δ_{47} calibration studies measuring modern marine gastropods with known environmental temperatures were conducted on the species *Conus ermineus* (Henkes et al., 2013) and *Cittarium pica* (Winkelstern et al., 2017, Zhang et al., 2021). Both studies concluded that Δ_{47}-temperatures were within error of instrumental temperatures, but uncertainty remains given that some of these data were collected prior to current best practices of standardization. For example, updating *C. ermineus* data (Henkes et al., 2013) using IUPAC parameters (Petersen et al., 2019) led Δ_{47}-temperatures from this species to deviate further from instrumental temperatures than in the initial study. Additionally, although the mean was within uncertainty of the true modern mean temperature, Δ_{47} data from *C. pica* (Zhang et al., 2021) suggested this species may display as much as a 3–6°C cold bias.

In terrestrial gastropods, some Δ_{47} calibration studies show good agreement with environmental temperatures if species- or season-specific calibrations are used (Wang et al., 2016, Zhang et al., 2018, Zhai et al., 2019, Bricker et al., 2023, Guo et al., 2024). Other studies suggest that Δ_{47}-temperatures are several degrees warmer than observed environmental temperatures (Zaarur et al., 2011, Dong et al., 2021). However, it remains unclear whether this observed warm bias is due to eco-physiological effects − i.e., darker-colored shells heating up

faster than lighter-colored shells (Zaarur et al., 2011), or body temperature up-regulation in colder environments (Guo et al., 2019) − or disequilibrium precipitation effects (Dong et al., 2021, Bao et al., 2023).

Disequilibrium precipitation behavior has been observed in some types of biogenic carbonates, as indicated by Δ_{47} values that deviate from established Δ_{47}-temperature relationships. To date, disequilibrium precipitation has been observed in cephalopods (Dennis et al., 2013, Davies et al., 2021), corals (Eiler, 2007, Thiagarajan et al., 2011, Saenger et al., 2012, Tripati et al., 2015, Spooner et al., 2016, Kimball et al., 2016, Guo et al., 2020, Davies et al., 2022), brachiopods (Came et al., 2014, Bajnai et al., 2018, Davies et al., 2023), juvenile oysters (Huyghe et al., 2022), cultured coccoliths (Clark et al., 2025), bryozoans (Pesnin et al., 2024), and the inner shell layers of some bivalves (Curley et al., 2023). These offsets have been hypothesized to derive from various mechanisms such as rapid precipitation of $CaCO_3$ (Huyghe et al., 2022), CO_2 absorption and degassing during calcification (Bajnai et al., 2020), and rapid switching between dissolution and precipitation from a finite-volume calcifying fluid (Curley et al., 2023). However, exact mechanisms have been challenging to pin down with only Δ_{47} and carbonate $\delta^{18}O$ to work with, as arguments are sometimes circular given the dual influence of temperature and the isotopic composition of the precipitating fluid ($\delta^{18}O_{water}$ or '$\delta^{18}O_w$') on carbonate $\delta^{18}O$ ($\delta^{18}O_{carb}$). For example, it is not always possible to determine the 'equilibrium' $\delta^{18}O_{carb}$ value and quantify a disequilibrium offset if there are substantial uncertainties in both $\delta^{18}O_w$ and temperature.

The clumped isotope community has recently developed a new method to identify and quantify the extent of disequilibrium precipitation in a new, more robust way using the paired analysis of Δ_{47} with Δ_{48}. Like Δ_{47}, Δ_{48} values are controlled by formation temperature

independent of the composition of the precipitating fluid. A given formation temperature corresponds to a unique pair of Δ_{47} and Δ_{48} values, tracing out an equilibrium curve in Δ_{47}/Δ_{48} space (Fiebig et al., 2019, Fiebig et al., 2021). If a carbonate precipitates in Δ_{47}/Δ_{48} equilibrium, its Δ_{47} and Δ_{48} compositions should fall on this equilibrium curve, specifically on the defined Δ_{47}/Δ_{48} coordinates corresponding to the true formation temperature. Disequilibrium growth conditions will push both Δ_{47} and Δ_{48} values away from their predicted position on the equilibrium curve to a lesser or greater degree depending on the extent of disequilibrium. For an unknown sample, the position in Δ_{47}/Δ_{48} space is a function of both formation temperature *and* the extent of disequilibrium due to kinetic effects.

Molecular theory can predict Δ_{47}/Δ_{48} departures from the equilibrium curve under different disequilibrium conditions and link Δ_{47}/Δ_{48} signatures to specific disequilibrium precipitation mechanisms (Guo, 2020). While an offset from equilibrium in Δ_{47} alone identifies the presence of a 'vital' effect or biologically-derived isotopic fractionation (BioDIF, Curley et al., 2023), combined offsets from equilibrium in both Δ_{47} and Δ_{48} can point to a specific disequilibrium precipitation mechanism. Recent studies have reported Δ_{47}/Δ_{48} measurements from speleothems (e.g., Bajnai et al., 2020), shallow-water corals (Bajnai et al., 2020, Davies et al., 2022), brachiopods (Bajnai et al., 2020, Davies et al., 2023), dolomites (Lu and Swart, 2024), amorphous carbonate precursors (Lucarelli et al., 2023), freshwater cements (Lu et al., 2024), and microbial autotrophy (Ingalls et al., 2024), all of which plot away from the Δ_{47}/Δ_{48} equilibrium curve in different directions with unique slopes, indicating different disequilibrium precipitation mechanisms in action.

Moving forward, proper interpretations of Δ_{48} data will require more rigorous, community-wide calibration efforts. It has been roughly 20 years since the first

Δ_{47} measurements have been published, resulting in Δ_{47} as a well-established paleothermometry method. International carbonate standards exist that cover a large range of δ^{47} and Δ_{47} space (Bernasoni et al., 2018), and a community-wide effort has determined Δ_{47} values for these standards. These values have been calibrated against gas standards (Dennis et al., 2011) and, through this, against theory (Bernasconi et al., 2021). Differences in Δ_{47} due to reacting samples at different acid digestion temperatures have been quantified in many studies (e.g., Defliese et al., 2015, Kelson et al., 2017, Petersen et al., 2019, Wacker et al., 2014). Unlike Δ_{47}, the field of Δ_{48} is much newer. Calibrated values for the circulated carbonate standards have only been published by 3 labs (Swart et al., 2021, Lucarelli et al., 2023, Fiebig et al., 2024). Furthermore, the carbonate standards do not span a wide range in Δ_{48}, requiring use of heated gases or low Δ_{48} carbonate standards like GU1. Most previously published values correspond to powders reacted at 90°C excluding some values reported in Bernecker et al. (2025) (i.e., Δ_{48} for calcite, aragonite, and witherite reacted at 90°C and 110°C), so hardly any quantification of differences in Δ_{48} due to different acid digestion temperatures has been done. Any lab reacting at a different temperature must grapple with this challenge before proceeding with interpretations of Δ_{48} relative to 90°C-anchored equilibrium lines.

In this study, we present subannual $\delta^{18}O$ and seasonally-targeted Δ_{47} and Δ_{48} records from selected modern marine gastropods representing 8 genera and 10 species. We compare seasonal Δ_{47} values to those expected from instrumental temperatures and determine which gastropods produce expected Δ_{47} values. We present the first estimate of the acid fractionation factor between 70°C and 90°C for Δ_{48}. After correcting our Δ_{48} data into a 90°C reference frame, we determine which species precipitate in Δ_{47}/Δ_{48} equilibrium. We also present new Δ_{47}-temperature data from 2 *Campanile* fossils dated to the middle Eocene. In doing this calibration,

we demonstrate the effectiveness of Δ_{47}/Δ_{48} as a tool to screen for disequilibrium precipitation in marine gastropods and give guidance on which marine gastropods may be viable targets for paleoclimate studies.

2.3 Materials and methods

2.3.1 Sample selection

Marine gastropods from 10 species across 8 genera were sampled in this study (Fig. 2.1): *Campanile symbolicum*, *Busycon carica*, *Sinistrofulgur perversum*, *Strombus alatus*, *Turritella (s.s.) bacillum*, *T. duplicata*, *Caviturritella gonostoma*, *C. leucostoma*, *Megastraea undosa*, and *Austrofusus glans*. We combine these new samples with data from previous studies targeting the species *Cittarium pica* (Zhang et al., 2021) and one targeting *Conus ermineus* (Henkes et al., 2013), bringing the total count to 12 species across 10 genera. *C. pica* was first measured by Winkelstern et al. (2017) but lacked clear calibration temperatures due to the way in which the shell was sampled. The same shells were re-drilled by Zhang et al. (2021), so we report re-processed data from this later study only.

These species represent various trophic levels, feeding, and motility behaviors. They inhabit common growth depths, employ different burrowing and tiering strategies, and grow to adult body sizes ranging from ~2.5 cm to ~13 cm in shell height. Samples were loaned from the University of Michigan Museum of Zoology (*Caviturritella/Turritella* sp.), collected by coauthors (*C. symbolicum*, *S. perversum* from Hollywood Beach, Florida), or obtained from citizen science beach collections (all other species), with collection localities spanning the globe (Fig. 2.2). *S. perversum* shells were collected from three sites in Pawleys Island, SC (SPer1), Boca Raton, FL (SPer2), and Hollywood Beach, FL (SPer3). The *B. carica* shell (BCar1) was collected from the same site as SPer1. The *A. glans* shell was collected from Mount Maunganui,

New Zealand (Au1). Three *S. alatus* shells were collected from two sites – two from Bonita Springs, FL (Str1, Str2) and one from Tampa, FL (Str3). The *M. undosa* shell was collected from Rincon Beach, CA (Meg1). Of shells loaned from the University of Michigan Museum of Zoology, the *C. gonostoma* and *C. leucostoma* shells were originally collected from Acapulco, Mexico (T1, T2), the *T. (s.s.) bacillum* shell was collected from Sri Lanka (T3), and the *T. duplicata* shell was collected from Tharangambadi, India (T4). The *C. symbolicum* shell was collected from Geographe Bay, Australia, with collection and habitat details previously reported in de Winter et al. (2020). More specific locality information can be found in Table S2.1 and pictures can be found in Fig. S2.1.

2.3.2 Subannual oxygen and carbon isotope sclerochronology

To reconstruct seasonality, ~20–30 powders were drilled per shell, with the total number depending on shell size. ~50 ug of powder was collected every 1–100 mm, with larger distance intervals used on larger shells, along the surface of each shell's spiral growth axis. Drilling was conducted using a low-speed dental drill, with care taken not to penetrate to interior layers which may have precipitated at a different time and/or from a different growth fluid, which therefore may not reflect seasonal environmental changes. Sampling began at the aperture in all cases and traced out anywhere from ~4 cm to ~25 cm of spiral growth. This resulted in sampling at least 1 and as many as 4 seasons of growth, depending on the shell. For larger shells, the 20–30 samples represented only a fraction of the total lifespan was captured, whereas for smaller shells (e.g., *Caviturritella*/*Turritella* sp.) most to all the mollusk's lifespan was captured.

All sample powders were analyzed for $\delta^{18}O$ and $\delta^{13}C$ using a Kiel IV automated carbonate device attached to a Thermo-Finnegan MAT 253 or DELTA V dual inlet mass spectrometer at the University of Michigan Stable Isotope Lab. Data were standardized against

NBS-18 and NBS-19 with units reported in per mille (‰) relative to the VPDB standard. Uncertainty was routinely better than 0.1‰ for both oxygen and carbon isotopes. Seasonal $\delta^{18}O$ profiles for *Caviturritella/Turritella* sp. were previously published in Scholz et al. (2024) and for *C. symbolicum* in de Winter et al. (2020).

2.3.3 Seasonally targeted clumped isotope measurements (Nu)

Zones of minimum and maximum $\delta^{18}O$ values were identified based on the oxygen isotope profiles and re-drilled to collect a larger amount of powder (~20 mg) for Δ_{47} and Δ_{48} analysis. This translated to 2–10 clumped isotope samples per shell depending on shell lifespan and size. This sampling scheme assumes seawater $\delta^{18}O$ ($\delta^{18}O_w$) values were constant or minimally varying throughout the year and that $\delta^{18}O$ maxima and minima therefore correspond to wintertime and summertime extreme conditions, respectively. If $\delta^{18}O_w$ varied throughout the year, it is possible that identified $\delta^{18}O_{carb}$ extrema may not correspond to seasonal temperature extrema (e.g., Caldarescu et al., 2021; de Winter et al., 2021).

Clumped isotope measurements were conducted using a NuCarb automated sample preparation device connected to a Nu Perspective mass spectrometer in the University of Michigan Stable Isotope Lab following procedures described by O'Hora et al. (2022) and Jones et al. (2022). Individual 3–4 mg aliquots of sample powder were reacted with phosphoric acid in individual vials at 70°C to produce CO_2, which was then purified for Δ_{47} and Δ_{48} analysis through two water traps and a Porapak-filled trap also containing silver wool. Δ_{47} and Δ_{48} data were collected in 'bellows mode' at a major ion beam current of 80nA, consistently maintained for 80 sample-reference cycles by continuous bellows adjustment. The shot noise limits for Δ_{47} and Δ_{48} are 0.0074‰ and 0.0248‰ respectively under this instrumental setup. A small

subset of Δ_{47} and Δ_{48} data from the *Campanile* sample were collected on a different mass spectrometer (see Section 2.3.4).

Sample powders were analyzed at least three times each. Measured Δ_{47} and Δ_{48} values were calculated from raw voltages through an R-code script (RDevelopment CORE TEAM, 2008) using updated IUPAC parameters following Petersen et al. (2019). During all sample measurement windows, Δ_{47} values were corrected into the I-CDES90 reference frame using ETH standards. First, ETH1 and ETH2 were used to calculate the δ_{47} vs. Δ_{47} slope (SlopeEGL), accounting for the 0.0033‰ difference in the defined InterCarb values for these standards (Bernasconi et al., 2021). Second, replicate-level data from all four ETH standards were used to determine the slope and intercept of the empirical transfer function using InterCarb values (Bernasconi et al., 2021). Δ_{48} values were corrected into a 'GU-CDES90′ reference frame using a similar two-step correction procedure. In addition to the four ETH standards, the low-Δ_{48} standard GU1 (Fiebig et al., 2021) was analyzed and included in the transfer function to better anchor the regression. 'True' Δ_{48} values for carbonate standards have been defined against gas standards by different labs (Swart et al., 2021, Lucarelli et al., 2023, Fiebig et al., 2024). We processed our data using the anchor values for ETH 1–4 from Swart et al. (2021) and Fiebig et al. (2024). We exhibit these data corrected using the anchor values from Swart et al. (2021) in the main figures and in the text but show versions of relevant Δ_{48} tables and figures corrected with the anchor values from Fiebig et al. (2024) in the Appendices.

Heated (1000°C) and equilibrated (25°C) gas standards (Dennis et al., 2011) were run alongside carbonate standards for a single measurement window within the larger study interval. Gas standards from within this 'calibration window' were used to independently calculate Δ_{47} and Δ_{48} values for the ETH standards and GU1 in the gas-based reference frame. To increase

the fidelity of the δ_{47} vs. Δ_{47} slope calculation, ETH1 and ETH2 were included in addition to the gas standards, but only gas standards were used to calculate the transfer function (see Appendices). Theoretical equilibrium (TE) values for Δ_{47} and Δ_{48} for heated (1000°C) and equilibrated (25°C) gases were derived from the supplementary table of Petersen et al. (2019) and Huntington and Petersen (2023), respectively, which are updated versions of calculations originally done by Wang et al. (2004). These $\Delta_{47\text{-TE}}$ and $\Delta_{48\text{-TE}}$ values were 0.0266‰ and −0.0020‰ for heated gases and 0.9198‰ and 0.3422‰ for equilibrated gases, respectively. This $\Delta_{48\text{-TE}}$ value for 25°C gases differs slightly from the value recently used in Fiebig et al. (2021) of 0.345‰.

Because carbonates in the NuCarb are reacted in acid at 70°C, to compare gas-corrected values to published Δ_{47} or Δ_{48} CDES90 values an acid fractionation factor must be applied to adjust for the 20°C difference in acid digestion temperature. For Δ_{47}, a value of 0.022‰ was applied from Petersen et al. (2019). For Δ_{48}, we calculated an acid fractionation factor ($\Delta_{48}{}^{*}{}_{70\text{-}90}$) of 0.0458‰ based on the difference between our calculated CDES70 mean values of ETH1 and ETH2 and the CDES90 values published by Swart et al. (2021) (see Section 2.4).

Throughout the entire study interval, four in-house carbonate standards were analyzed alongside gastropod samples. These include our Carrara Marble (CM), Bahamian Ooids (OO), a fully-crushed *Arctica islandica* bivalve from Iceland (Ice), and a fully-crushed *Cittarium pica* gastropod from Bermuda (Pica) as described previously (O'Hora et al., 2022, Fiebig et al., 2024). We used these to confirm the interchangeability of the carbonate-based I-CDES90/GU-CDES90 and the gas-based CDES90 reference frames (see Section 2.4) and track drift in the carbonate-based reference frames across multiple windows. To adjust for drift in the I-CDES90 and GU-CDES90 reference frames away from the gas-based reference frame over time, we apply

a window-specific fixed offset to all gastropod data using two low temperature standards (Ice, OO), leaving our third low temperature standard (Pica) as a check standard. This window-specific correction was conducted for both Δ_{47} and Δ_{48}. For Δ_{47}, this was done using 'true' values defined over a long period of time in the I-CDES90 reference frame, which is anchored in the gas-based reference frame. For Δ_{48}, this was done using 'true' values defined in the calibration window against gas standards, including the newly defined acid temperature correction of 0.0458‰ (see Section 2.4).

Fully corrected Δ_{47} values were converted to temperatures using the calibration equation from Anderson et al. (2021). Sample mean Δ_{47}-temperatures and $\delta^{18}O_{carb}$ were used to reconstruct Δ_{47}-derived $\delta^{18}O_w$ values for each powder using the mollusk-based equation from Grossman and Ku (1986). We found minor differences between reconstructed $\delta^{18}O_w$ values calculated using the synthetic aragonite equation from Kim et al. (2007) and the mollusk equation from Grossman and Ku (1986), so we only report values calculated using the equation from Grossman and Ku (1986). Errors on Δ_{47}-temperatures are reported as 95% confidence intervals using the long-term standard deviation of in-house standards after applying the window-specific correction and the number of replicate analyses for each sample powder. Long-term standard deviation is defined by combining up to 5 in-house carbonate standards at the replicate level to account for the variable number of replicates for each standard; the long-term standard deviation values for Δ_{47} and Δ_{48} are 0.0172‰ and 0.0752‰, respectively. For each carbonate standard replicate, the true value was first subtracted and then one standard deviation of these offsets was calculated combining all replicates of all standards. Uncertainty on Δ_{47}-derived $\delta^{18}O_w$ values was calculated based on the maximum and minimum possible $\delta^{18}O_w$ values considering 95% confidence intervals on temperature and $\delta^{18}O_{carb}$.

2.3.4 Seasonally targeted clumped isotope measurements (MAT 253)

Seasonally targeted samples C2-1 to C2-10 from the *Campanile symbolicum* shell were collected from the columella corresponding to points from the outer shell $\delta^{18}O$ profile. These samples were analyzed on two different mass spectrometers. Initial Δ_{47} analyses for samples C2-1 to C2-10 were conducted on a Thermo MAT 253, with sample preparation performed on a manual off-line preparation device described in Defliese et al. (2015). Samples were reacted with phosphoric acid in a common acid bath held at 75°C to produce CO_2 and purified for Δ_{47} analysis through two water traps and a Porapak-filled trap containing silver wool. Measured Δ_{47} values were calculated from raw voltages through the R-code script from Petersen et al. (2019). Δ_{47} values were converted into the absolute reference frame by applying a non-linearity correction using equilibrated (25°C) and heated CO_2 gas (1000°C) standards (Dennis et al., 2011). Unfortunately, Δ_{48} data from this instrument were not reliable enough to be considered. In-house standards Carrara marble and Ooids were run and used to determine a long-term SD in Δ_{47} of 0.0266‰. Samples C2-8, C2-9, and C2-10 from this shell were analyzed for both Δ_{47} and Δ_{48} on the Nu Perspective, as described in Section 2.3.3. The small amount of remaining powder from samples C2-1 to C2-7 were analyzed using 'coldfinger mode' on the Nu Perspective for both Δ_{47} and Δ_{48}. 'Coldfinger mode' sample preparation follows the same procedures as bellows mode, but the sample size range is ~250–300 ug. After purification, the gas is frozen into a cold finger adjacent to the changeover block. Reference gas fills an identical cold finger to a matching pressure. Pressures decline in tandem over 60 cycles. The shot noise limits for Δ_{47} and Δ_{48} are 0.0152‰ and 0.0511‰ respectively. Two (2) of 152 replicates were run in coldfinger mode – one for shell T3 and one for shell C2. Despite the larger uncertainty on coldfinger measurements,

these were averaged with bellows mode replicates; doing so does not affect our overall conclusions.

O'Hora et al. (2022) showed that Δ_{47} data from these two machines and sample preparation setups are interchangeable, so can be readily combined. Therefore, Δ_{47} values from all replicates of a given powder were averaged, regardless of instrument or mode. Only samples C2-8 to C2-10 have enough replicates analyzed with well-constrained Δ_{48} values to be interpreted on their own. The Δ_{48} values from the few replicates of samples C2-1 to C2-7 were included in the whole-shell average but not plotted as individual points due to prohibitively large uncertainties in Δ_{48} when only one or two replicates of a given powder were analyzed.

2.3.5 Previously published Δ_{47} data from marine gastropods

The data for both C. ermineus and C. pica presented here have been published in previous work. The $\delta^{18}O$ sclerochronology and Δ_{47}-temperature data for C. ermineus sample FGS-1 have previously been reported in Henkes et al. (2013), and the Δ_{47} data were re-processed by Petersen et al. (2019). The $\delta^{18}O$ sclerochronology (Winkelstern et al., 2017) and Δ_{47}-temperature data (Zhang et al., 2021) for C. pica sample BM2 have been previously published, while we present new data from a second C. pica shell (sample BM1). These data were analyzed at the University of Michigan on the MAT 253 using the methods described above.

2.3.6 Assigning calibration temperatures and $\delta^{18}O_w$ values

Instrumental summer and winter temperatures for each collection site were selected from the World Ocean Atlas (WOA) 2018 dataset (2005–2017 period, 1/4° resolution, monthly means) (Locarnini et al., 2019) for comparison to seasonally targeted Δ_{47}- and Δ_{48}-temperatures. Most gastropods species in this study live close to the surface, although some live deeper than others (Fig. 2.1). To account for depth, each calibration temperature was determined by

averaging temperatures over each species' known depth range in the grid cell nearest the collection site. Northern hemispheric winter (southern hemispheric summer) temperatures were calculated by averaging December, January, and February (DJF) monthly temperatures; Northern hemispheric summer (southern hemispheric winter) temperatures were calculated by averaging June, July, and August (JJA) monthly temperatures (Table S2.1). Predicted Δ_{47}/Δ_{48} equilibrium values for a given sample were calculated using the calibration equations from Fiebig et al. (2021) and the WOA18-based summer or winter temperature, or in some cases mean annual temperature when summer and winter extrema could not clearly be identified – i.e., first point of SPer2, second and third points of Str1. From $\delta^{18}O$ sclerochronology, the *B. carica* (BCar1) sample appeared to exhibit growth only during summers, so we calibrated all 3 Δ_{47}/Δ_{48} measurements from this sample to instrumental summer temperatures.

Instrumental $\delta^{18}O_w$ values were gathered from the NASA GISS $\delta^{18}O_w$ database (see Table S2.2) and interpolated $\delta^{18}O_w$ model output based off this dataset (LeGrande and Schmidt, 2006, Breitkreuz et al., 2018) for comparison to reconstructed Δ_{47}-derived $\delta^{18}O_w$ values. Seasonal-scale and shell-mean Δ_{47}-derived $\delta^{18}O_w$ values were compared to both the closest real $\delta^{18}O_w$ measurement and the interpolated value from the closest grid cell. Neither the NASA GISS database nor the interpolated model from LeGrande and Schmidt, 2006 reported seasonal variations in $\delta^{18}O_w$, so the same instrumental value was assigned for all seasons at all sites.

2.3.7 Statistical analysis of Δ_{47} residuals from the Anderson et al., 2021 calibration

To discern whether reconstructed Δ_{47}-temperatures deviated from established Δ_{47}-temperature relationships by a statistically significant amount, we applied a statistical method to determine if genus averages of Δ_{47} residuals were offset from the Anderson et al.

(2021) calibration line. First, we gathered our measured Δ_{47} sample means and analytical uncertainties (i.e., 95% CI based on long-term 1SD across the measurement interval). For samples analyzed on the MAT253, we applied a conservative +/- 0.03‰ error bar based on long-term standard deviation in Δ_{47} from the Carrara marble and Ooids standards over the measurement window. We considered analytical uncertainty for the *C. pica* and *C. ermineus* samples as +/- 2SE based on long-term 1SD Δ_{47} across their respective measurement intervals. Second, we calculated a predicted Δ_{47} value and uncertainty for each sample based on WOA-derived calibration temperatures and corresponding uncertainty (see Table S2.1). Next, we subtracted predicted Δ_{47} from measured Δ_{47} and propagated the errors to determine if genus-averaged signatures deviated from the calibration line, considering all these sources of uncertainty. Finally, we calculated the following statistics averaged by genus: weighted mean of the Δ_{47} residuals, weighted standard error, z-score, and p-value (Table S2.6). A p-value <0.05 suggests that the genus average is significantly different from 0. A similar differencing method was used to calculate whether genus weighted diverged significantly from Δ_{47}/Δ_{48} equilibrium as defined in Fiebig et al., 2021 (Tables 2.S7 and 2.S8).

2.3.8 Eocene Campanile data and processing

Two *Campanile giganteum* Eocene fossils (E1, E2) were collected from the Fleury-la-Rivière locality in France, with full details regarding sample physiology and site collection described in de Winter et al. (2020). Seasonality ranges for both E1 and E2 were previously estimated through subannual $\delta^{18}O$ sclerochronology as part of that initial study. E1 and E2 were re-drilled at seasonal extrema from the columella to collect larger amounts of powders for four and nine seasonally targeted Δ_{47} measurements, respectively. These Δ_{47} measurements were analyzed on the Nu Perspective using the procedures outlined in Section 2.3.3.

2.4 Results

2.4.1 Δ_{48} – gas-based vs. carbonate-based reference frames & acid fractionation factor calculation

Within the calibration window, the gas-based reference frame (i.e., including ETH1/ETH2 to define SlopeEGL) was used to define CDES70 values for the ETH standards and GU1 (Table 2.1). $\Delta_{48}{}^{*}{}_{70\text{-}90}$ was estimated by calculating the average offset of our raw Δ_{48} ETH1 and ETH2 values from published values. We find an average offset of 0.0458‰ when using ETH 'true' values from Swart et al. (2021) (Table 2.1) and 0.066 ‰ using 'true' values from Fiebig et al. (2024) (Table S2.4). Calculating SlopeEGL using only gases (i.e., without ETH1 and ETH2) does not significantly change these values.

When this $\Delta_{48}{}^{*}{}_{70\text{-}90}$ value is applied, ETH3 and ETH4 are brought into agreement with published values at the 1SE level (see Appendices). In-house standards also produce Δ_{48} values that are indistinguishable at the 1SE level between the carbonate-based GU-CDES90 reference frame and the gas-based CDES90 reference frame. This confirms that all Δ_{48} values calculated using the GU-CDES90 reference frame may be directly compared to CDES90 values from other labs and to published CDES90-anchored theoretical equilibrium lines (e.g., Fiebig et al., 2021). This is true whether we use the Δ_{48} values from Swart et al. (2021) or Fiebig et al. (2024), although the specific values differ.

Reproducibility (i.e., long-term 1SD) within the calibration window is around 0.044–0.053‰ in Δ_{48}, as demonstrated by in-house carbonate standards (excluding GU1, which reproduces more poorly at 0.056‰). This is better than performance across the entire study interval, where the long-term 1SD reproducibility of ETH standards is 0.065–0.080‰ after application of the window-specific corrections.

On average, uncorrected in-house standard values were determined to be higher than the Δ_{48} CDES90 values defined in the calibration window, by 0.029‰ on average. ETH3, the low temperature anchor not included in the offset calculation, also originally appeared too high on average by a similar amount (0.036‰ too high) prior to the correction. After application of the window-specific correction, the long-term average for ETH3 was error of the 'true' value: 0.2574‰ +/- 0.0054‰ (1SE, n=141) compared to 0.2690‰ +/- 0.015‰ (95% CI, n=20) (Swart et al., 2021). Mean Δ_{48} values for Pica, the check standard not included in any step of the correction, improved from an offset of 0.0436‰ to 0.0075‰ in Δ_{48} relative to CDES90 values. At the same time as clear improvement occurred for ETH3 and Pica, the fixed-offset approach to this window-specific correction reduced ETH1-2 by too much, moving corrected values farther away from the CDES90 known values. As the offsets were defined by two low temperature in-house standards, they best reflect bias in data within the low temperature range. Future studies using high temperature unknowns may need to take a different approach to window-specific corrections, perhaps including a compositionally dependent offset.

Application of the window-specific offset correction improved reproducibility of in-house standards slightly, from ~ 0.0757‰ to ~ 0.0726‰. Unlike Δ_{47}, which showed comparable reproducibility within the calibration window and across all windows, Δ_{48} reproducibility is worse over longer timescales, indicating our correction schemes may not be capturing all forms of drift.

2.4.2 Δ_{47} – gas-based vs. carbonate-based reference frames

Within the calibration window, in-house standards produce Δ_{47} values that are indistinguishable at the 1SE level between the carbonate-based I-CDES90 and gas-based CDES90 reference frames (Table 2.2). This confirms that all Δ_{47} values calculated using the I-

CDES90 reference frame may be directly compared to CDES90 values from other labs and to published CDES90-anchored theoretical equilibrium lines (e.g., Fiebig et al., 2021).

Reproducibility (i.e., long-term 1SD) within the calibration window is around 0.015–0.017‰ in Δ_{47}, as demonstrated by in-house carbonate standards (excluding GU1, which reproduces more poorly at 0.023‰). This is similar to performance across the entire study interval, where the long-term reproducibility of in-house standards is 0.015–0.019‰, excluding GU1 at 0.0276‰.

On average across the entire study interval, uncorrected in-house standard I-CDES90 values for Δ_{47} were determined to be slightly higher than the CDES90 Δ_{47} values defined in the calibration window by ~ 0.005‰ on average, a much smaller offset than in Δ_{48}. After application of the window-specific offset correction based on in-house carbonate standards Ice and Ooids, mean Δ_{47} values for Pica – the check standard that was not used in the window-specific corrections – improved from an offset of 0.0032‰ to 0.0003‰ in Δ_{47} relative to the CDES90 defined value. This again supports the application of the offset corrections.

2.4.3 $\delta^{18}O$ sclerochronology

The $\delta^{18}O$ sclerochronology data show fluctuations consistent with seasonal-scale temperature variability, with mean $\delta^{18}O_{carb}$ values varying with geographic location (Fig. 2.3). Some profiles are smooth and reflect an approximately sinusoidal pattern (e.g., T1), while others are not as smooth (e.g., SPer3). Most shells appear to record 1–2 annual temperature cycles (e.g., Sper2, T1), while the larger *M. undosa* and *C. symbolicum* shells exhibit several more years of growth. Absolute $\delta^{18}O$ values vary from as depleted as ~ -3‰ in *T. duplicata* (India) (Fig. 2.3C) to as enriched as ~ +2‰ in *A. glans* (New Zealand) (Fig. 2.3A). This spatial variability appears

to correlate primarily with $\delta^{18}O_w$ variability across the sampling sites (Table S2.2). As previously mentioned, we observe only apparent summertime growth for the *B. carica* sample (BCar1).

2.4.4 Reconstructed Δ_{47}-temperatures

Several species of gastropods appear to fall on an established Δ_{47}-temperature calibration curve derived from synthetic carbonates (Fig. 2.4A). These include *B. carica*, *S. perversum*, *S. alatus*, and *A. glans*, whose Δ_{47}-temperatures generally align with instrumental seasonality within the 95% CI of the calibration curve. Weighted means of Δ_{47} residuals for these genera are not significantly offset from the Anderson et al., 2021 calibration line (i.e., within weighted 1SE of 0‰) (Fig. 2.4D). Overall, visual observation of Fig. 2.4 and the statistical analysis described above combine to suggest equilibrium precipitation in these species.

In contrast, several other species of gastropods appear to fall off the established Δ_{47}-temperature calibration curve, with clusters of points falling clearly above or below the curve. 7 of 10 *C. symbolicum* points and 6 of 8 *Caviturritella/Turritella* sp. points are colder than their corresponding instrumental temperatures by ~5-10°C, while 6 of 6 *Megastraea undosa* points are warmer than corresponding instrumental temperatures by ~8-13°C. These offsets are large and consistent in the direction of bias within a given species. Weighted means of Δ_{47} residuals for these genera are significantly offset from the Anderson et al., 2021 calibration line (i.e., not within weighted 1SE of 0‰) (Fig. 2.4D), with genus means for *Caviturritella/Turritella* and *Campanile* positively offset (~+0.02‰ for both) and the genus mean for *Megastraea* negatively offset (−0.03‰). However, it is possible that the biases for these species may partially result from incorrectly assigned calibration temperatures as opposed to a 'vital' effect (see Section 2.5.4), making it less clear whether these deviations reflect precipitation out of isotopic equilibrium.

It is unclear whether previously published data from *C. ermineus* or *C. pica* suggest Δ_{47}-equilibrium precipitation. Previously published data from *C. ermineus* fall slightly below the calibration curve (Fig. 2.4C) but still show the expected temperature trend across samples, with the weighted mean of Δ_{47} residuals not significantly offset from the Anderson et al., 2021 calibration line (Fig. 2.4D). Some data points from *C. pica* appear to fall above the calibration curve while others fall on it within error (Fig. 2.4C). The weighted mean of Δ_{47} residuals for *C. pica* (+0.02‰) is significantly offset from the Anderson et al., 2021 calibration line (i.e., not within 1SE of 0‰) (Fig. 2.4D). The in-house standard Pica Δ_{47} value (Table 2.2) is also higher than expected based on the MAT of Bermuda (~23°C, 0.599‰), although this powder contains both inner and outer shell layer material which may introduce bias (Curley et al., 2023).

2.4.5 Reconstructed $\delta^{18}O_w$ values

We compared Δ_{47}-based $\delta^{18}O_w$ values calculated from each shell and compared them to modern instrumental values collected from as close as possible to each sample locality. However, agreement is not guaranteed due to the large distances between sample localities and the closest instrumental $\delta^{18}O_w$ collection sites. For example, we could not identify an instrumental site <500 km from the *A. glans* collection site. For the remainder of our samples, the distance between sample site and instrumental site varies between 0 and ~500 km (see Table S2.2).

For species that exhibit apparent equilibrium precipitation (*B. carica*, *S. perversum*, *A. glans*, *S. alatus*), Δ_{47}-based $\delta^{18}O_w$ values generally align with both instrumental and modeled $\delta^{18}O_w$ values from respective sampling locations (Fig. 2.5). Although the reconstructed $\delta^{18}O_w$ values from shells Sper3 and Str1 appear too low, the values from other samples of these

species (Sper1/SPer2 and Str2/Str3, respectively) largely agree with nearby modeled values and genus-averaged $\delta^{18}O_w$ residuals for these genera (Fig. S2.5) generally fall within error of 0.

On the other hand, for species that do not clearly demonstrate equilibrium precipitation (*Caviturritella*/*Turritella* sp., *C. symbolicum*, *M. undosa*) Δ_{47}-based $\delta^{18}O_w$ values deviate from instrumental and modeled $\delta^{18}O_w$ values (Fig. 2.5). The magnitude of the positive offset in reconstructed $\delta^{18}O_w$ values from *M. undosa* is similar to that from SPer3 and Str1. However, genus-averaged $\delta^{18}O_w$ residuals for *Caviturritella/Turritella* sp. and *Campanile* sp. (Fig. S2.5) are substantially depleted relative to instrumental and modeled values, over > 2‰ in some cases.

2.4.6 Paired Δ_{47}/Δ_{48}

Fig. 2.6 visualizes individual samples relative to the Δ_{47}/Δ_{48} equilibrium curve, but the expected target on the curve differs with calibration temperature (i.e., summer/winter/MAT by locality). We can also quantify and visualize the magnitudes and directions of offsets from Δ_{47}/Δ_{48} equilibrium as deviations, averaged by genus (Fig. 2.7). At the individual powder level, gastropods whose Δ_{47}-temperatures align with environmental temperatures generally fall within error of the Δ_{47}/Δ_{48} equilibrium curve defined by Fiebig et al. (2021). From visual observation, our paired data from *Caviturritella/Turritella* sp. fall further off from the equilibrium curve than other species (Fig. 2.7, Fig. S2.6). However, we find that all genus-averaged Δ_{48} offsets for measured genera are not statistically significant from 0 at the 95% confidence level (Table S2.8).

2.4.7 Fossil Δ_{47} data

In addition to data our modern gastropods, we also present Δ_{47}-paleotemperature data from two Eocene *Campanile giganteum* shells (E1 and E2) collected from the Paris Basin. Samples E1 and E2 show mean annual temperatures of ~22°C and ~24°C respectively (Fig. 2.8). After adding an adjustment of 6°C based on the offsets observed from the modern *C.*

symbolicum (Fig. 2.4), we recalculate mean annual temperatures of these samples as ~28°C and ~30°C, respectively.

2.5 Discussion

2.5.1 Δ_{48} Acid Fractionation Factors (AFFs) and 'true' Δ_{48} values

In this study, we produce the first-ever empirical estimate of a 70°C to 90°C Δ_{48} acid fractionation factor ($\Delta_{48}{}^{*}{}_{70\text{-}90}$) based on differences in calculated ETH1 and ETH2 values between labs. The accuracy of this proposed acid fractionation factor is confirmed by other carbonates measured in this study, regardless of whether ETH anchor values are used from either Swart et al. (2021) or Fiebig et al. (2024). In particular, ETH3, ETH4, and the four in-house carbonate standards, which were not used to determine $\Delta_{48}{}^{*}{}_{70\text{-}90}$, demonstrate remarkable agreement with GU-CDES90 values when this value is applied (Table 2.2).

When comparing our Δ_{48} values and $\Delta_{48}{}^{*}{}_{70\text{-}90}$ calculated using ETH 'true' values from Swart et al. (2021) vs. Fiebig et al. (2024), the gas-based reference frame for comparison remains the same but 'true' ETH values differ, resulting in different $\Delta_{48}{}^{*}{}_{70\text{-}90}$ values and different 'true' values for in-house carbonate standards. All unknowns were corrected by different amounts for the window-specific offset correction. After these procedures were applied, we find that the correction scheme using 'true' values from Swart et al. (2021) brings our in-house carbonate standards (Ice, Ooids) closer to Δ_{47}/Δ_{48} equilibrium (Table 2.2) than the correction scheme using 'true' values from Fiebig et al. (2024) (Table S2.5). Other studies of modern shells from our lab (e.g., Zhang and Petersen, 2023) also fall in better alignment with Δ_{47}/Δ_{48} equilibrium using this correction scheme. Therefore, we report our Δ_{48} data and $\Delta_{48}{}^{*}{}_{70\text{-}90}$ using the correction scheme based on ETH 'true' values from Swart et al. (2021).

Using values from Swart et al. (2021), our CM standard produces a Δ_{48} value of 0.1315‰ +/- 0.0126‰ (1SE, n=12), which is close to but lower than the published value for the Goethe University Carrara standard (0.1455‰ +/- 0.0029‰) or that from UCLA (0.160‰ +/- 0.010‰, 1SE, n=62; Lucarelli et al., 2023). Using the anchor values from Fiebig et al. (2024), this value is 0.1113‰. This remaining observed variability may be due to true isotopic differences in the different powders of this similar carbonate standard, uniquely prepared at each university. This comparison suggests that using anchor values from Swart et al. (2021) produces better agreement with other labs, even the lab at Goethe University.

Application of the 0.0458‰ $\Delta_{48}{}^{*}{}_{70\text{-}90}$ value also moves GU1 closer to but still higher than the published value (−0.3279‰ +/- 0.0154‰, 1SE, n=13 vs. −0.3998‰ +/- 0.0043‰, 1SE, n=149; Fiebig et al., 2024). As ETH4 and GU1 are at opposite ends of the isotopic range and all standards are improved to align with Δ_{47}/Δ_{48} equilibrium when including this acid fractionation factor, there does not appear to be a compositional effect on $\Delta_{48}{}^{*}{}_{70\text{-}90}$ and we may confidently apply $\Delta_{48}{}^{*}{}_{70\text{-}90}$ as a fixed offset to carbonates of any Δ_{48} composition. This confirms the findings from Lucarelli et al. (2023), which report negligible acid temperature-derived compositional dependence on Δ_{48}.

As previously mentioned, the magnitude of the difference between the CDES70 and CDES90 reference frames using the anchor values from Swart et al. (2021) is 0.0458‰. Using the ‘true’ values from Swart et al. (2021) results in a smaller acid fractionation factor than the value calculated using ‘true’ values from Fiebig et al. (2024) (0.066‰), which is closer to the theoretical estimate. Applying this fractionation factor of 0.0458‰ brings our biogenic carbonate standards (Ice, Ooids) closer to the equilibrium line than applying 0.066‰, which brings these standards left of Δ_{47}/Δ_{48} equilibrium (Fig. S2.8).

This value of 0.0458‰ is larger than offsets in Δ_{47} between 70°C and 90°C from experimental calculations (0.022‰; Petersen et al., 2019) and in Δ_{48} between 70°C and 90°C based on theoretical calculations (0.022‰, Guo et al., 2009). Most recently, Bernecker et al. (2025) report 110°C-90°C acid fractionation factors of −0.0147‰ and −0.0148‰ for Δ_{47} and Δ_{48} respectively. The magnitudes of the Δ_{47} values between studies are comparable, and the magnitude of the Δ_{48} acid fractionation factor in Bernecker et al. (2025) (0.0148‰) is considerably smaller than the value used in this study (0.0458‰). While the descriptions and data tables above detail why 0.0458‰ appears to be the correct value to apply in this study, it is possible that this value may include both the true $\Delta_{48}{}^{*}{}_{70\text{-}90}$ acid-derived offset as well as some window-specific component due to inaccuracies in our gas-based reference frame, as this calculation is based on standards from a relatively narrow period of time. The window-specific corrections we apply here tend to move Δ_{48} values lower, which therefore add to and do not counteract the acid correction. Future analyses of gas and ETH standards across multiple measurement windows will help verify the accuracy of this $\Delta_{48}{}^{*}{}_{70\text{-}90}$ value.

2.5.2 Interlaboratory differences in GU1 values

Using the gas-based reference frame, we calculate GU1 CDES90 values of 0.2542‰ and −0.3279‰ for Δ_{47} and Δ_{48}, respectively (Table 2.1, Table 2.2), which are significantly different than those defined by Fiebig et al. (2024) (0.2254‰ for Δ_{47}, −0.3998‰ for Δ_{48}). This difference is seen in Δ_{47}, where calculated values are in the ICDES-90 reference frame and in Δ_{48}, where it is only minorly impacted by use of the values from Swart et al. (2021) or Fiebig et al. (2024). The difference, at least, is present in both a gas-based reference frame and ETH1-4 based reference frames, both of which produce values ~0.03‰ higher than those from Fiebig et al. (2024). The offset in Δ_{48} from published values is also seen in both the gas-based reference and

the ETH1-4 based reference frame which excludes GU1 in the transfer function (see Appendices), both of which produce Δ_{48} values ~0.07‰ higher than those from Fiebig et al. (2024). GU1 also consistently reproduces more poorly than the other carbonate standards, regardless of the reference frame.

Because our Δ_{47} and Δ_{48} values for GU1 did not align with published values, perhaps these offsets are due to something inherent to GU1 and how it reacts in different sample preparation systems (i.e., individual vial vs. common acid bath) or how the reference frame or pressure baseline correction behaves at the outermost ends of the isotopic range. For instance, carbonate powders including the GU1 standard have been shown to facilitate clumped isotope resetting in CO_2 in a common acid bath (Staudigel et al., 2025). It is possible that the time spent pumping samples down is insufficient to remove adsorbed water, allowing GU1 to alter the isotopic composition of CO_2. However, our instrument uses a different sample preparation system, and it is unlikely that our GU1 data were affected in the same way. More focused work with additional standards in this isotopic range could help resolve these questions.

2.5.3 Clear equilibrium precipitation signatures

Our seasonally targeted Δ_{47} and Δ_{48} data suggest that several marine gastropods appear to precipitate in equilibrium and faithfully record environmental temperatures. Individual Δ_{47}-temperatures from *B. carica*, *S. perversum*, *A. glans*, and *S. alatus* fall within the instrumental seasonal range and match assigned instrumental temperatures on the established calibration curve, as observed both qualitatively by eye (Fig. 2.4) and quantitatively through simple statistical analysis (Table S2.6, Fig. 2.4D). We confirm this finding of equilibrium precipitation by pairing Δ_{47} with Δ_{48} (Fig. 2.6, Fig. 2.7). *Busycon/Sinistrofulgur* sp., *Austrofusus* sp., and *Strombus* sp. fall within error of the Δ_{47}/Δ_{48} equilibrium line and have therefore been deemed

'equilibrium calcifiers'. This assertion of equilibrium precipitation is supported by the reconstructed Δ_{47}-based $\delta^{18}O_w$ values for these species which tend to cluster around 0–1‰; this is consistent with isotopic signatures previously measured from North Atlantic water masses (Frew et al., 2000, Zhang and Petersen, 2023). Therefore, we deem these species viable for direct paleotemperature reconstruction.

2.5.4 Possible disequilibrium precipitation signatures

Our seasonally targeted Δ_{47} data show that several marine gastropods exhibit biased reconstructed temperatures and may have precipitated out of equilibrium. Most individual Δ_{47}-temperatures from *Caviturritella*/*Turritella* sp. and *C. symbolicum* fall outside the seasonal instrumental range and do not match assigned calibration temperatures. These data generally fall above the calibration curve (i.e., 'cold bias'), as observed both by eye (Fig. 2.4B) and through statistical analysis (Table S2.6, Fig. 2.4D). On the other hand, all Δ_{47}-temperatures from *M. undosa* fall outside the seasonal instrumental range and fall below the calibration curve, also as observed by eye (Fig. 2.4B) and through statistical analysis (Table S2.6, Fig. 2.4D). This species-specific pattern is unlikely to occur as a result of data correction issues.

If Δ_{47}-temperature data fall off the calibration line, this could be due to: (a) incorrect calibration temperatures; (b) disequilibrium precipitation (i.e., 'vital' effects); (c) both. Instrument effects or differences in sampling methods can also play a role. Using WOA data, *C. symbolicum* appears to exhibit a cold bias on the order of ~5–10°C. However, WOA reports average temperatures and can fail to capture local signals in some regions. A highly local instrumental record from within Geographe Bay itself demonstrates a substantially larger seasonal temperature range of ~13–26°C (Fig. 2.3) (de Winter et al., 2020) than WOA data (~19.6–20.5°C). Even when calibrating *C. symbolicum* to these alternate temperatures, we find

that Δ_{47}-temperatures still generally fall above the Anderson et al., 2021 calibration line (Fig. S2.3), with the statistical analysis using these alternate calibration temperatures also yielding the ~+0.02‰ offset and thus a ~6°C cold bias. Furthermore, if the calibration temperatures were incorrectly assigned, we would expect both Δ_{47} and Δ_{48} to be offset in the same direction. This is seen in 2 of 3 samples (Fig. S2.6), but more samples are needed to define this signature with greater confidence. It is also possible that instrument effects are artificially making these temperatures too cold, as 5 of 7 cooler-than-instrumental temperatures were obtained using the MAT253. Unlike all other modern shells in this study, this shell was drilled from the columella (i.e., inner core) as opposed to the outer shell layer, which may have precipitated from a different fluid than the shell exterior (see Section 2.5.5). Meanwhile, paired Δ_{47}/Δ_{48} data from the Eocene *Campanile giganteum* samples measured in this study, which were also taken from the columella, cluster around the Fiebig et al. (2021) equilibrium curve (Fig. S2.9). However, it is impossible to quantify disequilibrium because 'true' temperatures are not known. These data were also collected from fossil shells belonging to a different *Campanile* species. In summary, although the observed cold bias can partially be attributed to misassigned calibration temperatures or instrumental effects, it is possible that the columella of *C. symbolicum* (and potentially the *Campanile* genus) precipitates out of Δ_{47} equilibrium and exhibits a 'vital' effect.

Caviturritella and *Turritella* may also have lived in highly localized environments with environmental temperatures colder than the surface ocean (WOA) instrumental temperatures reported in Fig. 2.3. *Caviturritella*/*Turritella* sp. are known to live in relatively cold, nutrient-rich regions of the continental shelf (Allmon, 2011), with a necessity for nutrient abundance due to their filter feeding behavior. Evidence that upwelled waters may have been cooler than surface WOA temperatures exists for many of our collection localities.

Studies have reported the presence of upwelling along the coasts of Acapulco, Mexico (e.g., Portela et al., 2018, Chiappa-Carrara et al., 2019), Sri Lanka (e.g., de Vos et al., 2014), and the eastern coast of India (e.g., Ray et al., 2022). At Acapulco Mexico, the Western Mexican Current (WMC) flows northward as a subsurface current at temperatures between 27–30°C (Huante et al., 2018). Below the surface currents is the Subtropical Underwater mass (STUW) between the depths of 100–200 m. STUW temperatures below 20°C between the depths of 100–200 m in this region below are plausible (e.g., 13°C reported in Chiappa-Carrara et al., 2019). If *Turritella*/*Caviturritella* at these sites lived in upwelled deep waters, this would suggest that their growth temperatures would be significantly colder than the calibration temperatures suggested by WOA records.

Around Sri Lanka, seasonal upwelling during the seasonal monsoonal system from June to August has been thought to typically cause ~2–5°C decreases in sea surface temperatures (SSTs) relative to the open ocean average (de Vos et al., 2014), with a low mean SST value of 22.74°C reported by the continental shelf off Southern Sri Lanka (Sandamali et al., 2023). Along the east coast of India adjacent to the southwestern portion of the Bay of Bengal, monsoon winds are thought to drive upwelling from June to September (Ray et al., 2022). The difference between coastal SST and offshore SST ("UI_{SST}") in the Bay of Bengal rarely dips by more than −0.5°C relative to a mean of ~28–30°C, with 'low' SSTs reported at ~25°C (e.g., Muni Krishna, 2008). However, upwelling events in Sri Lanka or the western coast of India are more common than in Bay of Bengal.

These studies suggest it is possible that *Caviturritella*/*Turritella* sp. experienced growth temperatures ~6°C colder than surface ocean instrumental temperatures. However, 3 of the 4 Δ_{47}-temperatures from samples T3 and T4 fall below the lowest of these upwelling temperature

estimates (i.e., >6°C colder). As with *Campanile*, if we assigned incorrect calibration temperatures, we would expect Δ_{47} and Δ_{48} to be offset in the same direction. Because we do not observe statistically significant + Δ_{48} offsets (Fig. S2.7, Table S2.8), a 'vital' effect is likely contributing. We therefore suggest these signatures are likely a combination of both local upwelling effects and disequilibrium precipitation.

The measured *M. undosa* sample could have lived in local environmental temperatures warmer than the open ocean temperatures reported in Fig. 2.3. The relatively cool temperatures in this region are heavily influenced by nearly year-long upwelling off the coast of California (e.g., García-Reyes and Largier, 2010). However, the estimated depth habitat of this species ranges from 0-80 m (Fig. 2.1), and because this was a beach-collected specimen this sample could have lived in an environment influenced by upwelling waters at depth or lived in a smaller pool of still warm water (e.g., tide pool). Once again, if we assigned incorrect calibration temperatures, we would expect Δ_{47} and Δ_{48} offsets in the same direction; we do not observe significant Δ_{48} offsets (Table S2.8) and therefore determine that a 'vital' effect is likely present. Because we only measured one sample for this species, we encourage further study on more shells from this genus.

2.5.5 Preliminary insights into disequilibrium precipitation

The magnitudes and directions of offsets from Δ_{47}/Δ_{48} equilibrium for *Caviturritella*/*Turritella* sp. and *C. symbolicum* are variable (Fig. 2.7), which can potentially give us more specific information about disequilibrium precipitation. Upwelling alone cannot explain the turritellid cold bias and there is likely some degree of disequilibrium precipitation (i.e. 'vital' effect). Previous studies have demonstrated that Δ_{47}/Δ_{48} offset signatures predicted from molecular theory (Guo, 2020) can be linked to specific disequilibrium precipitation mechanisms

(e.g., Bajnai et al., 2020). *Caviturritella*/*Turritella* sp. exhibit positive Δ_{47} but minimal $+\Delta_{48}$ offsets from equilibrium, variable by species. Although the $+\Delta_{48}$ offsets are not statistically significant, it is worth noting that $+\Delta_{47}$/$+\Delta_{48}$ signatures are consistent with previously defined late-stage 'CO_2 degassing' or even 'dissolved inorganic carbon (DIC) diffusion' behavior at the solid–liquid interface (Guo, 2020). To date, only brachiopods (Davies et al., 2023) have been identified as possibly having undergone DIC diffusion during precipitation, and there are limited constraints on kinetic fractionations associated with diffusion. We encourage further study of *Turritella*/*Caviturritella* to elaborate on this potential 'vital' effect.

C. symbolicum exhibits small average $-\Delta_{47}$ and minimal Δ_{48} offsets from equilibrium, though the offsets from individual samples vary greatly. We observe a larger and more consistent positive Δ_{47} offset averaged across all 10 *C. symbolicum* sampling points (Fig. 2.4) and thus defer to these Δ_{47} data for interpretation. Because samples were collected from the columella as opposed to the outer shell layer, it is possible that this potential disequilibrium signature reflects differences in inner versus outer shell layer precipitation as previously observed in other mollusks (Curley et al., 2023).

The measured *M. undosa* shell exhibits $-\Delta_{47}$ and no Δ_{48} offsets. These signatures are not consistent with any disequilibrium precipitation mechanisms previously defined in Guo (2020). Because we only detect this signature from one shell, it is unclear whether this disequilibrium effect is widespread across the genus or whether this signature partially stems from misassigned calibration temperatures. Thus, we encourage further study of shells from this genus to elaborate on equilibrium versus disequilibrium precipitation.

2.5.6 Unclear signatures

Based on our current data, it remains unclear whether the previously published *C. pica* falls on the established Δ_{47}-temperature curve. Both Winkelstern et al., (2017) and Zhang et al. (2021) suggest that *C. pica* is viable for direct paleotemperature reconstruction and unaffected by 'vital' effects. Contradicting these assertions, the reprocessed Δ_{47} data reveal a possible cold bias of 3–6°C (Fig. 2.5), supported by the statistically significant offset from genus averaging (Fig. 2.4D, Table S2.6). However, the *C. pica* standard used to reprocess the Δ_{47} data to the modern reference frame consists of crushed whole shell, meaning that the working powder includes carbonate from the inner layer that may have precipitated out of isotopic equilibrium (Curley et al., 2023). Further, by crushing the whole shell, seasonal growth biases (e.g., growth weighted towards the warm season) in either the outer or inner layer may make our mean annual temperature assignment incorrect.

Previously published *C. ermineus* data shows the expected trend in Δ_{47} with temperature, but absolute values differ from expected given environmental temperatures. This may indicate a disequilibrium bias or may be the result of differences in analytical methods. The lack of paired Δ_{47}/Δ_{48} data prevents distinction between these two possibilities. Although data from Henkes et al. (2013) were updated as best as possible by Petersen et al. (2019), we cannot rule out some impact of differences in measurement technique and/or standardization between this study and other data presented here. Therefore, more work on these data, including the addition of Δ_{48} measurements, is needed to determine whether both *C. pica* and *C. ermineus* should be classified as 'equilibrium' or 'disequilibrium' calcifiers.

2.5.7 Application to paleoclimate

Recent studies have used fossil *Turritella* for Δ_{47}-paleotemperature reconstructions, but our data suggest that these paleotemperature estimates can be influenced by combined upwelling and disequilibrium precipitation, resulting in paleotemperature estimates several degrees cooler than SSTs. Meyer et al. (2018) reconstruct Late Cretaceous (~76–66 Ma) Δ_{47}-temperatures along the Gulf and Atlantic coasts from various mollusks including *Turritella paravertebroides*, with a reported temperature of ~13°C +/- 3°C from a few bulk shell measurements (Fig. 2.8). These bulk Δ_{47}-temperatures are ~4°C cooler than the mean temperature of ~17°C recorded in coeval bivalves, suggesting that upwelling of colder waters could have occurred in the Gulf Coast in the Late Cretaceous and that the cooler temperatures recorded by these *Turritella* may reflect upwelling temperatures as opposed to surface SSTs.

We also present new Δ_{47}-temperature data from 2 *Campanile giganteum* shells, E1 and E2, collected from the Paris Basin and dated to the Lutetian (Eocene) (de Winter et al., 2020); these shells exhibit Δ_{47}-temperatures of ~22°C and ~24°C. These Eocene fossil temperature estimates align with previously published non-$\delta^{18}O$ based paleotemperature ranges from other archives around this region (e.g., Evans et al., 2018) as well as an estimated temperature range from paleoclimate modelling (Hollis et al., 2019) (Fig. 2.8). Because the paired Δ_{47}/Δ_{48} data from these *Campanile giganteum* samples cluster around the Fiebig et al. (2021) equilibrium curve (Fig. S2.9), it is possible that an adjustment may not be necessary for this species (see Section 2.5.5). Adding the 6°C adjustment based on the modern *C. symbolicum* offsets places Δ_{47}-temperatures in the upper end of the estimated temperature ranges from other proxy archives and modelling, while un-adjusted temperatures fall on the lower end of both ranges.

2.6 Conclusions

We find that several marine gastropods (*B. carica*, *S. perversum*, *A. glans*, *S. alatus*) are viable for direct paleotemperature reconstruction using the clumped proxy (Δ_{47}), as they follow the same Δ_{47}-T relationship as other carbonates. *Caviturritella*/*Turritella* sp. exhibit biased Δ_{47}-temperatures and appear to precipitate out of Δ_{47}/Δ_{48} equilibrium, though this is partially due to actual growth temperatures deviating from the instrumental temperatures used for calibration. *C. symbolicum* and *M. undosa* appear to exhibit disequilibrium precipitation, but more shells of these species should be measured to verify this preliminary interpretation. Our results confirm marine gastropods as a suitable archive for paleoclimate reconstruction, though with caution for *Caviturritella/Turritella* sp., *C. symbolicum*, *M. undosa* and previously analyzed gastropods (*C. ermineus*, *C. pica*). These findings have impacts across the paleoclimate community, as many studies utilize archives marine gastropods such as *Turritella* (e.g., Scholz et al., 2024, Banerjee and Ghosh, 2024) and *Campanile* (e.g., de Winter et al., 2020, Willems et al., 2021) to study past climate systems and especially hothouse climates. Δ_{47} and paired Δ_{47}/Δ_{48} were crucial tools to screen for equilibrium versus disequilibrium precipitation in these gastropods. To properly evaluate our Δ_{48} data in the established CDES90 reference frame, we also define a new acid fractionation factor ($\Delta_{48}{}^{*}{}_{70\text{-}90}$) of ~0.0458‰ and we encourage further study of Δ_{48} acid fractionation factors to account for acid digestion temperature differences between labs. Although uncertainty on individual Δ_{48} measurements is high when replicated only three times each, pooling Δ_{47}/Δ_{48} data across multiple powders still allows us to obtain useful information about these gastropod species. Future efforts should involve measuring additional gastropod species, especially those whose equilibrium signatures are less clear, for seasonally targeted Δ_{47} (and more precise Δ_{48}) measurements to more confidently determine whether any gastropods

precipitate out of isotopic equilibrium. Further, community development of more reliable Δ_{48} standards will improve interlaboratory and measurement-theory comparisons.

2.7 Acknowledgments

I would like to thank Becca Heaman for help with sclerochronology drilling; Serena Scholz for the *Caviturritella*/*Turritella* $\delta^{18}O$ profiles and some drilling and data analysis; Susan Petersen, Gayle Clover, and Adam Simon for citizen science shell collection and donation; Brendan Anderson for correcting identifications of *Caviturritella* and *Turritella* species; Kacey Lohmann and Lora Wingate for $\delta^{18}O$ measurements; Ashling Neary and Justin VanDeVelde for Δ_{47}/Δ_{48} measurements; and the NSF-GRFP, University of Michigan Rackham Research Grants, and the University of Michigan Department of Earth and Environmental Science's Turner Grants provided to AAQ.

2.8 Appendices

2.8.1 Calibration window and Δ_{48} standards

In a purely gas-based reference frame (Dennis et al., 2011), we find separation in the Δ_{47} values of ETH1 and ETH2 that suggest gases alone are not able to correctly capture the compositional non-linearity defined by SlopeEGL. ETH1 corrects to a value of 0.175‰ +/- 0.003‰ (1SE, n=24) and ETH2 corrects to a value of 0.225‰ +/- 0.003‰ (1SE, n=22) (see Table S2.3). However, across all four ETH standards, the average offset from InterCarb values is 0.0001‰, indicating good overall agreement between I-CDES90 and CDES90 for Δ_{47}.

Because of the large separation between ETH1 and ETH2, we tried including both for calculation of SlopeEGL alongside the heated and equilibrated gas standards. This flattened and increased the precision of the calculated SlopeEGL from 0.0026 +/- 0.0012 (1SE) to 0.0012 +/-

0.0002 (1SE). In this hybrid ETH1-2 gas-based reference frame, ETH1 corrects to 0.195‰ +/- 0.003‰ (1SE, n=24) and ETH2 corrects to 0.199‰ +/- 0.003‰ (1SE, n=22), by definition displaying the correct 0.003‰ offset between the two. While the average offset across all four ETH standards is slightly higher (0.003‰), the range of offsets is smaller (-0.005‰ to +0.011‰ vs. -0.028‰ to +0.031‰ for the gas-based reference frame).

This shift to a flatter slope results in Δ_{47} increases for all of our in-house standards and a decrease in GU1. In particular, this shifts our Carrara Marble standard from 0.281‰ +/- 0.005‰ to 0.301‰ +/- 0.005‰ (1SE, n=12), bringing it into closer alignment with other previously reported values for Carrara Marble (0.309‰-0.395‰, Dennis et al., 2011; Kluge and Affek, 2012; Upadhyay et al., 2021; Fiebig et al., 2024). GU1 shifts from 0.2866‰ +/- 0.0065‰ to 0.2542‰ +/- 0.0065‰ (1SE, n=13), closer to the reported value of 0.2254‰ +/- 0.0008‰ (Fiebig et al., 2024). We therefore treat this hybrid reference frame as our best estimate of CDES90 and use it to define true Δ_{47} and Δ_{48} values for our in-house standards.

We confirm that our hybrid CDES90 reference frame is interchangeable with I-CDES90 in Δ_{47} by comparison of the in-house standards, all of which overlap within 1SE error (see Table 2.2). This indicates that any Δ_{47} values reported in I-CDES90 may be directly compared to the equilibrium line reported in Fiebig et al. (2021).

For Δ_{48}, the gas-based and hybrid reference frames produce values in CDES70 due to our acid reaction occurring at 70°C instead of 90°C as used in other labs. To directly compare, we must apply an acid fractionation factor (AFF). No $\Delta_{48}{}^{*}{}_{70\text{-}90}$ has been previously defined. Here, we define one by comparing the mean value of ETH1 and ETH2 measured in our CDES70 reference frame to published values from Swart et al., 2021 (ETH1-4) and Fiebig et al., 2024 (GU1, GM) presented in the CDES90 reference frame (see justification for this decision in

Section 2.5.1). Our mean value of 0.196‰ (CDES70, from gases only) produces an offset of 0.047‰ when compared to the Fiebig et al., 2024 mean of 0.149‰. Including ETH1 and ETH2 in the calculation of SlopeEGL barely shifts the mean values of ETH1 and ETH2 and therefore produces an indistinguishable offset of 0.0458‰. Because these results are indistinguishable and we achieved best performance in Δ_{47} using the hybrid ETH1/2 gas-based reference frame, we choose to use 0.0458‰ as our $\Delta_{48}{}^{*}{}_{70\text{-}90}$ value.

The accuracy of this proposed $\Delta_{48}{}^{*}{}_{70\text{-}90}$ acid fractionation factor is confirmed by other measured carbonates. Applying the acid fractionation factor to ETH3 produces an adjusted CDES90 value of 0.2690‰ +/- 0.0065‰ (1SE, n=27), well within 1SE agreement with the published value from Swart et al. (2021) of 0.269‰ +/- 0.015‰ (95% CI, n=20). ETH4 becomes 0.2359‰ +/- 0.0075‰ (1SE, n=22), slightly higher than the published value from Swart et al., 2021 of 0.231‰ +/- 0.018‰ (95% CI, n=14). GU1 also moves closer to the published value, but remains higher (-0.3279‰ +/-0.0154‰, 1SE n=13 vs. -0.3998‰ +/- 0.0043‰, 1SE, n=149; Fiebig et al., 2024). As the Δ_{47} value for GU1 did not align with the published value, perhaps this offset is due to something inherent to GU1 and how it reacts in different sample preparation systems (individual vial vs. common acid bath) or how the reference frame or pressure baseline behaves at the outermost ends of the isotopic range. More focused work with additional standards in this isotopic range could help resolve these questions. As ETH4 and GU1 are at opposite ends of the isotopic range, there does not appear to be a compositional effect on the $\Delta_{48}{}^{*}{}_{70\text{-}90}$, so we may apply it as a fixed offset to carbonates of any Δ_{48} composition.

We use the hybrid ETH1-2 gas-based CDES70 reference frame and the 0.0458‰ acid fractionation factor to define CDES90 values for our other in-house standards (see Table 2.2). Of note, our version of Carrara Marble produces a Δ_{48} value of 0.1315‰ +/- 0.0126‰ (1SE, n=12),

which is within 2SE of the published value for the Goethe University Carrara standard (0.1455‰ +/- 0.0057‰).

Fiebig et al., 2019 defined a $\Delta_{48\text{-}64}$* of 0.136‰ as the difference between the theoretical value for carbonate equilibrated at 600°C (0.002‰) and the measured Δ_{48}-CDES90 value of gas produced from ETH1 and ETH2 (0.140‰). This was subsequently updated to an offset of 0.1214‰ (Fiebig et al., 2021; Fiebig et al., 2024).

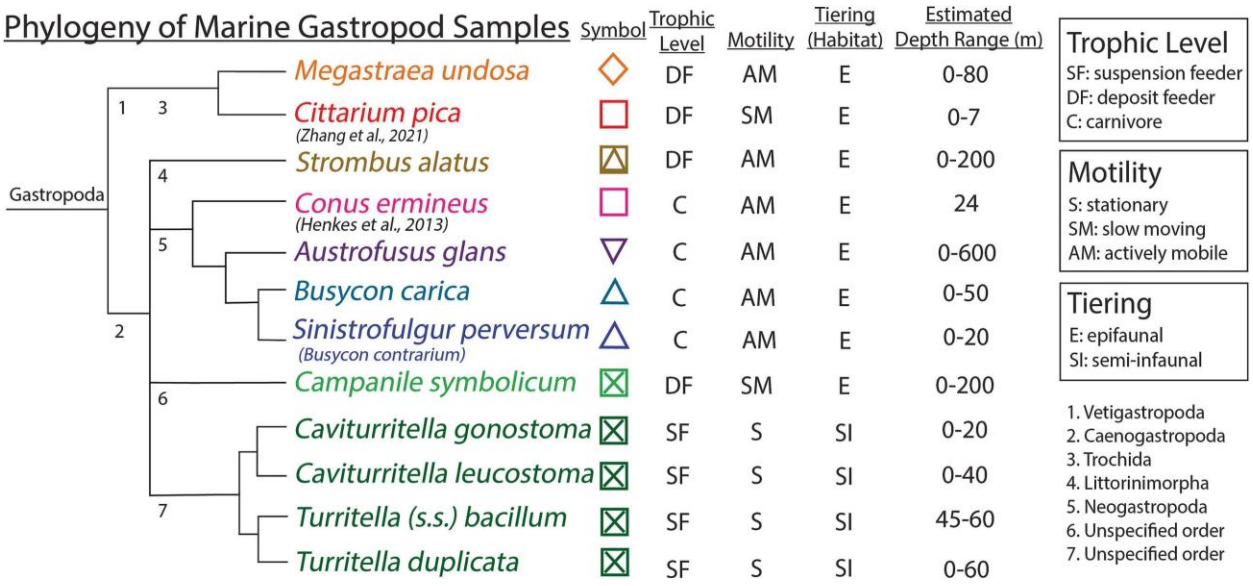

Figure 2.1. Phylogenetic relationships within class Gastropoda and relevant physiological characteristics of modern marine gastropods measured in this study or previously measured by Zhang et al. (2021) (C. pica) and Henkes et al. (2013) (C. ermineus).

Sinistrofulgur perversum is the modern species name for Busycon contrarium, which is exclusively a fossil species. Revised Turritella nomenclature are included from Friend et al. (2023). Symbology shown here is used throughout all other figures.

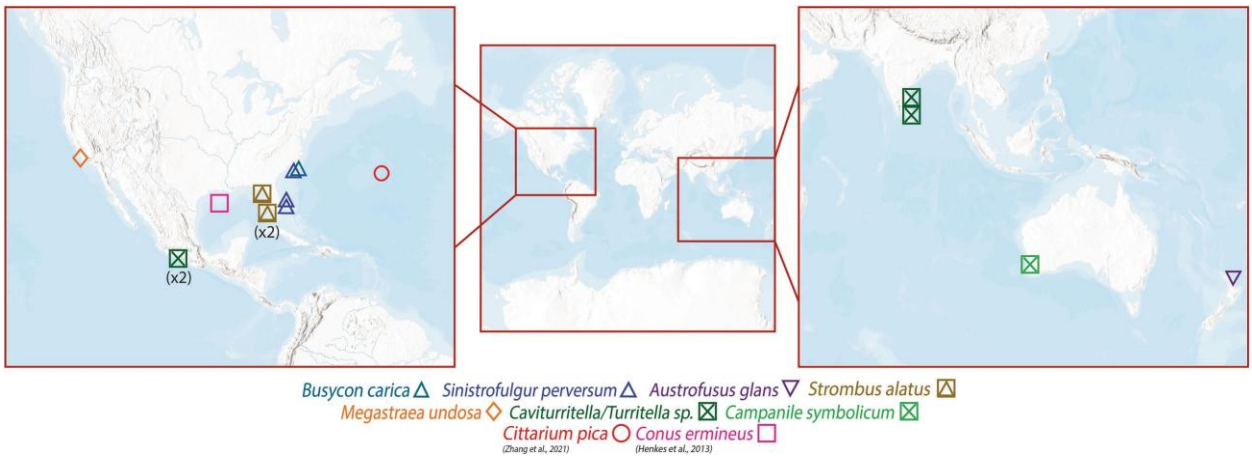

Figure 2.2. Map of sample localities for marine gastropods analyzed in this study.

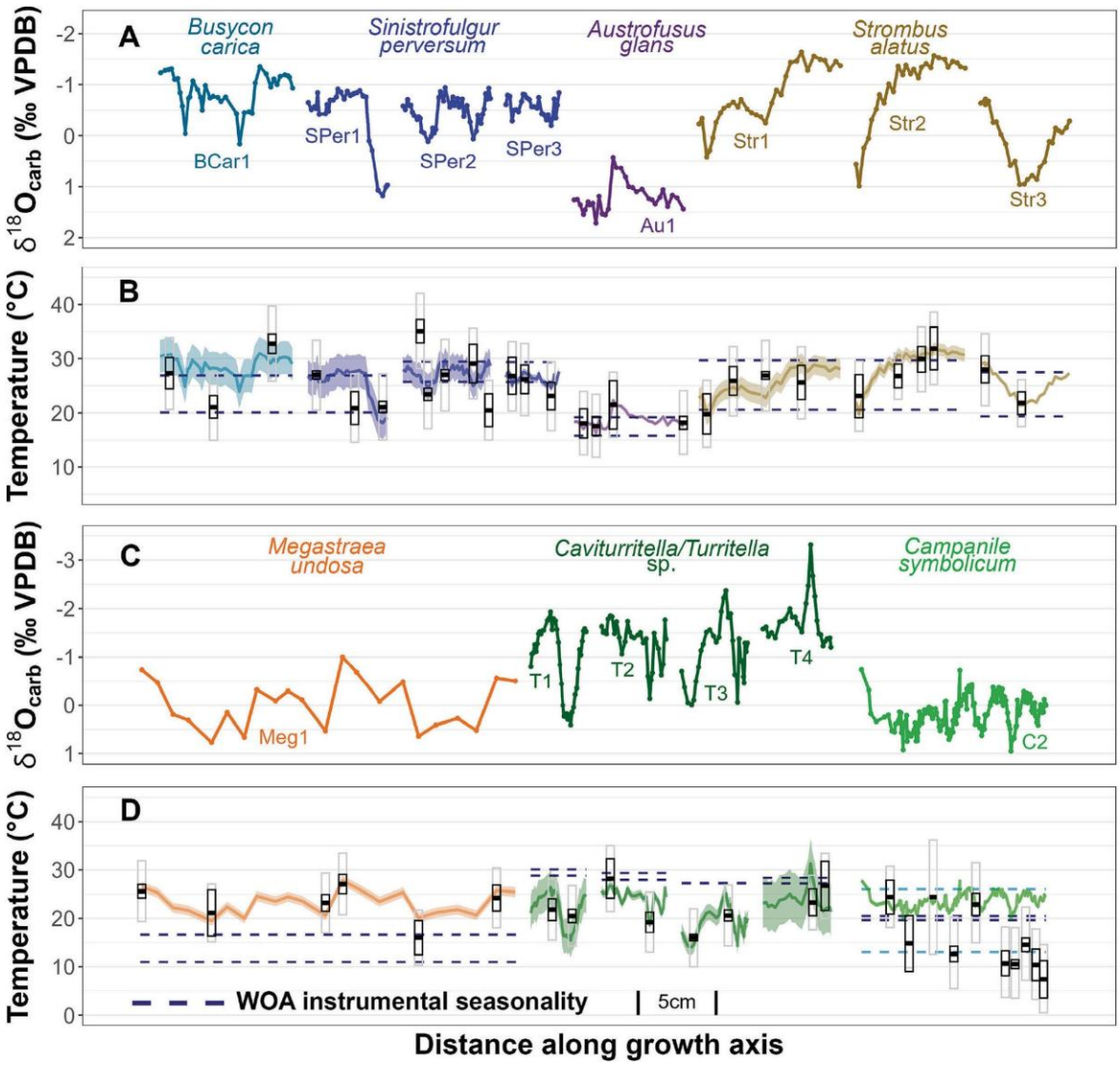

Figure 2.3. $\delta^{18}O$ sclerochronology and reconstructed $\delta^{18}O$-temperatures (colored) and seasonally targeted Δ_{47}-temperatures (black) for marine gastropods analyzed in this study.

Distance along the curved growth axis was measured from aperture to apex of each shell. Shaded error bars for $\delta^{18}O$-temperatures represent +/- internal 1SE in Δ_{47}-based $\delta^{18}O_w$. Larger grey and smaller black error bars for Δ_{47}-temperatures represent 95% confidence intervals and +/- internal 1SE in Δ_{47}, respectively. Dotted dark blue lines represent winter and summer instrumental temperatures for the corresponding collection locality, according to the World Ocean Atlas 2018 database (see text for details). The dotted light blue lines for sample C2 represent winter and summer instrumental temperatures from a local Geographe Bay temperature record (reported in de Winter et al. (2020)). $\delta^{18}O$ sclerochronology and seasonally targeted measurements for the previously measured C. pica can be found in Fig. S2.2.

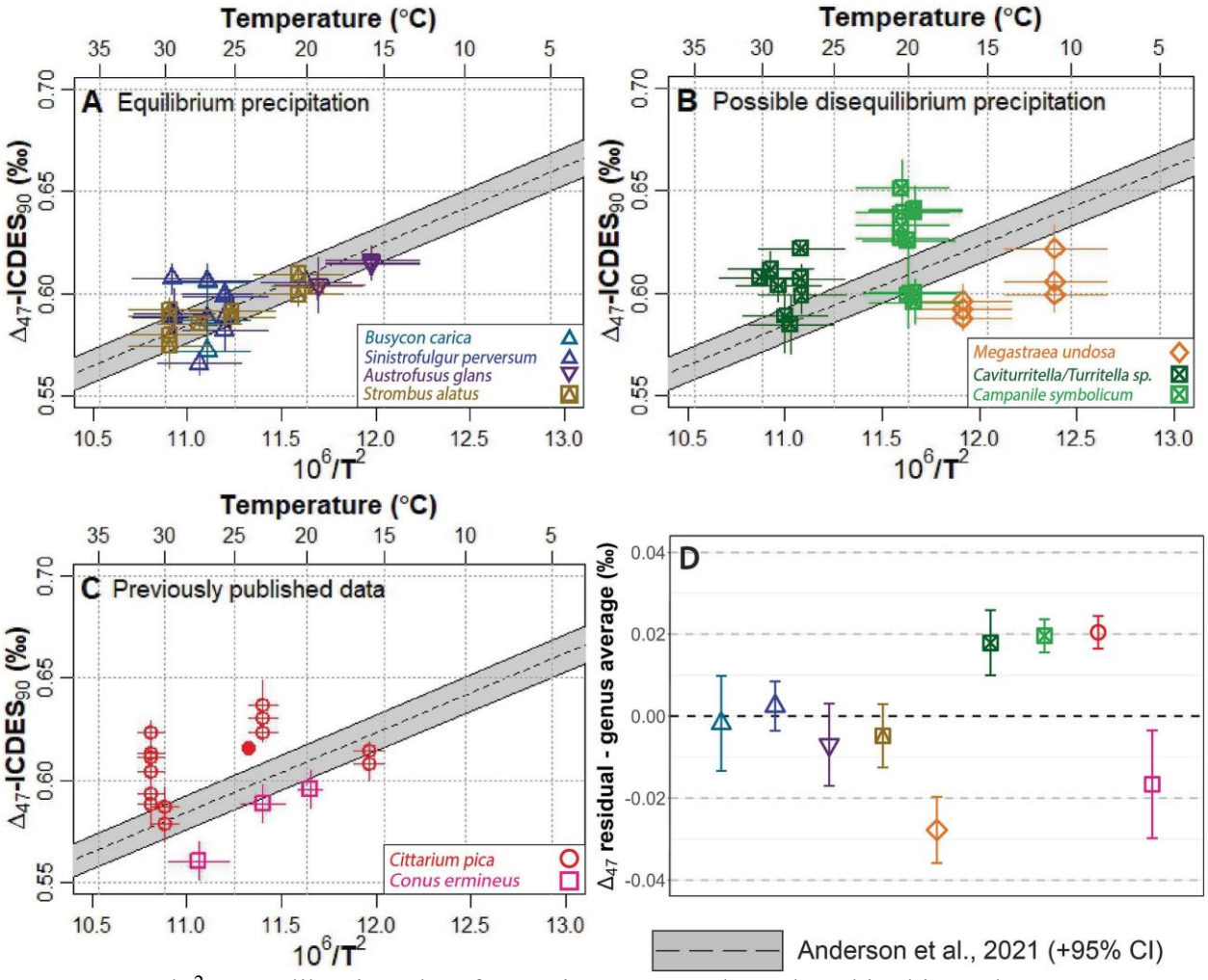

Figure 2.4. $1/T^2$-Δ_{47} calibration plots for marine gastropods analyzed in this study.

Separated into the following groups described in the text: (A) equilibrium calcifiers; (B) possible disequilibrium calcifiers; (C) previously published marine gastropods (ambiguous whether they precipitate in equilibrium). Details about colors and symbology can be found in Fig. 2.1. The linear regression and shaded 95% confidence interval come from Anderson et al. (2021). Vertical error bars represent +/- 1 internal SE and horizontal error bars represent +/- 3°C, except for C. ermineus and C. pica, with the original errors reported in Henkes et al. (2013) and Zhang et al. (2021). The shaded circle in Fig. 2.4C represents the long-term value for the UM Stable Isotope Lab's internal C. pica standard. The Δ_{47} residuals averaged by genus (D) were calculated using the procedures described in Section 2.3.7. Points represent weighted means; error bars represent +/- weighted 1SE (see Table S2.6).

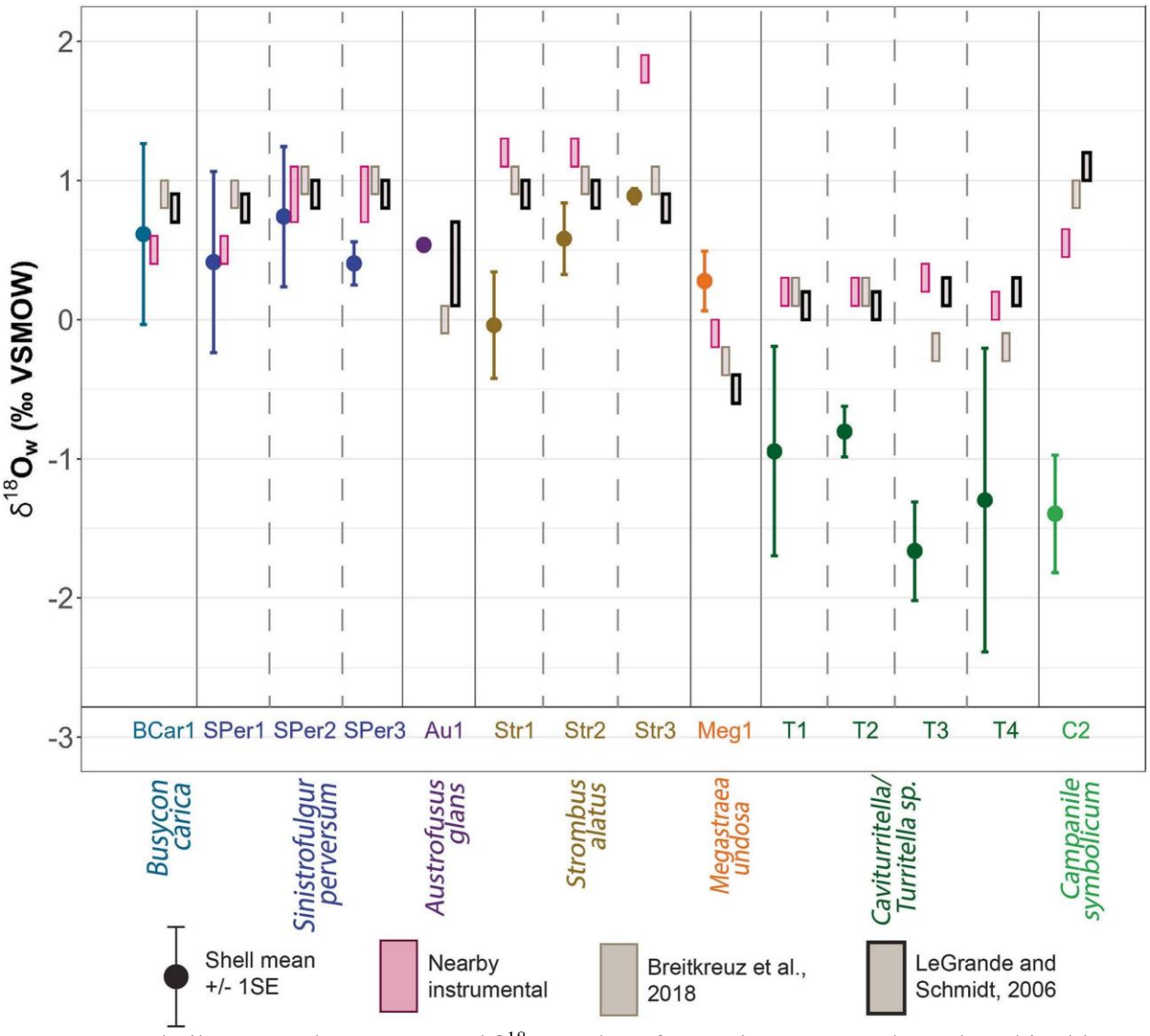

Figure 2.5. Shell-averaged reconstructed $\delta^{18}O_w$ values for marine gastropods analyzed in this study.

Calculated using the mollusk equation from Grossman and Ku (1986). Error bars represent +/- internal 1SE with respect to the shell average. Colored boxes represent closest instrumental and modeled $\delta^{18}O_w$ values for comparison. Note that no seawater instrumental $\delta^{18}O_w$ values could be found within ~ 500 km of the sampling site of A. glans (Au1). Data at the individual sample level can be found in Fig. S2.4.

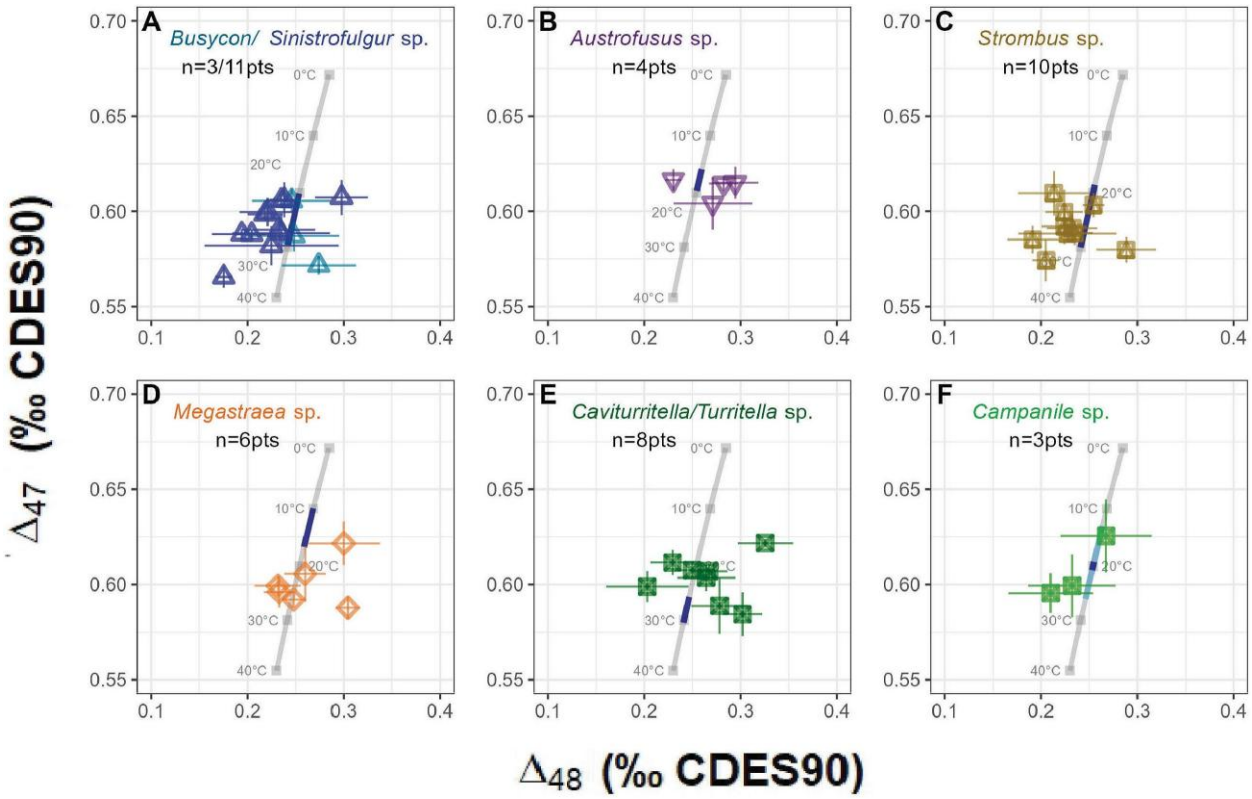

Figure 2.6. Δ_{47}/Δ_{48} data for all marine gastropods analyzed in this study.

The faded grey line represents Δ_{47}/Δ_{48} equilibrium as defined in Fiebig et al. (2021). Dark blue line segments represent predicted Δ_{47}/Δ_{48} values calculated using minimum and maximum World Ocean Atlas (WOA) instrumental temperatures for each genus and equations from Fiebig et al. (2021). Colored points represent individual seasonally targeted samples; error bars represent +/- internal 1SE. The dotted light blue line for C. symbolicum represents the seasonal instrumental temperature range from a local Geographe Bay temperature record (reported in de Winter et al. (2020)).

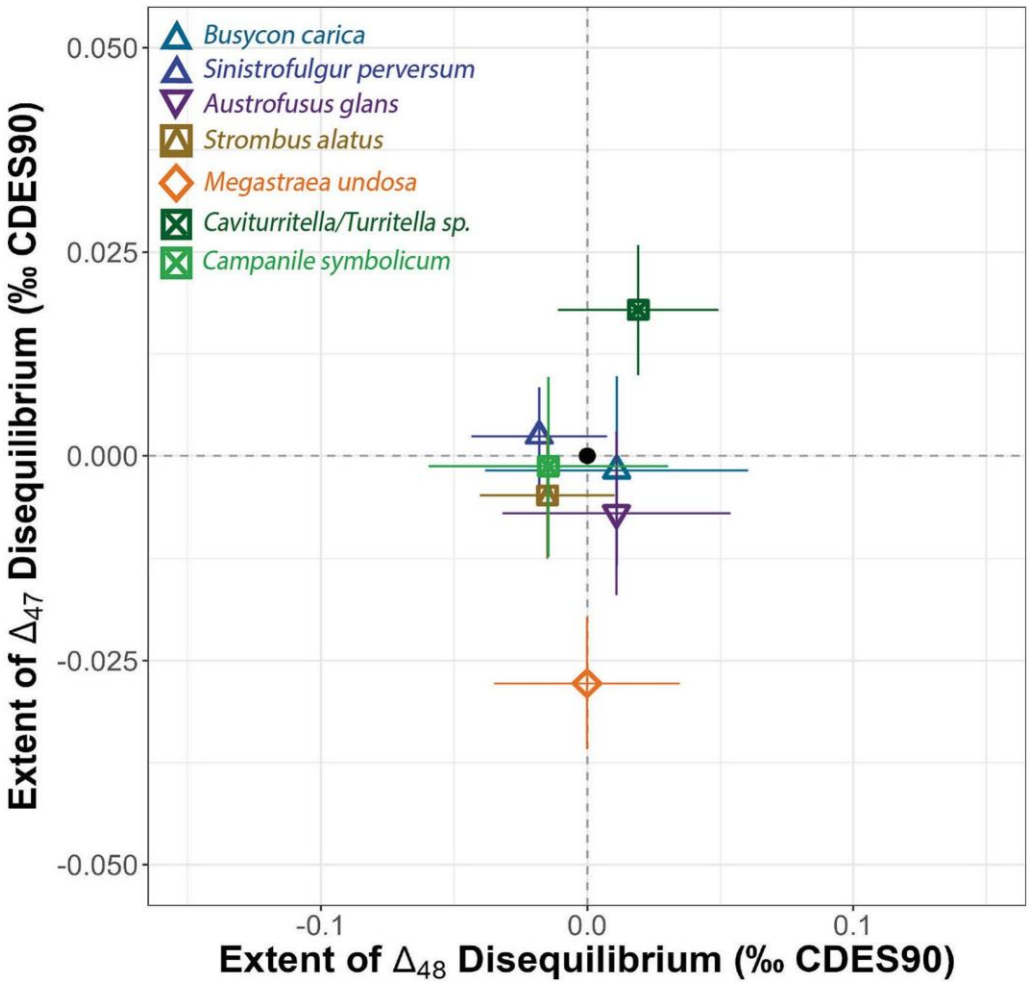

Figure 2.7. Δ_{47}/Δ_{48} offsets from equilibrium as defined in Fiebig et al. (2021) for marine gastropods analyzed in this study.

Colored points represent weighted means, averaged by genus; error bars represent +/- weighted 1SE (see Tables 2.S7 and 2.S8).

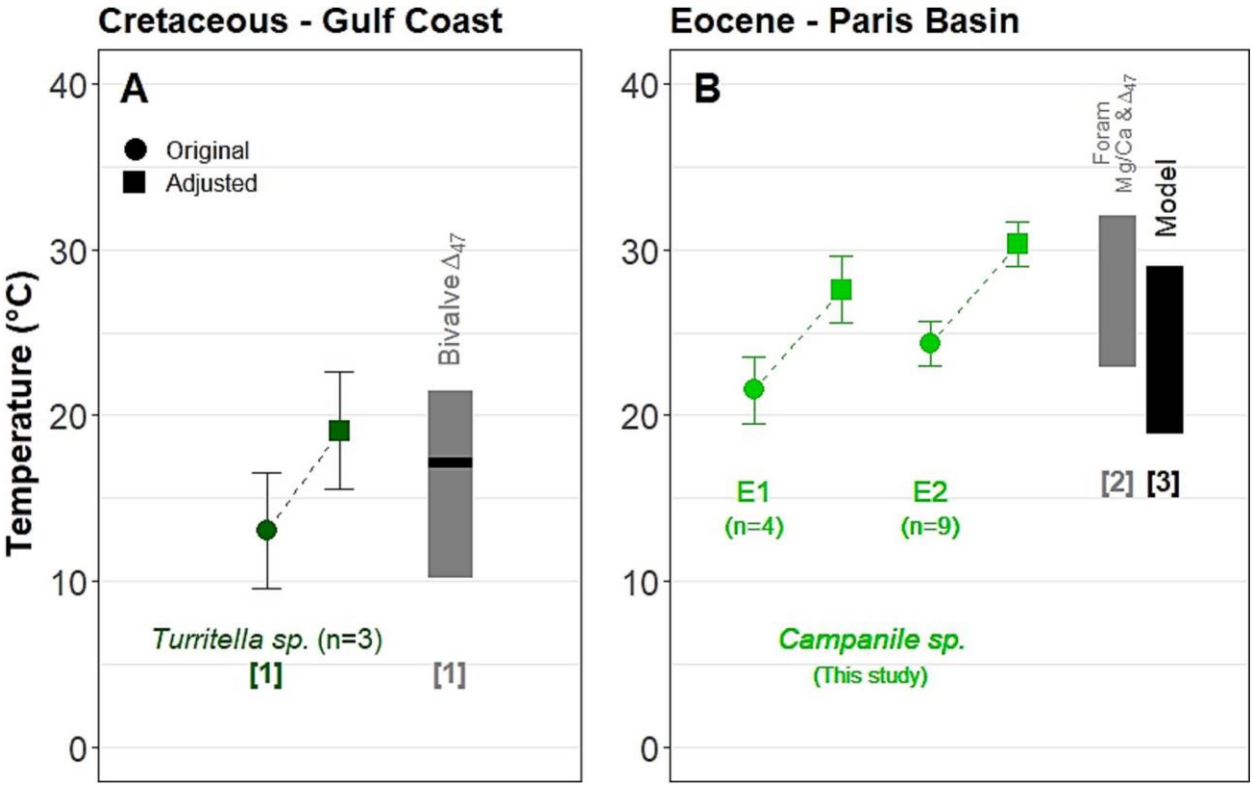

Figure 2.8. Previously reported and new Δ_{47}-paleotemperatures from (A) Late Cretaceous, and (B) Eocene fossil gastropods.

Error bars represent +/- internal 1SE. The Eocene Campanile giganteum samples were obtained from the Paris Basin. Previously published temperature estimates come from the following sources: (1) Meyer et al. (2018); (2) Evans et al. (2018); (3) Hollis et al. (2019).

Standard	n	Δ_{48}-CDES70 (this study, +/- 1SE) (‰)	Δ_{48}-CDES90 ('true') (‰)	Offset: CDES90-CDES70 (‰)	Adjusted Δ_{48}-CDES90 (this study) (‰)*
ETH1	24	0.1933 +/- 0.0051	0.1450 +/- 0.0125	0.0483	0.1475
ETH2	22	0.1963 +/- 0.0088	0.1530 +/- 0.0100	0.0433	0.1505
ETH3	27	0.3148 +/- 0.0065	0.2690 +/- 0.0075	0.0458	0.2690
ETH4	22	0.2817 +/- 0.0075	0.2310 +/- 0.0090	0.0507	0.2359
GU1	13	-0.2821 +/- 0.0154	-0.3998 +/- 0.0042	0.1177	-0.3279
Carrara Marble (CM)	12	0.1773 +/- 0.0126	[&]0.1455 +/- 0.0029	0.0318	0.1315
			[#]**Proposed $\Delta_{48}{}^{*}{}_{70\text{-}90}$ value**	**0.0458**	

[#]Calculated as the mean of the ETH1 and ETH2 offsets. $\Delta_{48,CDES70} - 0.0458 = \Delta_{48,CDES90}$.
[&]Unlike ETH1-4 and GU1, this Carrara is not an identical powder to that of Fiebig et al. (2024) but a separate aliquot of CM made at a different university from similar starting material.
*Uncertainty is the same as uncertainty in the column containing un-adjusted values.

Table 2.1. Calculation of $\Delta_{48}{}^{*}{}_{70\text{-}90}$ using ETH standards within the calibration window.

See Section 2.3.3 for more details about the calibration window. 'True' values for ETH1-4 were obtained from Swart et al. (2021); 'true' values for GU1 and CM were obtained from Fiebig et al. (2024).

Standard	n	Δ_{47}: Hybrid gas-based CDES90 (‰)[&]	Δ_{47}: Carbonate-based I-CDES90 (‰)[#]	Δ_{48}: Hybrid gas-based CDES90 (‰)*	Δ_{48}: Carbonate-based GU-CDES90 (‰)[+]
Carrara Marble (CM)	12	0.3006 +/- 0.0049	0.3070 +/- 0.0047	0.1315 +/- 0.0126	0.1169 +/- 0.0143
Islandic *Arctica islandica* (Ice)	14	0.6450 +/- 0.0046	0.6384 +/- 0.0044	0.2462 +/- 0.0122	0.2454 +/- 0.0138
Joulters Cay Ooids (OO)	11	0.6010 +/- 0.0046	0.5961 +/- 0.0045	0.2419 +/- 0.0133	0.2413 +/- 0.0151
Bermudan *Cittarium pica* (Pica)	12	0.6080 +/- 0.0051	0.6029 +/- 0.0049	0.2340 +/- 0.0142	0.2321 +/- 0.0161
GU1	13	0.2542 +/- 0.0065	0.2609 +/- 0.0063	-0.3279 +/- 0.0154	N/A

[&]Calculates SlopeEGL using gases and ETH1-2. Gases only used for the transfer function. An acid fractionation factor of 0.022‰ was applied.
[#]Calculates SlopeEGL using ETH1-2. ETH1-4 used for the transfer function using InterCarb ETH 'true' values. No acid fractionation factor needed.
*Calculates SlopeEGL using gases and ETH1-2. Gases only used for the transfer function. An acid fractionation factor of 0.0458‰ was applied and derived from ETH1-2.
[+]Calculates SlopeEGL using ETH1-2. ETH1-4 and GU1 used for the transfer function using 'true' values from Swart et al. (2021). No acid fractionation factor needed.

Table 2.2. Comparison of standards performance reported in gas-based and carbonate-based references frames within the calibration window.

See Section 2.3.3 for more details about the calibration window. All errors represent +/- 1SE on the mean. See Table S2.5 for the same table with Δ_{48} data instead corrected using ETH 1-4 'true' values from Fiebig et al. (2024).

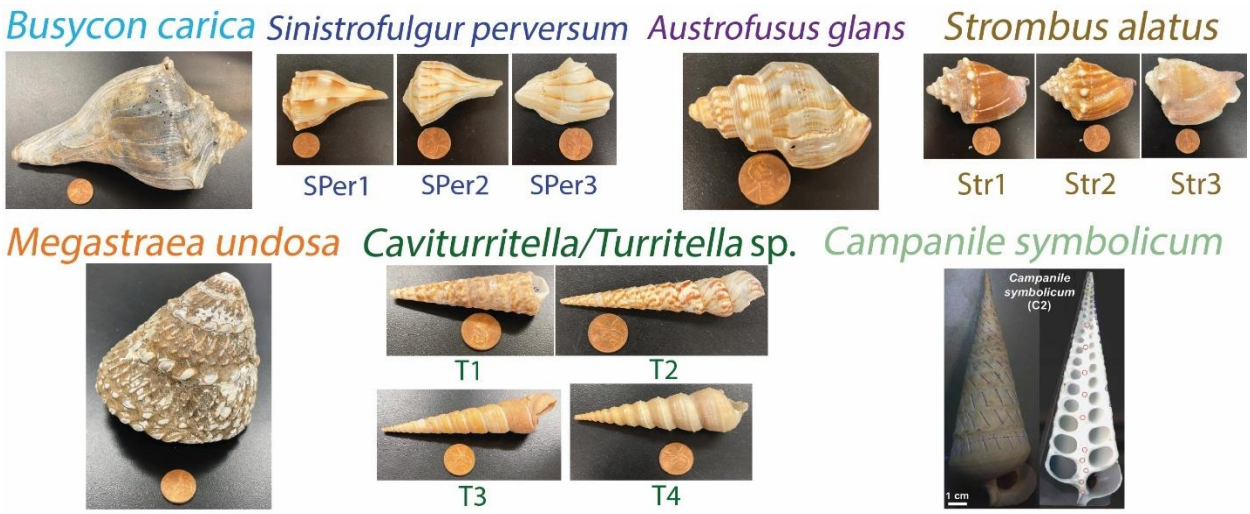

Figure S2.1. Pictures of shells of marine gastropods analyzed in this study.

Penny included in each picture for scale (except for C. symbolicum, which includes a 1cm scale bar).

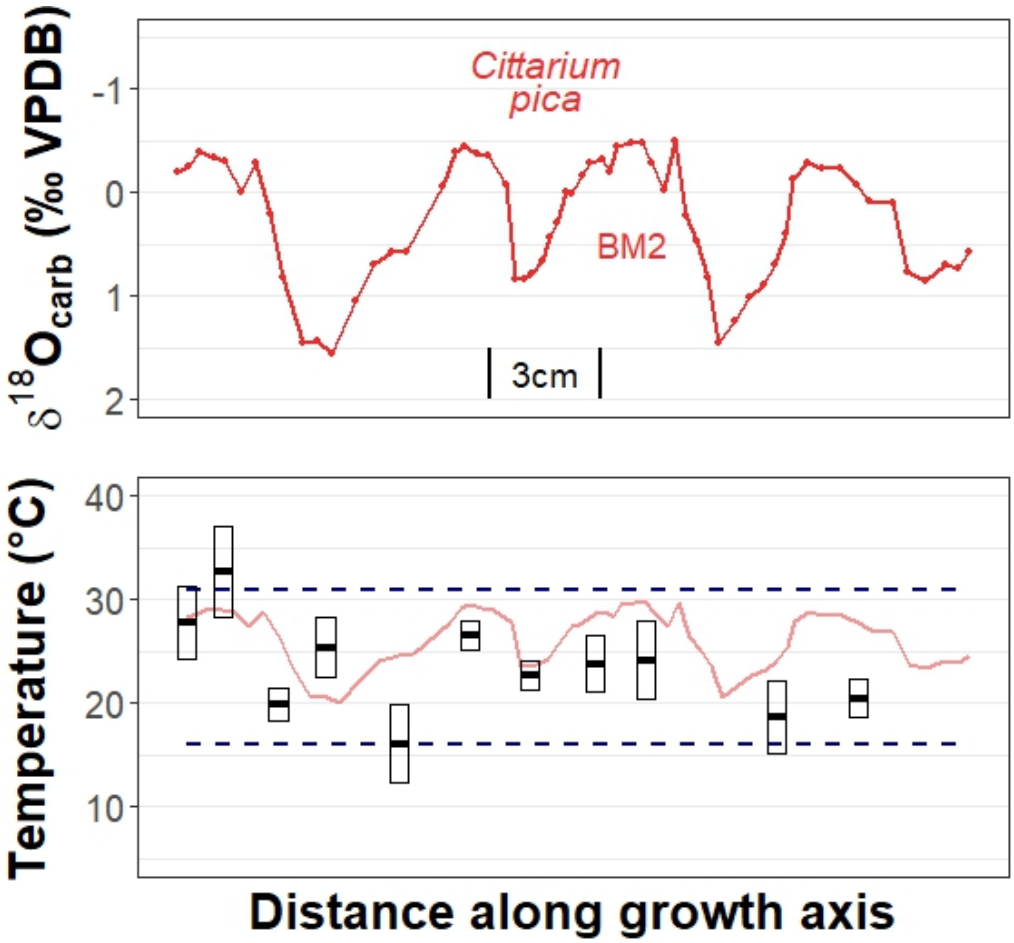

Figure S2.2. $\delta^{18}O$ sclerochronology and seasonally targeted Δ_{47}-temperatures from sample BM2 (Cittarium pica).

Data were originally reported in Zhang et al. (2021). The dotted lines represent instrumental temperatures from the World Ocean Atlas database. Points represent sample averages; the black boxes represent +/- 1SE.

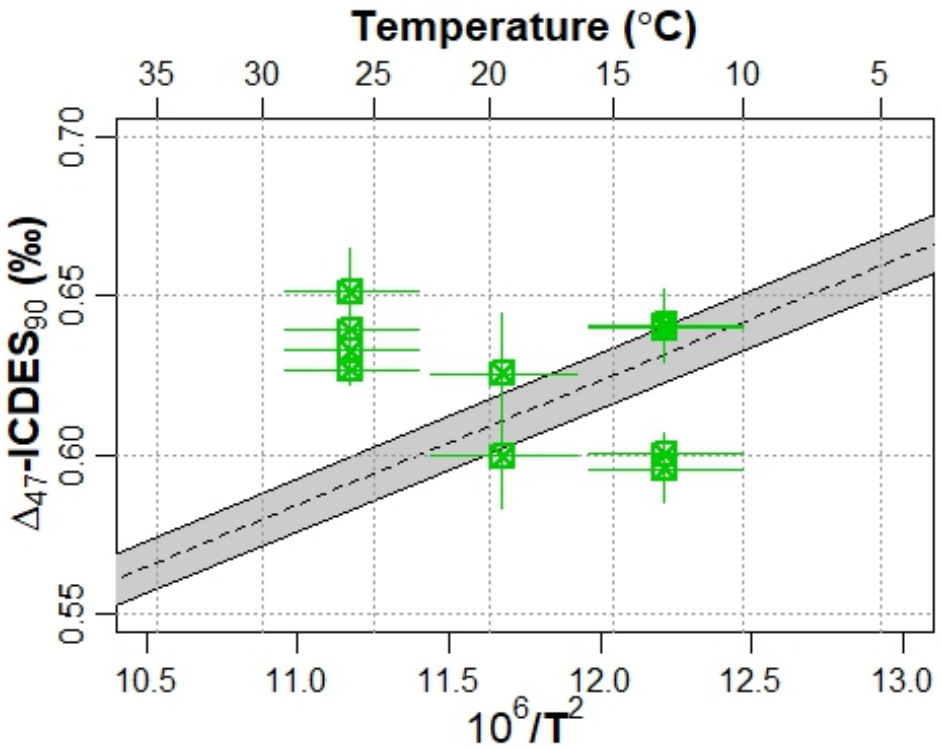

Figure S2.3. $1/T^2$ calibration plot for sample C2 (Campanile symbolicum), using assigned calibration temperatures reported from a local Geographe Bay temperature cited in de Winter et al. (2020).

The linear regression and shaded 95% confidence interval come from Anderson et al. (2021). Vertical error bars represent +/- 1 internal SE and horizontal error bars represent +/- 3°C.

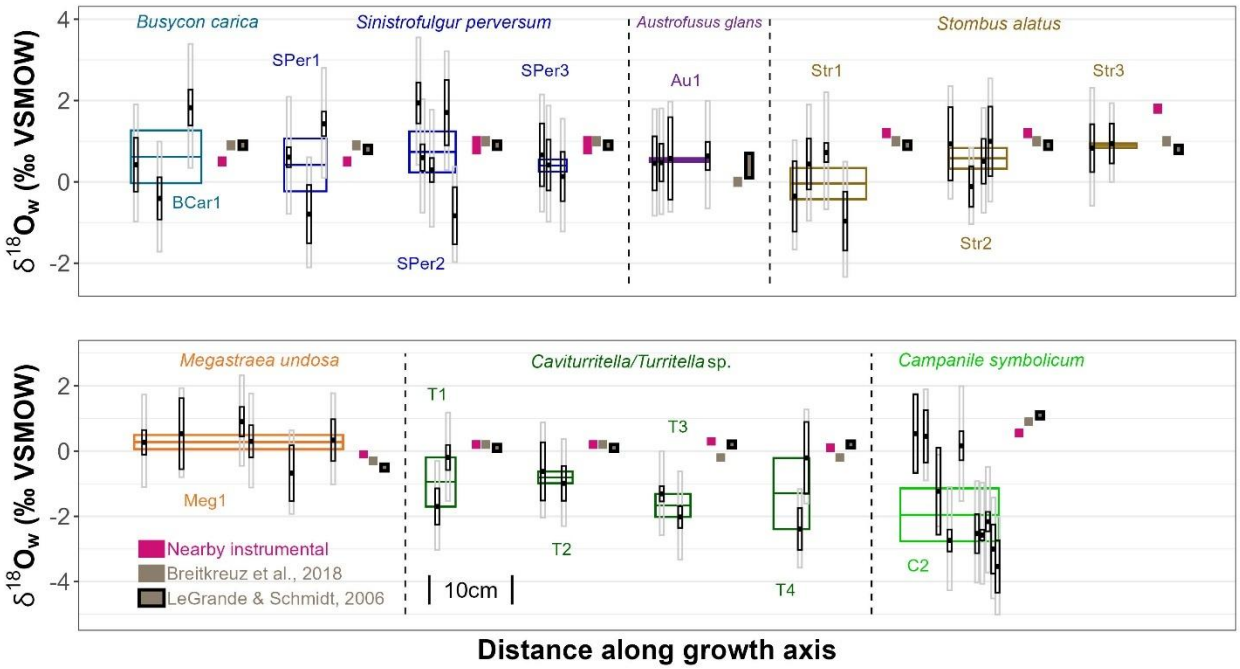

Figure S2.4. Shell-averaged reconstructed $\delta^{18}O_w$ values for marine gastropods analyzed in this study

Calculated using the mollusk equation from Grossman and Ku (1986). Colored rectangles represent shell-average values +/- 1SE from averaging all samples per shell. Black error bars represent +/- 1SE with respect to sample averages. Grey error bars represent 95% confidence intervals with respect to sample averages. Colored boxes to the right of shell values represent closest instrumental and modeled $\delta^{18}O_w$ values for comparison. Note that no seawater instrumental $\delta^{18}O_w$ values could be found within ~500km of the sampling site of A. glans (Au1).

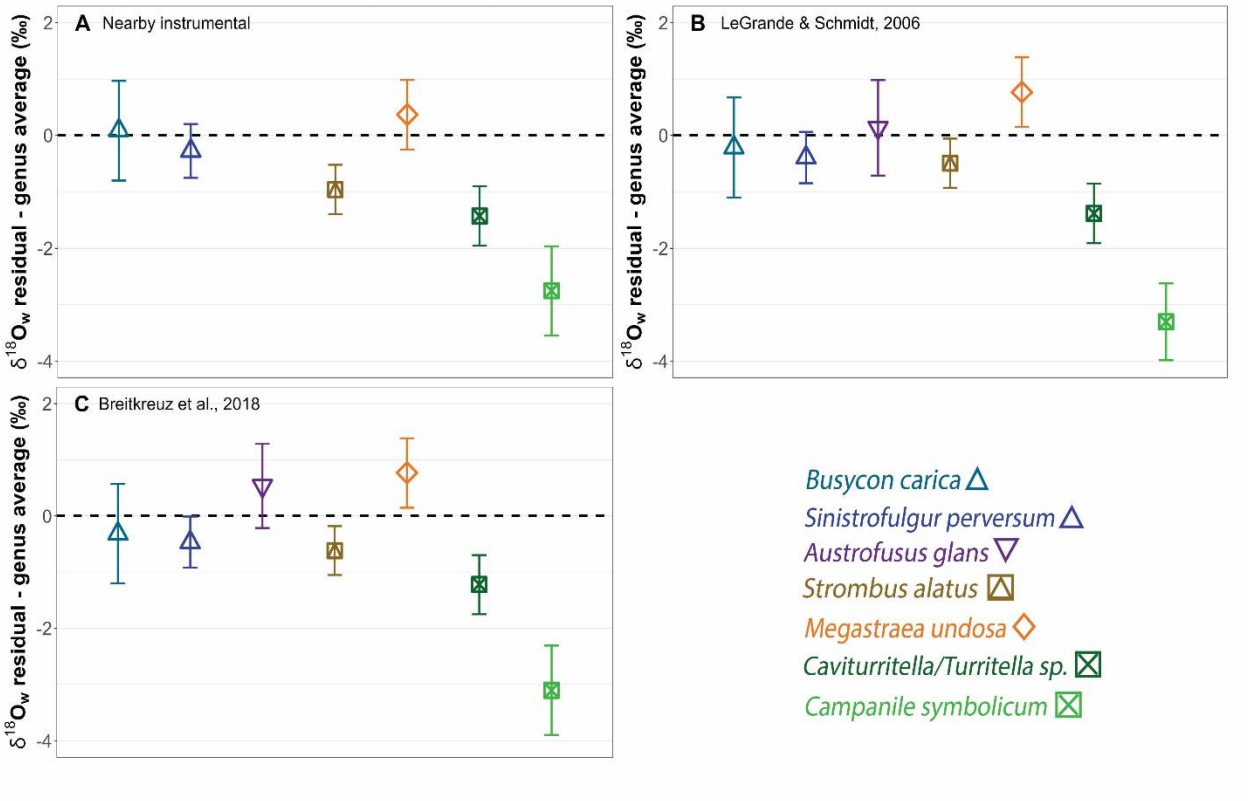

Figure S2.5. $\delta^{18}O_w$ residuals averaged by genus.

I.e., differences between reconstructed $\delta^{18}O_w$ and (A) nearby instrumental $\delta^{18}O_w$, (B) modeled $\delta^{18}O_w$ from LeGrande and Schmidt (2006), (C) modeled $\delta^{18}O_w$ from Breitkreuz et al. (2018). Reconstructed $\delta^{18}O_w$ values were calculated using the mollusk equation from Grossman and Ku (1986). Points represent weighted means; error bars represent +/- weighted 1SE (see Section 2.3.7 for a full explanation).

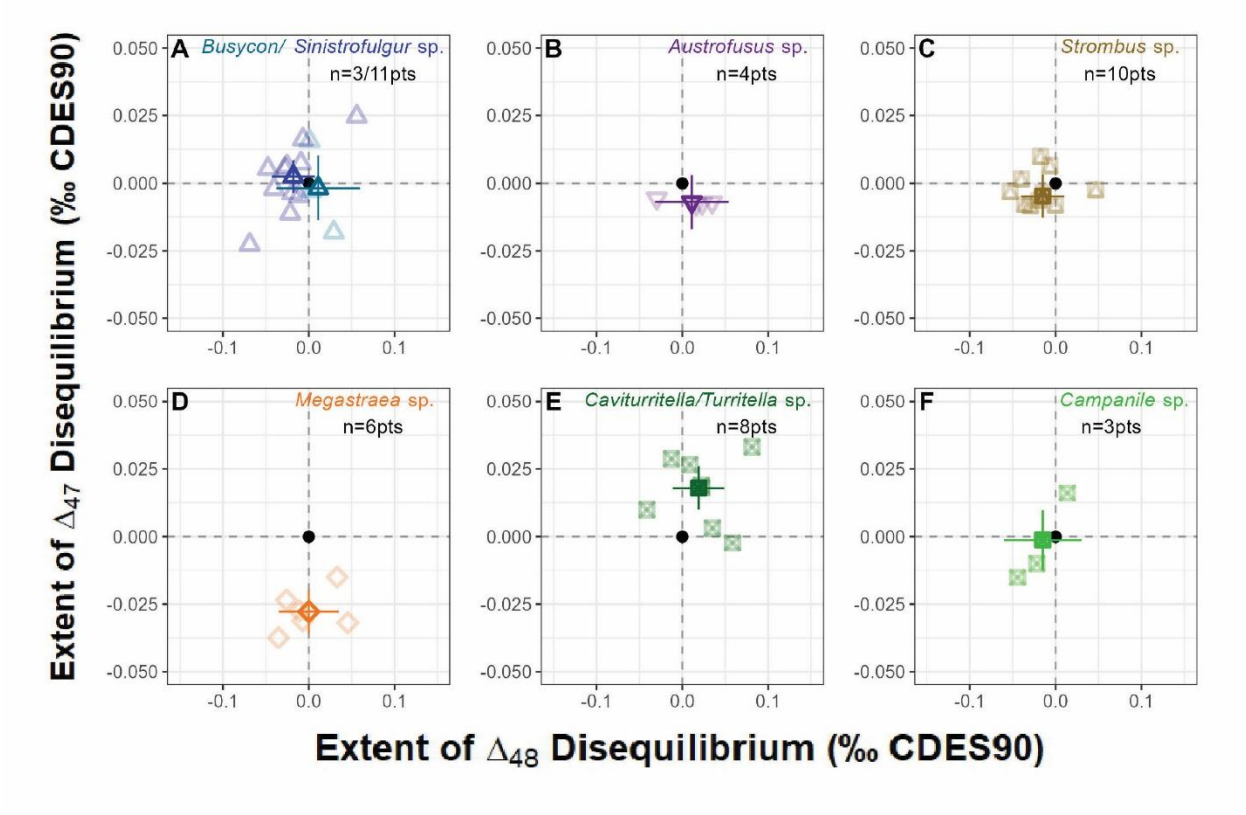

Figure S2.6. Δ_{47}/Δ_{48} offsets from equilibrium as defined in Fiebig et al. (2021) for marine gastropods analyzed in this study.

Faded colored points represent individual seasonally targeted samples. Dark colored points represent weighted means, averaged by genus. Error bars represent +/- weighted 1SE from sample averaging as reported in Tables 2.S7 and 2.S8.

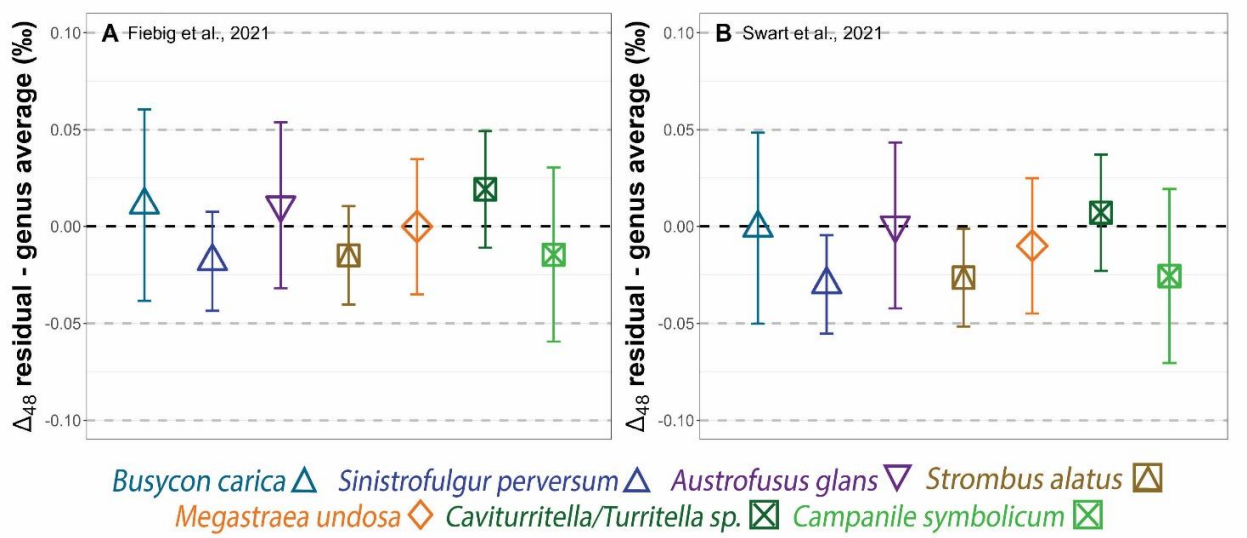

Figure S2.7. Δ_{48} residuals averaged by genus from compared to the Fiebig et al. (2021) (A) and Swart et al. (2021) (B) calibration lines.

Points represent weighted means; error bars represent +/- weighted 1SE. Δ_{48} values presented here were processed using the ETH1-4 'true' values from Swart et al. (2021).

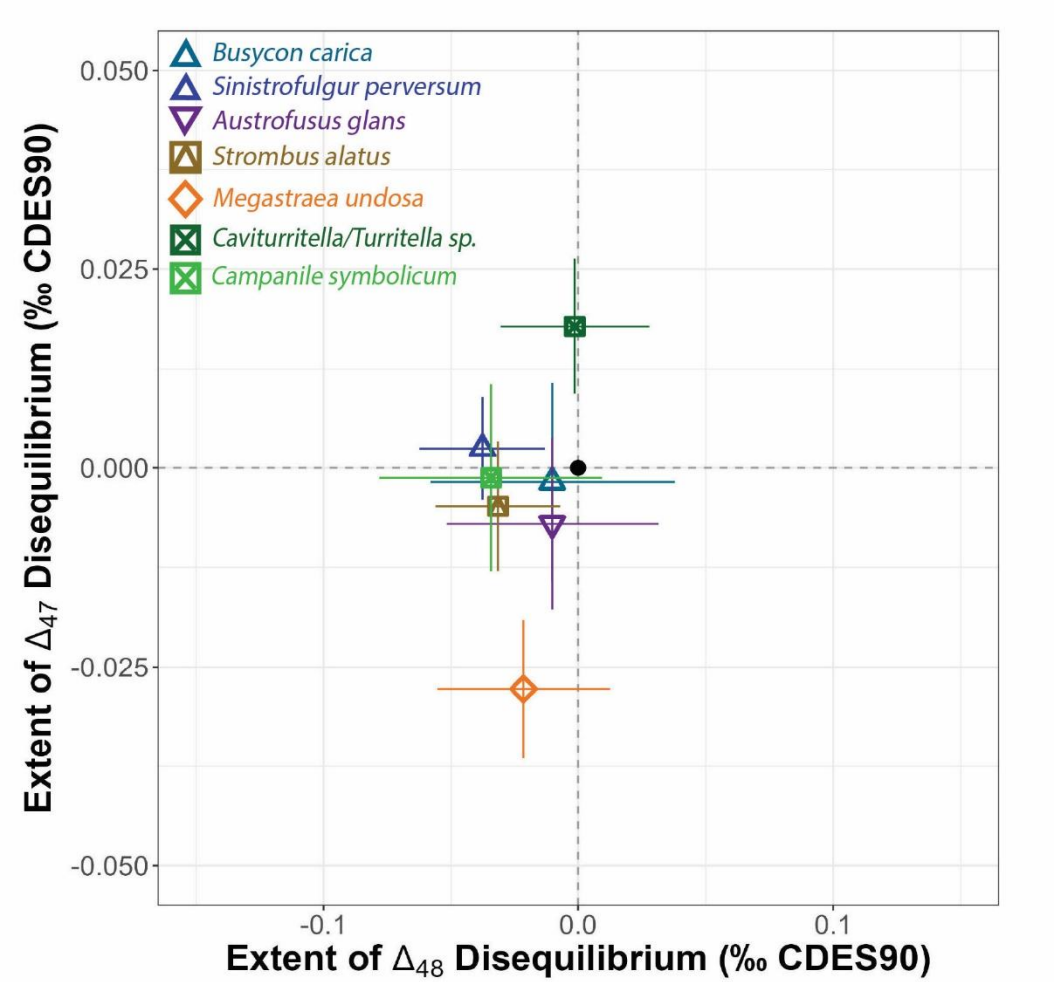

Figure S2.8. Δ_{47}/Δ_{48} offsets from equilibrium as defined in Fiebig et al. (2021) for marine gastropods analyzed in this study.

Δ_{48} data were processed using ETH1-4 'true' values from Fiebig et al. (2024) as opposed to Swart et al., 2021. Colored points represent weighted means, averaged by genus; error bars represent +/- weighted 1SE (Tables 2.S7 and 2.S8).

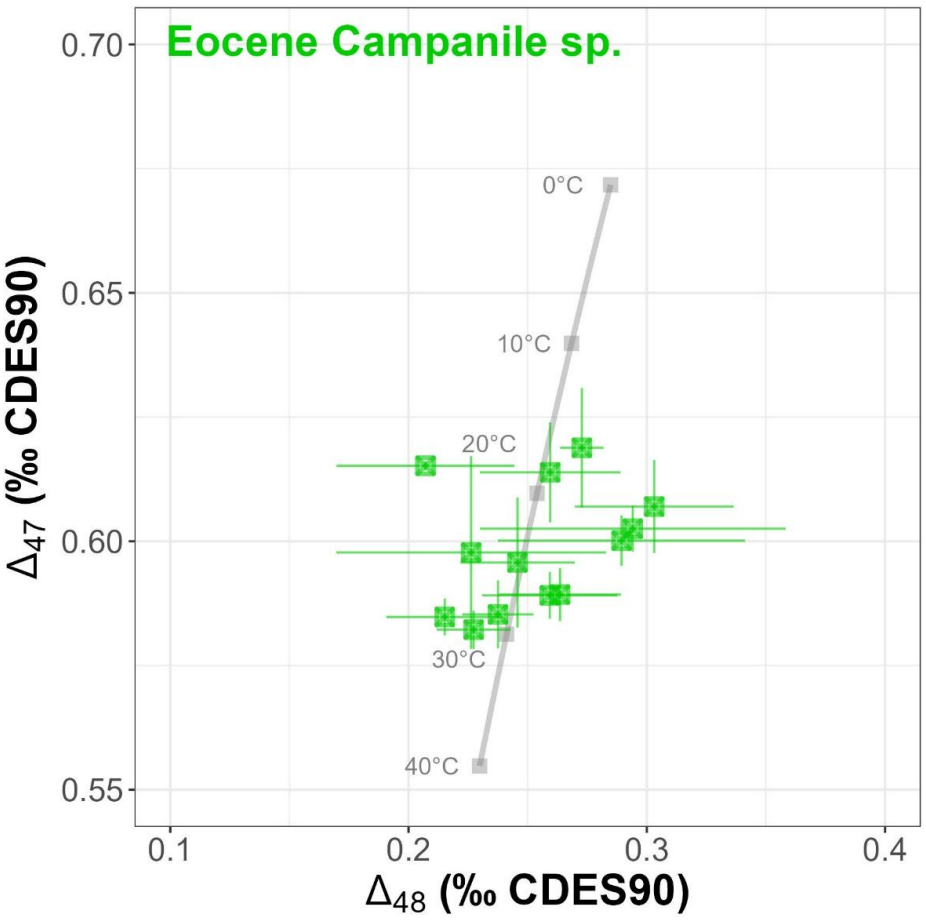

Figure S2.9. Δ_{47}/Δ_{48} data for the 2 Eocene *Campanile giganteum* shells measured in this study.

Colored points represent individual seasonally targeted samples; error bars represent +/- internal 1SE.

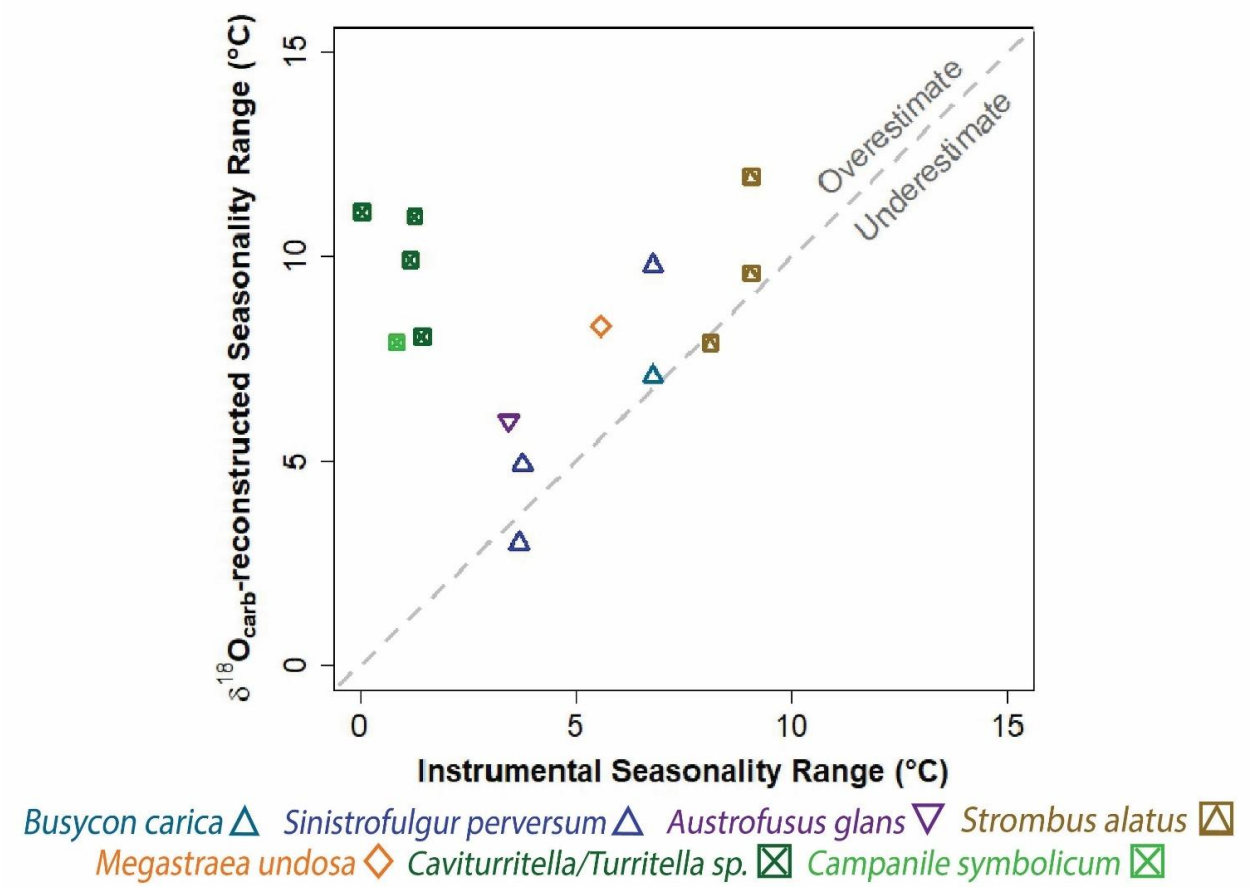

Figure S2.10. $\delta^{18}O$-reconstructed vs. instrumental seasonality (World Ocean Atlas) cross plot for marine gastropods analyzed in this study.

Species Collected	Sample Names	Sample Location; Approximate Latitude	Instrumental Mean Annual Temperature (°C)	Instrumental Summer Temperature (°C)	Instrumental Winter Temperature (°C)
Megastraea undosa	Meg1	Rincon Beach, California (USA); 34N	12.7 +/- 2.8	16.6 +/- 0.1	11.0 +/- 0.1
Cittarium pica	BM1 BM2	Coopers Island, Bermuda; 32N	23.0 +/- 0.1	31.0 +/- 0.1	16.0 +/- 0.1
Strombus alatus	Str3	Tampa, Florida (USA); 28N	23.9 +/- 2.3	27.5 +/- 5.6	19.4 +/- 0.9
Strombus alatus	Str1 Str2	Bonita Springs, Florida (USA); 26N	25.2 +/- 0.7	29.7 +/- 1.0	20.6 +/- 0.7
Conus ermineus	FGS-1	Stetson Bank, Gulf of Mexico; 28N	22.6 +/- 0.1	30.0 +/- 0.1	17.0 +/- 0.1
Austrofusus glans	Au1	Mount Maunganui, New Zealand; 38S	17.5 +/- 0.2	19.2 +/- 0.5	15.8 +/- 0.1
Sinistrofulgur perversum ***Busycon carica***	SPer1 BCar1	Pawleys Island, South Carolina; 33N	23.3 +/- 0.2	26.9 +/- 0.2	20.1 +/- 0.1
Sinistrofulgur perversum	SPer2	Boca Raton, Florida (USA); 26N	27.5 +/- 0.1	29.5 +/- 0.2	25.7 +/- 0.1
Sinistrofulgur perversum	SPer3	Hollywood Beach, Florida (USA); 26N	27.5 +/- 0.4	29.4 +/- 0.3	25.7 +/- 0.7
Campanile symbolicum	C2	Geographe Bay, Australia; 33S	20.1 +/- 0.4	20.5 +/- 0.5	19.6 +/- 0.4
Caviturritella gonostoma	T1	Acapulco, Mexico; 17N	29.4 +/- 0.5	30.1 +/- 0.4	28.8 +/- 0.4
Caviturritella leucostoma	T2		28.5 +/- 2.6	29.4 +/- 2.5	28.0 +/- 2.4
Turritella (s.s.) bacillum	T3	Sri Lanka; 8N	27.4 +/- 0.9	27.2 +/- 1.6	27.3 +/- 0.5
Turritella duplicata	T4	Tharagambadi, India; 11N	28.3 +/ 1.8	28.4 +/- 2.5	27.2 +/- 0.7

Table S2.1. Table of climatological data for each sampling site, mostly obtained from the World Ocean Atlas 2018 database.

Temperatures for Stetson Bank, Gulf of Mexico were previously reported in Gentry et al. (2008); winter and summer temperature estimates for Coopers Island, Bermuda were previously reported in Winkelstern et al. (2017).

Species Collected	Sample Names	Sample Location; Approximate Latitude	Instrumental $\delta^{18}O_c$ (‰ VSMOW)	Source	Source Distance to Site (km)	Modeled $\delta^{18}O_c$ from Breitkreuz et al., 2018 (‰)	Modeled $\delta^{18}O_c$ from LeGrande & Schmidt, 2006 (‰)
Megastraea undosa	Meg1	Rincon Beach, California (USA); 34N	-0.1 +/- 0.1	*Grossman, 1984*	103	-0.5 +/- 0.1	-0.5 +/- 0.1
Cittarium pica	BM1 BM2	Coopers Island, Bermuda; 32N	1.2 +/- 0.1	*Zhang et al., 2021*	0	0.7 +/- 0.1	0.8 +/- 0.1
Strombus alatus	Str3	Tampa, Florida (USA); 28N	1.8 +/- 0.1	*Zhang and Petersen, 2023*	56	1.0 +/- 0.1	0.8 +/- 0.1
Strombus alatus	Str1 Str2	Bonita Springs, Florida (USA); 26N	1.2 +/- 0.1	*Zhang and Petersen, 2023*	39	1.0 +/- 0.1	0.9 +/- 0.1
Conus ermineus	FGS-1	Stetson Bank, Gulf of Mexico; 28N	0.7 +/- 0.5	*Grossman and Ku, 1986*	31	0.6 +/- 0.1	0.5 +/- 0.1
Austrofusus glans	Au1	Mount Maunganui, New Zealand; 38S	-	-	-	0.0 +/- 0.1	0.4 +/- 0.3
Sinistrofulgur perversum	SPer1	Pawleys Island, South Carolina; 33N	0.5 +/- 0.1	*Zhang and Petersen, 2023*	49	0.9 +/- 0.1	0.9 +/- 0.1
Busycon carica	BCar1		0.5 +/- 0.1		49	0.9 +/- 0.1	0.8 +/- 0.1
Sinistrofulgur perversum	SPer2	Boca Raton, Florida (USA); 26N	0.9 +/- 0.2	*Zhang and Petersen, 2023*	56	1.0 +/- 0.1	0.9 +/- 0.1
Sinistrofulgur perversum	SPer3	Hollywood Beach, Florida (USA); 26N	0.9 +/- 0.2	*Zhang and Petersen., 2023*	0	1.0 +/- 0.1	0.9 +/- 0.1
Campanile symbolicum	C2	Geographe Bay, Australia; 33S	0.55 +/- 0.1	*LeGrande & Schmidt, 2006 (value reported in deWinter et al., 2020)*	-	0.9 +/- 0.1	1.1 +/- 0.1
Caviturritella gonostoma	T1	Acapulco, Mexico; 17N	0.2 +/- 0.1	*Benway and Mix, 2004*	502	0.2 +/- 0.1	0.1 +/- 0.1
Caviturritella leucostoma	T2		0.2 +/- 0.1	*Benway and Mix, 2004*	502	0.2 +/- 0.1	0.1 +/- 0.1
Turritella (s.s.) bacillum	T3	Sri Lanka; 8N	0.3 +/- 0.1	*Singh et al., 2010*	110	-0.2 +/- 0.1	0.2 +/- 0.1
Turritella duplicata	T4	Tharagambadi, India; 11N	0.1 +/- 0.1	*Singh et al., 2010*	165	-0.2 +/- 0.1	0.2 +/- 0.1

Table S2.2. Table of instrumental and modeled $\delta^{18}O_w$ data for each sampling site.

Standard	$\Delta_{47\text{-TE}}$ (‰)	Source	$\Delta_{48\text{-TE}}$ (‰)	Source
HG1000	0.0266	Petersen et al., 2019	-0.0020	Recalculated following Petersen et al., 2019 (Fiebig, etc. use 0.0 from Wang et al., 2004)
EG25	0.9198	Petersen et al., 2019	0.3422	Recalculated following Petersen et al., 2019 (Fiebig, etc. use 0.345 from Wang et al., 2004)
ETH1	0.2052	Bernasconi et al., 2021	0.145 0.1277	Swart et al., 2021 Fiebig et al., 2024
ETH2	0.2085	Bernasconi et al., 2021	0.153 0.1299	Swart et al., 2021 Fiebig et al., 2024
ETH3	0.6132	Bernasconi et al., 2021	0.269 0.2481	Swart et al., 2021 Fiebig et al., 2024
ETH4	0.4505	Bernasconi et al., 2021	0.231 0.2041	Swart et al., 2021 Fiebig et al., 2024
GU1	0.2254	*Fiebig et al., 2024	-0.3998	*Fiebig et al., 2024
Carrara Marble (CM)	0.3092	*Fiebig et al., 2024	0.1455	*Fiebig et al., 2024
Pica	0.6093	*Fiebig et al., 2024	0.2307	*Fiebig et al., 2024

*not used to correct

Table S2.3. Theoretical equilibrium Δ_{47} and Δ_{48} values for calibration standards used in this study.

Standard	n	Δ_{48}-CDES70 (this study, +/- 1SE) (‰)	Δ_{48}-CDES90 ('true') (‰)	Offset: CDES90-CDES70 (‰)	Adjusted Δ_{48}-CDES90 (this study) (‰)*
ETH1	24	0.1933 +/- 0.0051	0.1277 +/- 0.0015	0.0656	0.1273
ETH2	22	0.1963 +/- 0.0088	0.1299 +/- 0.0016	0.0664	0.1303
ETH3	27	0.3148 +/- 0.0065	0.2481 +/- 0.0071	0.0667	0.2488
ETH4	22	0.2817 +/- 0.0075	0.2041 +/- 0.0071	0.0776	0.2157
GU1	13	-0.2821 +/- 0.0154	-0.3998 +/- 0.0043	0.1177	-0.3481
Carrara Marble (CM)	12	0.1773 +/- 0.0126	0.1455 +/- 0.0029[#]	0.0318	0.1113
			[&]Proposed $\Delta_{48}{}^{*}{}_{70\text{-}90}$ value	**0.066**	

[&]Calculated as the mean of the ETH1 and ETH2 offsets. $\Delta_{48,CDES70} - 0.0458 = \Delta_{48,CDES90}$.
[#]Unlike ETH1-4 and GU1, this Carrara is not an identical powder to that of Fiebig et al. (2024) but a separate aliquot of CM made at a different university from similar starting material.
*Uncertainty is the same as uncertainty in the column containing un-adjusted values.

Table S2.4. Calculation of $\Delta_{48}{}^{*}{}_{70\text{-}90}$ using ETH standards within the calibration window.

See Section 2.3.3 for more details about the calibration window. 'True' values for ETH1-4, GU1, and CM were obtained from Fiebig et al. (2024).

Standard	n	Δ_{47}: Hybrid gas-based CDES90 (‰)[&]	Δ_{47}: Carbonate-based I-CDES90 (‰)[#]	Δ_{48}: Hybrid gas-based CDES90 (‰)*	Δ_{48}: Carbonate-based GU-CDES90 (‰)[+]
Carrara Marble (CM)	12	0.3006 +/- 0.0049	0.3070 +/- 0.0047	0.1113 +/- 0.0126	0.1020 +/- 0.0137
Islandic *Arctica islandica* (Ice)	14	0.6450 +/- 0.0046	0.6384 +/- 0.0044	0.2260 +/- 0.0122	0.2264 +/- 0.0132
Joulters Cay Ooids (OO)	11	0.6010 +/- 0.0046	0.5961 +/- 0.0045	0.2217 +/- 0.0133	0.2217 +/- 0.0144
Bermudan *Cittarium pica* (Pica)	12	0.6080 +/- 0.0051	0.6029 +/- 0.0049	0.2138 +/- 0.0142	0.2131 +/- 0.0154
GU1	13	0.2542 +/- 0.0065	0.2609 +/- 0.0063	-0.3481 +/- 0.0154	N/A

[&]Calculates SlopeEGL using gases and ETH1-2. Gases only used for the transfer function. An acid fractionation factor of 0.022‰ was applied.
[#]Calculates SlopeEGL using ETH1-2. ETH1-4 used for the transfer function using InterCarb ETH 'true' values. No acid fractionation factor needed.
*Calculates SlopeEGL using gases and ETH1-2. Gases only used for the transfer function. An acid fractionation factor of 0.0458‰ was applied and derived from ETH1-2.
[+]Calculates SlopeEGL using ETH1-2. ETH1-4 and GU1 used for the transfer function using 'true' values from Swart et al. (2021). No acid fractionation factor needed.

Table S2.5. Comparison of standards performance reported in gas-based and carbonate-based references frames within the calibration window.

See Section 2.3.3 for more details about the calibration window. ETH1-4 'true' Δ_{48} values were obtained from Fiebig et al. (2024). All errors represent +/- 1SE on the mean.

Genus	n (# of samples averaged together)	Weighted mean of Δ_{47} difference (‰)	Weighted standard error (‰)	z-score	p-value
***Busycon* sp.**	3	-0.0018	0.012	-0.153	0.878
***Sinistrofulgur* sp.**	11	0.0025	0.006	0.409	0.682
***Austrofusus* sp.**	4	-0.0048	0.010	-0.696	0.487
***Strombus* sp.**	10	-0.0037	0.008	-0.622	0.534
***Megastraea* sp.**	6	-0.0278	0.008	-3.436	0.001
***Turritella/Caviturritella* sp.**	8	0.0179	0.008	2.252	0.024
***Campanile* sp.**	10	0.0196	0.004	4.900	<<0.001
***Cittarium* sp.**	11	0.0204	0.004	5.148	<<0.001
***Conus* sp.**	3	-0.0166	0.013	-1.264	0.206

Table S2.6. Table of statistics of genus-averaged Δ_{47} residuals from the Anderson et al. (2021) calibration line.

p-values <0.05 suggest that the genus average is statistically significant from 0 at the 95% confidence level.

Genus	n (# of samples averaged together)	Weighted mean of Δ_{47} difference (‰)	Weighted standard error (‰)	z-score	p-value
***Busycon* sp.**	3	-0.0018	0.012	-0.153	0.878
***Sinistrofulgur* sp.**	11	0.0025	0.006	0.409	0.682
***Austrofusus* sp.**	4	-0.0070	0.010	-0.696	0.487
***Strombus* sp.**	10	-0.0048	0.008	-0.622	0.534
***Megastraea* sp.**	6	-0.0278	0.008	-3.436	0.001
***Turritella/Caviturritella* sp.**	8	0.0179	0.008	2.252	0.024
***Campanile* sp.**	*3	-0.0013	0.011	-0.115	0.908

*measured for both Δ_{47} and Δ_{48}

Table S2.7. Table of statistics of genus-averaged Δ_{47} residuals from the Fiebig et al. (2021) calibration line.

p-values <0.05 suggest that the genus average is statistically significant from 0 at the 95% confidence level.

Genus	n (# of samples averaged together)	Weighted mean of Δ_{48} difference (‰)	Weighted standard error (‰)	z-score	p-value
***Busycon* sp.**	3	0.011	0.049	0.224	0.823
***Sinistrofulgur* sp.**	11	-0.018	0.025	-0.710	0.478
***Austrofusus* sp.**	4	0.011	0.043	0.256	0.798
***Strombus* sp.**	10	-0.015	0.025	-0.592	0.554
***Megastraea* sp.**	6	0.000	0.035	-0.003	0.997
***Turritella/Caviturritella* sp.**	8	0.019	0.030	0.635	0.525
***Campanile* sp.**	3	-0.015	0.045	-0.326	0.745

Table S2.8. Table of statistics of genus-averaged Δ_{48} residuals from the Fiebig et al. (2021) calibration line.

p-values <0.05 suggest that the genus average is statistically significant from 0 at the 95% confidence level.

2.9 References

Allmon, W.D., 2011. Natural History of Turritelline Gastropods (Cerithiodea: Turritellidae): A Status Report. Malacologia 54(1-2), 15-202.

Anderson, N.T., Kelson, J.R., Kele, S., Daëron, M., Bonifacie, M., Horita, J., Mackey, T.J., John, C.M., Kluge, T., Petschnig, P., Jost, A.B., Huntington, K.W., Bernasconi, S.M., Bergmann, K.D., 2021.

Anderson, N. T., Kelson, J. R., Kele, S., Daëron, M., Bonifacie, M., Horita, J., Mackey, T. J., John, C. M., Kluge, T., Petschnig, P., Jost, A. B., Huntington, K. W., Bernasconi, S. M., Bergmann, K. D., 2021. A Unified Clumped Isotope Thermometer Calibration (0.5–1,100°C) Using Carbonate-Based Standardization. Geophys. Res. Lett. 48, e2020GL092069.

Bajnai, D., Fiebig, J., Tomašových, A., Milner Garcia, S., Rollion-Bard, C., Raddatz, J., Löffler, N., Primo-Ramos, C., Brand, U., 2018. Assessing kinetic fractionation in brachiopod calcite using clumped isotopes. Sci. Rep. 8, 533.

Bajnai, D., Guo, W., Spötl, C., Coplen, T. B., Methner, K., Löffler, N., Krsnik, E., Gischler, E., Hansen, M., Henkel, D., Price, G. D., Raddatz, J., Scholz, D., Fiebig, J., 2020. Dual clumped isotope thermometry resolves kinetic biases in carbonate formation temperatures. Nat. Commun. 11, 4005.

Banerjee, Y., Ghosh, P., 2024. Freshwater plume-like condition near the north-eastern coastal Arabian Sea during early Miocene: Evidence from the stable isotope record in the growth bands of gastropods (Turritella sp.). Terra Nova.

Bao, R., Sheng, X., Li, C., Cui, C., Yan, H., Ji, J., Chen, J., 2023. Calibration of the carbonate clumped isotope thermometer of land snail shells. Chem. Geol. 641, 121773.

Benway, H.M., Mix, A.C., 2004. Oxygen isotopes, upper-ocean salinity, and precipitation sources in the eastern tropical Pacific. EPSL 224(3-4), 493-507.

Bernasconi, S. M., Daëron, M., Bergmann, K. D., Bonifacie, M., Meckler, A. N., Affek, H. P., Anderson, N., Bajnai, D., Barkan, E., Beverly, E., Blamart, D., Burgener, L., Calmels, D., Chaduteau, C., Clog, M., Davidheiser-Kroll, B., Davies, A., Dux, F., Eiler, J., Elliott, B., Fetrow, A. C., Fiebig, J., Goldberg, S., Hermoso, M., Huntington, K. W., Hyland, E., Ingalls, M., Jaggi, M., John, C. M., Jost, A. B., Katz, S., Kelson, J., Kluge, T., Kocken, I. J., Laskar, A., Leutert, T. J., Liang, D., Lucarelli, J., Mackey, T. J., Mangenot, X., Meinicke, N., Modestou, S. E., Müller, I. A., Murray, S., Neary, A., Packard, N., Passey, B. H., Pelletier, E., Petersen, S., Piasecki, A., Schauer, A., Snell, K. E., Swart, P. K., Tripati, A., Upadhyay, D., Vennemann, T., Winkelstern, I., Yarian, D., Yoshida, N., Zhang, N., Ziegler, M., 2021. InterCarb: A Community Effort to Improve Interlaboratory Standardization of the Carbonate Clumped Isotope Thermometer Using Carbonate Standards. Geochem. Geophys. Geosystems 22, e2020GC009588.

Bernasconi, S. M., Müller, I. A., Bergmann, K. D., Breitenbach, S. F. M., Fernandez, A., Hodell, D. A., Jaggi, M., Meckler, A. N., Millan, I., Ziegler, M., 2018. Reducing Uncertainties in Carbonate Clumped Isotope Analysis Through Consistent Carbonate-Based Standardization. Geochem. Geophys. Geosystems 19, 2895–2914.

Bernecker, M., Hofmann, S., Staudigel, P.T., Davies, A.J., Tagliavento, M., Meijer, N., Ballian, A., Fiebig, J., 2023. A robust methodology for triple (Δ_{47}, Δ_{48}, Δ_{49}) clumped isotope analysis of carbonates. Chem. Geol. 642, 121803.

Bernecker, M., Bonifacie, M., Staudigel, P., Meijer, N., Siebert, J., Wehr, N., Haussühl, Bernasconi, S.M., Petrash, D.A., Dietzel, M., Fiebig, J., 2025. Effects of mineralogy on Δ_{47} and Δ_{48} of carbonate-derived CO_2 below analytical resolution. Geochim. Cosmochim. Acta 401, 89-103.

Bigeleisen, J., Mayer, M. G., 2004. Calculation of Equilibrium Constants for Isotopic Exchange Reactions. J. Chem. Phys. 15, 261–267.

Bouchet, P., Rocroi, J.-P., Hausdorf, B., Kaim, A., Kano, Y., Nützel, A., Parkhaev, P., Schrödl, M., Strong, E. E., 2017. Revised Classification, Nomenclator and Typification of Gastropod and Monoplacophoran Families. Malacologia 61, 1–526.

Breitenbach, S. F. M., Mleneck-Vautravers, M. J., Grauel, A.-L., Lo, L., Bernasconi, S. M., Müller, I. A., Rolfe, J., Gázquez, F., Greaves, M., Hodell, D. A., 2018. Coupled Mg/Ca and clumped isotope analyses of foraminifera provide consistent water temperatures. Geochim. Cosmochim. Acta 236, 283–296.

Breitkreuz, C., Paul, A., Kurahashi-Nakamura, T., Losch, M., Schulz, M., 2018. A Dynamical Reconstruction of the Global Monthly Mean Oxygen Isotopic Composition of Seawater. Journal of Geophysical Research 123(10), 7206-7219.

Bricker, H. L., Bateman, J. B., Elliott, B., Mitsunaga, B. A., Mering, J., Foster, I. S., Yanes, Y., Oches, E. A., Eagle, R. A., Tripati, A., 2023. A multi-region study of carbonate clumped isotope data from terrestrial snails. Palaeogeogr. Palaeoclimatol. Palaeoecol. 628, 111754.

Caldarescu, D.E., Sadatzki, H., Andersson, C., Schäfer, P., Fortunato, H., Meckler, A.N., 2021. Clumped isotope thermometry in bivalve shells: A tool for reconstructing seasonal upwelling. Geochim. Cosmochim. Acta 294, 174-191.

Came, R. E., Brand, U., Affek, H. P., 2014. Clumped isotope signatures in modern brachiopod carbonate. Chem. Geol. 377, 20–30.

Chiappa-Carrara, X., Enríquez, C., Papiol, V., Mariño-Tapia, I., Reyes-Hernández, C., 2019. Pacific coast of Mexico. World seas: an environmental evaluation 655-671.

Clark, A.J., Jaggi, M., Bernasconi, S.M., Fiebig, J., Stoll, H.M., 2025. Clumped isotope temperatures of coccolithophores from global sediment traps. Paleoceanogr. Paleoclimatol. 40(6), e2024PA005054.

Clark, A.J., Torres-Romero, I., Jaggi, M., Bernasconi, S.M., Stoll, H.M., 2024. A clumped isotope calibration of coccoliths at well-constrained culture temperatures for marine temperature reconstructions. Climate of the Past 20(9), 2081-2101.

Curley, A. N., Petersen, S. V., Edie, S. M., Guo, W., 2023. Biologically driven isotopic fractionations in bivalves: from palaeoenvironmental problem to palaeophysiological proxy. Biol. Rev. 98, 1016–1032.

Daëron, M., Vermeesch, P., 2023. Omnivariant generalized least squares regression: Theory, geochronological applications, and making the case for reconciled Δ_{47} calibrations. Chem. Geol., 121881.

Davies, A. J., Brand, U., Tagliavento, M., Bitner, M. A., Bajnai, D., Staudigel, P., Bernecker, M., Fiebig, J., 2023. Isotopic disequilibrium in brachiopods disentangled with dual clumped isotope thermometry. Geochim. Cosmochim. Acta 359, 135–147.

Davies, A. J., Davis, S., John, C. M., 2021. Evidence of taxonomic non-equilibrium effects in the clumped isotope composition of modern cephalopod carbonate. Chem. Geol. 578, 120317.

Davies, A. J., Guo, W., Bernecker, M., Tagliavento, M., Raddatz, J., Gischler, E., Flögel, S., Fiebig, J., 2022. Dual clumped isotope thermometry of coral carbonate. Geochim. Cosmochim. Acta 338, 66–78.

Defliese, W. F., Hren, M. T., Lohmann, K. C., 2015. Compositional and temperature effects of phosphoric acid fractionation on Δ_{47} analysis and implications for discrepant calibrations. Chem. Geol. 396, 51–60.

Dennis, K. J., Cochran, J. K., Landman, N. H., Schrag, D. P., 2013. The climate of the Late Cretaceous: New insights from the application of the carbonate clumped isotope thermometer to Western Interior Seaway macrofossil. Earth Planet. Sci. Lett. 362, 51–65.

de Vos, A., Pattiaratchi, C.B., Wijeratne, E.M.S., 2014. Surface circulation and upwelling patterns around Sri Lanka. Biogeosciences 11, 5909-5930.

de Winter, N.J., Vellekoop, J., Clark, A.J., Stassen, P., Speijer, R.P., Claeys, P., 2020. The giant marine gastropod Campanile giganteum (Lamarck, 1804) as a high-resolution archive of seasonality in the Eocene greenhouse world. Geochem. Geophys. Geosystems 21, e2019GC008794.

de Winter, N.J., Müller, I.A., Kocken, I.J., Thibault, N., Ullmann, C.V., Farnsworth, A., Lunt, D.J., Claeys, P., Ziegler, M., 2021. Absolute seasonal temperature estimates from clumped isotopes in bivalve shells suggest warm and variable greenhouse climate. Commun. Earth Environ. 2, 1-8.

de Winter, N.J., Witbaard, R., Kochen, I.J., Müller, I.A., Guo, J., Goudsmit, B., Ziegler, M., 2022. Temperature dependence of clumped isotopes (Δ_{47}) in aragonite. Geophys. Res. Lett. 49, e2022GL099479.

Dong, J., Eiler, J., An, Z., Li, X., Liu, W., Hu, J., 2021. Clumped isotopic compositions of cultured and natural land-snail shells and their implications. Palaeogeogr. Palaeoclimatol. Palaeoecol. 577, 110530.

Dyer, K.R., 1998. The typology of intertidal mudflats. Geological Society Publications 139, 11-24.

Eagle, R. A., Eiler, J. M., Tripati, A. K., Ries, J. B., Freitas, P. S., Hiebenthal, C., Wanamaker, A. D. J., Taviani, M., Elliot, M., Marenssi, S., Nakamura, K., Ramirez, P., Roy, K., 2013. The influence of temperature and seawater carbonate saturation state on ^{13}C–^{18}O bond ordering in bivalve mollusks. Biogeosciences 10, 4591–4606.

Eagle, R. A., Enriquez, M., Grellet-Tinner, G., Pérez-Huerta, A., Hu, D., Tütken, T., Montanari, S., Loyd, S. J., Ramirez, P., Tripati, A. K., Kohn, M. J., Cerling, T. E., Chiappe, L. M., Eiler, J. M., 2015. Isotopic ordering in eggshells reflects body temperatures and suggests differing thermophysiology in two Cretaceous dinosaurs. Nat. Commun. 6, 8296.

Eiler, J. M., 2007. "Clumped-isotope" geochemistry—The study of naturally-occurring, multiply-substituted isotopologues. Earth Planet. Sci. Lett. 262, 309–327.

Evans, D., Sagoo, N., Renema, W., Cotton, L. J., Müller, W., Todd, J. A., Saraswati, P. K., Stassen, P., Ziegler, M., Pearson, P. N., Valdes, P. J., Affek, H. P., 2018. Eocene greenhouse climate revealed by coupled clumped isotope-Mg/Ca thermometry. Proc. Natl. Acad. Sci. 115, 1174–1179.

Fiebig J., Bajnai D., Löffler N., Methner K., Krsnik E., Mulch A., Hofmann S., 2019. Combined high-precision Δ_{48} and Δ_{47} analysis of carbonates. Chem. Geol. 522, 186–191.

Fiebig, J., Daëron, M., Bernecker, M., Guo, W., Schneider, G., Boch, R., Bernasconi, S. M., Jautzy, J., Dietzel, M., 2021. Calibration of the dual clumped isotope thermometer for carbonates. Geochim. Cosmochim. Acta 312, 235–256.

Fiebig, J., Bernecker, M., Meijer, N., Methner, K., Staudigel, P.T., Davies, A.J., Bayarjargal, L., Spahr, D., Winkler, B., Hofmann, S., Granzin, M., Petersen, S.V., 2024. Carbonate clumped isotope values compromised by nitrate-derived NO2 interferent. Chem. Geol. 670, 122382.

Frew, R.D., Dennis, P.F., Heywood, K.J., Meredith, M.P., Boswell, S.M., 2000. The oxygen isotope composition of water masses in the northern North Atlantic. Deep Sea Research Part I: Oceanographic Research Papers 47(12), 2265-2286.

Friend, D.S., Anderson, B.M., Altier, E., Sang, S., Petsios, E., Portell, R.W., Allmon, W.D., 2023. Systematics and Phylogeny of Plio-Pleistocene Species of Turritellidae (Gastropoda) from Florida and the Atlantic Coastal Plain. Bull. Am. Paleontol. 402.

García-Reyes, M., Largier, J., 2010. Observations of increased wind-driven coastal upwelling off central California. J. Geophys. Res. 115, C04011.

Ghosh, P., Adkins, J., Affek, H., Balta, B., Guo, W., Schauble, E. A., Schrag, D., Eiler, J. M., 2006. 13C–18O bonds in carbonate minerals: A new kind of paleothermometer. Geochim. Cosmochim. Acta 70, 1439–1456.

Ghosh, P., Eiler, J., Campana, S. E., Feeney, R. F., 2007. Calibration of the carbonate 'clumped isotope' paleothermometer for otoliths. Geochim. Cosmochim. Acta 71, 2736–2744.

Grossman, E.L., 1984. Stable isotope fractionation in live benthic foraminifera from the southern California Borderland. Palaeogeogr. Palaeoclim. Palaeoecol. 47(3-4), 301-327.

Grossman, E. L., Ku, T.-L., 1986. Oxygen and carbon isotope fractionation in biogenic aragonite: Temperature effects. Chem. Geol. Isot. Geosci. Sect. 59, 59–74.

Guo, W., Mosenfelder, J.L., Goddard, III W.A., Eiler, J.M., 2009. Isotopic fractionations associated with phosphoric acid digestion of carbonate minerals: Insights from first-principles theoretical modeling and clumped isotope measurements. Geochim. Cosmochim. Acta 73(24), 7203-7225.

Guo, J., Ziegler, M., Wanders, N., Vreeken, M., Yin, Q., Lu H., Fuchs, L., Dong, J., Sun, Y., Peterse, F., 2024. Robust land surface temperature record for north China over the past 21,000 years. Science Advances 10, eadj4800.

Guo, W., 2020. Kinetic clumped isotope fractionation in the DIC-H2O-CO2 system: Patterns, controls, and implications. Geochim. Cosmochim. Acta 268, 230–257.

Guo, Y., Deng, W., Wei, G., Lo, L., Wang, N., 2019. Clumped isotopic signatures in land-snail shells revisited: Possible palaeoenvironmental implications. Chem. Geol. 519, 83-94.

Guo, Y., Deng, W., Wei, G., Chen, X., Liu, X., Wang, X., Lo, L., Cai, G., Zeng, T. 2020. Exploring the Temperature Dependence of Clumped Isotopes in Modern Porites Corals. J. Geophys. Res. Biogeosciences 125, e2019JG005402.

Henkes, G. A., Passey, B. H., Wanamaker, A. D., Grossman, E. L., Ambrose, W. G., Carroll, M. L., 2013. Carbonate clumped isotope compositions of modern marine mollusk and brachiopod shells. Geochim. Cosmochim. Acta 106, 307–325.

Hollis, C. J., Dunkley Jones, T., Anagnostou, E., Bijl, P. K., Cramwinckel, M. J., Cui, Y., Dickens, G. R., Edgar, K. M., Eley, Y., Evans, D., Foster, G. L., Frieling, J., Inglis, G. N., Kennedy, E. M., Kozdon, R., Lauretano, V., Lear, C. H., Littler, K., Lourens, L., Meckler, A. N., Naafs, B. D. A., Pälike, H., Pancost, R. D., Pearson, P. N., Röhl, U., Royer, D. L., Salzmann, U., Schubert, B. A., Seebeck, H., Sluijs, A., Speijer, R. P., Stassen, P., Tierney, J., Tripati, A., Wade, B., Westerhold, T., Witkowski, C., Zachos, J. C., Zhang, Y. G., Huber, M., Lunt, D. J., 2019. The DeepMIP contribution to PMIP4: methodologies for selection, compilation and analysis of latest Paleocene and early Eocene climate proxy data, incorporating version 0.1 of the DeepMIP database. Geosci. Model Dev. 12, 3149–3206.Huntington K.W., Petersen S.V., 2023. Frontiers of Carbonate Clumped Isotope Thermometry. Annu. Rev. Earth Planet. Sci. 51, 611-641.

Huante, A.G., Cueto, Y.R., Silva, R., Mendoza, E., Vega, L.A., 2018. Determination of the Potential Thermal Gradient for the Mexican Pacific Ocean. J. Mar. Sci. Eng. 6(1), 20.

Huntington, K.W., Petersen, S.V., 2023. Frontiers of carbonate clumped isotope thermometry. Annu. Rev. Earth Planet Sci. 51, 611-641.

Huyghe, D., Daëron, M., de Rafelis, M., Blamart, D., Sébilo, M., Paulet, Y.-M., Lartaud, F., 2022. Clumped isotopes in modern marine bivalves. Geochim. Cosmochim. Acta 316, 41–58.

Ingalls, M., Leapaldt, H.C., Lloyd, M.K., 2024. Microbial Autotrophy Recorded by Carbonate Dual Clumped Isotope Disequilibrium. Geochem. Geophys. Geosyst. 25, 6, e2024GC011590.

Jautzy, J. J., Savard, M. M., Dhillon, R. S., Bernasconi, S. M., Smirnoff, A., 2020. Clumped isotope temperature calibration for calcite: Bridging theory and experimentation. Geochem. Perspect. Lett. 14, 36–41.

Jones M. M., Petersen S. V., Curley A. N., 2022. A tropically hot mid-Cretaceous North American Western Interior Seaway. Geology 50, 954–958.

Katz, A., Bonifacie, M., Hermoso, M., Cartigny, P., Calmels, D., 2017. Laboratory-grown coccoliths exhibit no vital effect in clumped isotope (Δ_{47}) composition on a range of geologically relevant temperatures. Geochim. Cosmochim. Acta 208, 335–353.

Kelson, J. R., Huntington, K. W., Schauer, A. J., Saenger, C., Lechler, A. R., 2017. Toward a universal carbonate clumped isotope calibration: Diverse synthesis and preparatory methods suggest a single temperature relationship. Geochim. Cosmochim. Acta 197, 104–131.

Kim, S.-T., O'Neil, J. R., Hillaire-Marcel, C., Mucci, A., 2007. Oxygen isotope fractionation between synthetic aragonite and water: Influence of temperature and Mg2+ concentration. Geochim. Cosmochim. Acta 71, 4704–4715.

Kimball, J., Eagle, R., Dunbar, R., 2016. Carbonate “clumped” isotope signatures in aragonitic scleractinian and calcitic gorgonian deep-sea corals. Biogeosciences 13, 6487–6505.

Kluge, T., John, C. M., Jourdan, A.-L., Davis, S., Crawshaw, J., 2015. Laboratory calibration of the calcium carbonate clumped isotope thermometer in the 25–250°C temperature range. Geochim. Cosmochim. Acta 157, 213–227.

LeGrande, A. N., Schmidt, G. A., 2006. Global gridded data set of the oxygen isotopic composition in seawater. Geophys. Res. Lett. 33.

Locarnini, R.A., Mishonov, A.V., Baranova, O.K., Boyer, T.P., Zweng, M.M., García, H.E., Reagan, J.R., Seidov, D., Weathers, K., Paver, C.R., Smolyar, I., 2019. World Ocean Atlas 2018, Volume 1: Temperature. Mishonov, A.V. (Ed.), NOAA Atlas NESDIS 81, 52 pp.

Lu, C., Swart, P. K., 2023. The application of dual clumped isotope thermometer (Δ_{47} and Δ_{48}) to the understanding of dolomite formation. Geology 52, 56–60.

Lu, C., Murray, S.T., Klaus, J., McNeill, D.F., Swart, P.J., 2024. Dual clumped isotopes (Δ_{47} and Δ_{48}) reveal non-equilibrium formation of freshwater cements. Geochim. Cosmochim. Acta 379, 145-157.

Lucarelli, J. K., Purgstaller, B., Ulrich, R. N., Parvez, Z., Leis, A., Goetschl, K. E., Eagle, R. A., Dietzel, M., Tripati, A., 2023. Dual clumped (Δ_{47}-Δ_{48}) isotope data for amorphous carbonates and transformation products reveal a novel mechanism for disequilibrium clumped isotope effects. Geochim. Cosmochim. Acta 359, 119–134.

Meinicke, N., Ho, S. L., Hannisdal, B., Nürnberg, D., Tripati, A., Schiebel, R., Meckler, A. N., 2020. A robust calibration of the clumped isotopes to temperature relationship for foraminifers. Geochim. Cosmochim. Acta 270, 160–183.

Meyer, K. W., Petersen, S. V., Lohmann, K. C., Winkelstern, I. Z., 2018. Climate of the Late Cretaceous North American Gulf and Atlantic Coasts. Cretac. Res. 89, 160–173.

Muni Krishna, K., 2008. View on Bay of Bengal upwelling area on the basis of 19-years of satellite sea surface temperature. Int. J. Digit. Earth 1(3).

O’Hora, H. E., Petersen, S. V., Vellekoop, J., Jones, M. M., Scholz, S. R., 2022. Clumped-isotope-derived climate trends leading up to the end-Cretaceous mass extinction in northwestern Europe. Clim. Past 18, 1963–1982.

Peral, M., Daëron, M., Blamart, D., Bassinot, F., Dewilde, F., Smialkowski, N., Isguder, G., Bonnin, J., Jorissen, F., Kissel, C., Michel, E., Vázquez Riveiros N., Waelbroeck, C., 2018. Updated calibration of the clumped isotope thermometer in planktonic and benthic foraminifera. Geochim. Cosmochim. Acta 239, 1–16.

Pesnin, M., Thaler, C., Daëron, M., Nomade, S., Rollion-Bard, C., 2024. Mineralogical and environmental effects on the $\delta^{13}C$, $\delta^{18}O$, and clumped isotope composition of modern bryozoans. Chem. Geol. 662, 122148.

Petersen, S. V., Defliese, W. F., Saenger, C., Daëron, M., Huntington, K. W., John, C. M., Kelson, J. R., Bernasconi, S. M., Colman, A. S., Kluge, T., Olack, G. A., Schauer, A. J., Bajnai, D., Bonifacie, M., Breitenbach, S. F. M., Fiebig, J., Fernandez, A. B., Henkes, G. A., Hodell, D., Katz, A., Kele, S., Lohmann, K. C., Passey, B. H., Peral, M. Y., Petrizzo, D. A., Rosenheim, B. E., Tripati, A., Venturelli, R., Young, E. D., Winkelstern, I. Z., 2019. Effects of Improved 17O Correction on Interlaboratory Agreement in Clumped Isotope Calibrations, Estimates of Mineral-Specific Offsets, and Temperature Dependence of Acid Digestion Fractionation. Geochem. Geophys. Geosystems 20, 3495–3519.

Petrizzo, D. A., Young, E. D., Runnegar, B. N., 2014. Implications of high-precision measurements of 13C–18O bond ordering in CO2 for thermometry in modern bivalved mollusc shells. Geochim. Cosmochim. Acta 142, 400–410.

Piasecki, A., Bernasconi, S. M., Grauel, A.-L., Hannisdal, B., Ho, S. L., Leutert, T. J., Marchitto, T. M., Meinicke, N., Tisserand, A., Meckler, N., 2019. Application of Clumped Isotope Thermometry to Benthic Foraminifera. Geochem. Geophys. Geosystems 20, 2082–2090.

Portela, E., Beier, E., Barton, E.D., Sánchez-Velasco, L., 2018. Surface Salinity Balance in the Tropical Pacific Off Mexico. Journal of Geophysical Research: Oceans 123(8), 5763-5776.

Prasanna, K., Ghosh, P., Eagle, R. A., Tripati, A., Kapur, V. V., Feeney, R. F., Fosu, B. R., Mishra, D., 2021. Temperature Estimates of Lower Miocene (Burdigalian) Coastal Water of Southern India Using a Revised Otolith “Clumped” Isotope Paleothermometer. Geochem. Geophys. Geosystems 22, e2020GC009601.

Ray, S., Swain, D., Ali, M.M., Bourassa, M.A., 2022. Coastal upwelling in the Western Bay of Bengal: role of local and remote windstress. Remote Sensing 14(19), 4703.

RDevelopment CORE TEAM, R., 2008. R: A language and environment for statistical computing. R foundation for statistical computing Vienna, Austria.

Saenger, C., Affek, H. P., Felis, T., Thiagarajan, N., Lough, J. M., Holcomb, M., 2012. Carbonate clumped isotope variability in shallow water corals: Temperature dependence and growth-related vital effects. Geochim. Cosmochim. Acta 99, 224–242.

Sandamali, G.A.J., Thilakarathne, E.P.D.N., Jayarathna, W.N.D.S., Abeygunawardana, A.P., Warnasuriya, T.W.S., Egodauyana, K.P.U.T., 2023. Chlorophyll-a variability in different zones of the Indian Ocean around Sri Lanka concerning monsoon patterns and sea surface temperature. Reg. Stud. Mar. Sci. 61, 102904.

Schauble, E. A., Ghosh, P., Eiler, J. M., 2006. Preferential formation of 13C–18O bonds in carbonate minerals, estimated using first-principles lattice dynamics. Geochim. Cosmochim. Acta 70, 2510–2529.

Scholz, S.R., Petersen, S.V., Anderson, B.M., 2024. Modern reconstructions of mean and seasonal-scale climate from coastal marine gastropods (Turritellidae). Palaeogeogr. Palaeoclimatol. Palaeoecol. 655, 112553.

Singh, A., Jani, R.A., Ramesh, R., 2010. Spatiotemporal variations of the $\delta^{18}O$-salinity relation in the northern Indian Ocean. Deep Sea Research Part I: Oceanographic Research Papers 57(11), 1422-1431.

Spooner, P. T., Guo, W., Robinson, L. F., Thiagarajan, N., Hendry, K. R., Rosenheim, B. E., Leng, M. J., 2016. Clumped isotope composition of cold-water corals: A role for vital effects? Geochim. Cosmochim. Acta 179, 123–141.

Staudigel, P., Bernecker, M., Curley, A., Meijer, N., Bayarjargal, L., Dietzel, M., Fiebig, J., 2025. Isotopic resetting of CO_2 in the presence of carbonate samples: Implications for oxygen- and clumped-isotope analyses. Chem. Geol. 694, 123012.

Swart, P.K., Lu, C., Moore, E.W., Smith, M.E., Murray, S.T., Staudigel, P.T., 2021. A calibration equation between Δ_{48} values of carbonate and temperature. RCM 35, 17, e9147.

Thiagarajan, N., Adkins, J., Eiler, J., 2011. Carbonate clumped isotope thermometry of deep-sea corals and implications for vital effects. Geochim. Cosmochim. Acta 75, 4416–4425.

Tripati, A. K., Eagle, R. A., Thiagarajan, N., Gagnon, A. C., Bauch H., Halloran P. R., Eiler J. M., 2010. 13C–18O isotope signatures and 'clumped isotope' thermometry in foraminifera and coccoliths. Geochim. Cosmochim. Acta 74, 5697–5717.

Tripati, A. K., Hill, P. S., Eagle, R. A., Mosenfelder, J. L., Tang, J., Schauble, E. A., Eiler, J. M., Zeebe, R. E., Uchikawa, J., Coplen, T. B., Ries, J. B., Henry, D., 2015. Beyond temperature: Clumped isotope signatures in dissolved inorganic carbon species and the influence of solution chemistry on carbonate mineral composition. Geochim. Cosmochim. Acta 166, 344–371.

Urey, H.C., 1947. The Thermodynamics Properties of Isotopic Substances. J. Chem. Soc., 562-581.

Underwood, A. J., 1979. The Ecology of Intertidal Gastropods. In Advances in Marine Biology (eds. F. S. Russell and M. Yonge). Academic Press. pp. 111–210.

Wacker, U., Fiebig, J., Tödter, J., Schöne, B. R., Bahr, A., Friedrich, O., Tütken, T., Gischler, E., Joachimski, M. M., 2014. Empirical calibration of the clumped isotope paleothermometer using calcites of various origins. Geochim. Cosmochim. Acta 141, 127–144.Wang Z.,

Schauble E.A., Eiler J.M., 2004. Equilibrium thermodynamics of multiply substituted isotopologues of molecular gases. Geochim. Cosmochim. Acta 68(23), 4779-4797.

Wang, X., Cui, L., Zhai, J., Ding, Z., 2016. Stable and clumped isotopes in shell carbonates of land snails Cathaica sp. and Bradybaena sp. in north China and implications for ecophysiological characteristics and paleoclimate studies. Geochem. Geophys. Geosystems 17, 219–231.

Willems, A., Vellekoop, J., Doubrawa, M., Speijer, R.P., 2021. A paleoenvironmental reconstruction of the Campanile giganteum (Lamarck, 1804) bed (Lutetian, Paris Basin) utilizing quantitative macro- and micropaleontological data. Geosciences Made in Belgium 217.

Wang, Z., Schauble, E.A., Eiler, J.M., 2004. Equilibrium thermodynamics of multiply substituted isotopologues of molecular gases. Geochim. Cosmochim. Acta 68 (23), 4779-4797.

Winkelstern, I. Z., Rowe, M. P., Lohmann, K. C., Defliese, W. F., Petersen, S. V., Brewer, A. W., 2017. Meltwater pulse recorded in Last Interglacial mollusk shells from Bermuda. Paleoceanography 32, 132–145.

Zaarur, S., Olack, G., Affek, H. P., 2011. Paleo-environmental implication of clumped isotopes in land snail shells. Geochim. Cosmochim. Acta 75, 6859–6869.

Zhai, J., Wang, X., Qin, B., Cui, L., Zhang, S., Ding, Z., 2019. Clumped isotopes in land snail shells over China: Towards establishing a biogenic carbonate paleothermometer. Geochim. Cosmochim. Acta 257, 68–79.

Zhang, J. Z., Petersen, S. V., Winkelstern, I. Z., Lohmann, K. C., 2021. Seasonally Variable Aquifer Discharge and Cooler Climate in Bermuda During the Last Interglacial Revealed by Subannual Clumped Isotope Analysis. Paleoceanogr. Paleoclimatology 36, e2020PA004145.

Zhang, J.Z., Petersen, S.V., 2023. Clumped and oxygen isotope sclerochronology methods tested in the bivalve Lucina pensylvanica. Chemical Geology 620, 121346.

Zhang, N., Yamada, K., Kano, A., Matsumoto, R., Yoshida, N., 2018. Equilibrated clumped isotope signatures of land-snail shells observed from laboratory culturing experiments and its environmental implications. Chem. Geol. 488, 189–199.

Chapter 3 'Vital' (Disequilibrium) Effects in Turritellid Gastropods – A Case Study With Colombian Mid-Miocene Fossils

3.1 Abstract

Turritellid gastropods are widespread in the fossil record from the past ~130 million years and are frequently used for paleoenvironmental reconstruction via stable isotope analysis (e.g., $\delta^{18}O$ sclerochronology). Application of the more advanced 'clumped' isotope paleothermometry (Δ_{47}), which avoids some of the limitations of traditional $\delta^{18}O$ paleothermometry, is a natural next step in paleoclimate research using turritellids. However, previous work suggests that turritellids may precipitate their shells out of isotopic equilibrium (i.e., display vital effects) resulting in a cold bias in their Δ_{47}-temperatures. In this study, we expand these data through Δ_{47} measurements from two more modern and seven Mid-Miocene turritellids collected from the Guajira Peninsula of Colombia. New modern turritellid data support previous findings of a ~6°C cold bias in Δ_{47}-temperatures. Fossil turritellid Δ_{47}-temperatures, adjusted to account for this ~6°C offset, estimate Mid-Miocene seawater temperatures between ~25-33°C, consistent with other regional proxy estimates. These data suggest Mid-Miocene SSTs were comparable to or slightly warmer than modern (~26-27°C). $\delta^{13}C$ values and Δ_{47}-temperatures appear to have briefly decreased between ~16.5 and ~15 Ma, possibly indicative of a local upwelling pulse amidst peak global warmth during the Mid-Miocene Climatic Optimum.

3.2 Introduction

Turritellids are one of the most important and recognizable gastropod groups in the fossil record over the past ~130 million years, and their natural history is well-documented (e.g., Allmon, 1988; Allmon, 2011; Friend et al., 2023). They are widespread in marine deposits since the Cretaceous, tend to live in dense clusters, and are the dominant species in many macrofossil assemblages where they are found (Allmon, 2007). Previous studies have reported occurrences of turritellid assemblages across the globe, typically in mid- to low-latitude regions with high nutrient levels and relatively cool waters.

Because they are so widespread, fossil turritellids have frequently been used for paleoenvironmental reconstruction via stable isotope analysis (e.g., $\delta^{18}O$ sclerochronology) (Andreasson and Schmitz, 1996; Waite and Allmon, 2013; Scholz et al., 2020). Specifically, $\delta^{18}O_{carb}$ thermometry (e.g., Urey, 1947; Epstein et al., 1953) has been applied to turritellids to reconstruct seasonal-scale temperature variations from warm periods such as the middle Eocene (e.g., Andreasson and Schmitz, 1996). However, there are uncertainties associated with these methods due to gaps in knowledge of past $\delta^{18}O_w$. On the other hand, the relatively newer method of 'clumped' isotope thermometry (Δ_{47}) (e.g., Ghosh et al., 2006; Schauble et al., 2006; Eiler, 2007) allows for paleotemperature reconstructions from biogenic carbonates independently of $\delta^{18}O_w$. Thus, Δ_{47} has tremendous potential as a tool for paleotemperature reconstruction in regions with variable $\delta^{18}O_w$, such as where rainfall or upwelling rates vary throughout the year.

Unfortunately, fossil turritellids may not be viable for standard use of Δ_{47}-paleothermometry. Quizon et al. (2025) demonstrated that Δ_{47}-temperatures from modern turritellids are an average of ~6°C cooler than modern sea surface temperatures (SSTs) at their respective collection sites in Mexico, India, and Sri Lanka. They proposed that this cold bias was

likely due to a combination of influence from inhabiting cooler upwelled waters and shell precipitation out of equilibrium (i.e., vital effects). From this, Quizon et al. (2025) suggested that it may still be possible to estimate accurate paleo-SSTs by adding a flat ~6°C to unadjusted fossil turritellid Δ_{47}-temperatures. These preliminary findings, however, come from a small number (n=4) of modern shells (Quizon et al., 2025).

Here, we expand the number of modern turritellids studied for Δ_{47} with data from two additional modern turritellid shells. We also present Δ_{47} measurements from seven Mid-Miocene fossil turritellids from Colombia and explore the potential of applying a fixed offset correction to recover more accurate environmental temperatures. Finally, we synthesize these data to discuss Mid-Miocene climate and hydrology in the equatorial Atlantic.

3.3 Materials and Methods

3.3.1 Site selection

Modern and fossil turritellids were obtained from the Guajira Peninsula in Colombia (12°N, paleolatitude 8°N) (Fig. 3.1). Several Neogene outcrops have been described in this region primarily consisting of limestone, sandstone, and mudstone, indicative of shallow marine to marginal marine depositional environments (Moreno et al., 2015). The ages of the Jimol and Castilletes Formations from these deposits are well-constrained from Sr isotope stratigraphy (Hendy et al., 2015) and are thought to span the middle Miocene (~18-14 Ma), including the Mid-Miocene Climatic Optimum (MMCO) (~17.3-14.7 Ma).

3.3.2 Samples and sampling methods

Two modern and seven fossil turritellids originally measured for $\delta^{18}O$ sclerochronology by Scholz et al. (2020) were resampled for Δ_{47} (Table S3.3, Fig. S3.1). Preservation assessment

conducted by Scholz et al. (2020) determined that all samples preserve original aragonite with no secondary calcite. For each Δ_{47} measurement, >3mg of powder were extracted from the outer shell layer using a dental drill on low speed. The two modern shells (628A, 628B) were sampled at three and five locations on the shell respectively (see Fig. S3.1 for drill positions). Of the seven fossil shells, three were sampled for bulk Δ_{47} (i.e., material accumulated over at least 1 year of growth) and four were sampled for seasonally targeted Δ_{47} measurements (see Appendices for details about data processing). Δ_{47}-temperatures and Δ_{47}-derived $\delta^{18}O_{water}$ values ($\delta^{18}O_{rsw}$) from modern shells were compared to modern sea surface and upwelling temperatures (Locarnini et al., 2019; Andrade and Barton, 2005) and to instrumental and modelled $\delta^{18}O_{water}$ values (Epstein and Mayeda, 1953; LeGrande and Schmidt, 2006; Breitkreuz et al., 2018).

3.4 Results

3.4.1 Modern turritellids

Five of eight Δ_{47}-temperatures measured on modern shells are ~8-13°C cooler than modern SSTs (~26-27°C, Locarnini et al., 2019) and ~3-8°C cooler than modern upwelling temperatures in the region (~22-23°C, Andrade and Barton, 2005). All three Δ_{47}-temperatures from shell 628A fall between 15°C and 19°C and are substantially below modern minimum SSTs and upwelling temperatures. Four of five Δ_{47}-temperatures from shell 628B fall within a similar range of ~14-26°C (Fig. 3.2A). Although 628B-cm2 reproduced more poorly than the other samples, the sample mean follows the trends seen in other data. It is unclear why sample 628B-ctip exhibits an anomalously high temperature of 36°C; this is not likely an environmental signal and may instead have resulted from factors such as poorer preservation in the sampled part of the shell (see Fig. S3.1) or accidental measurement of some detrital carbonate.

$\delta^{18}O_{rsw}$ values from the modern turritellids fall between -2.9‰ and -0.4‰, except for 628B-cm1 which is much higher at 1.9‰ (Fig. 3.2B). This high $\delta^{18}O_{rsw}$ value is likely an artifact of the high Δ_{47}-temperature translating through the $\delta^{18}O_{rsw}$ calculation. Excluding this one high point, remaining $\delta^{18}O_{rsw}$ values are ~2-4‰ depleted relative to modern instrumental and modelled values. Altogether, Δ_{47} and $\delta^{18}O_{rsw}$ values broadly exhibit consistent positive Δ_{47} and negative $\delta^{18}O_{rsw}$ from equilibrium (Fig. 3.2C).

3.4.2 Fossil (Mid-Miocene) turritellids

Δ_{47}-temperatures from the Mid-Miocene turritellids were consistently between ~19-27°C through the study interval (Fig. 3.3C), with the coolest samples occurring between ~16.5 and 15 Ma. These temperatures are ~2-7°C cooler than modern SSTs, but some overlap with minimum modern upwelling temperatures in the Guajira Peninsula region (~22-23°C, Andrade and Barton, 2005). Differences between apparent summer and winter Δ_{47}-temperatures are limited to 3°C, consistent with the low latitude of the site.

$\delta^{18}O_{rsw}$ values from the fossil turritellids fall between -3‰ and -1‰ (Fig. 3.3D), ~3-4‰ lower than measured modern $\delta^{18}O_w$ values in the region. The reconstructed summer and winter $\delta^{18}O_w$ values are distinct, with differences of up to ~2‰ within a single shell, consistent with previous interpretations of a highly seasonal hydrological cycle (Scholz et al., 2020).

3.5 Discussion

3.5.1 Presence of vital effects in modern turritellids

Our data support the presence of vital (disequilibrium) effects in modern turritellids, as previously suggested by Quizon et al. (2025). The authors reported Δ_{47}-temperatures in turritellids from Mexico, Sri Lanka, and India that were cooler than both local SSTs and upwelling temperatures (Fig. S3.6), with an average cold bias of ~6°C from SSTs. They

proposed the full 6°C offset was likely due to a combination of living in cooler upwelling waters and disequilibrium precipitation. However, true environmental temperatures from these sites were not well-constrained due to vague documentation of collection sites for museum specimens. Δ_{47}-temperatures from modern turritellids in the current study, where the collection site is well-documented, confirm the previous conclusion that the cold bias must be at least partially driven by vital effects, as Δ_{47}-temperatures are again cooler than not only modern SSTs but also modern upwelling temperatures (Andrade and Barton, 2005) (Fig. 3.2A). Furthermore, these offsets do not appear to be a result of analytical differences as the cold bias was observed across six shells, four locations, and two mass spectrometers with Δ_{47}-temperatures calculated years apart using different standards (carbonate vs. gas standards).

Although the magnitude of the Δ_{47}-temperature offset varies from sample to sample, the average offset is consistent across studies. The cold bias averaged across both modern shells in this study is 5.5°C +/- 7.5°C (1SD) relative to modern SSTs (and 1.5°C +/- 7.5°C relative to modern upwelling temperatures); without sample 628B-cm1, the respective cold bias averages are slightly higher (7.7°C relative to surface, 3.7°C relative to upwelling). This aligns with the previous offset of ~6°C +/- 3°C observed by Quizon et al. (2025). Our results add confidence to the magnitude of the turritellid vital effect by adding another sample location and support the potential of applying a flat correction of ~6°C to reconstruct environmental temperatures from turritellids. It is worth noting the turritellid species measured in this study are different than those measured in Quizon et al. (2025), and future work could corroborate this correction by providing measurements from additional species.

Previous studies reporting $\delta^{18}O_{carb}$ data from turritellids did not detect this vital effect because turritellids appear to precipitate in $\delta^{18}O_{carb}$ equilibrium (Fig. S3.5). If $\delta^{18}O_w$ is known,

$\delta^{18}O_{carb}$ measurements can thus be used to calculate accurate temperatures (e.g., Waite and Allmon, 2013). However, based on known precipitation mechanisms, disequilibrium precipitation that produces a cold bias in Δ_{47} must also produce a cold bias in $\delta^{18}O_{carb}$ via kinetic effects, though it would smaller in magnitude (Guo, 2020). Curley et al. (2023) suggest the possibility of shell precipitation from a pocket of precipitation fluid separate from seawater, meaning that $\delta^{18}O_w$ values used for calculations could be incorrect. It is possible that the combination of vital effects in Δ_{47}, $\delta^{18}O_w$, and $\delta^{18}O_{carb}$ cancel out in a fortuitous way such that $\delta^{18}O_{carb}$ appears unaffected. More work, possibly with modern cultured turritellids, would be needed to refine the turritellid precipitation mechanism and to fully explain vital effect signatures.

3.5.2 Mid-Miocene paleoclimate

Although Mid-Miocene temperatures are not known a priori, Mid-Miocene turritellid data also appear to exhibit a vital effect-induced cold bias. The Mid-Miocene Climatic Optimum was a brief warm interval during broader Cenozoic cooling, with global mean surface temperatures between ~3-10°C higher than modern for ~2 Myr (e.g., Burls et al., 2021; Hönisch et al., 2024). Given this, Mid-Miocene SSTs and upwelling temperatures were likely warmer than modern by at least 3°C. The apparent Δ_{47}-temperature range of ~19-26°C from the Mid-Miocene turritellids – which overlaps modern upwelling temperatures and falls below modern SSTs – does not align with this understanding of a warm Mid-Miocene climate.

Adding the determined offset of ~6°C to the MMCO turritellid Δ_{47}-temperatures results in a range of ~25-33°C, which would suggest that regional SSTs were comparable to or slightly warmer than modern SSTs (~26-27°C, Locarnini et al., 2019) (Fig. 3.4). This adjusted range is consistent with the estimates from other Miocene proxy-derived SSTs from the equatorial

Atlantic (25-33°C) (e.g., Greenop et al., 2017; Sosdian et al., 2018; van der Weijst et al., 2022; Wubben et al., 2024).

Combined modern turritellid data do not suggest any patterns in the turritellid cold bias relating to season, mean annual temperature, or species. Therefore, it is still possible to interpret subannual variability from seasonally targeted samples even if the true offset is not 6°C. Analyzed fossils exhibit <3°C temperature differences between apparent winter and summer temperatures across four shells (Fig. 3.3C), which is consistent with low seasonality typically observed in the tropics. This assumption of reduced temperature seasonality supports previous work of Scholz et al. (2020), in which they suggest $\delta^{18}O_w$ (i.e., salinity) and not temperature variability drives the large amplitude in $\delta^{18}O_{carb}$ variability. Our data are consistent with these findings, as seasonal fluctuations of up to 2‰ are observed in both the seasonal $\delta^{18}O_{carb}$ and $\delta^{18}O_{rsw}$ data (Fig. 3.3B; Fig. 3.3D). Altogether, these results support the proposed hypothesis of a northward shift of the Intertropical Convergence Zone (ITCZ) during the MMCO resulting in enhanced seasonality of precipitation.

3.5.3 Mid-Miocene Climatic Optimum (MMCO) at the Guajira Peninsula

The coolest observed Δ_{47}-temperature occurs at ~15.7 Ma, which aligns with the peak of the MMCO. This apparent decrease may be due to temporarily lower regional SSTs and/or enhanced regional upwelling. Studies show that upwelling tends to decrease seawater $\delta^{13}C$ values by up to ~1.5‰ (Kroopnick, 1985). The lowest Δ_{47}-temperatures (Fig. 3.4A) are also associated with a decline in $\delta^{13}C_{carb}$ values (Fig. 3.4B) (~0‰ vs. 1-3‰ baseline), supporting the mechanism of enhanced upwelling resulting in lower temperatures. Thus, climate change within the MMCO interval may have changed upwelling conditions locally, at least briefly, around ~16-15.5 Ma.

Slightly reduced $\delta^{18}O_{carb}$ ranges are observed during the MMCO intervals relative to the other intervals, associated with a reduction in $\delta^{18}O_w$ variability but no substantial change in seasonality (Fig. 3.4C). This may be consistent with enhanced upwelling making coastal regions less sensitive to runoff, or this may indicate larger scale hydrological or oceanographic changes (though it is impossible to distinguish based on this dataset). This region could serve as a good target for future studies in determining how the tropics responded to the MMCO.

3.6 Conclusions

In this study, we confirm previous work that showed that modern turritellid Δ_{47}-temperatures are biased cold by ~6°C below SSTs due to a combination of upwelling and vital effects as previously proposed by Quizon et al. (2025). Despite this bias, the consistency of these findings suggests that turritellids are still viable for paleoenvironmental reconstruction on subannual and relative timescales. Their fast growth rates (e.g., Allmon, 2011) make them good targets for paleoseasonality reconstruction via $\delta^{18}O$ sclerochronology (Scholz et al., 2024), and this study demonstrates that it is still possible to access seasonal extremes (i.e., mean annual range in temperature) from these profiles, even if absolute temperatures are uncertain. Past temperatures can be roughly approximated by applying the 6°C offset, which brings our estimates in line with those other tropical Mid-Miocene proxies. Finally, pulling $\delta^{13}C$, $\delta^{18}O$, Δ_{47}, and $\delta^{18}O_{rsw}$ data together stratigraphically suggests possible locally enhanced upwelling during the MMCO that warrants further study.

3.7 Acknowledgments

We would like to thank Ashling Neary for Δ_{47} measurements; the attendees of the Geochemistry, Climate, and Life seminar (UM EARTH) for their assistance with project review and development; Carlos Jaramillo and Jaime Escobar for their assistance with sample

collections; and the NSF-GRFP, University of Michigan Rackham Research Grants, and the University of Michigan Department of Earth and Environmental Science's Turner Grants provided to AAQ.

3.8 Appendices

3.8.1 Modern climatology and hydrology

Modern regional SSTs in the Guajira Peninsula (~25.7-27.1°C) were obtained from the World Ocean Atlas 2018 (WOA18) database (2005-2017 period, 1/4° resolution, monthly means) (Locarnini et al., 2019). Winter and summer temperatures were calculated as the mean of three months (December, January, February for winter; June, July, August for summer) and mean annual temperatures as the mean across all 12 monthly averages. Modern upwelling temperatures in the Guajira Peninsula (~22-23°C) were originally reported by Andrade and Barton (2005). The modern regional instrumental $\delta^{18}O_w$ value was obtained from Epstein and Mayeda (1953). Modelled regional $\delta^{18}O_w$ values were obtained via output from LeGrande and Schmidt (2006) and Breitkreuz et al. (2018).

3.8.2 Fossil Δ_{47} sampling, data processing procedures, and temperature calculations

Three fossil shells were sampled for bulk Δ_{47} measurements, which capture at least one year of mean annual temperature (MAT); this was done by re-drilling across enough $\delta^{18}O$ sclerochronology sampling positions to capture at least one year of growth. Four fossil shells were sampled for seasonally targeted Δ_{47} measurements, for which material was re-drilled from apparent winter and summer time positions determined from $\delta^{18}O$ sclerochronology.

All Δ_{47} measurements were made on a Thermo-Finnegan MAT 253 in the University of Michigan Stable Isotope Lab, with sample preparation conducted on a manual off-line preparation

device originally described in Defliese et al. (2015). Samples were digested in a common acid bath with H_3PO_4 at 75°C to produce CO_2 and purified for Δ_{47} analysis through two H_2O traps and a Porapak-filled trap containing silver wool. Measured Δ_{47} values were calculated from raw voltages through the R-code script from Petersen et al. (2019) and subsequently converted into the absolute reference frame by applying a non-linearity correction using equilibrated (25°C) and heated CO_2 gas (1000°C) standards (Dennis et al., 2011). Standard error in Δ_{47} for each sample was calculated from the standard deviation of all replicates (n >= 3). 95% confidence intervals for Δ_{47} were calculated from the long-term standard deviation in Δ_{47} from two carbonate standards (Carrara marble, Ooids), determined to be 0.0163‰. $\delta^{18}O$ and $\delta^{13}C$ values were simultaneously collected alongside Δ_{47} measurements and reported relative to the Pee Dee Belemnite (PDB) standard.

All Δ_{47}-temperatures were calculated from mean Δ_{47} values in the $CDES_{90}$ reference frame via the Δ_{47}-T calibration equation from Anderson et al. (2021). An alternate set of figures (Fig. S3.2-S3.4) were produced using Δ_{47}-temperatures calculated via the 'UNICAL' equation (Petersen et al., 2019) but do not meaningfully impact the main conclusions. Sample mean Δ_{47}-temperatures and $\delta^{18}O_{carb}$ values were used to reconstruct Δ_{47}-derived $\delta^{18}O_w$ ($\delta^{18}O_{rsw}$) for each powder via the aragonitic mollusk calibration equation from Grossman and Ku (1986).

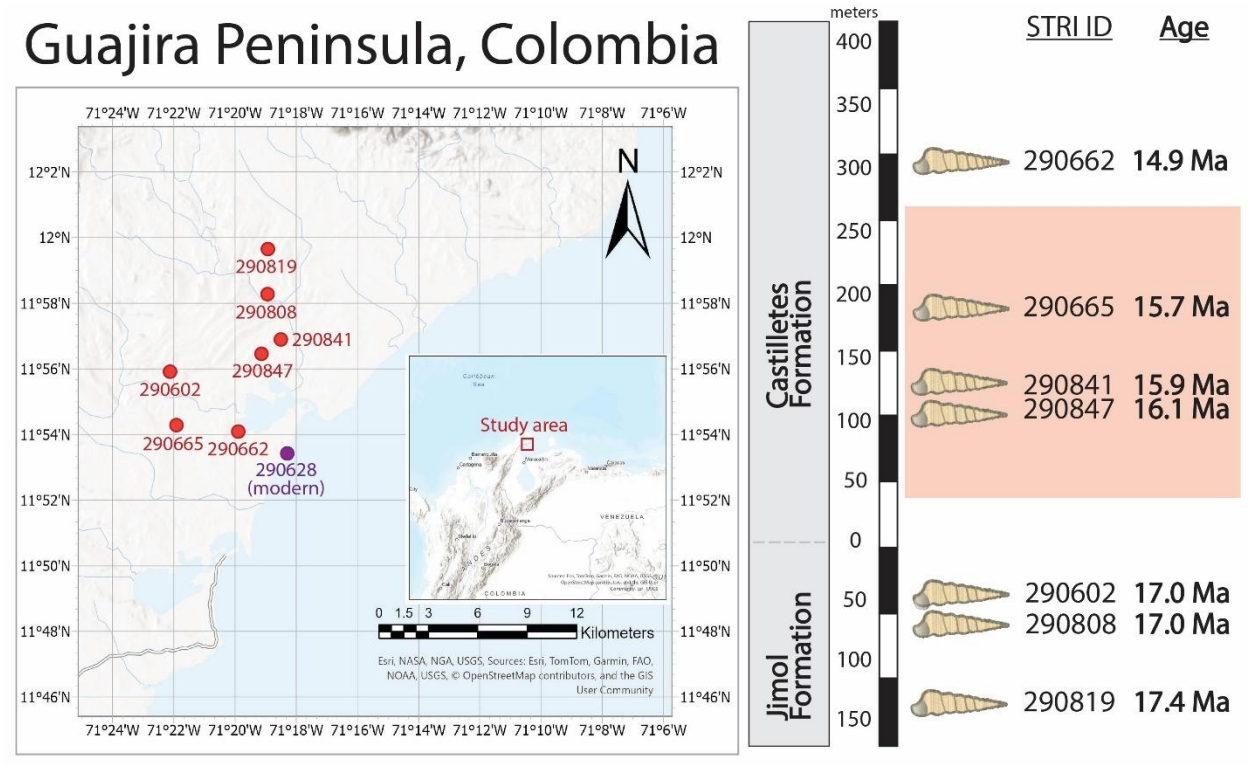

Figure 3.1. Map of sample sites and simplified composite stratigraphic cross-section of the Cocinetas Basin deposits (Jimol and Castilletes Formations) spanning the Mid-Miocene Climatic Optimum (MMCO), adapted from Moreno et al. (2015) and Scholz et al. (2020).

Ages were determined by Sr isotope stratigraphy in Hendy et al. (2015). The shaded red box represents the approximate position of peak warmth during the MMCO.

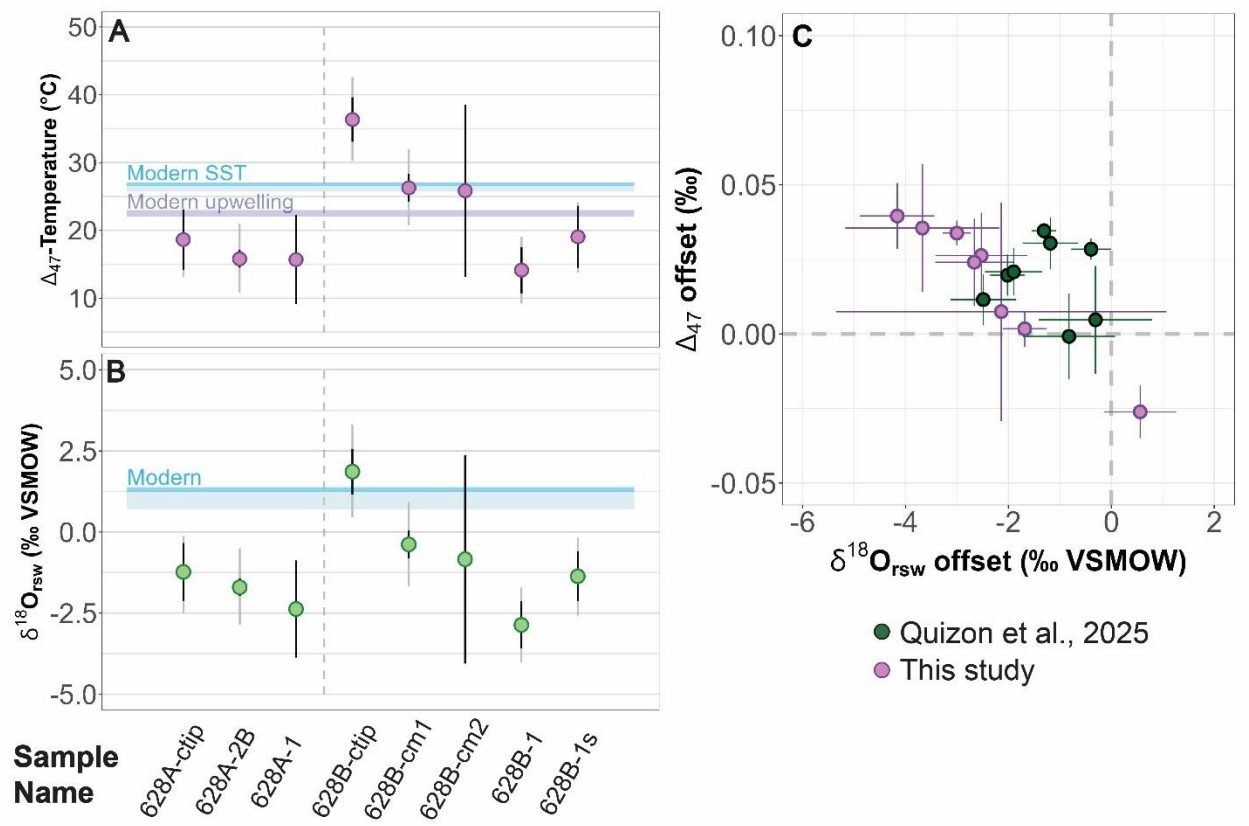

Figure 3.2. Δ_{47}-temperatures (A) and reconstructed $\delta^{18}O_{sw}$ ('$\delta^{18}O_{rsw}$') values (B) for the modern turritellids measured in this study, with Δ_{47} and $\delta^{18}O_{rsw}$ offsets (i.e., measured minus predicted) from both this study and Quizon et al. (2025) displayed in (C).

Black and grey error bars in (A) and (B) represent +/- internal 1SE and 95% confidence intervals based on long-term performance of in-house carbonate standards, respectively; colored error bars in (C) represent 95% confidence intervals. See Section 3.8 for details about error calculations. The modern seasonal temperature range (Locarnini et al., 2019) and modern upwelling temperatures (Andrade and Barton, 2005) are shown for comparison in (A). The range from modern instrumental and modelled $\delta^{18}O_{sw}$ values (Epstein and Mayeda, 1953; LeGrande and Schmidt, 2006; Breitkreuz et al., 2018) are shown for comparison in (B).

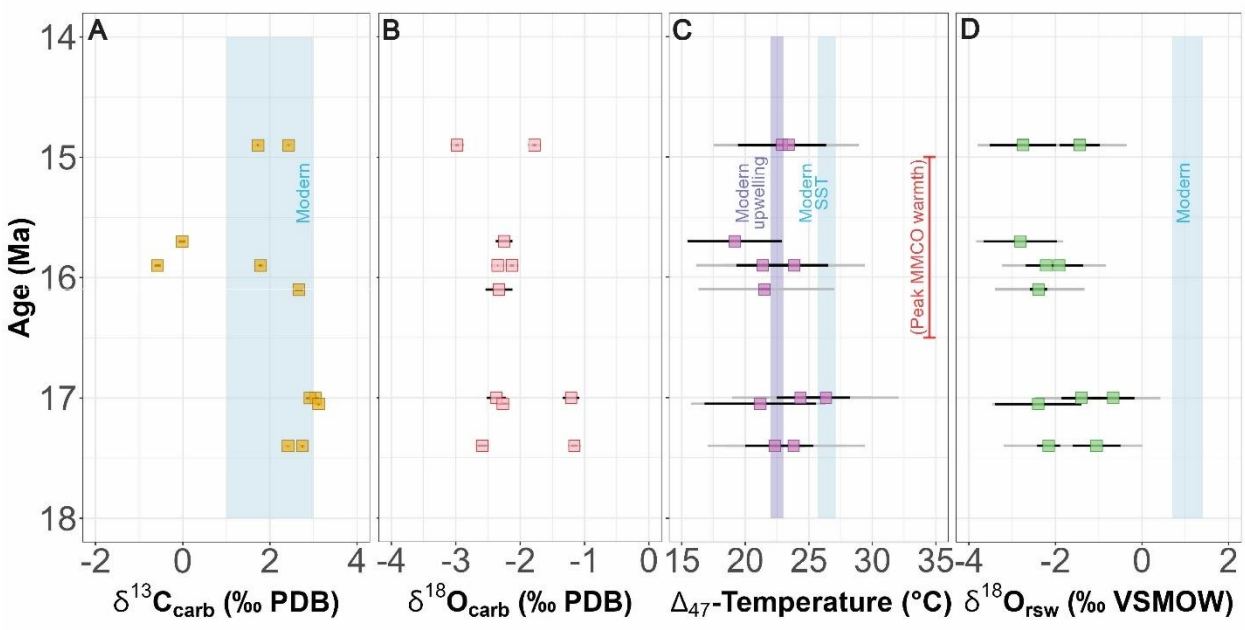

Figure 3.3. Isotopic data from the seven fossil turritellids measured in this study.

Panels show $\delta^{13}C_{carb}$ (A), $\delta^{18}O_{carb}$ (B), Δ_{47}-temperatures (C), and reconstructed $\delta^{18}O_{sw}$ (D). Horizons with two data points represent summer and winter conditions; horizons with one data point represent mean annual conditions. Black error bars represent +/- internal 1SE; grey error bars represent 95% confidence intervals based on long-term performance of in-house carbonate standards. See Section 3.8 for details about error calculations. See Figure 3.2 for explanations of modern temperature and $\delta^{18}O_{sw}$ values.

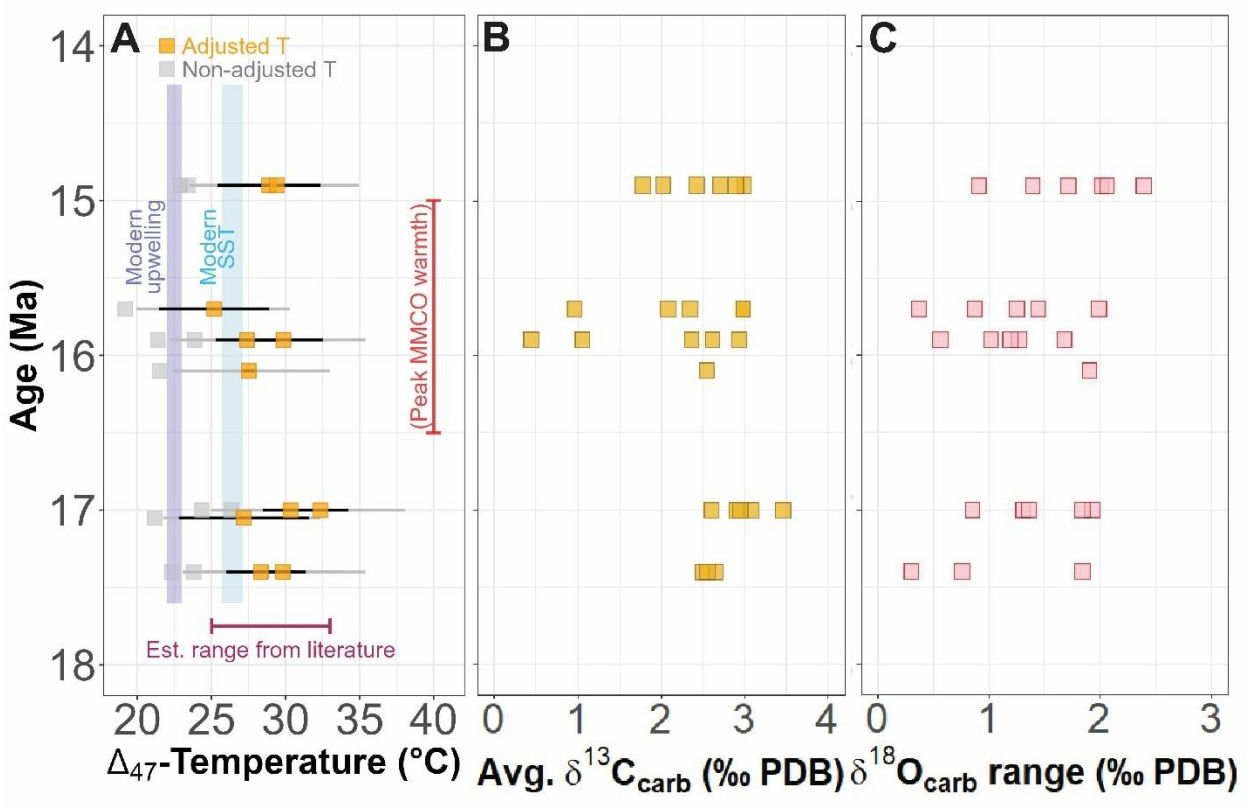

Figure 3.4. Adjusted Mid-Miocene turritellid Δ_{47}-temperatures calculated by adding the 6°C offset observed from modern turritellids in Quizon et al. (2025) (A); average $\delta^{13}C$ values (B) and intra-shell $\delta^{18}O$ ranges (C) from all Miocene turritellid sclerochronology profiles reported in Scholz et al. (2020).

Black error bars represent +/- internal 1SE; grey error bars represent 95% confidence intervals based on long-term performance of in-house carbonate standards. The red line represents the estimated interval of peak Mid-Miocene Climatic Optimum warmth (~16.5-15 Ma) reported in previous studies. The estimated Mid-Miocene temperature range of ~25-33°C in the equatorial Atlantic from the literature comes from values reported in Greenop et al. (2017), Sosdian et al. (2018), van der Weijst et al. (2022), and Wubben et al. (2024).

Sample Latitude & Longitude	Instrumental Mean Annual Temperature	Instrumental Summer (JJA) Temperature	Instrumental Winter (DJF) Temperature
12.0°N, 71.5°W	26.8°C +/- 0.2°C	26.8°C +/- 0.4°C	26.2°C +/- 0.5°C

Table S3.1. Instrumental temperature data for the latitude/longitude information roughly corresponding to Guajira Peninsula, Colombia.

Temperatures were gathered from the World Ocean Atlas (WOA) 2018 dataset (2005-2017 period, 1/4° resolution, monthly means) for comparison the reconstructed isotopic temperatures (Locarnini et al., 2019).

Sample Latitude & Longitude	Insrumental $\delta^{18}O_{sw}$ (‰ VSMOW)	Source	Modeled $\delta^{18}O_{sw}$ from Breitkreuz et al., 2018 (‰ VSMOW)	Modeled $\delta^{18}O_{sw}$ from LeGrande and Schmidt, 2006 (‰ VSMOW)
12.0°N, 71.5°W	1.3 +/ -0.1	Epstein and Mayeda, 1953	0.8 +/- 0.1	0.9 +/- 0.1

Table S3.2. Instrumental and modeled $\delta^{18}O_{sw}$ data for the latitude/longitude information roughly corresponding to the sample collection sites in Guajira Peninsula, Colombia.

Sample Name	Species	STRI Site ID	Approximate Age (Ma)	Δ_{47} Sampling Method
290662-A	*Turritella machapoorensis*	290662	14.9	Seasonally targeted
290665-A	*Turritella larensis*	290665	15.7	Bulk
290841-A	*Turritella matarucana*	290841	15.9	Seasonally targeted
290847-A	*Turritella machapoorensis*	290847	16.1	Bulk
290602-A	*Turritella matarucana*	290602	17.0	Seasonally targeted
290808-A	*Turritella larensis*	290808	17.0	Bulk
290819-B	*Turritella larensis*	290819	17.4	Seasonally targeted
290628-A	*Turritella variegata*	290628	0 (modern)	Various (see Fig. S3.1)
290628-B (290628-1)	*Turritella variegata*	290628	0 (modern)	Various (see Fig. S3.1)

Table S3.3. Names of samples measured in this study and how they were sampled for Δ_{47}.



Figure S3.1. Photos of the modern specimens (628A, 628B) and the locations on the shells where samples were collected.

Quarter is included in each photo for scale.

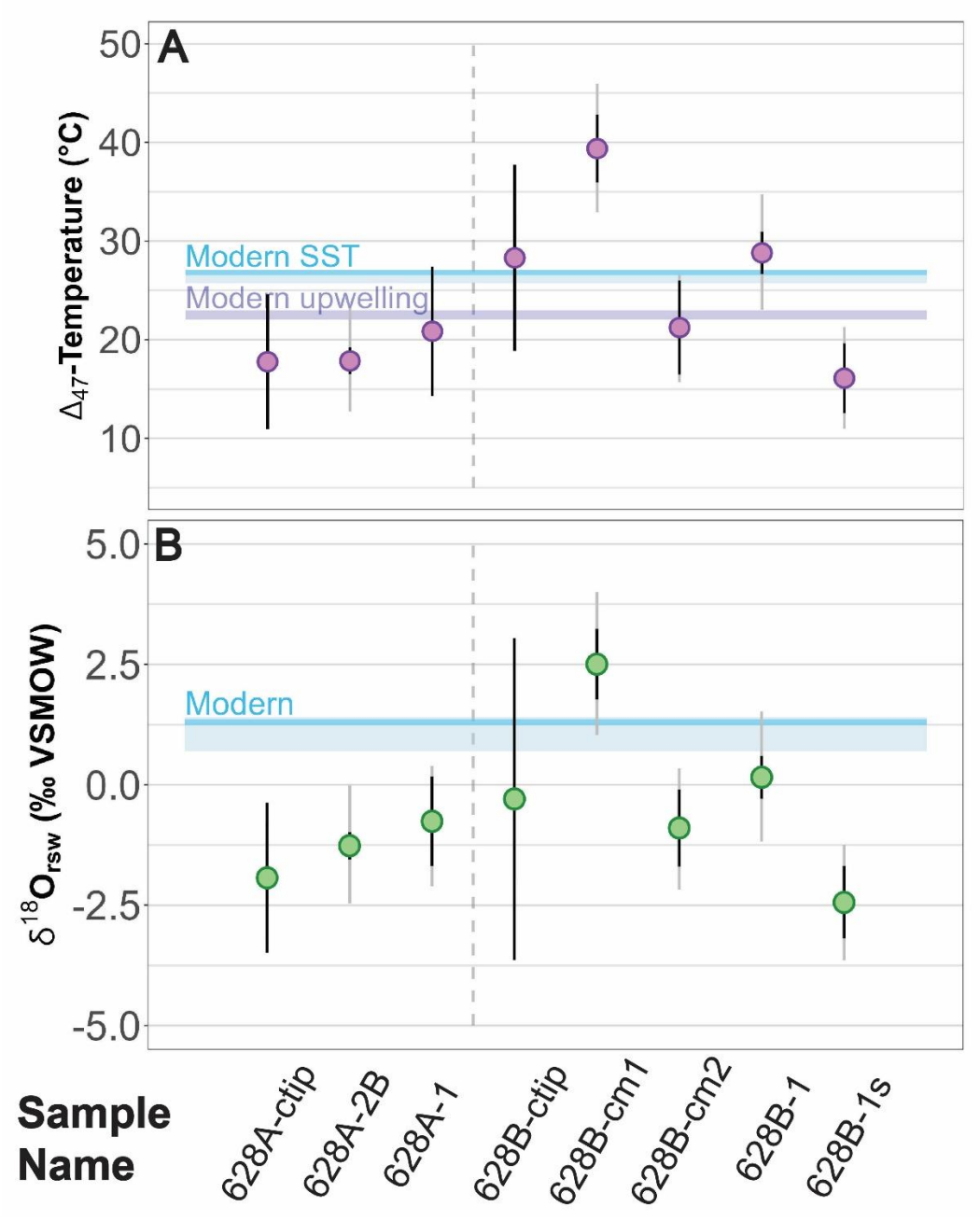

Figure S3.2. Δ_{47}-temperatures (A) and reconstructed $\delta^{18}O_{sw}$ ('$\delta^{18}O_{rsw}$') values for the modern turritellids measured in this study, with Δ_{47}-temperatures calculated using the 'UNICAL' equation from Petersen et al. (2019). Average Δ_{47}-temperature offsets from modern SSTs and upwelling temperatures are 3.2 +/- 7.9°C and -1.2 +/- 7.9°C, respectively.

See Figure 3.2 from the main text for other details.

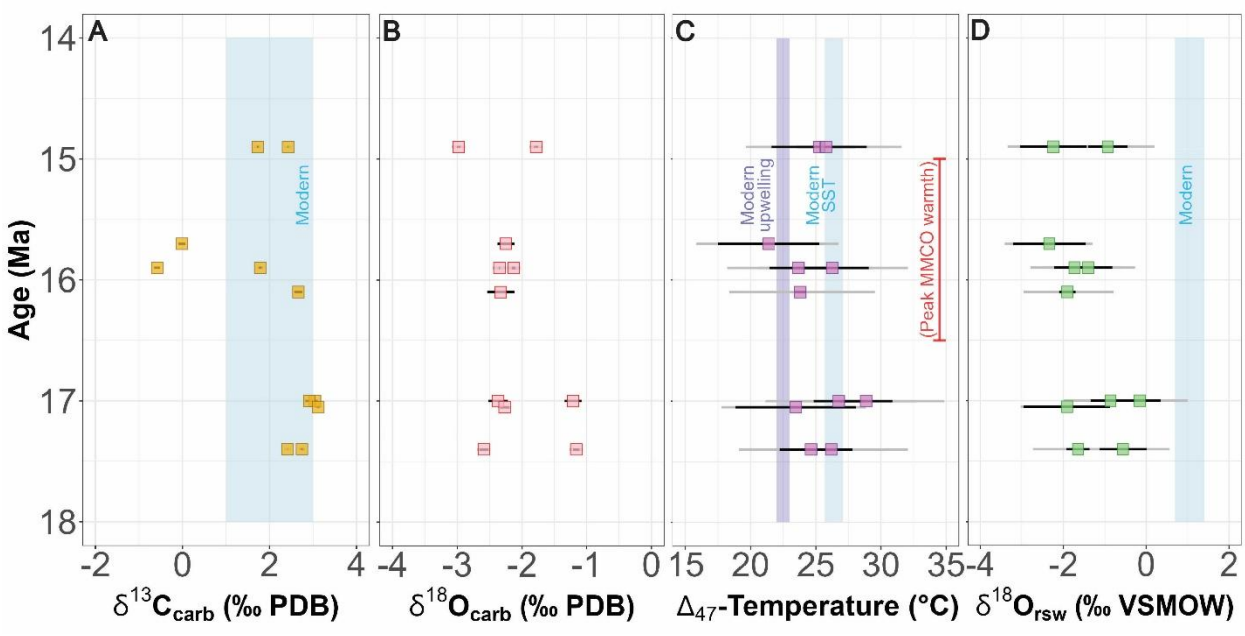

Figure S3.3. Isotopic data from the seven fossil turritellids measured in this study.

Panels show $\delta^{13}C_{carb}$ (A), $\delta^{18}O_{carb}$ (B), Δ_{47}-temperatures (C), and reconstructed $\delta^{18}O_{sw}$ (D), with Δ_{47}-temperatures calculated using the 'UNICAL' equation from Petersen et al. (2019). See Figure 3.3 from the main text for other details.

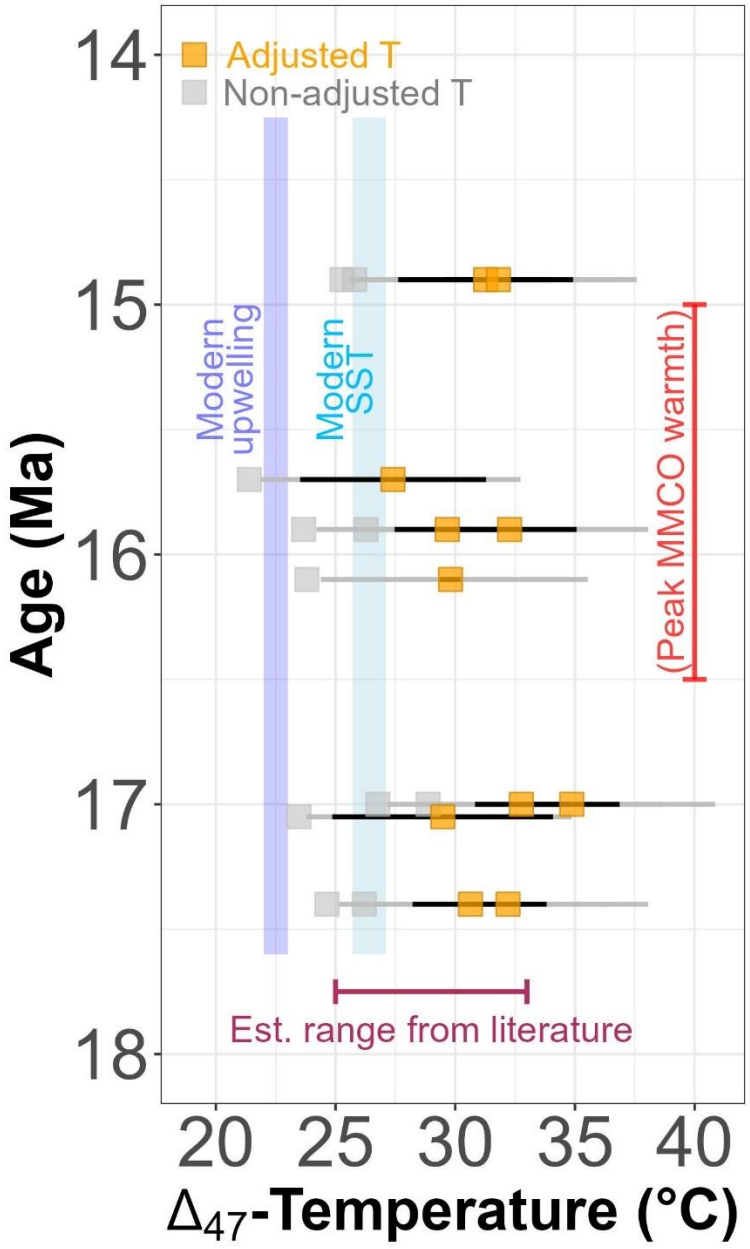

Figure S3.4. Adjusted Mid-Miocene turritellid Δ_{47}-temperatures calculated by adding the 6°C offset observed from modern turritellids in Quizon et al. (2025), with Δ_{47}-temperatures calculated using the 'UNICAL' equation from Petersen et al. (2019).

See Figure 3.4 from the main text for other details.

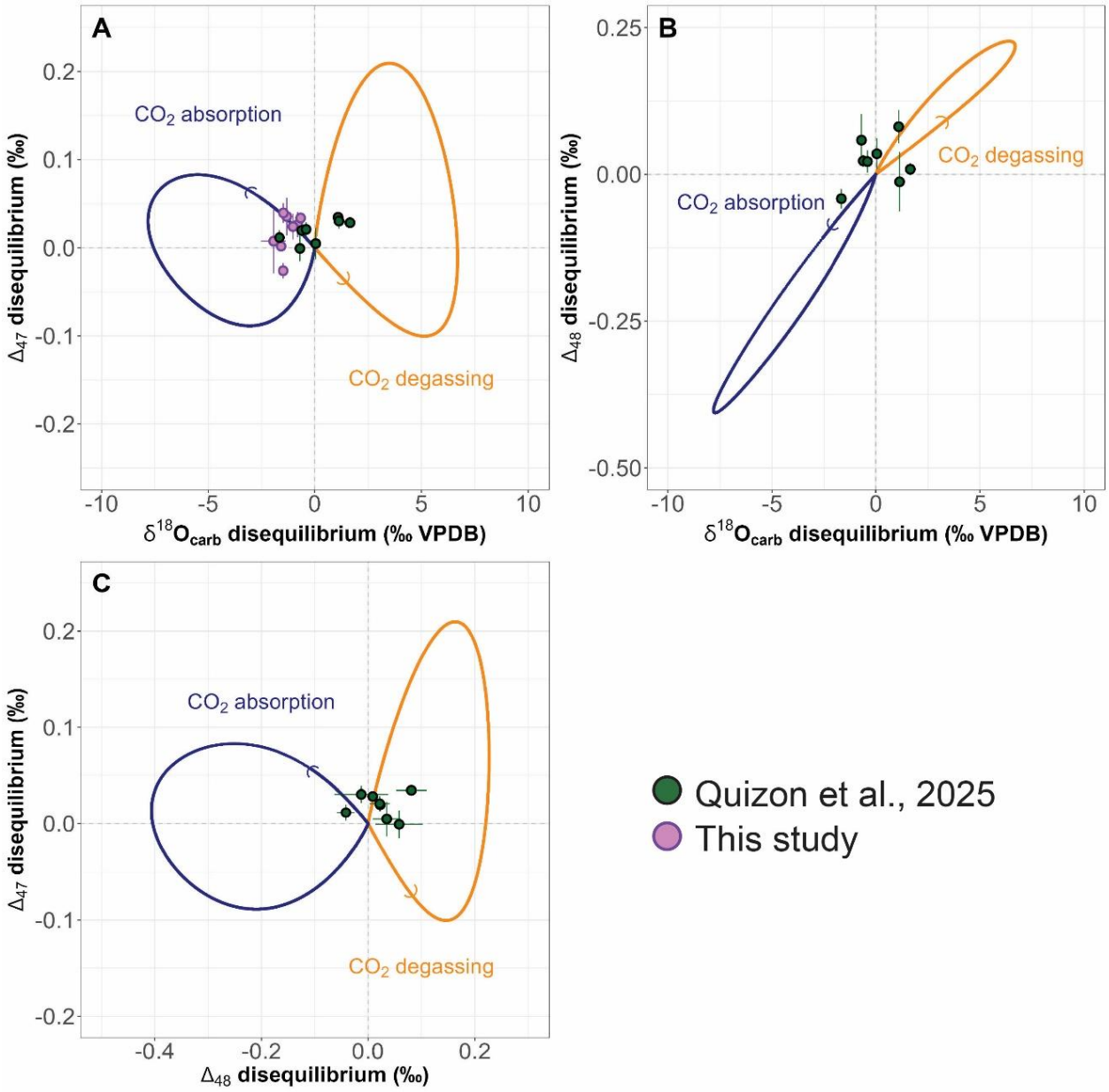

Figure S3.5. Disequilibrium plots (i.e., offsets of measured values from predicted values) for turritellids measured in this study (purple) and previously by Quizon et al. (2025) (green).

Colored lines represent possible disequilibrium precipitation trajectories described in Guo (2020) and provided in the IsoDIC Matlab package. Predicted $\delta^{18}O_{carb}$ values were calculated from modern instrumental temperature and $\delta^{18}O_{sw}$; predicted Δ_{47} and Δ_{48} values were calculated from modern instrumental temperatures. Error bars represent +/- internal 1SE.

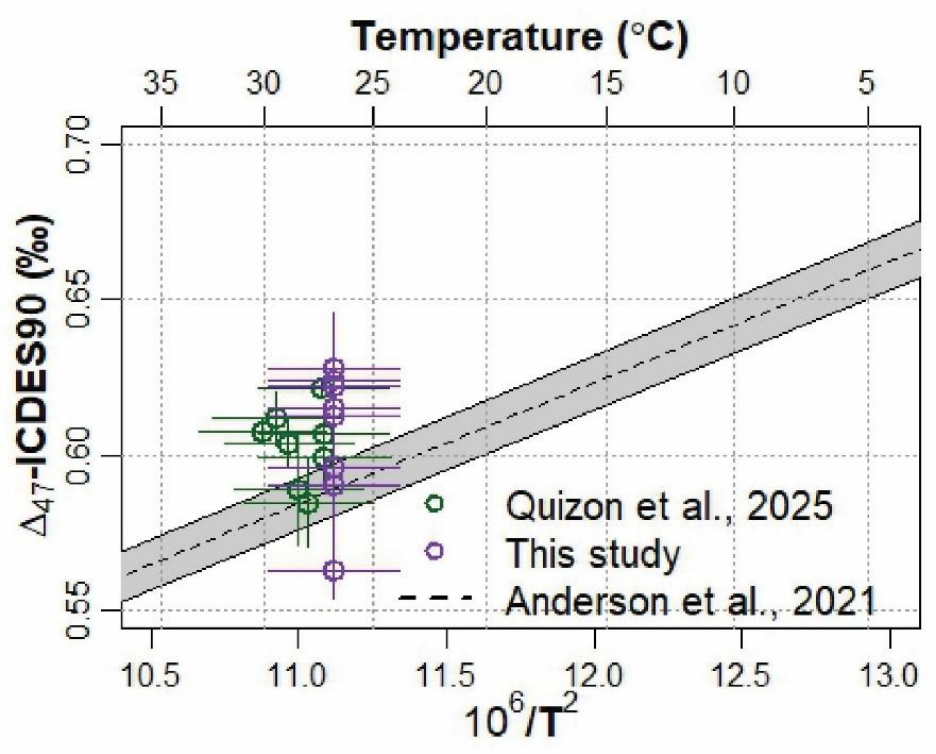

Figure S3.6. Δ_{47}-temperature calibration from Anderson et al., 2021 overlain with modern turritellid data from this study and Quizon et al. (2025).

Vertical error bars in (A) represent +/- internal 1SE; horizontal error bars represent +/- 3°C. Error bars in (B) represent +/- internal 1SE.

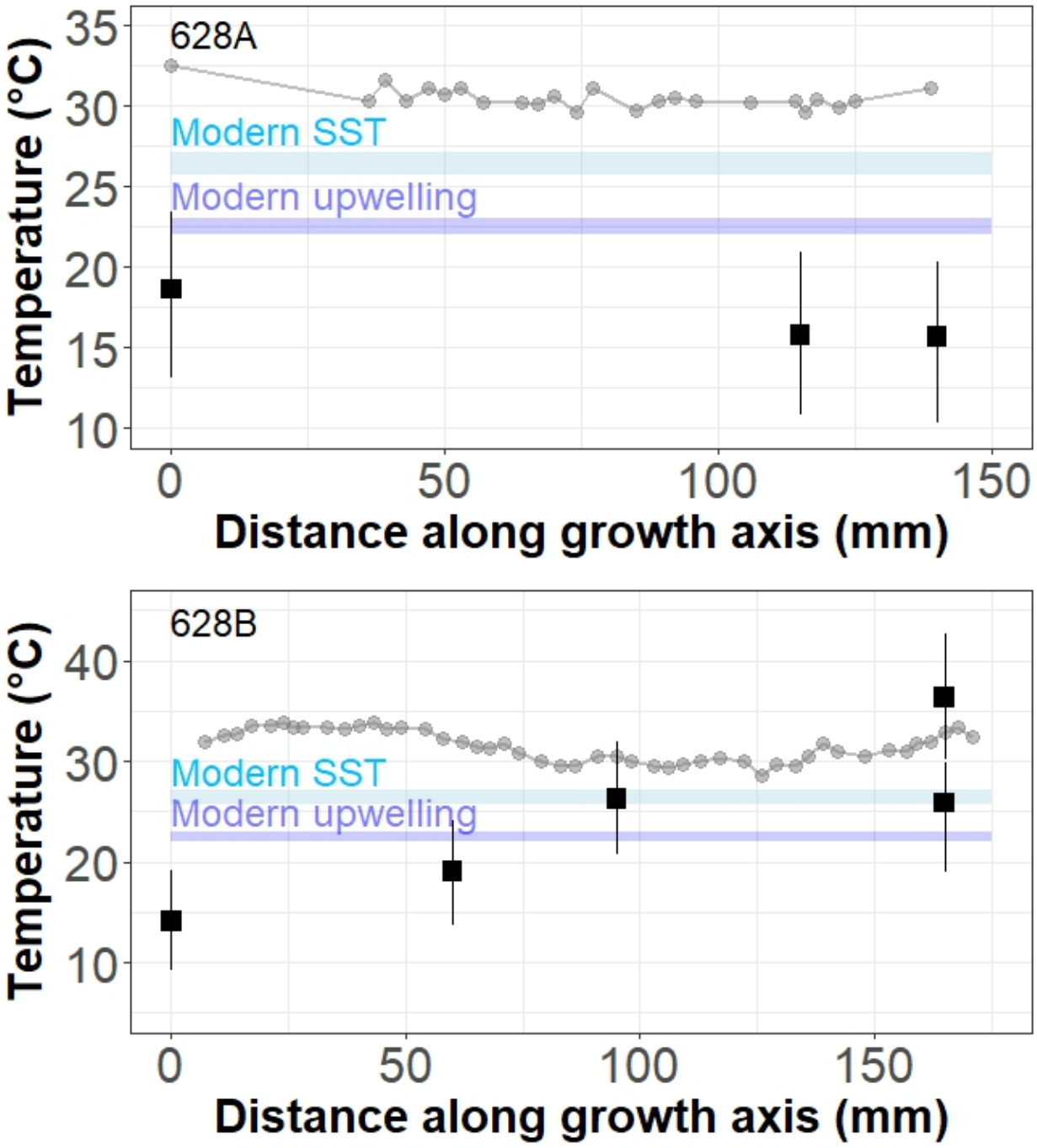

Figure S3.7. $\delta^{18}O$ sclerochronology (grey circles) and Δ_{47} measurements (black squares) for modern turritellid samples 628A (top) and 628B (bottom).

$\delta^{18}O$-temperatures were calculated using the aragonitic mollusk equation from Grossman and Ku (1986), assuming the regional instrumental $\delta^{18}O_w$ value of 1.3‰ reported in Epstein and Mayeda (1953).

3.9 References

Allmon, W.D., 2011, Natural history of turritelline gastropods (Cerithiodea: Turritellidae): a status report: Malacologia, v. 54, no. 1-2, p. 159-202, doi:10.4002/040.054.0107

Anderson, B.M., 2018, The evolution of unusual shell morphologies in fossil and living Turritellidae (Gastropoda): Ph.D. thesis, Cornell University, 1–14. Available at: https://ecommons.cornell.edu/handle/1813/59723

Anderson, B.M., and Allmon, W.D., 2024, Phylogeny and Systematics of Fossil and Recent *Vermicularia* (Caenogastropoda: Turritellidae): Malacologia, v. 66, no. 1-2, p. 1-59, doi:10.4002/040.066.0101

Andrade, C.A., and Barton, E.D., 2005, The Guajira upwelling system: Continental Shelf Research, v. 25, no. 9, p. 1003-1022, doi:10.1016/j.csr.2004.12.012

Andreasson, F.P., and Schmitz, B., 1996, Winter and summer temperatures of the early middle Eocene of France from *Turritella* $\delta^{18}O$ profiles: Geology, v. 24, no. 12, p. 1067-1070

Breitkreuz, C., Paul, A., Kurahashi-Nakamura, T., et al, 2018, A Dynamical Reconstruction of the Global Monthly Mean Oxygen Isotopic Composition of Seawater: Journal of Geophysical Research: Oceans, v. 123, no. 10, p. 7206-7219, doi:10.1029/2018JC014300

Burls, N.J., Bradshaw, C.D., De Boer, A.M., et al, 2021, Simulating Miocene Warmth: Insights From an Opportunistic Mutli-Model Ensemble (MioMIP1): Paleoceanography and Paleoclimatology, v. 36, no. 5, e2020PA004054, doi:10.1029/2020PA004054

Curley, A.N., Petersen, S.V., Edie, S.M., and Guo, W., 2023, Biologically driven isotopic fractionations in bivalves: from palaeoenvironmental problem to palaeophysiological proxy: Biological Reviews, v. 98, no. 4, p. 1016-1032, doi:10.1111/brv.12940

Defliese, W.F., Hren, M.T., and Lohmann, K.C., 2015, Compositional and temperature effects of phosphoric acid fractionation on Δ_{47} analysis and implications for discrepant calibrations: Chemical Geology, v. 396, p. 51-60, doi:10.1016/j.chemgeo.2014.12.018

Dennis, K.J., Affek, H.P., Passey, B.H., Schrag, D.P., and Eiler, J.M., 2011, Defining an absolute reference frame for 'clumped' isotopes studies of CO_2: Geochimica et Cosmochimica Acta, v. 75, no. 22, p. 7117-7131, doi:10.1016/j.gca.2011.09.025

Eiler, J.M., 2007, "Clumped-isotope" geochemistry – The study of naturally-occurring, multiply-substituted isotopologues: Earth and Planetary Science Letters, v. 262, no. 3-4, p. 309-327, doi:10.1016/j.epsl.2007.08.020

Epstein, S., and Mayeda, T., 1953, Variation of O18 content of waters from natural sources: Geochimica et Cosmochimica Acta, v. 4, no. 5, p 213-224, doi:10.1016/0016-7037(53)90051-9

Friend, D.S,. Anderson, B.M., Altier, E., et al, 2023, Systematics and phylogeny of Plio-Pleistocene species of Turritellidae (Gastropoda) from Florida and the Atlantic Coastal Plain: Bulletins of American Paleontology, no. 402, p. 1-74, doi:10.32857/bap.2023.402.01

Ghosh, P., Adkins, J., Affek, H., et al, 2006, ^{13}C-^{18}O bonds in carbonate minerals: A new kind of paleothermometer: Geochimica et Cosmochimica Acta, v. 70, no. 6, p. 1439-1456, doi:10.1016/j.gca.2005.11.014

Greenop, R., Hain, M.P., Sosdian, S.M., et al, 2017, A record of Neogene seawater $\delta^{11}B$ reconstructed from paired $\delta^{11}B$ analyses on benthic and planktic foraminifera: Climate of the Past, v. 13, no. 2, p. 149-170, doi:10.5194/cp-13-149-2017

Grossman, E.L., and Ku, T-L., 1986, Oxygen and carbon isotope fractionation in biogenic aragonite: Temperature effects: Chemical Geology, v. 59, p. 59-74, doi:10.1016/0168-9622(86)90057-6

Guo, W., 2020, Kinetic clumped isotope fractionation in the DIC-H_2O-CO_2 system: Patterns, controls, and implications: Geochimica et Cosmochimica Acta, v. 268, p. 230-257, doi:10.1016/j.gca.2019.07.055

Hendy, A.J.W., Jones, D.S., Moreno, F., et al, 2015, Neogene molluscs, shallow marine paleoenvironments, and chronostratigraphy of the Guajira Peninsula, Colombia: Swiss Journal of Palaeontology, v. 134, p. 45-75, doi:10.1007/s13358-015-0074-1

Hönisch, B., Witkowski, C.R., Penman, D.E., et al, 2024, Paleo-atmospheric CO_2 reconstructions from deep-ocean sediments: PAGES Magazine, v. 32, no. 2, p. 84-85.

Kroopnick, P.M., 1985, The distribution of ^{13}C of ΣCO_2 in the world oceans: Deep Sea Research Part A. Oceanographic Research Papers, v. 32, no. 1, p. 57-84, doi:10.1016/0918-0149(85)90017-2

LeGrande, A.N., and Schmidt, G.A., 2006, Global gridded data set of the oxygen isotopic composition in seawater: Geophysical Research Letters, v. 33, no. 12, LI2604, doi:10.1029/2006GL026011

Locarnini, R.A., Mishonov, A.V., Baranova, O.K., et al, 2019: World Ocean Atlas 2018, Volume 1: Temperature. Mishonov, A.V. (Ed.), NOAA Atlas NESDIS 81, 52 pp.

Moreno, F., Hendy, A.J.W., Quiroz, L., et al, 2015, Revised stratigraphy of Neogene strata in the Cocinetas Basin, La Guajira Colombia: Swiss Journal of Palaeontology, v. 134, p. 5-43, doi:10.1007/s13358-015-0071-4

Petersen, S.V., Defliese, W.F., Saenger, C., et al, 2019, Effects of Improved ^{17}O Correction on Interlaboratory Agreement in Clumped Isotope Calibrations, Estimates of Mineral-

Specific Offsets, and Temperature Dependence of Acid Digestion Fractionation: Geochemistry, Geophysics, Geosystems, v. 20, no. 7, p. 3495-3519, doi:10.1029/2018GC008127

Schauble, E.A., Ghosh, P., and Eiler, J.M., 2006, Preferential formation of ^{13}C-^{18}O bonds in carbonate minerals, estimated using first-principles lattice dynamics: Geochimica et Cosmochimica Acta, v. 70, no. 10, p. 2510-2529, doi:10.1016/j.gca.2006.02.011

Scholz, S.R., Petersen, S.V., Escobar, J., et al, 2020, Isotope sclerochronology indicates enhanced seasonal precipitation in northern South America (Colombia) during the Mid-Miocene Climatic Optimum: Geology, v. 48, no. 7, p. 668-672, doi:10.1130/G47235.1

Scholz, S.R., Petersen, S.V., and Anderson, B.M., 2024, Modern reconstructions of mean and seasonal-scale climate from coastal marine gastropods (Turritellidae): Palaeogeography, Palaeoclimatology, Palaeoecology, v. 655, 112553, doi:10.1016/j.palaeo.2024.112553

Sosdian, S.M., Greenop, R., Hain, M.P., et al, 2018, Constraining the evolution of Neogene ocean carbonate chemistry using the boron isotope pH proxy: Paleoceanography and Paleoclimatology, v. 498, p. 362-376, doi:10.1016/j.epsl.2018.06.017

Tagliabue, A., and Bopp, L., 2008, Towards understanding global variability in ocean carbon-13: Global Biogeochemical Cycles, v. 22, no. 1, doi:10.1029/2007GB003037

Quizon, A.A., Petersen, S.V., de Winter, N.J., and Vellekoop, J., 2025, Clumped isotope thermometry (Δ_{47}) measurements in marine gastropods suggest equilibrium precipitation: Geochimica et Cosmochimica Acta, v. 410, p. 234-249, doi:10.1016/j.gca.2025.10.023

van der Weijst, C.M.H., van der Laan, K.J., Peterse, F., et al, 2022, A 15-million-year surface- and subsurface-integrated TEX_{86} temperature record from the eastern equatorial Atlantic: Climate of the Past, v. 18, no. 8, doi:10.5194/cp-18-1947-2022

Waite, R., and Allmon, W.D., 2013, Observations on the Biology and Sclerochronology of *Turritella leucostoma* (Valenciennes, 1832; Cerithiodea: Turritellidae) from the Gulf of California: American Malacological Bulletin, v. 31, no. 2, p. 297-310, doi:10.4003/006.031.0209

Wubben, E., Spiering, B.R., Veenstra, T., et al, 2024, Tropical Warming and Intensification of the West African Monsoon During the Miocene Climatic Optimum: Paleoceanography and Paleoclimatology, v. 39, no. 5, e20203PA004767, doi:10.1029/2023PA004767

Chapter 4 Seawater Salinity and Oxygen Isotopes Along the U.S. East Coast From 24°N to 44°N

4.1 Abstract

Oxygen isotope measurements of seawater ($\delta^{18}O_w$) are an important tool in the study of climate, oceanography, and hydrology, both today and in the past. $\delta^{18}O_w$ and salinity are controlled by the same hydrologic processes, but $\delta^{18}O_w$ is more readily recorded in geologic materials than salinity and is thus more accessible for paleoceanographic reconstructions. Modern instrumental $\delta^{18}O_w$ data exist, but these data can be sparse in certain regions and/or sporadically collected through time - some predating modern instrumentation and current standardization practices. In this dataset, we present 358 new paired salinity and $\delta^{18}O_w$ measurements from seawater samples collected along the U.S. Eastern Seaboard, nearly tripling the existing data in this region and dramatically improving spatial coverage. These data may be used to better understand nearshore hydrologic processes as well as basin-scale ocean dynamics both today and in the past. We hope this dataset can demonstrate the benefits of collecting $\delta^{18}O_w$ at high spatial resolution and will further expand the utility of $\delta^{18}O_w$ as a tool for both modern oceanography and paleoceanography.

4.2 Background & Summary

The field of oceanography traces its origin back to roughly the 1800s. Historically, oceanography measurements were collected during individual scientific research cruises. Over time, oceanographic efforts expanded to international collaborative programs such as the International Ocean Discovery Program (IODP) (IODP, 2011) and the Global Ocean Ship-based

Hydrographic Investigations Program (GO-SHIP) (Sloyan et al., 2019), which continue to operate to this day. Some routine measurements of ocean chemistry conducted by these and other research cruises include seawater temperature, salinity, dissolved nutrient content, dissolved inorganic carbon and total alkalinity, trace metal concentrations, pH, and other parameters. Technological advancements such as Argo floats (Roemmich et al., 2009) and remote sensing techniques such as satellite detection of seawater properties (Devi et al., 2015) have further expanded data coverage. This increase in sampling resolution has produced substantial increases in knowledge and understanding of important oceanographic processes.

One non-routine measurement that is useful for studies of both modern oceanography and paleoceanography is the oxygen isotope composition of seawater ($\delta^{18}O_w$). This parameter represents the abundance of heavier (^{18}O) to lighter (^{16}O) oxygen atoms in water relative to an international standard according to the following equation:

$$\delta^{18}O_w = (([^{18}O/^{16}O]_{water}/[^{18}O/^{16}O]_{standard}) - 1) \times 1000 \quad (1)$$

$\delta^{18}O_w$ and salinity are generally governed by the same hydrologic processes (Sharp, 2007). These include evaporation and precipitation, ice sheet growth and decay, moisture transport, rainout intensity, mixing of riverine and marine inputs, and others. For example, ^{16}O atoms are preferentially brought into the salt-free vapor phase during evaporation of seawater while ^{18}O atoms are preferentially left behind in the progressively saltier liquid phase. As clouds move over the ocean the raindrops that fall first contain preferentially more ^{18}O (but still less than the water body of origin), with consecutive periods of rainout progressively distilling the cloud's water vapor (Rayleigh, 1896; Dansgaard, 1964). When this isotopically depleted vapor eventually rains out over the continental interior, precipitation depleted in $\delta^{18}O_w$ fills rivers and lakes and even more depleted precipitation falls as snow and ice at higher latitudes and elevations. Variations in

$\delta^{18}O_w$ signatures within these terrestrial reservoirs are controlled by other hydrologic factors, both local and regional; for instance, strong $\delta^{18}O$ depletions in ice core records have been interpreted as reflecting greater rainout of isotopically enriched precipitation along the transport path and high humidity conditions at the source site (Jouzel et al., 1982).

$\delta^{18}O_w$ in the oceans is comparatively less variable than terrestrial waters because ocean waters are well-mixed and precipitation-evaporation constantly recycles ^{18}O back into the system. $\delta^{18}O_w$ data have previously been used to track modern oceanographic and hydrologic processes such as ocean circulation (Conroy et al., 2023; Stevenson et al., 2023), melting of ice sheets (Sima et al., 2006; Kim & Timmermann, 2024), and surface fluxes of freshwater (Cooper et al., 2022) or submarine groundwater discharge into the oceans (Zhang et al., 2024).

While changes in both salinity and $\delta^{18}O_w$ reflect the same hydrologic processes, $\delta^{18}O_w$ is more easily recorded in geologic archives. For examples, variations in $\delta^{18}O_w$ in glacial ice from Greenland and Antarctica reflect changes in factors such as temperature, moisture source, and atmospheric circulation back hundreds of thousands of years (Dansgaard et al., 1993; Grootes et al., 1993; Petit et al., 1999; Watanabe et al., 2003; EPICA Community Members, 2004; NGRIP Members, 2004; Jouzel et al., 2007; NEEM Community Members, 2013). In the marine realm, microscopic plankton (e.g., foraminifera) record information about past ocean temperatures and $\delta^{18}O_w$ in their carbonate skeletons ($\delta^{18}O_{carb}$). $\delta^{18}O_{carb}$ measurements on benthic foraminifera have led to foundational paleoclimate discoveries about global temperature changes in the Cenozoic (Zachos et al., 2001) and Plio-Pleistocene (Lisiecki & Raymo, 2005).

Reconstruction of deep ocean $\delta^{18}O_w$ is possible from porewaters, but this method is limited to the Last Glacial Maximum (Adkins and Schrag, 2001; Schrag et al., 2002). Use of paired non-isotopic proxies (e.g., Mg/Ca, Sr/Ca) (Chave, 1954; Weber, 1973; Beck et al., 1992;

Nürnberg et al., 1996) or temperature proxies that are independent of $\delta^{18}O_w$ variability such as 'clumped' isotopes ($\mathbf{\Delta}_{47}$) (Ghosh et al., 2006; Schauble et al., 2006; Eiler, 2007) has allowed reconstruction of ancient seawater $\delta^{18}O_w$, at times finding surprising variability (Meckler et al., 2022). However, in order to correctly interpret reconstructed $\delta^{18}O_w$, thorough documentation of modern spatial and temporal $\delta^{18}O_w$ variability is necessary.

Over the past few decades, modern instrumental $\delta^{18}O_w$ measurements have been collected and stored in databases such as CISE-LOCEAN (Reverdin et al., 2022), GEOTRACES (Anderson et al., 2014), NASA GISS (Schmidt et al., 1999), and waterisotopes.org (Bowen). Analyzing $\delta^{18}O_w$ requires a mass spectrometer, or more recently a laser system, so $\delta^{18}O_w$ measurements have not typically been measured shipboard on research cruises. Recent advancements in laser-based systems (Munksgaard et al., 2012) may make this theoretically possible, but it has yet to be widely applied. Measurements of $\delta^{18}O_w$ compiled in the NASA GISS database (Schmidt et al., 1999) show sporadic point source samples along ship tracks, mostly of surface waters, with some regions containing very few measurements. For example, the southeastern parts of the Pacific and Indian Oceans contain less than 30 measurements each.

Despite coverage that is spotty at times, existing data has revealed global-scale patterns showing that surface seawater $\delta^{18}O_w$ varies broadly with latitude. Peak $\delta^{18}O_w$ values are observed in extratropical latitudes due to evaporative enrichment driven by contact with dry air in the downwelling arm of the Hadley cell, and minimum $\delta^{18}O_w$ values are observed at high latitudes due to proximity to melting glacial ice (Craig & Gordon, 1965). Equatorial $\delta^{18}O_w$ values are depleted relative to extratropical values due to rainfall recycling heavier isotopes back into seawater but are not as depleted as high latitude regions. As this pattern is driven by global

atmospheric circulation patterns that are fundamental to the Earth system, it is likely that this general structure of $\delta^{18}O_w$ values has been present throughout Earth's oceanographic history.

While these large-scale patterns have emerged and new measurements continue to be added to the above-mentioned databases, persistent data gaps hinder use of $\delta^{18}O_w$ to study finer scale processes or more thoroughly investigate oceanographic processes. These data gaps are important, considering that several studies have used existing incomplete datasets to interpolate and model $\delta^{18}O_w$ across the globe (Schmidt et al., 1999; LeGrande & Schmidt, 2006; Murray et al., 2023), define region-specific $\delta^{18}O_w$-salinity relationships (Frew et al., 2000; LeGrande & Schmidt, 2006; Tiwari et al., 2013; Voelker et al., 2015; Benetti et al., 2017; Conroy et al., 2017; Stevenson et al., 2018; Belem et al., 2019; Murray et al., 2023), and validate Earth system model output (Brady et al., 2019). Where models are based on fewer real measurements, these efforts are more likely to misrepresent $\delta^{18}O_w$ variability in the modern ocean.

Given these data gaps, the need is clear for more systematically-collected $\delta^{18}O_w$ datasets, especially those targeting finer spatial scales than previously measured or oceanographic regions that have largely been overlooked. There are efforts underway to obtain higher-resolution $\delta^{18}O_w$ records in the Pacific (Dee et al., 2023; Atwood et al., in review), and we encourage more campaigns worldwide to capture $\delta^{18}O_w$ variability at as high spatial and temporal resolution as possible. With higher spatial and temporal coverage in $\delta^{18}O_w$ measurements, the oceanography community can expect its understanding of oceanographic and hydrologic processes to expand in kind.

One region in particular worth investigating further is the U.S. Eastern Seaboard, as it is home to many hydrologically complex coastal ecosystems (e.g. estuaries, tidal flats, lagoons, and salt marshes) (Dame et al., 2000; Roman et al., 2000; Anthony et al., 2009; Guimond &

Tamborski, 2021). This region also spans a wide range of latitudes, climates, and moisture regimes, from the warmer and more humid tropics (i.e., southern Florida) to the cooler humid continental climates of mid-latitude regions (i.e., Maine). This regional variability has been previously identified in modelling studies, with Murray et al. (2023) most recently dividing this area into 3 subregions ("Atlantic Ocean Primary"; "Delaware Coastal Current"; "Bahamas, Florida, Mid-Atlantic Coast"), each with their own defined $\delta^{18}O_w$-salinity relationship in surface seawater. More data is needed here specifically to populate subregions and properly define variability within each one and the boundaries between them.

In this dataset – which we abbreviate as the "SeaSOx" dataset – we present 364 new paired salinity and $\delta^{18}O_w$ measurements from localities along the U.S. Eastern Seaboard, where salinity (and $\delta^{18}O_w$) varies over fairly small spatial scales. This work nearly triples the existing data in the North Atlantic and is the first study to explore $\delta^{18}O_w$ variability on such a fine yet expansive spatial scale. We hope these data will encourage more systematic studies of $\delta^{18}O_w$ and aid in the development of $\delta^{18}O_w$ as a tool for both modern oceanography and paleoceanography research.

4.3 Methods

4.3.1 Sample localities

Water samples were collected from a total of 139 sites across the Eastern Seaboard, from Maine to southern Florida, with typically less than ~30km of coastline between sampling locations (Figure 4.1). Latitude and longitude coordinates were recorded using a Garmin eTrex 30x handheld GPS system. Samples were collected during several one-to-two week campaigns occurring during 2023-2025 (East Coast Water 1 (ECW1), East Coast Water 2 (ECW2), Florida 1 (FL1), Florida 2 (FL2) - see Table 4.1 for more details). These intensive campaigns were

supplemented with miscellaneous samples collected at a few additional locations in Maine, Florida, and South Carolina. At some sites, 3-5 samples were taken at a single beach with <5m between collection points to assess small-scale spatial variability, which was later measured to be <1 parts per thousand (ppt) and <0.3‰ for salinity and $\delta^{18}O_w$ respectively. Some locations were revisited (e.g., Virginia), and some measurements were repeatedly collected over the years to assess temporal variability (e.g., Hollywood Beach, Florida). Six (6) data points were previously published (Zhang & Petersen, 2023) but are included here under "Miscellaneous", as they were run in the same lab following similar procedures and relate to the same geographical study area.

4.3.2 Sample collection procedures

Samples were collected and stored in 30-mL ThermoScientific Nalgene Wide-Mouth high-density polyethylene (HDPE) vials. Prior to collecting a sample, the sample vial was rinsed three times with the water to be sampled. To collect the sample itself, the vial was fully submerged and capped underwater to include as little air as possible. Vials were shipped or carried to the University of Michigan Stable Isotope Lab, where they were analyzed within two to three weeks of their return.

4.3.3 Salinity measurements

For each sample, salinity was measured using an EXTECH EC170 Salinity Meter either at the site during sample collection (e.g., ECW1) or in the lab using water from the sample bottle prior to isotopic analysis (e.g., ECW2). The salinity meter was calibrated in the lab using a commercially available salinity standard (Vernier Science Education); the resolution and accuracy of the meter were 2 ppt and +/- 0.05 ppt, respectively. All salinity data are presented in ppt (Figure 4.2a).

4.3.4 $\delta^{18}O$ measurements

For oxygen isotope measurements, 400 microliters (μL) of sample water were pipetted into a 12 milliliter (mL) Exetainer (LabCo), then flushed with a mixture of helium and 0.3% CO_2 before equilibrating for three days. Equilibrated CO_2 from the headspace was then measured with a GasBench II coupled to a MAT 253 mass spectrometer, both Thermo Fisher Scientific. All $\delta^{18}O$ values are expressed in units of per mille (‰) and reported relative to Vienna Standard Mean Ocean Water (VSMOW) (Figure 4.2b). Measurements were corrected for instrument drift and scale compression by comparison to United States Geological Survey (USGS) isotope standards USGS45 (Biscayne Aquifer Drinking Water: -2.238‰ VSMOW), USGS46 (Ice Core Water: -29.80‰ VSMOW), and USGS50 (Lake Kyoga Water: +4.95‰ VSMOW). Eight consecutive CO_2 injections were averaged per sample. Analytical precision was measured to be <0.1‰.

4.4 Results

4.4.1 Regional $\delta^{18}O_w$ and salinity variability

$\delta^{18}O_w$ and salinity values span the ranges of -2 to +2‰ and 26-40 ppt, respectively, though the degree of variability in $\delta^{18}O_w$ within geographic regions differs along the Eastern Seaboard (Fig. 4.3). Massachusetts, Delaware, and Maryland/Virginia exhibit <1‰ variability across sites. Meanwhile, $\delta^{18}O_w$ values from regions such as New Jersey, the Carolinas, and Eastern Florida vary by >1‰, with the Cape Hatteras, North Carolina region exhibiting the greatest amount of variability (>2‰). However, this variability also appears to be temporal, as $\delta^{18}O_w$ values from this region sampled in 2024 are substantially depleted relative to those originally sampled in 2023. Salinity measurements also reflect these trends, with greater variability in the southern regions where more complex hydrological systems such as brackish-

estuarine environments, tidal flats, and back barrier islands are more prominent. These freshwater influences could have attributed to depleted $\delta^{18}O_w$ values at Georgia relative to the other southern regions.

4.4.2 $\delta^{18}O_w$ covariance with salinity across latitudes

$\delta^{18}O_w$ and salinity covary across latitudes along the U.S. East Coast (Fig. 4.4), which is consistent with previous studies demonstrating a clear $\delta^{18}O_w$-salinity relationship in the broader North Atlantic region (Frew et al., 2000; LeGrande and Schmidt, 2006; Murray et al., 2023). Furthermore, $\delta^{18}O_w$ and salinity values generally fall within one of two 'clusters'. The first 'cluster' falls within the ~35-45°N latitude band (26-31 ppt, -2 to 0‰); the second falls within the ~25-35°N latitude band (31-40 ppt, 0 to 2‰). These discrete clusters are divided by a distinct boundary at ~35°N.

4.5 Discussion

4.5.1 Uncertainties in $\delta^{18}O$-based temperature reconstructions

$\delta^{18}O_w$ varies spatially in $\delta^{18}O_w$ by >1‰ across several regions along the U.S. Eastern Seaboard, which has significant implications for paleotemperature and paleohydrological interpretations. For instance, 1‰ uncertainty in $\delta^{18}O_w$ corresponds to ~5°C uncertainty in $\delta^{18}O$-based paleothermometry estimates (e.g., Grossman and Ku, 1986; Kim et al., 2007). $\delta^{18}O_w$ also varies temporally, as values from Cape Hatteras, North Carolina collected in 2024 were depleted by >1‰ relative to those from 2023 (Fig. S4.1). These depleted values were likely influenced by historic regional flooding that had occurred the week before sample collection in September 2024, which would have brought in an influx of isotopically light precipitation and decreased $\delta^{18}O_w$ values in the short term. This is an example of how short-term, intense hydrological

occurrences could have produced substantial paleo-$\delta^{18}O_w$ variability and, in turn, $\delta^{18}O$-temperature uncertainty. These uncertainties could have been amplified with higher abundances of brief but intense hydrological events in the past (e.g., ice rafting during Pleistocene glacial-interglacial cycles).

Significant spatial and temporal $\delta^{18}O_w$ variability (>2‰) at Cape Hatteras, North Carolina reflects the difficulties of paleotemperature and paleohydrological reconstructions from coastal mixing zones in particular. Paleogeography changes and higher sea level could have impacted the position of coastal currents in the past (e.g., Johnson et al., 2017), resulting in uncertainties of how $\delta^{18}O_w$ may have changed in the region over time.

4.5.2 Distinct $\delta^{18}O_w$ signatures for the Labrador Current and Gulf Stream

$\delta^{18}O_w$ and salinity measurements fall within two discrete 'clusters' (Fig. 4.5), which likely correspond to the regional Labrador Current and Gulf Stream boundary currents. This clear separation is consistent with the lack of mixing and deflection of these currents at 35°N. The Labrador Current is influenced by substantial meltwater and riverine inputs, resulting in fresh, isotopically depleted waters off the northern portion of the Eastern Seaboard. The Gulf Stream consists of highly evaporated waters with limited continental freshwater inputs, resulting in more saline, isotopically enriched signatures off the southern portion of the Eastern Seaboard.

These data are not entirely consistent with several previously proposed $\delta^{18}O_w$-salinity mixing lines for water masses in this region (e.g., LeGrande and Schmidt, 2006; Murray et al., 2023). The 'Labrador Current' data cluster generally falls on the mixing line for the Delaware Coastal Current (Murray et al., 2023). The 'Gulf Stream' data fall between the mixing lines defined for the regions 'Atlantic Ocean Primary' and 'Bahamas, Florida, Mid-Atlantic coast'. (Murray et al., 2023). However, these previously defined mixing lines were generated from a

sparse instrumental dataset in the broader North Atlantic region, creating uncertainties in exact line slopes and intercepts. Furthermore, the amount of inherent regional variability in salinity and $\delta^{18}O_w$ makes it difficult to constrain linear fits to the data, making it easier to qualitatively describe 'clusters' than to quantitatively calculate linear regressions. It would be more appropriate to link these $\delta^{18}O_w$-salinity signatures to the Labrador Current and Gulf Stream, which are defined oceanographically as distinct water masses.

4.6 Data Records

The complete dataset named "SeaSOx: Seawater Salinity and Oxygen isotopes ($\delta^{18}O_{sw}$) along the U.S. East Coast from 24°N to 44°N" is readily available on waterisotopes.org (Bowen). Our data-gathering template consists of the following columns for data entry: campaign; month; year; date of collection; time of day; sampling 'area'; site name; sample name; latitude; longitude; salinity; $\delta^{18}O_w$; analytical 1SD (standard deviation) $\delta^{18}O_w$; in-house reproducibility (i.e., long-term standard deviation of standard USGS45); designation (marine, brackish-marine, brackish); hydrologic environment; precipitation (Y/N); other sampling notes. Individual samples were also averaged by locality and a complementary template contains many of the same data columns and additional columns for locality average, 1SD, and 1SE (standard error), for both salinity and $\delta^{18}O_w$. Sampling 'area' is considered as the geographic region, with sampling 'areas' within states differentiated by the regional hydrology and oceanography (e.g., Boston vs. Cape Cod, West Florida vs. East Florida). Samples were designated as 'marine' or 'brackish-marine' (see Table 4.2). Sample environments were included to specify local hydrologic conditions that could have impacted salinity and $\delta^{18}O_w$. All samples were collected from publicly available access points.

Sampling locations consisted of a variety of coastal and marginal marine environments, including estuaries, creeks, semi-restricted bays, inlets, and back barrier environments, sometimes leading to salinities that were below what would be typically classified as "marine". For classification purposes we designated each sample as "marine" or "brackish-marine" based on a combination of the measured salinity compared to regional baselines and visual observation of the surrounding environmental setting at the site (e.g., open beach vs. semi-restricted bay). Because fully-marine salinity baselines vary along the East Coast, we developed separate salinity thresholds for three geographic zones, distinguished by the distinct hydrology that dominated each region: (1) Maine to North Carolina, primarily dominated by the Labrador Current; (2) North Carolina to Georgia, primarily dominated by the Gulf Stream Current; (3) Florida, noted for its varied complex hydrologic systems (i.e., salt marshes, barrier islands, everglades). If it was unclear whether a sample should be designated "marine" or "intermediate" based on the thresholds, we deferred to visual observation of the sampling location environment (e.g., open beach vs. semi-restricted bay) to determine a designation. Samples measured to have salinities less than the lower end of the brackish threshold were not included in this dataset.

4.7 Technical Validation

The University of Michigan Stable Isotope Lab (SIL) participated in the International Atomic Energy Agency (IAEA) 2024 Water Stable Isotope Intercomparison (WICO) test, for which results from the lab's GasBench II/MAT 253 instrument setup were compared to the IAEA's continuous-flow IRMS setup. Six unique water samples were compared, consisting of a variety of meteoric waters and lab tap waters with bulk $\delta^{18}O_w$ compositions ranging from -22 to +1‰ (see Table 4.3). The average deviation from accepted $\delta^{18}O$ for the six samples was 0.04‰, with the largest deviation being 0.11‰. This aligns with the analytical precision determined

from repeat measurements of our check standard, which indicates consistent reproducibility at the <0.1‰ level. The lab received a "satisfactory" performance based on additional statistical tests. Individual documentation for the water standards used in calibrating oxygen isotope data (i.e., USGS45, USGS46, USGS50) are available at the USGS Reston Stable Isotope Laboratory website: https://www.usgs.gov/labs/reston-stable-isotope-laboratory/reference-materials-and-calibration-services.

4.8 Acknowledgments

I would like to acknowledge Adriana Brown, Erin Kim, Kailey Koshorek, Tara Lonsdorf, Lloyd Anderson, Laurie Warren, Eric Kort, Warren Kort, and Naya Kort for their assistance with sample collections. Authors were supported by the NSF-GRFP (to AAQ), Sloan Research Fellowship (to SVP), NSF-OCE grant #1903237 (to SVP), and NSF Career grant #2237429 (to SVP), and the Rackham Merit Fellowship (to LDG).

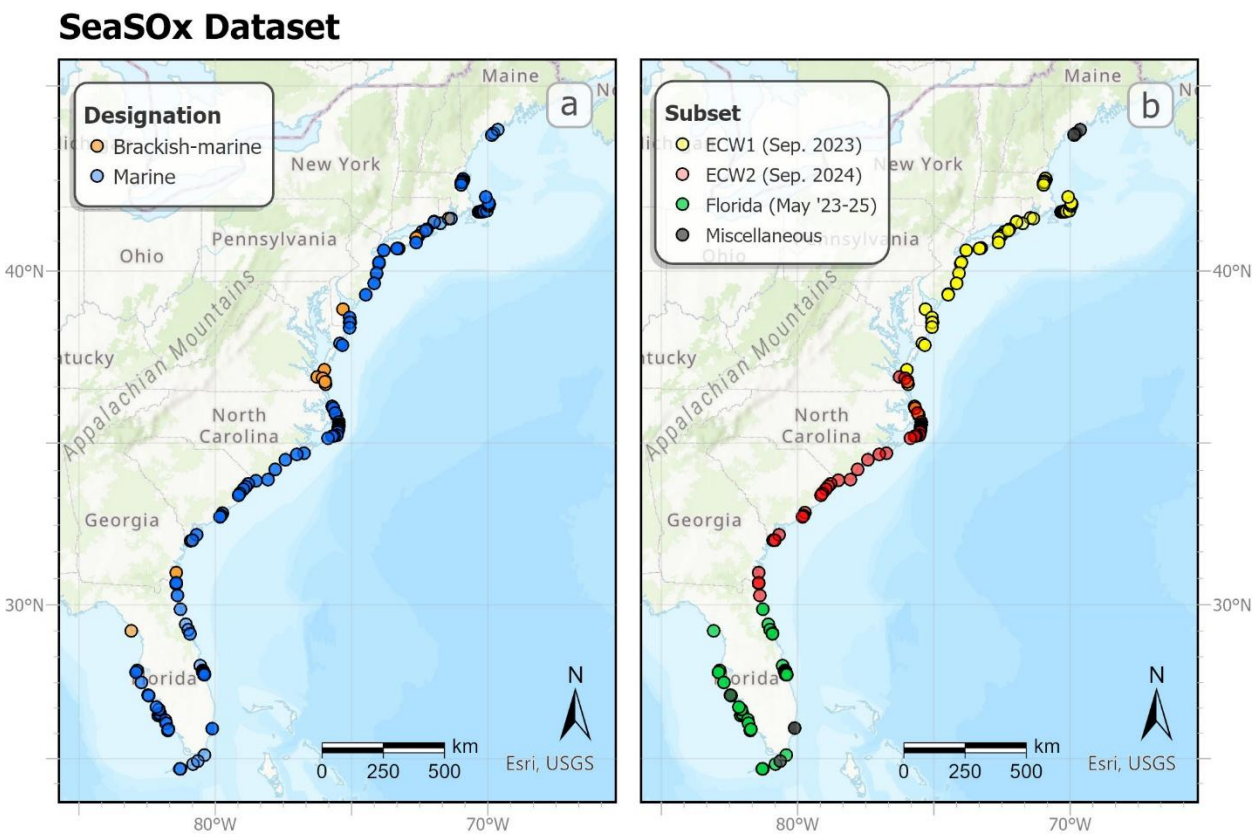

Figure 4.1. Sample locations.

a) Samples grouped by salinity threshold. b) Samples grouped by collection effort.

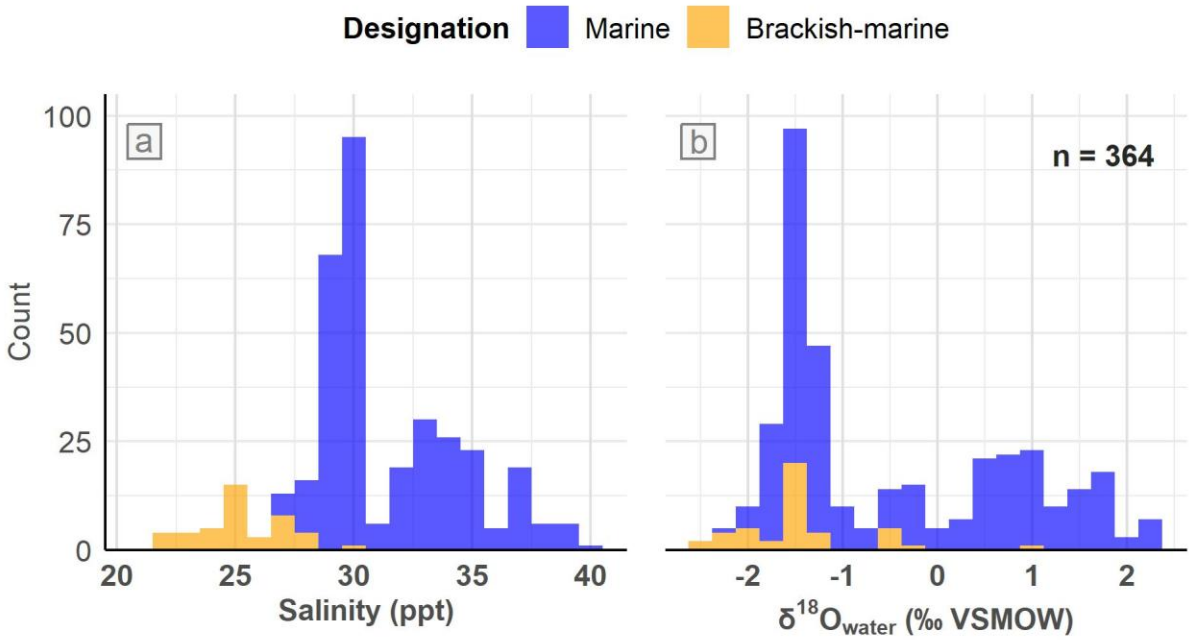

Figure 4.2. Stacked histogram distributions of water sample (a) salinity and (b) $\delta^{18}O_w$ values. Salinity thresholds for "marine" and "brackish-marine" vary slightly by region (see Table 4.2).

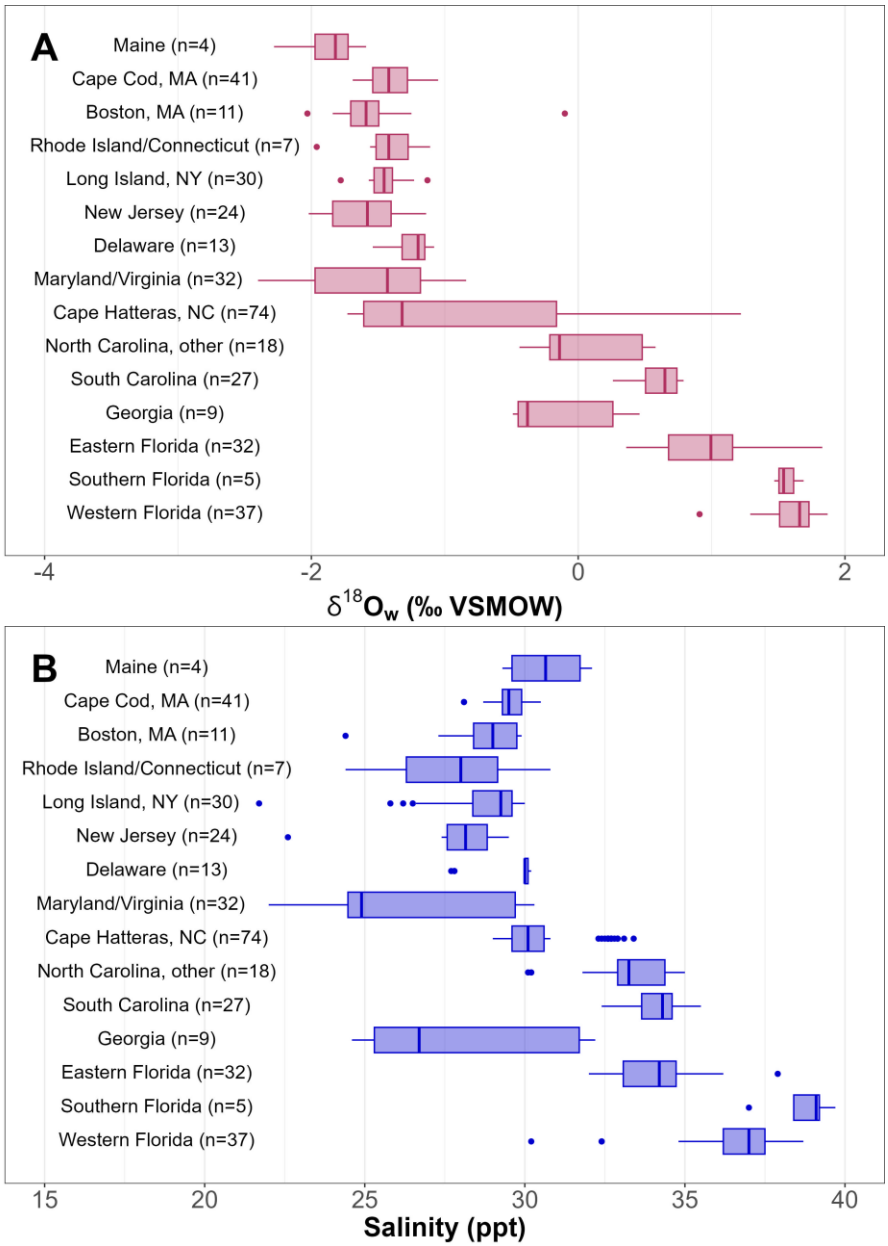

Figure 4.3. Box plots of (A) $\delta^{18}O_w$ and (B) salinity from the SeaSOx dataset, separated by geographic region.

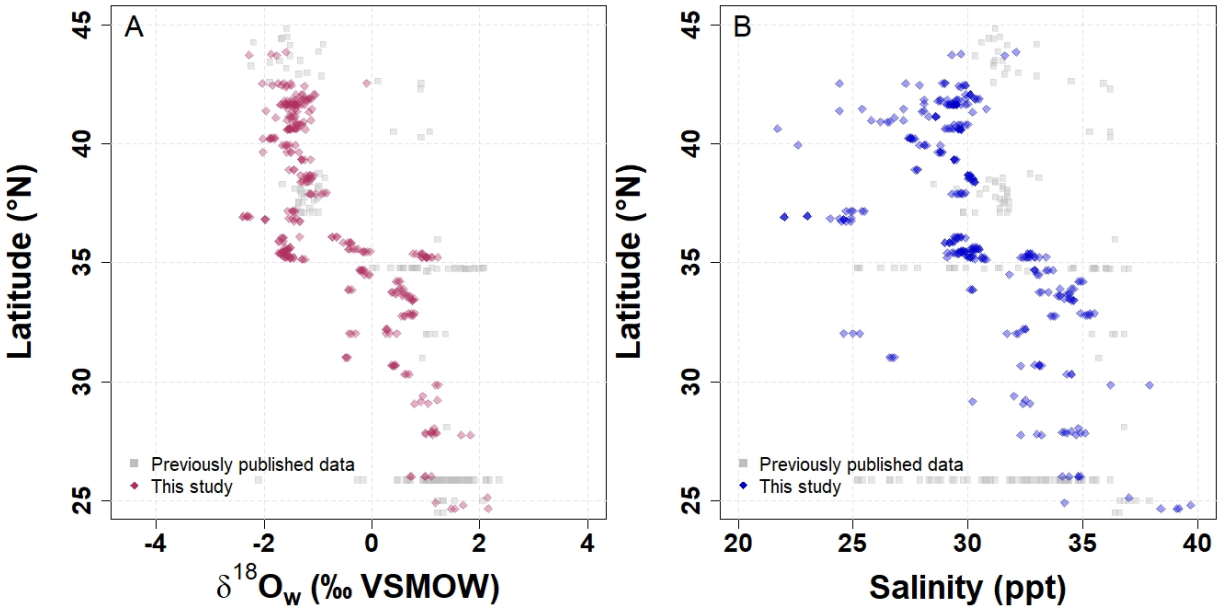

Figure 4.4. $\delta^{18}O_w$ (A) and salinity (B) measurements versus latitude along the U.S. Eastern Seaboard, excluding samples in the SeaSOx dataset collected from West Florida.

The grey points represent data previously recorded in the NASA GISS database.

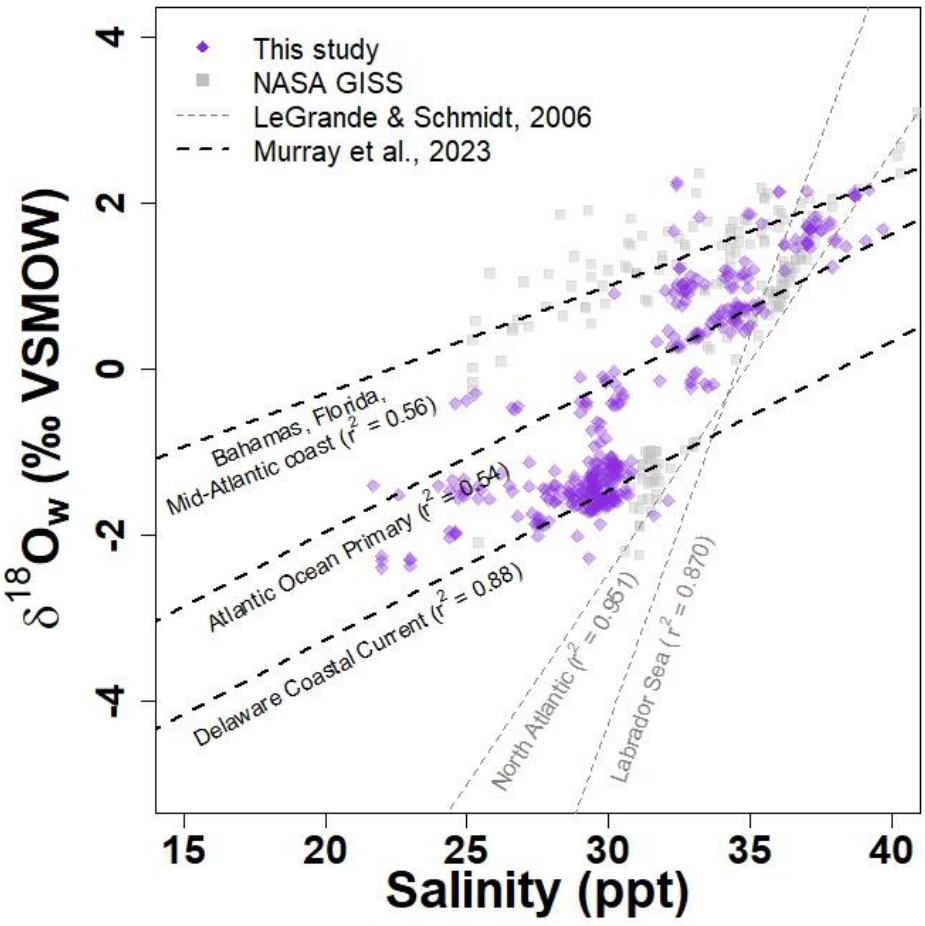

Figure 4.5. $\delta^{18}O_w$-salinity data for samples collected in the SeaSOx dataset.

Grey and black dashed lines represent $\delta^{18}O_w$-salinity relationships for various water masses or oceanographic regions previously reported in LeGrande & Schmidt (2006) and Murray et al. (2023), respectively.

Campaign	Dates	Number of sites	Number of 'brackish-marine' samples	Number of 'marine' samples	Total number of samples
ECW1	9/2/23 -9/10/23	59	28	156	184
ECW2	9/19/24 -9/24/24	37	15	96	111
FL1	5/28/23 -6/4/23	15	0	15	15
FL2	5/2/25 -5/18/25	10	0	22	22
Miscellaneous	Miscellaneous - 2024-2025	18	1	31	32
Total		139	44	320	364

Table 4.1. Sample collection campaigns for this study.

See Table 4.2 for descriptions about 'intermediate' and 'marine' designations. ECW = East Coast Water; FL = Florida.

Geographic Zone	Brackish-marine (ppt)	Marine (ppt)
Maine to North Carolina	20-27.5	27.5+
North Carolina to Georgia	25-30	30+
Florida	30-32	32+

Table 4.2. Salinity thresholds for designations of collected water samples, reported in units of parts per thousand (ppt).

Sample Name	Source	Deviation (‰)	UM SIL $\delta^{18}O$ (‰ VSMOW)	UM SIL SD (‰)	WICO 2024 $\delta^{18}O$ (‰ VSMOW)	WICO 2024 SD (‰)
OH31	Snowfall from Oberwaltersdorf, Austria collected on 12/3/2023	0.01	-16.06	0.10	-16.07	0.09
OH32	Water from Lake Neusiedl in Podersdorf, Austria collected in August 2021	-0.04	+1.18	0.10	+1.22	0.09
OH33	Snowfall from Oberwaltersdorf, Austria collected on 12/6/2023	0.11	-22.18	0.13	-22.29	0.09
OH34	50-50 mixture of lab tap water and Lake Neusiedl water collected in August 2020	0.01	-5.05	0.10	-5.06	0.08
OH35	Tap water	0.02	-10.66	0.10	-10.68	0.09
OH36	OH35 + NaCl	0.05	-10.64	0.10	-10.69	0.08
Average		0.04				

Table 4.3. WICO 2024 Intercomparison test results for the University of Michigan Stable Isotope Lab.

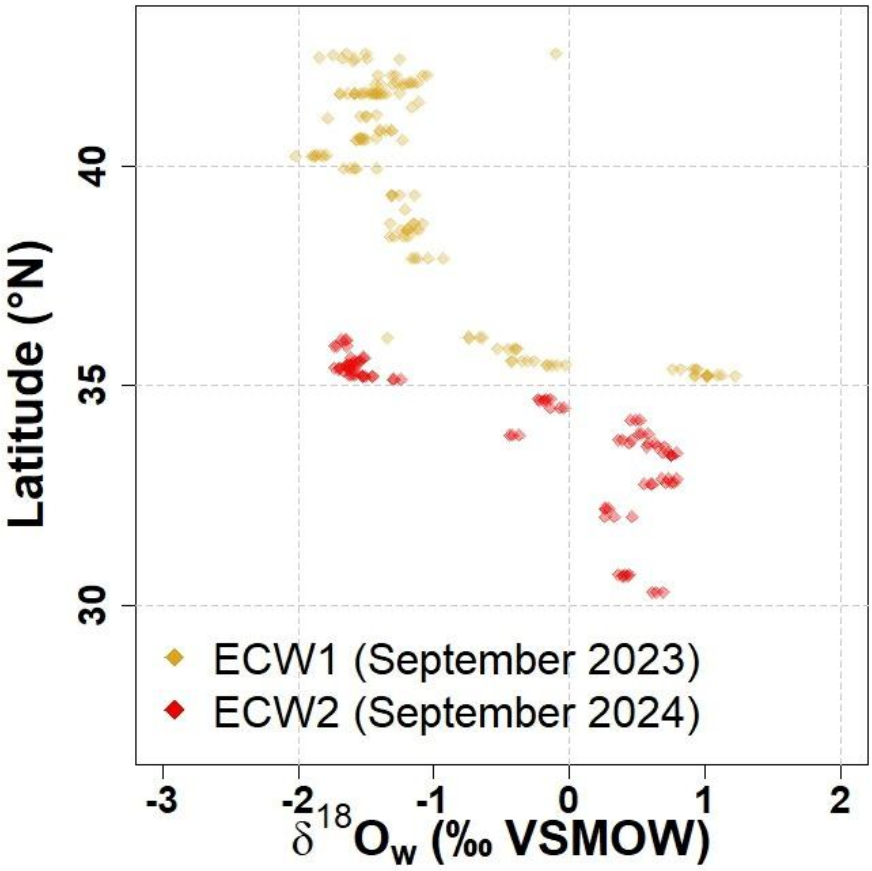

Figure S4.1. $\delta^{18}O_w$ (A) and salinity (B) measurements versus latitude along the U.S. Eastern Seaboard, colored by year of sampling campaign.

4.9 References

Adkins, J.F. & Schrag, D.P. Pore fluid constraints on deep ocean temperature and salinity during the Last Glacial Maximum. *Geophysical Research Letters* **28(5)**, 771-774, https://doi.org/10.1029/2000GL011597 (2001).

Anderson, R. F., Mawji, E., Cutter, G. A., Measures, C. I. & Jeandel, C. GEOTRACES: Changing the way we explore ocean chemistry. *Oceanography* **27**, 50–61, https://doi.org/10.5670/oceanog.2014.07 (2014).

Anthony, A., Atwood, J., August, P., Byron, C., Cobb, S., Foster, C., Fry, C., Gold, A., Hagos, K., Heffner, L., Kellogg, D.Q., Lellis-Dibble, K., Opaluch, J.J., Oviatt, C., Pfeiffer-Herbert, A., Rohr, N., Smith, L., Smythe, T., Swift, J. & Vinhateiro, N. Coastal Lagoons and Climate Change: Ecological and Social Ramifications in U.S. Atlantic and Gulf Coast Ecosystems. *Ecology and Society* **14(1)**, 8 (2009).

Atwood, A. R., Moore, A. L., DeLong, K. L., Long, S. E., Sanchez, S. C., Hargreaves, J. A., Morris, C. A., Pauly, R. E., Dassie, E. P., Felis, T., Voelker, A. H. L., Murty, S. A. & Cobb, K. M. The PAGES CoralHydro2k Seawater $\delta^{18}O$ Database: A FAIR-aligned compilation of seawater $\delta^{18}O$ data to uncover 'hidden' insights from the global ocean. *Earth System Science Data & Discussions* [preprint], https://doi.org/10.5194/essd-2025-467 (in review, 2025).

Beck, J.W., Edwards, R.L., Ito, E., Taylor, F.W., Recy, J., Rougerie, F., Joannot, P., & Henin, C. Sea-Surface Temperature from Coral Skeletal Strontium/Calcium Ratios. *Science* **257(5070)**, 644-647, https://doi.org/10.1126/science.257.5070.644 (1992).

Belem, A.L., Caricchio, C., Albuquerque, A.L.S., Venancio, I.M., Zucchi, M.D.R., Dos Santos, T.H.R. & Alvarez, Y.G. Salinity and stable oxygen isotope relationship in the Southwestern Atlantic: constraints to paleoclimate reconstructions. *An Acad Bras Cienc* **91**, e20180226, https://doi.org/10.1590/0001-3765201920180226 (2019).

Benetti, M., Reverdin, G., Aloisi, G., & Sveinbjörnsdóttir, Á. Stable isotopes in surface waters of the Atlantic Ocean: Indicators of ocean-atmosphere water fluxes and oceanic mixing processes. *Journal of Geophysical Research: Oceans* **122(6)**, 4723-4742, https://doi.org/10.1002/2017JC012712 (2017).

Bowen, G.J. Waterisotopes.org. University of Utah, http://waterisotopes.org (accessed 31 Oct 2025).

Brady, E., Stevenson, S., Bailey, D., Liu, Z., Noone, D., Nusbaumer, J., Otto-Bliesner, B.L., Tabor, C., Tomas, R., Wong, T., Zhang, J. & Zhu, J. The Connected Isotopic Water Cycle in the Community Earth System Model Version 1. *Journal of Advances in Modeling Earth Systems* **11**, 2547-2566, https://doi.org/10.1029/2019MS001663 (2019).

Chave, K.E. Aspects of the Biogeochemistry of Magnesium 1. Calcareous Marine Organisms. *The Journal of Geology* **62(3)** (1954).

Conroy, J.L., Thompson, D.M., Cobb, K.M., Noone, D., Rea, S. & LeGrande, A.N. Spatiotemporal variability in the $\delta^{18}O$-salinity relationship of seawater across the tropical Pacific Ocean. *Paleoceanography and Paleoclimatology* **32**, 484-497, https://doi.org/10.1002/2016PA003073 (2017).

Conroy, J.L., Murray, N.K., Patterson, G.S., Schore, A.I.G., Ikuru, I., Cole, J.E., Chillagana, D. & Echeverria, F. Equatorial Undercurrent Influence on Surface Seawater $\delta^{18}O$ Values in the Galápagos. *Geophysical Research Letters* **50**, e2022GL102074, https://doi.org/10.1029/2022GL102074 (2023).

Cooper, L.W., Magen, C. & Grebmeier, J.M. Changes in the oxygen isotope composition of the Bering Sea contribution to the Arctic Ocean are an independent measure of increasing freshwater fluxes through the Bering Strait. *PLoS ONE* **17**, e0273065, https://doi.org/10.1371/journal.pone.0273065 (2022).

Craig, H. & Gordon, L.I. Deuterium and Oxygen 18 Variations in the Ocean and the Marine Atmosphere. *Stable Isotopes in Oceanographic Studies* 9-130 (1965).

Dame, R., Alber, M., Allen, D. & Mallin, M. Estuaries of the South Atlantic Coast of North America: Their Geographical Signatures. *Estuaries and Coasts* **23(6)**, 793-819, https://doi.org/10.2307/1352999 (2000).

Dansgaard, W. Stable isotopes in precipitation. *Tellus* **16(4)**, 436-468, https://doi.org/10.3402/tellusa.v16i4.8993 (1964).

Dansgaard, W., Johnsen, S.J., Clausen, H.B., Dahl-Jensen, D., Gundestrup, N.S., Hammer, C.U., Hvidberg, C.S., Steffensen, J.P., Sveinbjörnsdottir, A.E., Jouzel, J. & Bond, G. Evidence for general instability of past climate from a 250-kyr ice-core record. *Nature* **364**, 218-220, https://doi.org/10.1038/364218a0 (1993).

Dee, S., Bailey, A., Conroy, J.L., Atwood, A., Stevenson, S., Nusbaumer, J. & Noone, D. Water isotopes, climate variability, and the hydrological cycle: recent advances and new frontiers. *Environmental Research: Climate* **2**, 022002, https://doi.org/10.1088/2752-5295/accbe1 (2023).

Devi, G.K., Ganasri, B.P. & Dwarakish, G.S. Applications of Remote Sensing in Satellite Oceanography: A Review. *Aquatic Procedia* **4**, 579-584, https://doi.org/10.1016/j.aqpro.2015.02.075 (2015).

Eiler, J.M. "Clumped-isotope" geochemistry - The study of naturally-occurring, multiply-substituted isotopologues. *Earth and Planetary Science Letters* **262(3-4)**, 309-327, https://doi.org/10.1016/j.epsl.2007.08.020 (2007).

EPICA Community Members. Eight glacial cycles from an Antarctic ice core. *Nature* **429**, 623-628, https://doi.org/10.1038/nature02599 (2004).

Frew, R.D., Dennis, P.D., Heywood, K.J., Meredith, M.P. & Boswell, S.M. The oxygen isotope composition of water masses in the northern North Atlantic. *Deep Sea Research Part I: Oceanographic Research Papers* **47**, 2265-2286, https://doi.org/10.1016/S0967-0637(00)00023-6 (2000).

Ghosh, P., Adkins, J., Affek, H., Balta, B., Guo, W., Schauble, E.A., Schrag, D., & Eiler, J.M. ^{13}C-^{18}O bonds in carbonate minerals: A new kind of paleothermometer. *Geochimica et Cosmochimica Acta* **70(6)**, 1439-1456, https://doi.org/10.1016/j.gca.2005.11.014 (2006).

Grootes, P.M., Stuiver, M., White, J.W.C., Johnsen, S. & Jouzel, J. Comparison of oxygen isotope records from the GISP2 and GRIP Greenland ice cores. *Nature* **366**, 552-554, https://doi.org/10.1038/366552a0 (1993).

Grossman, E.L., & Ku, T-L. Oxygen and carbon isotope fractionation in biogenic aragonite: Temperature effects. *Chemical Geology* **59**, 59-74. https://doi.org/10.1016/0168-9622(86)90057-6 (1986).

Guimond, J. & Tamborski, J. Salt Marsh Hydrogeology: A Review. *Water* **13(4)**, 543, https://doi.org/10.3390/w13040543 (2021).

International Ocean Discovery Program. *IODP Science Plan: Illuminating Earth's Past, Present, and Future, 2013–2023*. Integrated Ocean Drilling Program Management International, Inc., Washington, DC (2011).

Johnson, A.L.A., Valentine, A., Leng, M.J., Sloane, H.J., Schöne, B.R., & Balson, P.S. Isotopic temperatures from the early and mid-Pliocene of the US Middle Atlantic Coastal Plain, and their implications for the cause of regional marine climate change. *PALAIOS* **32**(4), 250-269. https://doi.org/10.2110/palo.2016.080 (2017).

Jouzel, J., Merlivat, L., & Lorius, C. Deuterium excess in an East Antarctic ice core suggests higher relative humidity at the oceanic surface during the last glacial maximum. *Nature* **299**, 688-691 (1982).

Jouzel, J., Masson-Delmonte, V., Cattani, O., Dreyfus, G., Falourd, S., Hoffmann, G., Minster, B., Nouet, J., Barnola, J.M., Chappellaz, J., Fischer, H., Gallet, J.C., Johnsen, S., Leuenberger, M., Loulergue, L., Luethi, D., Oerter, H., Parrenin, F., Raisbeck, G., Raynaud, D., Schilt, A., Schwander, J., Selmo, E., Souchez, R., Spahni, R., Stauffer, B., Steffensen, J.P., Stenni, B., Stocker, T.F., Tison, J.L., Werner, M., & Wolff, E.W. Orbital and Millennial Antarctic Climate Variability over the Past 800,000 Years. *Science* **317(5839)**, 793-796, https://doi.org/10.1126/science.1141038 (2007).

Kim, S-T., O'Neil, J.R., Hillaire-Marcel, C., & Mucci, A.. Oxygen isotope fractionation between synthetic aragonite and water: Influence of temperature and Mg^{2+} concentration.

Geochimica et Cosmochimica Acta **71**(19), 4704-4715. https://doi.org/10.1016/j.gca.2007.04.019 (2007).

Kim, H. & Timmermann, A. Seawater oxygen isotopes as a tool for monitoring future meltwater from the Antarctic ice sheet. *Communications Earth & Environment* **5**, 343, https://doi.org/10.1038/s43247-024-01514-4 (2024).

LeGrande, A.N. & Schmidt, G.A. Global gridded data set of the oxygen isotopic composition in seawater. *Geophysical Research Letters* **33**, L12604, https://doi.org/10.1029/2006GL026011 (2006).

Lisiecki, L.E. & Raymo, M.E. A Pliocene-Pleistocene stack of 57 globally distributed benthic $\boldsymbol{\delta}^{18}$O records. *Paleoceanography and Paleoclimatology* **20(1)**, PA1003, https://doi.org/10.1029/2004PA001071 (2005).

Meckler, A.N., Sexton, P.F., Piasecki, A.M., Leutert, T.J., Marquardt, J., Ziegler, M., Agterhuis, T., Lourens, L.J., Rae, J.W.B., Barnet, J., Tripati, A. & Bernasconi, S.M. Cenozoic evolution of deep ocean temperature from clumped isotope thermometry. *Science* **377(6601)**, 86-90, https://doi.org/10.1126/science.abk0604 (2022).

Munksgaard, N.C., Wurster, C.M., Bass, A., Zagorskis, I. & Bird, M.I. First continuous shipboard $\boldsymbol{\delta}^{18}$O and $\boldsymbol{\delta}$D measurements in sea water by diffusion sampling - cavity ring-down spectrometry. *Environmental Chemistry Letters* **10**, 301-307, https://doi.org/10.1007/s10311-012-0371-5 (2012).

Murray, N.K., Muñoz, A.R. & Conroy, J.L. Machine Learning Solutions to Regional Surface Ocean δ^{18}O-Salinity Relationships for Paleoclimatic Reconstruction. *Paleoceanography and Paleoclimatology* **38**, e2023PA004612, https://doi.org/10.1029/2023PA004612 (2023).

NEEM Community Members. Eemian interglacial reconstructed from a Greenland folded ice core. *Nature* **493**, 489-494, https://doi.org/10.1038/nature11789 (2013).

North Greenland Ice Core Project Members. High-resolution record of Northern Hemisphere climate extending into the last interglacial period. *Nature* **431**, 147-151, https://doi.org/10.1038/nature02805 (2004).

Nürnberg, D., Bijma, J., & Hemleben, C. Assessing the reliability of magnesium in foraminiferal calcite as a proxy for water mass temperatures. *Geochimica et Cosmochimica Acta* **60(5)**, 803-814, https://doi.org/10.1016/0016-7037(95)00446-7 (1996).

Petit, J.R., Jouzel, J., Raynaud, D., Barkov, N.I., Barnola, J.-M., Basile, I., Bender, M., Chappellaz, J., Davis, M., Delaygue, G., Delmotte, M., Kotlyakov, V.M., Legrand, M., Lipenkov, V.Y., Lorius, C., Pépin, L., Ritz, C., Saltzman, E., & Stievenard, M. Climate and atmospheric history of the past 420,000 years from the Vostok ice core, Antarctica. *Nature* **399**, 429-436, https://doi.org/10.1038/20859 (1999).

Rayleigh, L. Theoretical considerations respecting the separation of gases by diffusion and similar processes. *Philosophical Magazine* **42**, 493-498, https://doi.org/10.1080/14786449608620944 (1896).

Reverdin, G., Waelbroeck, C., Pierre, C., Akhoudas, C., Aloisi, G., Benetti, M., Bourlès, B., Danielsen, M., Demange, J., Diverrès, D., Gascard, J-C., Houssais, M-N., Le Goff, H., Lherminier, P., Lo Monaco, C., Mercier, H., Metzl, N., Morisset, S., Naamar, A., Reynaud, T., Sallée, J-B., Thierry, V., Hartman, S.E., Mawji, E.W., Olafsdottir, S., Kanzow, T., Velo, A., Voelker, A., Yashayaev, I., Haumann, F.A., Leng, M.J., Arrowsmith, C., & Meredith, M. The CISE-LOCEAN seawater isotopic database (1998-2021). *Earth System Science Data* **14**, 2721-2735, https://doi.org/10.5194/essd-14-2721-2022 (2022).

Roemmich, D., Johnson, G.C., Riser, S., Davis, R., Gilson, J., Brechner Owens, W., Garzoli, S.L., Schmid, C., & Ignaszewski, M. The Argo Program: Observing the Global Ocean with Profiling Floats. *Oceanography* **22(2)**, 34-43 (2009).

Roman, C.T., Jaworski, N., Short, F.T., Findlay, S. & Warren, R.S. Estuaries of the northeastern United States: Habitat and land use signatures. *Estuaries* **23(6)**, 743-764, https://doi.org/10.2307/1352997 (2000).

Schauble, E.A., Ghosh, P., & Eiler, J.M. Preferential formation of ^{13}C-^{18}O bonds in carbonate minerals, estimated using first-principles lattice dynamics. *Geochimica et Cosmochimica Acta* **70(10)**, 2510-2529, https://doi.org/10.1016/j.gca.2006.02.011 (2006).

Schmidt, G.A., Bigg, G. R., & E. J. Rohling. Global Seawater Oxygen-18 Database - v1.22. https://data.giss.nasa.gov/o18data/ (1999).

Schrag, D.P., Adkins, J.F., McIntyre, K., Alexander, J.L., Hodell, D.A., Charles, C.D. & McManus, J.F. The oxygen isotopic composition of seawater during the Last Glacial Maximum. *Quaternary Science Reviews* **21(1-3)**, 331-342, https://doi.org/10.1016/S0277-3791(01)00110-X (2002).

Sharp, Z. *Principles of Stable Isotope Geochemistry*. (Pearson Prentice Hall, Upper Saddle River, NJ, 2007).

Sima, A., Paul, A., Schulz, M. & Oerlemans, J. Modeling the oxygen-isotopic composition of the North American Ice Sheet and its effect on the isotopic composition of the ocean during the last glacial cycle. *Geophysical Research Letters* **33**, L15706, https://doi.org/10.1029/2006GL026923 (2006).

Sloyan, B.M., Wanninkhof, R., Kramp, M., Johnson, G.C., Talley, L.D., Tanhua, T., McDonagh, E., Cusack, C., O'Rourke, E., McGovern, E., Katsumata, K., Diggs, S., Hummon, J., Ishii, M., Azetsu-Scott, K., Boss, E., Ansorge, I., Perez, F.F., Mercier, H., Williams, M.J.M., Anderson, L., Lee, J.H., Murata, A., Kouketsu, S., Jeansson, E., Hoppema, M., &

Campos, E. The Global Ocean Ship-Based Hydrographic Investigations Program (GO-SHIP): A Platform for Integrated Multidisciplinary Ocean Science. *Frontiers in Marine Science* **6(445)**, https://doi.org/10.3389/fmars.2019.00445 (2019).

Stevenson, S., Powell, B., Cobb, K.M., Nusbaumer, J., Merrifield, M. & Noone, D. Twentieth Century Seawater $\delta^{18}O$ Dynamics and Implications for Coral-Based Climate Reconstruction. *Paleoceanography and Paleoclimatology* **33**, 606-625, https://doi.org/10.1029/2017PA003304 (2018).

Stevenson, S., Cobb, K.M., Merrifield, M., Powell, B., Sanchez, S., Nusbaumer, J., O'Connor, G. & Atwood, A. Contrasting Central Equatorial Pacific Oxygen Isotopic Signatures of the 2014/2015 and 2015/2016 El Niño Events. *Geophysical Research Letters* **50**, e2023GL104454, https://doi.org/10.1029/2023GL104454 (2023).

Tiwari, M., Nagoji, S.S., Kartik, T., Drishya, G., Parvathy, R.K. & Rajan, S. Oxygen isotope-salinity relationships of discrete oceanic regions from India to Antarctica vis-à-vis surface hydrological processes. *Journal of Marine Systems* **113-114**, 88-93, https://doi.org/10.1016/j.jmarsys.2023.01.001 (2013).

Voelker, A.H.L., Colman, A., Olack, G., Waniek, J.J. & Hodell, D. Oxygen and hydrogen isotope signatures of Northeast Atlantic water masses. *Deep Sea Research Part II: Topical Studies in Oceanography* **116**, 89-106, https://doi.org/10.1016/j.dsr2.2014.11.006 (2015).

Watanabe, O., Jouzel, J., Johnsen, S., Parrenin, F., Shoji, H., & Yoshida, N. Homogeneous climate variability across East Antarctica over the past three glacial cycles. *Nature* **422**, 509-512, https://doi.org/10.1038/nature01525 (2003).

Weber, J.N. Incorporation of strontium into reef coral skeletal carbonate. *Geochimica et Cosmochimica Acta* **37(9)**, 2173-2190, https://doi.org/10.1016/0016-7037(73)90015-X (1973).

Zachos, J., Pagani, M., Sloan, L., Thomas, E., & Billups, K. Trends, Rhythms, and Aberrations in Global Climate 65 Ma to Present. *Science* **292(5517)**, 686-693, https://doi.org/10.1126/science.1059412 (2001).

Zhang, J.Z. & Petersen, S.V. Clumped and oxygen isotope sclerochronology methods tested in the bivalve *Lucina pensylvanica*. *Chem. Geol.* **620**, 121346, https://doi.org/10.1016/j.chemgeo.2023.121436 (2023).

Zhang, J.Z., Petersen, S.V., Lavis, S. & Williams, B. Quantifying variations in $\delta^{18}O_w$ and salinity in modern Bermudan waters on hourly to monthly timescales. *Frontiers in Marine Science* **11**, https://doi.org/10.3389/fmars.2024.1441113 (2024).

Chapter 5 MIS5 Paleoclimate and Paleoceanography Along the Atlantic Coastal Plain

5.1 Abstract

Marine Isotope Stage 5 (MIS5) was a dynamic Pleistocene interglacial that saw both a warm climate (i.e., MIS 5e, ~130-115 ka) and cool climate accompanied by ice sheet growth and sea level decrease (i.e., MIS 5a, ~80 ka). MIS 5e has long been considered a potential 'analog' for future climate given warmer-than-modern temperatures and higher sea level, while MIS 5a represents an intermediate cooling period reflecting the transition into the subsequent glacial. Therefore, investigations of MIS5 can shed light on future climate conditions. Previous studies have identified fossiliferous sedimentary deposits dating to both MIS 5e and 5a along the Atlantic Coastal Plain – a region populated by millions of people that is particularly susceptible to the impacts of climate change. However, quantitative temperature estimates from this region during MIS 5e and especially during MIS 5a are sparse, with most proxy estimates reported from open-ocean sites (as opposed to coastal sites). Although traditional stable oxygen isotope paleothermometry ($\delta^{18}O$) has been previously applied to fossil carbonates from this coastal region for other time periods, seawater $\delta^{18}O$ ($\delta^{18}O_w$) in this region has been shown to vary substantially, creating uncertainties in paleotemperature estimates. The newer 'clumped' isotope paleothermometer (Δ_{47}) operates independently of $\delta^{18}O_w$, and the combination of Δ_{47} with $\delta^{18}O$ allows for simultaneous calculation of paleotemperatures and reconstructed paleo-$\delta^{18}O_w$ values. In this study, we present new amino acid geochronology data and Δ_{47}-derived paleotemperatures and paleo-$\delta^{18}O_w$ values from fossil bivalves collected from nine sites along the Atlantic Coastal Plain. New AAR data confirm relative stratigraphy (MIS 5e and/or MIS 5a) within each

collection site. Isotopic temperature data reveal MIS 5a temperatures cooler than modern by ~1-5°C on average and MIS 5e temperatures generally similar to modern, which aligns with global temperature trends. However, collective MIS 5e temperatures from this region suggest the occurrence of multiple depositional episodes during both peak MIS 5e and late MIS 5e conditions, with warmer-than-modern temperatures at northern latitudes consistent with early Last Interglacial conditions and cooler-than-modern temperatures at subtropical sites consistent with late Last Interglacial conditions. Finally, paleo-$\delta^{18}O_w$ signatures roughly align with modern $\delta^{18}O_w$ signatures for the Labrador Current and Gulf Stream, demonstrating the potential for Δ_{47}-derived paleo-$\delta^{18}O_w$ to be used as a regional water mass tracer.

5.2 Introduction

MIS 5 (~130-80 ka) is the most recent interglacial period and can serve as a potential 'analog' for future climate, with continental configurations resembling those of today. Although pCO_2 is thought to be lower than present (e.g., Schneider et al., 2013), peak global mean sea level (GMSL) was 6-9m higher (e.g., Dutton and Lambeck, 2012; Dumitru et al., 2023), indicating a larger degree of sea level rise from ice sheet melt than expected from modern conditions. Within MIS 5 were five substages (MIS 5a to MIS5e). Peak warmth occurred during MIS 5e (~130-115 ka), when global temperatures were thought to have been warmer than present on average by 0-2°C (e.g., Turney & Jones, 2010; McKay et al., 2011; Otto-Bliesner et al., 2013; Turney et al., 2020). MIS 5e is relatively well-characterized and is often cited as a loose benchmark for future climate under current warming conditions (e.g., Kukla et al., 1997; Yin & Berger, 2015). The MIS 5d (~115-106 ka) and MIS 5b (~93-80ka) cool intervals were followed by the relatively warmer intervals MIS 5c (~106-93 ka) and MIS 5a (~80 ka) (e.g., Lisiecki and Raymo, 2005). However, proxy temperature data are largely lacking from MIS 5a

(~80 ka). In the absence of substantial temperature proxies during MIS 5a, previous studies that temperatures cooled from MIS 5e to MIS 5a as observed in the long-term Plio-Pleistocene $\delta^{18}O_{carb}$ record (Lisiecki & Raymo, 2005). Other proxy and modelling studies suggest that sea level decreased (e.g., Potter et al., 2004; Simms et al., 2009; Muhs et al., 2012; Creveling et al., 2017; Thompson & Creveling, 2021; Tawil-Morsink et al., 2022; Weiss et al., 2022; Hsia et al., 2024), and continental ice sheets must have expanded based on the magnitude of sea level decrease throughout MIS 5 (e.g., Grant et al., 2012; Weiss et al., 2022; Andrews et al., 2024).

MIS 5 orbital forcings are well-understood with warming driven by high Northern Hemispheric summer insolation and virtually no CO_2 forcing (e.g., Berger, 1989; Loutre & Berger, 2003; Stone et al., 2016). Thus, MIS 5 cannot be considered a direct analog for future climate due to a lack of greenhouse gas forcing. However, investigations of MIS 5 may still shed light on *processes* (Chadwick et al., 2022) such as ice sheet behavior, albedo feedbacks, and ocean circulation.

To investigate MIS 5 further, several sedimentary deposits along the Atlantic Coastal Plain have been sectioned and dated to the MIS 5 substages (see Table 5.1 for ages and references therein). In some places, absolute dating via U-Th dating of corals was possible. These age estimates were sometimes supplemented with optically stimulated luminescence (OSL) or electron spin resonance (ESR). However, many deposits cannot be dated with absolute dating techniques due to the lack of appropriate coral samples. Instead, there have been extensive efforts to correlate these deposits via a relative dating technique known as amino acid racemization (AAR) dating of mollusk shells (e.g., Wehmiller et al., 2021). AAR relates the abundances of the L- and D-enantiomer configurations of amino acids in a fossil organism to its age. When an organism dies, the L-enantiomers of the amino acids begin to racemize into their

respective D-enantiomers, with older fossils thus producing higher "D/L" amino acid ratios. Given that D/L decay rates are also temperature-dependent (e.g., Miller et al., 2013; Wehmiller, 2013) and temperatures vary with latitude along the Atlantic Coastal Plain, D/L values vary with latitude for a single substage. Previous studies (e.g., Wehmiller, 2013) have thus demonstrated that latitudinal age gradients of AAR values, anchored to U-Th dates where available, can be used to assign relative dates to new sites within this region.

Mollusk shells in these deposits can also serve as a useful archive for paleoclimate and paleoceanographic information. For instance, oxygen isotope ($\delta^{18}O$) sclerochronology measurements (i.e., sequential sampling along the shell's growth axis) have previously been used to reconstruct seasonal-scale temperature variability from the Plio-Pleistocene in the North Atlantic (e.g., Winkelstern et al., 2013; Johnson et al., 2022; Braniecki et al., 2024; Johnson et al., 2024; Braniecki et al., 2025). However, $\delta^{18}O$-based temperature calculations rely on estimates of the isotopic composition of seawater in the past ($\delta^{18}O_w$), which are not well-constrained. Global average $\delta^{18}O_w$ varies from -1‰ for an ice-free world (e.g., Shackleton, 1986) to +1‰ for climate states with significant ice sheet extent such as the Last Glacial Maximum (e.g., Schrag et al., 1996; Waelbroeck et al., 2002; Adkins et al., 2002; Clark et al., 2025). Yet ice volume, and thus $\delta^{18}O_w$, likely fluctuated between and within substages of MIS 5, producing uncertainties in assumed past $\delta^{18}O_w$ estimates from this time. Further, assumptions about regional variations in $\delta^{18}O_w$ in the modern (e.g., continental runoff of low $\delta^{18}O_w$ waters – Gomes et al., in prep) do not necessarily apply to the geologic past, adding uncertainties in assumed $\delta^{18}O_w$.

Along the Atlantic Coastal Plain, there are a few published datasets that have reported modern instrumental $\delta^{18}O_w$ measurements for reference (Khim and Krantz, 1996; Schmidt et al.,

1999; Zhang and Petersen, 2023; Zhang et al., 2024). Collectively, these studies showcase a latitudinal $\delta^{18}O_w$ gradient along the Eastern Seaboard and a sharp, distinct boundary at the Cape Hatteras, North Carolina region. The SeaSOx dataset (Quizon et al., in prep) captured this sharp boundary and latitudinal gradient in more detail and demonstrated a correlation with the regional salinity gradient. Altogether, these studies highlight the clear distinction between a fresher, isotopically depleted northern water mass (i.e., Labrador Current) and a more saline, isotopically enriched southern water mass (i.e., Gulf Stream). The position of these water masses could have shifted through time during the Plio-Pleistocene (e.g., Johnson et al., 2017), adding to the uncertainty in past $\delta^{18}O_w$ especially in mid-coastal regions close to the modern-day $\delta^{18}O_w$ boundary. Furthermore, $\delta^{18}O_w$ has been shown to vary on local scales, especially in coastal regions along the U.S. Eastern Seaboard with freshwater influences (e.g., Gomes et al., in review). Fossil *Mercenaria* sp. often used for $\delta^{18}O$-paleotemperature reconstructions live in coastal environments, adding to uncertainties in assumed $\delta^{18}O$ values.

'Clumped' isotope (Δ_{47}) paleothermometry can be applied to circumvent these uncertainties in $\delta^{18}O_w$. Δ_{47} thermometry (e.g., Ghosh et al., 2006; Schauble et al., 2006; Eiler, 2007) relates the abundance of 'clumped' isotope bonds (i.e., ^{18}O-^{13}C) in a carbonate to its formation temperature. Δ_{47} is independent of $\delta^{18}O_w$ variability, and combination of Δ_{47} with $\delta^{18}O_{carb}$ measurements enables the calculation of reconstructed $\delta^{18}O_w$ values ($\delta^{18}O_{rsw}$) in addition to more accurate paleotemperatures. Several studies have applied Δ_{47} paleothermometry on various bivalve mollusks to reconstruct temperatures and $\delta^{18}O_w$ values in the modern (e.g. Henkes et al., 2013; Caldarescu et al., 2021; Huyghe et al., 2022; Schlidt et al., 2025) and from past periods such as the Cretaceous (e.g., deWinter et al., 2021; Jones et al., 2022; O'Hora et al., 2022; Curley et al., 2025; Hoffman et al., 2025; deWinter et al., 2025), the Eocene (e.g., Kniest

et al., 2024; Schlidt et al., 2025), and the Pleistocene (e.g,. Winkelstern et al., 2017; Zhang et al., 2021; Minnebo et al., 2024; Winkelstern et al., 2025). Thus, Δ_{47} thermometry is a particularly useful tool for paleotemperature (and paleo-$\delta^{18}O_w$) reconstructions in times and places where past $\delta^{18}O_w$ remains uncertain – such as the MIS 5 interglacial.

Although several studies have reported MIS 5e proxy paleotemperatures from the North Atlantic (e.g., Cortijo et al., 1999; Chapman et al., 2000; Oppo et al., 2006; Irvali et al., 2012; Bashirova et al., 2014; Martrat et al. 2014; Irvali et al., 2016; Winkelstern et al., 2017; Turney et al., 2020; Zhang et al., 2021; Minnebo et al., 2024; Winkelstern et al., 2025), nearly all of these estimates come from open-ocean sites, and MIS 5e data are lacking from coastal regions along the Eastern Seaboard. Furthermore, MIS 5a paleotemperature data from the North Atlantic are even more scarce (Martrat et al., 2007; Bahr et al., 2013) and nonexistent from the Atlantic Coastal Plain. Additional paleotemperature estimates, especially along the Eastern Seaboard, would help refine our understanding of Last Interglacial climatic and oceanography in this region.

In this study, we present Δ_{47}-derived paleotemperature and paleo-$\delta^{18}O_w$ estimates from MIS 5e and MIS 5a-dated mollusk fossils collected from several sites along the Atlantic Coastal Plain. These measurements improve regional temperature estimates for MIS 5e – a potential 'analog' for future climatic and oceanographic processes – and fill in the vast data gaps for the relatively understudied MIS 5a substage. We also compare our paleo-$\delta^{18}O_w$ estimates to modern instrumental $\delta^{18}O_w$ data in the region and discuss the potential of using paleo-$\delta^{18}O_w$ to detect a possible change in the positions of the Labrador Current and the Gulf Stream.

5.3 Study Sites & Stratigraphy

Several deposits along the Atlantic Coastal Plain have been dated to either MIS 5e or MIS 5a (Table 5.1). However, site-to-site correlation with non-geochronological methods (e.g., sedimentology, biostratigraphy) is nearly impossible due to a lack of lateral continuity and variability in coastal paleoenvironments, with many deposits now located in commercial quarries. These sediments were deposited along a paleo-coastline within variable hydrological paleoenvironments (e.g., embayments, tidal flats, barrier islands) similar to modern. Previous studies have provided an assortment of absolute age estimates from U-Th coral dating, OSL, and ESR for numerous sites. AAR geochronology, anchored with absolute age estimates from these studies, estimate relative ages for sites *without* well-constrained age estimates. New AAR data are reported in this study to complement these efforts. The following sections consist of site descriptions (including UDAMS site number, as reported in the University of Delaware AAR Database; Wehmiller & Pellerito, 2015) and specific details about previous geochronology efforts at each site from which mollusk fossils were obtained and analyzed.

5.3.1 Gomez Pit, Virginia (GPVA) – UDAMS 06076

The Gomez Pit (36.78°N, 76.20°W) is located in southeastern Virginia, with an outcrop elevation range of -2m to 8m above sea level (Wehmiller et al., 2004). The Gomez Pit consists of the following units as previously described in Mirecki et al. (1995) and Lamothe et al. (1998), from bottom to top: (1) a unit of paludal (marshy) silt; (2) a laterally extensive oyster (*Crassostrea*) reef; (3) a fossiliferous layer of estuarine / inner shelf sand and salt; (4) a laterally continuous serpulid bed; and (5) a layer of barrier island sand. Coral samples were found in the serpulid bed and measured for U-Th geochronology, with three samples collectively producing ages of ~63-84 ka (Szabo, 1985). Mollusk samples for AAR and ESR analyses were collected

from the oyster reef and fossiliferous sand units. AAR data were used to define three aminozones (Wehmiller et al., 1988), with "Aminozone IIa" roughly spanning the fossiliferous sand layer. ESR data for the Aminozone IIa fossils (Skinner, 1989) produce age estimates from 93 to 125 ka, which is insufficient to constrain the age of these fossils to MIS 5a or MIS 5e (or 5c). AAR data from Aminozone II fossil reported in Mirecki et al. (1995) also suggest a broad age estimate of 80 to 130 ka (i.e., MIS 5). But with constraints from U-Th geochronology (including newer U-Th coral measurements reported in Wehmiller et al., 2004), these data altogether suggest an approximate MIS 5a age estimate for the Aminozone IIa fossils at Gomez Pit, as further supported by *Mulinia* AAR data reported in Wehmiller et al. (2021). Samples measured for isotopes in this study were collected in 1989 from the fossiliferous Aminozone IIa unit, with new AAR data in this study corroborating the previous MIS 5a age assignment for these fossils. Note that the samples analyzed for AAR in this study (1989/1995 series) are different than the *Mercenaria* samples measured in Mirecki et al. (1995) (1983/1987 series) and were measured using updated AAR cleaning, purification, and analysis procedures (e.g., Wehmiller et al., 2021).

5.3.2 Moyock Pit, North Carolina (MPNC) – UDAMS 07800, 07000

The Moyock Pit (36.51°N, 76.15°W) is located by the boundary between modern-day Virginia and North Carolina, with an outcrop elevation range of 0 to 4m (Parham et al., 2013) at UDAMS 07800. No stratigraphic descriptions have been previously published for this site, though the outcrops are known to contain an abundance of *Mercenaria* fossils. U-Th coral dates of ~MIS 5a have been collected for this outcrop at UDAMS 07000 (Cronin et al. 1981; Szabo, 1985) and UDAMS 07800 (Wehmiller et al., 1998; Wehmiller et al., 2004), though coral samples were collected from the spoil piles. More recent unpublished U-Th data from a coral attached to a *Mercenaria* obtained from the fossiliferous units at UDAMS 07000 (L. Edwards,

pers. comm.) suggest an age estimate of 75 to 65 ka (i.e., younger MIS 5a). Therefore, it is strongly believed that the fossiliferous layers at Moyock Pit are MIS 5a in age. Samples measured for isotopes in this study were collected from the fossiliferous units between 1983 and 1992, with new AAR data in this study corroborating the MIS 5a age assignment for these fossils.

5.3.3 Forbes Pit, North Carolina (FPNC) – UDAMS 07730, 07731

The Forbes Pit (36.32°N, 76.02°W) is also located in northeastern North Carolina. This site has been previously described in Parham et al. (2013), with an age estimate of ~60-43 ka (i.e., MIS 3) for the uppermost quartz sand layer at the outcrop, though this study does not provide a stratigraphic description for the older (i.e., MIS 5) fossiliferous units. Unpublished OSL results suggest the presence of two aminozones below the supposed MIS 3 layer – one consisting of MIS 5e fossils (-142 series) overlain by another consisting of MIS 5a fossils (-141 series) (pers. comm. from D. Mallinson to J. Wehmiller, Jan. 2026). Samples measured for isotopes in this study were collected in 2004 from UDAMS sites 07730 (upper layer) and 07731 (lower layer), with new AAR in this study corroborating MIS 5a and MIS 5e age assignments for the upper (-141) and lower (-142) layer fossils respectively.

5.3.4 East Lake Pit, North Carolina (ELPNC) – UDAMS 07556

The East Lake Pit (35.89°N, 75.96°W) is located in northeastern North Carolina, with an outcrop elevation range of -10m to 0m above sea level (Parham et al., 2013). The fossiliferous portion was previously characterized by P. Parham and K. Burdette and is found in the lower 3m of the outcrop. This section consists of the following layers with colloquial names indicated in parentheses, from bottom to top: (1) a *Mulinia*-dominated grey muddy sand (‘167’); (2) a *Mercenaria*-dominated lagoonal bed characterized by undulatory topography (‘166’); (3) another

Mulinia-dominated grey muddy sand layer (‘165’); (4) a dark-grey winnowed oyster bed with a muddy sand matrix (‘164’); (5) another *Mercenaria*-dominated lagoonal bed with a grey muddy sand matrix, overlain by a blue-grey sandy mud (‘163’); (6) mud clasts overlain by a light-grey sand with trace amount of shells, including *Ensis* sp. (‘162’); (7) a *Mulinia*-dominated light-grey sand overlain by another *Mercenaria*-dominated lagoonal bed (‘161’); (8) another section of a *Mulinia*-dominated sand overlain by a *Mercenaria*-dominated bed (‘160’). Sections 161-167 fit within the section ELP-01 as defined in Parham et al. (2013), which was measured to have a mean age of ~100 ka from OSL geochronology. AAR data suggest that fossils from the 161-163 series, obtained from the Mu2/Mu2+ aminozones, are roughly MIS 5a in age as supported by coral U-Th age estimates of ~84-78 ka (Wehmiller et al., 2021) and OSL results (Parham et al., 2013). Samples measured for isotopes in this study were collected in 2008 from the 161 (MIS 5a) and 164 (unknown) layers, with new AAR in this study suggesting MIS 5a and MIS 5e age assignments for the 161 and 164 series fossils respectively.

5.3.5 RP3 Site (ICWSC) – UDAMS 08306

The RP3 site (33.81°N, 78.73°W) is located on the Intracoastal Waterway in South Carolina, with an approximate outcrop elevation range of 2.5m above sea level as reported in the University of Delaware AAR Database (Wehmiller & Pellerito, 2015). The outcrop at this site consists of an oyster hummock (“RP3-Low”) overlain by two fossiliferous layers abundant in *Mercenaria* (“RP3-Mid”, “RP3-Top”). AAR and U-Th data from various Intracoastal Waterway sites and nearby sites in South Carolina have been reported in previous studies (McCartan et al., 1982; Wehmiller et al., 1988; Hollin & Hearty, 1990; Wehmiller et al., 2013), though these studies revealed large ambiguities in the age estimates as these estimates disagreed. At the RP3 site specifically, a closed-system U-Th date of ~126 ka has been reported from a coral collected

near the base of the outcrop, suggesting that at least the base of the deposits is MIS 5e in age (Poirier, pers. comm.). Samples measured for isotopes in this study from the oyster hummock and two *Mercenaria*-rich layers were collected in 2021, with new AAR data in this study corroborating a MIS 5e age assignment for these fossils.

5.3.6 Berkeley Pit, SC (BPSC) – UDAMS 08136

The Berkeley Pit (32.86°N, 79.78°W) is located in southeastern South Carolina, with an outcrop elevation range of 1m below to 6m above sea level (Wehmiller et al., 2004). The fossiliferous outcrops at Berkeley Pit and nearby sites in South Carolina do not exhibit obvious lateral continuity. These deposits generally consist of sand, clay, silt, and gravel textures (Cronin et al., 1981); only one fossiliferous section is described, which falls within the late Wando Formation. Several studies have reported coral U-Th geochronology data from proximal deposits (Venning, SC; Mount Pleasant, SC), producing absolute age estimates between ~90 and 120 ka for this region (Cronin et al., 1981; McCartan et al., 1982; Mixon et al., 1982; Szabo, 1985). However, Wehmiller et al. (2004) raised concerns about contamination issues by detrital minerals for these samples (i.e., improper cleaning prior to analysis) and reported more recent U-Th age estimates of ~80-84 ka (MIS 5a) for three *Septastrea* coral samples from Berkeley Pit. Samples measured for isotopes in this study from the single fossiliferous section in 1992, with new AAR data in this study corroborating a MIS 5a age assignment for these fossils.

5.3.7 Jones Pit, Georgia (JPGA) – UDAMS 09007

The Jones Pit (31.92°N, 81.07°W) was located on the coastline near the boundary between modern-day South Carolina and Georgia, with an outcrop elevation range of -1m to 4m above sea level (Wehmiller et al., 2004). This site was a private excavation that is now flooded. The fossils and deposits at Jones Pit were originally described in Hulbert & Pratt (1998) and

consist of the following, from bottom to top: (1) dark brown peat or greenish-gray clay; (2) a quartz sand grain layer containing mollusk shells and fragments, in addition to other invertebrates (i.e., barnacles, bryozoans, echinoids, coral, serpulid worm tubes); (3) and an un-fossiliferous, micaceous quartz sand layer. Wehmiller et al. (2004) reported age estimates of ~85-82 ka based on U-Th geochronology from five *Septastrea* corals from the fossiliferous layer, and thus this layer is assigned an MIS 5a age. It is possible that these corals came from the spoil piles, though a newer U-Th result on a coral from the fossiliferous units (pers. comm. from W. Thompson to J. Wehmiller, July 2012) confirms these published results. Samples measured for isotopes in this study were collected from the fossiliferous layer between 1995 and 2000 and are thought to be MIS 5a in age based on the aforementioned U-Th age estimates.

5.3.8 WCQ Site (WCQFL) – UDAMS 10185

The WCQ site (29.88°N, 81.35°W) is located on the Atlantic-facing coast of Florida in St. Augustine. The fossiliferous deposits at this outcrop fall within the upper part of the Anastasia Formation (Sellards, 1912) in Florida. U-Th dating of fossils from the Cape Kennedy area indicate a principal depositional episode around ~110 ka (Osmond et al., 1970), which aligns with the OSL age estimates of ~125-107 ka from nearby sites Wilson Coquina Quarry, Dalboro Road, and Haulover Canal reported in Burdette et al. (2009). Collectively, these data suggest a roughly MIS 5e (going into MIS 5c) age assignment for these deposits. The sample measured for isotopes in this study was collected from the fossiliferous layers in 2009 (fossil collection layer unknown), with new AAR data in this study corroborating a MIS 5e age assignment for these fossils.

5.3.9 Daytona Beach Site (DBPFL) – UDAMS 10100

The Daytona Beach site (29.16°N, 81.02°W) is located on the Atlantic-facing coast of Florida on the western end of South Daytona, with an outcrop elevation range of -2m to 2m above sea level (Wehmiller, pers. comm.). The outcrop at this site consists of the following sections, from bottom to top: (1) a sandy shell layer; (2) an overlying quartz sand layer; (3) a "bone bed" containing humate, highly organic sand with mastodon and giant ground sloth fossil bones; (4) another quartz sand layer dominated by *Mercenaria*; (5) another quartz sand layer with many fragmented shells. An unpublished U-Th date of ~118 ka from a coral obtained from these deposits (fossil collection layer unknown) suggests that these deposits are roughly MIS 5e in age (pers. comm. from W. Thompson to J. Wehmiller, July 2012). The samples measured for isotopes in this study were collected between 1999 and 2010 (fossil collection layer unknown), with new AAR data in this study corroborating a MIS 5e age assignment for these fossils.

5.4 Methods

5.4.1 Screening for preservation (Raman spectroscopy)

Raman spectra from the outer layers of most *Mercenaria* samples were collected to assess mineralogy and thus preservation (see Fig. S5.1). Spectra from all shells indicate the preservation of original aragonite with no evidence of diagenetic alterations from recrystallization or secondary calcite precipitation. Thus, isotopic signatures measured in these shells almost certainly preserve information about original environmental conditions without alterations. All analyses were done on the Raman microprobe in the Microbe-Mineral Lab at the University of Michigan.

5.4.2 Amino Acid Racemization (AAR)

AAR is a geochronological method which relates the abundances of the L- and D-enantiomer forms of an amino acid in an organism to that organism's age (e.g., Wehmiller et al., 2021). Shells from 8 of 9 sites in this study were sampled for AAR measurements (Table 5.2). A diamond wheel Dremel was used to extract >50mg fragments from one half of each shell. These samples were measured at Northern Arizona University's Amino Acid Geochronology Lab. Samples were mechanically cleaned and chemically cleaned with dilute HCl to remove at least 20% of shell carbonate. Cleaning was followed by dissolution, hydrolysis, and instrumental analysis, with samples measured for D/L ratios of eight amino acids on an Agilent series 1100/1200 reverse phase chromatograph or a gas chromatograph (for the WCQFL and DBPFL samples). Previous studies (e.g., Wehmiller et al., 2021) recommend using D/L ratios of glutamic acid (Glu) and aspartic acid (Asp) for age interpretation due to their high abundances in mollusk shells.

5.4.3 Isotopic Measurements ($\delta^{18}O$, Δ_{47}, $\delta^{18}O_{sw}$)

Various isotopic measurements were collected from samples to reconstruct paleotemperatures and paleo-$\delta^{18}O_{rsw}$ values (Table 5.2), consisting of: (1) bulk Δ_{47} measurements; (2) Δ_{47} sclerochronology; and (3) $\delta^{18}O$ (and $\delta^{13}C$) sclerochronology measurements (see Appendices for details).

Bulk Δ_{47} measurements from each shell (n=3 or more replicates) capture several years of mean annual temperature (MAT) across each shell's lifespan and were collected by using a dental drill on low speed to extract >3mg of powder ~1cm deep from the outer layer of each shell, typically on the ventral margin. Δ_{47} measurements were collected on a NuCarb sample preparation device attached to a NuPerspective mass spectrometer in the University of Michigan

Stable Isotope Lab. Δ_{47}-temperatures for all bulk samples were calculated via the calibration equation from Anderson et al. (2021); bulk Δ_{47}-derived $\delta^{18}O_w$ values were calculated via the aragonite-water fractionation from Kim et al. (2007).

Δ_{47} sclerochronology measurements were collected for 1 shell per site, excluding the MIS 5a unit at ELPNC. Sequential powders were collected every 2.5-5mm along the surface of each shell's growth axis using a low-speed dental drill with care taken not to penetrate to interior layers, with powder weights of >3mg. Because Δ_{47} sclerochronology powders were measured as single replicates on the NuPerspective, 3-point averaging was applied to smooth these profiles. Seasonal-scale temperatures were calculated via the calibration equation from Anderson et al. (2021); seasonal-scale Δ_{47}-derived $\delta^{18}O_w$ values were calculated via the aragonite-water fractionation from Kim et al. (2007) for each sample.

$\delta^{18}O$ sclerochronology measurements were collected for 1 additional shell per site, excluding the MIS 5e units at FPNC, ELPNC, WCQFL, and DBPFL. As with Δ_{47} sclerochronology, sequential powders were collected every 2.5-5mm along the growth axis with smaller weights of >50ug. $\delta^{18}O$ (and $\delta^{13}C$) measurements were collected on a Kiel IV automated carbonate device attached to a Thermo-Finnegan MAT 253 dual-inlet mass spectrometer in the University of Michigan Stable Isotope Lab. Reconstructed $\delta^{18}O_w$ values from respective powders drilled for Δ_{47} were used to calculate $\delta^{18}O$-temperatures for shells measured for $\delta^{18}O$ sclerochronology.

To calculate unit averages at each site, bulk Δ_{47}-temperatures and $\delta^{18}O_w$ values were averaged with the mean Δ_{47}-temperature and $\delta^{18}O_w$ from Δ_{47} sclerochronology profiles (see Table 5.3).

5.4.4 Modern climatology and hydrology

Reconstructed isotopic temperatures and $\delta^{18}O_w$ values were compared to modern climatology and hydrology. Instrumental sea surface temperatures (SSTs) for each collection site were selected from the World Ocean Atlas (WOA) 2018 dataset (2005-2017 period, 1/4° resolution, monthly means) (Locarnini et al., 2019) for comparison. The seasonal range was calculated from winter (December, January, February – DJF) and summer temperature averages (June, July, August – JJA). Modern $\delta^{18}O_w$ values were obtained from the SeaSOx dataset (Quizon et al., in prep).

5.5 Results

5.5.1 AAR data

D/L ratios for aspartic acid and glutamic acid from *Mercenaria* sp. in this study fall within the ranges of ~0.5-0.8 and ~0.2-0.5, respectively, and AAR data confirm relative stratigraphy within each collection site (Fig. 5.2). For sites with multiple layers – i.e., ELPNC, FPNC – supposed older samples (MIS 5e) produced higher values than supposed younger samples (MIS 5a), which aligns with observed stratigraphic positions. Overall, most samples appear to fall within the MIS 5e or MIS 5a latitudinal "gradients" extrapolated from these data and AAR data from previous studies (Mirecki et al., 1995; Wehmiller et al., 2021; Winkelstern et al., 2025; SSMA – Quizon et al., in prep). Exceptions include D/L values for both amino acids from the -161 series fossils at ELPNC (which appear low) and the glutamic D/L value for the top layer at ICWSC (which appears low). These values indicate that these units may have been deposited during a later stage of MIS 5e, as opposed to during peak warmth. For example, the individual layers at the RP3 site could have been deposited during different intervals between

MIS 5e and MIS 5a, as apparent MIS 5e/5c/5a-aged units along the Intracoastal Waterway were deposited at the nearly the same elevation (Dean et al., 2026).

5.5.2 Isotopic temperature and $\delta^{18}O_{rsw}$ data

Reconstructed isotopic temperatures and $\delta^{18}O_w$ values for apparent MIS5e-dated fossil mollusks fall within the ranges of ~10-35°C and ~-2‰ to 4‰, respectively (Fig. 5.3). MIS 5e temperatures from FPNC and EPLNC (~36°N) are generally in alignment (~10-25°C), though reconstructed $\delta^{18}O_w$ values at ELPNC are overall enriched relative to values from FPNC by ~1‰. The ICWSC site (~34°N) exhibits the most variability, with temperatures spanning the full range of ~10-35°C and $\delta^{18}O_w$ values spanning ~-2‰ to ~3‰ and unit-average temperature and $\delta^{18}O_w$ values of 22.2°C +/- 1.2°C and 0.9‰ +/- 0.4‰, respectively. Specifically, temperatures and $\delta^{18}O_w$ values from the lowermost unit at ICWSC are generally higher than values from the middle and uppermost units at this site (Table 5.3), which could reflect separate depositional episodes and thus separate time intervals within MIS 5e. Reconstructed temperatures and $\delta^{18}O_w$ values from the Florida sites (WCQFL, DBPFL) fall on the lower end of the full range (~10-25°C; ~-2‰ to ~3‰) and below values from ICWSC on average.

Reconstructed isotopic temperatures and $\delta^{18}O_w$ values for apparent MIS5a-dated fossils fall within similar (albeit slightly lower) ranges of ~5-32°C and ~-4‰ to 2‰, respectively (Fig. 5.3). Values from nearby sites GPVA and MPNC (~37°N) are generally in agreement, with the observed temperatures and $\delta^{18}O_w$ values roughly spanning their full respective ranges. FPNC (~36°N) temperatures and $\delta^{18}O_w$ values fall on the lower ends of the respective cumulative ranges (~10-20°C; ~-3‰ to 0‰) Temperatures at ELPNC fall roughly align with the temperature range from these sites, although reconstructed $\delta^{18}O_w$ values are relatively enriched by 1‰ on average and produce a range of ~-1‰ to 2‰. BPSC and JPGA exhibit similar temperatures to

these other sites on average, though variability does not span the full range (~10-25°C). Reconstructed $\delta^{18}O_w$ values at BPSC and JPGA (~-2‰ to 2‰) align with values from ELPNC and are depleted relative to the values from the more northern MIS 5a sites.

Overall, these data support the application of Δ_{47} sclerochronology as a means of reconstructed seasonal-scale paleotemperatures and paleo-$\delta^{18}O_w$ values, as used and validated in previous studies (e.g., Zhang & Petersen, 2023). For nearly all sites (excluding ICWSC), the range from bulk Δ_{47}-temperatures and $\delta^{18}O$-temperatures generally aligns with the temperature range from Δ_{47} sclerochronology and bulk Δ_{47}-derived $\delta^{18}O_w$ values also generally align with $\delta^{18}O_w$ values from Δ_{47} sclerochronology. However, there are several sites at which bulk reconstructed temperatures and $\delta^{18}O_w$ values fall on the lower end of the range from Δ_{47} sclerochronology (Fig. 5.3). This result could be attributed to a seasonal bias from various factors including each organism's preferred growth season, growth rates, and how the shells were sampled (i.e., bias towards season of death), yet the growth biases would also impact Δ_{47} sclerochronology profiles (see Fig. S5.4). To mitigate these biases, bulk Δ_{47}-temperatures and $\delta^{18}O_w$ values were averaged with the mean Δ_{47}-temperature and $\delta^{18}O_w$ from Δ_{47} sclerochronology profiles to obtain 'average' conditions for each unit in the following figures.

5.6 Discussion

5.6.1 MIS 5e paleoclimate

Globally, MIS 5e temperatures were thought to have been 0-2°C warmer than modern on average (e.g., Otto-Bliesner et al., 2013; Turney et al., 2020). However, the LIG climatic optimum may only have lasted 2-3ka (e.g., Oppo et al., 2006), and the proxy data suggest LIG warm anomalies in this region to varying extents. It is therefore likely that proxy data span several time intervals within the Last Interglacial and thus do not represent only peak warmth

during this interval. Previous studies support the occurrence of multiple depositional episodes within the Last Interglacial in the North Atlantic, as previously suggested for Bermuda (e.g., Winkelstern et al., 2017), the Turks and Caicos islands (e.g., Fouke & Kerans, 2024) and the Bahamas (e.g., Winkelstern et al., 2025).

To assess the possibility of multiple depositional episodes captured by the isotopic data in this study, Figure 5.4 visualizes MIS 5e-site average Δ_{47}-temperatures and reconstructed $\delta^{18}O_w$ values along the Atlantic Coastal Plain, along with previously reported MIS 5e in the North Atlantic from Nantucket, Massachusetts (Quizon et al., in prep) and the Bahamas (Winkelstern et al., 2025). The Δ_{47}-temperature data (Fig. 5.4A) show a latitudinal trend along the with respect to modern climatology: temperatures are warmer than modern at the northern sites (SSMA), similar to modern at the mid-latitude sites (FPNC, ELPNC, ICWSC), and cooler than modern at the most southern sites (WCQFL, DBPFL, BAHA). As previously suggested, this result could be attributed to the occurrence of multiple highstands within the MIS 5e interglacial, with peak Last Interglacial warmth reflected at the northern sites (i.e., 130-125 ka) and cooler, late Last Interglacial conditions reflected at the southern sites (i.e., <120 ka).

These separate depositional episodes would have likely been induced by differing responses at each site to the melting of the Laurentide Ice Sheet (LIS) and glacial isostatic adjustment (GIA) effects. SSMA was thought to be located at the terminal moraine of the LIS (e.g., Desor & Cabot, 1849; Verrill, 1875), making it a near-field site that would have experienced rapid isostatic uplift before peak ice sheet melt, relative sea level (RSL) rise, and thus a highstand early during the Last Interglacial. Meanwhile, the North and South Carolina sites were close to the LIS but still beyond the peripheral bulge, and the Florida and the Bahamas sites even further south (Muhs et al., 2020). It is thus possible that eustatic sea level rise first

produced a local highstand at the mid-latitude sites during a cooler interval within the Last Interglacial post-ice sheet retreat, then another local highstand at the southern sites during a later, even cooler interval (i.e., MIS 5e into MIS 5d).

The $\delta^{18}O_w$ data from these sites (Fig. 5.4B) support this GIA mechanism to explain multiple depositional episodes. MIS 5e $\delta^{18}O_w$ values at Massachusetts were depleted relative to modern due to a substantial influx of ice sheet melt, including from further north, while values are broadly centered around the global mean value of 0‰ at all other sites during their respective depositional episodes. Mid-latitude $\delta^{18}O_w$ values broadly align with modern instrumental, but low-latitude $\delta^{18}O_w$ values were isotopically depleted relative to modern as ice sheet meltwater pulses continued to contribute freshwater to the lower-latitude sites.

5.6.2 MIS 5a paleoclimate

Despite the general scarcity of MIS 5a paleotemperature estimates from proxy records, MIS 5a temperatures are thought to have been cooler than modern (e.g., Lisiecki & Raymo, 2005). This study presents the first reconstructed isotopic temperatures from the Atlantic Coastal Plain. Figure 5.5 visualizes MIS 5a site-average Δ_{47}-temperatures and reconstructed $\delta^{18}O_w$ values from *Mercenaria* sp. in this study, along with data from the supposed MIS 5a-dated Moon Rock Pond locality reported in Winkelstern et al. (2025). Most sites (except MPNC) produced temperatures similar to or cooler than modern instrumental by ~1-5°C, which is consistent with previous proxy records in the region (Martrat et al., 2007; Bahr et al., 2013). Reconstructed $\delta^{18}O_w$ values at most sites (excluding ELPNC and Moon Rock Pond) generally fall within the modern instrumental range and align with the latitudinal $\delta^{18}O_w$ trend along the East Coast observed in the SeaSOx dataset (Quizon et al., in prep), although the position of the abrupt $\delta^{18}O_w$ shift could be attributed to differences in ocean circulation during MIS 5a (see Section 5.6.3).

5.6.3 Mid-coastal MIS 5e vs. MIS 5a comparison

Figure 5.6 shows MIS 5e and MIS 5a average Δ_{47}-temperatures and reconstructed $\delta^{18}O_w$ values from central Atlantic Coastal Plain sites (i.e., Virginia to South Carolina). The samples from FPNC exhibit the greatest amount of cooling by ~6°C on average, which supports the AAR-based interpretation of the lower and upper units as MIS 5e and MIS 5a in age, respectively (Fig. 5.2). Meanwhile, marginal temperature shifts are observed at ELPNC (slight warming by ~1°C) and between the South Carolina sites (slight cooling by ~1°C). None of these sites appear to produce substantial shifts in $\delta^{18}O_w$ between MIS 5e and MIS 5a, though values from the more southern sites (ELPNC, ICWSC, BPSC) are enriched relative to values from the northern sites (GPVA, MPNC, FPNC).

The cooling at FPNC between units aligns with the expected global cooling trend between MIS 5e and MIS 5a (Lisiecki & Raymo, 2005; Martrat et al., 2007; Bahr et al., 2013), though the magnitude of cooling (~6°C) is slightly greater than expected from long-term proxy records in the North Atlantic (~2-4°C). However, this cooling is not observed at nearby site ELPNC or between the South Carolina localities. Although the FPNC site is proximal to the ELPNC and ICWSC sites, this temperature difference could be due to depositional episodes at the ELPNC and ICWSC sites further south during a slightly later time during the MIS 5e interglacial. This interpretation for ELPNC is supported by the AAR data (Fig. 5.2), which show the ELPNC D/L values falling slightly below the MIS 5e latitudinal gradient, indicative of deposition during a later stage of MIS 5e.

The most notable trend observed from the mid-coastal data is the distinction between the relatively depleted $\delta^{18}O_w$ signatures from the northern sites and the relatively enriched $\delta^{18}O_w$ signatures from the southern sites (Fig. 5.6B). Taking into account 95% confidence intervals,

$\delta^{18}O_w$ values from the more northerly sites fall as low as -2‰ to -3‰ while $\delta^{18}O_w$ values from the southern sites reach as high as +2‰ to +3‰. This trend aligns with the observed distinction between the apparent Labrador Current and Gulf Stream $\delta^{18}O_w$ signatures, with respective $\delta^{18}O_w$ ranges of roughly -2 to 0‰ and 0 to 2‰. However, the sharp $\delta^{18}O_w$ transition occurs at Cape Hatteras in the modern (~35°N) (Quizon et al., in prep) but appears to have occurred at a more northerly position between FPNC and ELPNC (~36°N) during MIS 5a and potentially MIS 5e (Fig. 5.6B).

This position of the $\delta^{18}O_w$ transition zone could be attributed to a more northerly shift in Gulf Stream influence due to differences in coastal morphology. This interpretation has been previously proposed by Johnson et al., (2017) for the Pliocene, during which sea level was several meters higher than modern, though this does coincide with the closure of the Central American Seaway which could have strengthened the Gulf Stream. However, a similar logic could be applied for MIS 5e, as GMSL was thought to be 6-9m higher than today (e.g., Dutton & Lambeck, 2012; Dumitru et al., 2023) and even MIS 5a if peak GMSL (Thompson et al., 2023) or RSL (e.g., South Carolina – Dean et al., 2026) did match estimates from MIS 5e. Although a greater influence of the Gulf Stream during MIS 5e has not been explicitly demonstrated, previous studies have reported broader incursions of warm, subtropical waters into subpolar regions of the North Atlantic during peak MIS 5e due to a weakening of the subpolar gyre (e.g., Steinsland et al., 2023; Zeng et al., 2025).

5.6.4 Paleo-$\delta^{18}O_w$ as a water mass tracer

There are several ongoing efforts to develop paleocirculation proxies, which include Pa/Th in sediments (e.g., Marchal et al., 2000), Nd isotopic composition in sediments (e.g., Jeandel et al., 2007), Cd/Ca paired with nutrient measurements (e.g., phosphorus) in foraminifera

(e.g., Boyle, 1988; Elderfield & Rickaby, 2000), $\delta^{13}C$ in foraminifera (e.g., Curry et al., 1988; Duplessy et al., 1988), and $\Delta^{14}C$ in sediments (e.g., Stocker & Wright, 1996; Matsumoto, 2007). Although the theoretical frameworks for these proxies are strong, many of them are indirect tracers of water mass movement (i.e., changes in nutrient and oxygen concentrations in various parts of the water column) and tend to record vertical transport (e.g., upwelling). There have also been numerous recent attempts to establish paleosalinity proxies such as B/Ga and excess B concentrations (Algeo et al., 2025).

Alternatively, as demonstrated $\delta^{18}O_w$ is more readily recorded in geologic archives than salinity. Previous studies have combined $\delta^{18}O_{carb}$-based paleothermometry with separate temperature proxy data (e.g., Mg/Ca in forams, Sr/Ca in corals) to reconstruct regional ocean circulation patterns with back-calculated paleo-$\delta^{18}O_w$ (e.g., Adkins et al., 2002; Zinke et al., 2022). These calculations are routinely done with Δ_{47} thermometry measurements (e.g., Meckler et al., 2022), and in this study we demonstrate the potential for Δ_{47}-derived paleo-$\delta^{18}O_w$ measurements to be used to track the position of coastal currents during MIS 5e and MIS 5a. It is worth noting that salinity and $\delta^{18}O_w$ are regionally correlated (e.g., Craig & Gordon, 1965), limiting the application of these measurements to interpretations of *regional* changes in ocean circulation. Regardless, this opens new possibilities in interpreting reconstructed Δ_{47}-derived $\delta^{18}O_w$ data, helping to unravel changes in past circulation patterns in addition to previous interpretations of hydrologic variability (i.e., riverine inputs, ice sheet melt, sea level rise).

5.7 Conclusions

In this study, we report new AAR data and isotopically reconstructed paleotemperatures and paleo-$\delta^{18}O_w$ values from nine sites along the Atlantic Coastal Plain. AAR data confirm the previously proposed MIS 5e or MIS 5a assignments for these deposits. MIS 5e temperatures are

similar to modern while MIS 5a temperatures are cooler than modern, which is consistent with global findings for these substages of MIS5. However, the large variability in MIS 5e temperatures reflects the likely occurrence of multiple depositional episodes within the MIS 5e interval at these outcrops, with temperatures spanning peak Last Interglacial warmth to end-Last Interglacial cooling. These temperature estimates can help not only assist with climate model simulations but also refine our understanding of the magnitude and timings of climate variability, ice sheet melt, and sea level rise – both local and global – along the U.S. East Coast during the Last Interglacial. Finally, MIS 5e and 5a paleo-$\delta^{18}O_w$ latitudinal trends broadly align with latitudinal trends from modern instrumental $\delta^{18}O_w$ data that track the Labrador and Gulf Stream boundary currents. These data highlight the potential of this tool as a regional water mass tracer, and we encourage further exploration of using Δ_{47}-derived paleo-$\delta^{18}O_w$ to track past water mass movement in other regions of the world.

5.8 Acknowledgments

We would like to acknowledge Ashling Neary and Justin VanDeVelde for their assistance with Δ_{47} measurements; Kacey Lohmann for $\delta^{18}O_{carb}$ measurements; Cecilie Phillips for her assistance with sclerochronology drilling; Darrell Kaufman, Jordon Bright, and the members of the Amino Acid Geochronology Lab at Northern Arizona University for their assistance with AAR data procurement; Kaitlin Koshurba and Leanne Rossi for their assistance with collecting Raman spectra; Lillian Minnebo, Gretchen Anderson, Lucas Gomes, and Jade Zhang for their assistance with sample collections at ICWSC; Roger Portell for his assistance with procuring sample collections from all other sites; and Will Doar and Rob Poirier for their assistance with geochronology and stratigraphy.

5.9 Appendices

5.9.1 Modern climatology and hydrology

Modern SSTs at each site were obtained from the World Ocean Atlas 2018 (WOA18) database (2005-2017 period, 1/4° resolution, monthly means) (Locarnini et al., 2019). Winter and summer temperatures were calculated as the mean of three months (DJF, JJA) and mean annual temperatures as the mean across all 12 monthly averages. Temperatures were averaged across closest grid cells to each collection site and across depths 0-20m to account for *Mercenaria*'s known depth range (Ansell, 1968). Modern instrumental $\delta^{18}O_w$ values for (nearby) each site were previously reported in the SeaSOx dataset (Quizon et al., in prep).

5.9.2 Isotopic sampling and data processing

Clumped isotope measurements were measured on a NuCarb automated sample preparation device connected to a Nu Perspective mass spectrometer in the University of Michigan Stable Isotope Lab. Full procedures for this setup can be found in O'Hora et al. (2022), Jones et al. (2022), and Quizon et al. (2025). 3-4 mg aliquots of sample powder were reacted with phosphoric acid in individual vials at 70°C to produce CO_2; this gas was purified for Δ_{47} analysis through two water traps and a Porapak-filled trap containing silver wool. Δ_{47} data were collected in 'bellows mode' at a major ion beam current of 80nA, consistently maintained for 80 sample-reference cycles by continuous bellows adjustment. The shot noise limit for Δ_{47} is 0.0074‰ under this instrumental setup.

Throughout the entire study interval, five in-house carbonate standards and four community carbonate standards were analyzed alongside samples. The in-house carbonate standards include our Carrara Marble (CM), Bahamian Ooids (OO), a fully-crushed *Arctica islandica* bivalve from Iceland (Ice), a synthetic carbonate (GU1), and a fully-crushed *Cittarium*

pica gastropod from Bermuda (Pica) as described previously (O'Hora et al., 2022). The community carbonate standards referenced are the ETH1-4 standards (Bernasconi et al., 2021). To adjust for drift in the I-CDES90 reference frame over time, we apply a window-specific fixed offset to all Δ_{47} data using two low temperature standards (Ice, OO), leaving our third low temperature standard (Pica) as a check standard. The long-term standard deviation in Δ_{47} from the check standard (Pica) over the measurement interval is 0.014‰, compared to the long-term standard deviation in Δ_{47} from all other standards of 0.021‰. Measured Δ_{47} values were calculated from raw voltages through an R-code script (RDevelopment CORE TEAM, 2008) using updated IUPAC parameters following Petersen et al. (2019).

Bulk Δ_{47} measurements from each shell (n=3 or more replicates) capture at least one year of mean annual temperature (MAT) across each shell's lifespan. Using a low-speed dental drill, we extracted >3mg of powder ~1cm deep from the outer layer of each shell, typically on the ventral margin. Because these powders were drilled from multiple layers (i.e., at least one year of growth), we suggest that they should be compared to mean annual temperature conditions. Δ_{47}-temperatures were calculated from the mean Δ_{47} value using the calibration equation from Anderson et al. (2021). Sample mean Δ_{47}-temperatures and $\delta^{18}O_{carb}$ values were used to reconstruct Δ_{47}-derived $\delta^{18}O_{sw}$ for each powder via aragonite-water fractionation from Kim et al. (2007).

~20-30 sequential >3mg powders were drilled per *Mercenaria* sp. shell. Powders were collected every 2.5-5mm along the surface of each shell's growth axis using a low-speed dental drill with care taken not to penetrate to interior layers. The same procedures described above to obtain bulk Δ_{47} measurements were used to obtain Δ_{47} sclerochronology measurements, convert to temperatures, and calculate $\delta^{18}O_{rsw}$ values. However, since each powder was measured as a

single replicate, 3-point averaging was applied to these Δ_{47} measurements to 'smooth' the sclerochronology profiles (Zhang & Petersen, 2023). For these samples, $\delta^{18}O$ and $\delta^{13}C$ sclerochronology measurements were collected along the way.

~50ug of powder was collected every 2.5-5mm along each shell's growth axis using a low-speed dental drill, again making sure not to penetrate interior layers. Sample powders only analyzed for $\delta^{18}O$ and $\delta^{13}C$ sclerochronology) were measured using a Kiel IV automated carbonate device attached to a Thermo-Finnegan MAT 253 dual inlet mass spectrometer at the University of Michigan Stable Isotope Lab. Data were standardized against the NBS-18 and NBS-19 standards, with units reported in per mille (‰) relative to the VPDB standard. Uncertainty was routinely better than 0.1‰ for both oxygen and carbon isotopes. Temperatures were calculated using the aragonite-water fractionation equation from Kim et al. (2007) using shell-averaged $\delta^{18}O_w$ from Δ_{47} sclerochronology (if measured) or bulk $\delta^{18}O_w$ (if not measured for Δ_{47} sclerochronology).

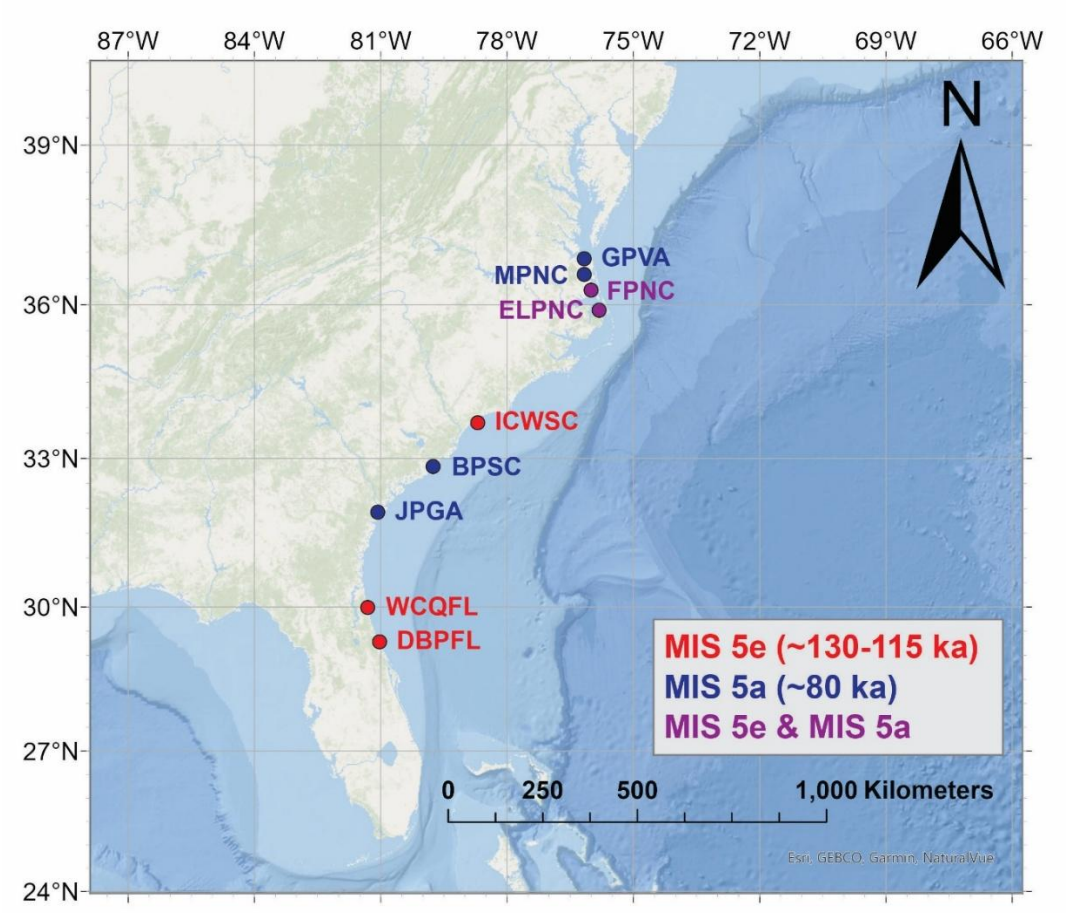

Figure 5.1. Map of localities from which fossil samples were obtained and analyzed, colored by apparent ages of deposits. Abbreviations for site names can be found in Table 5.1.

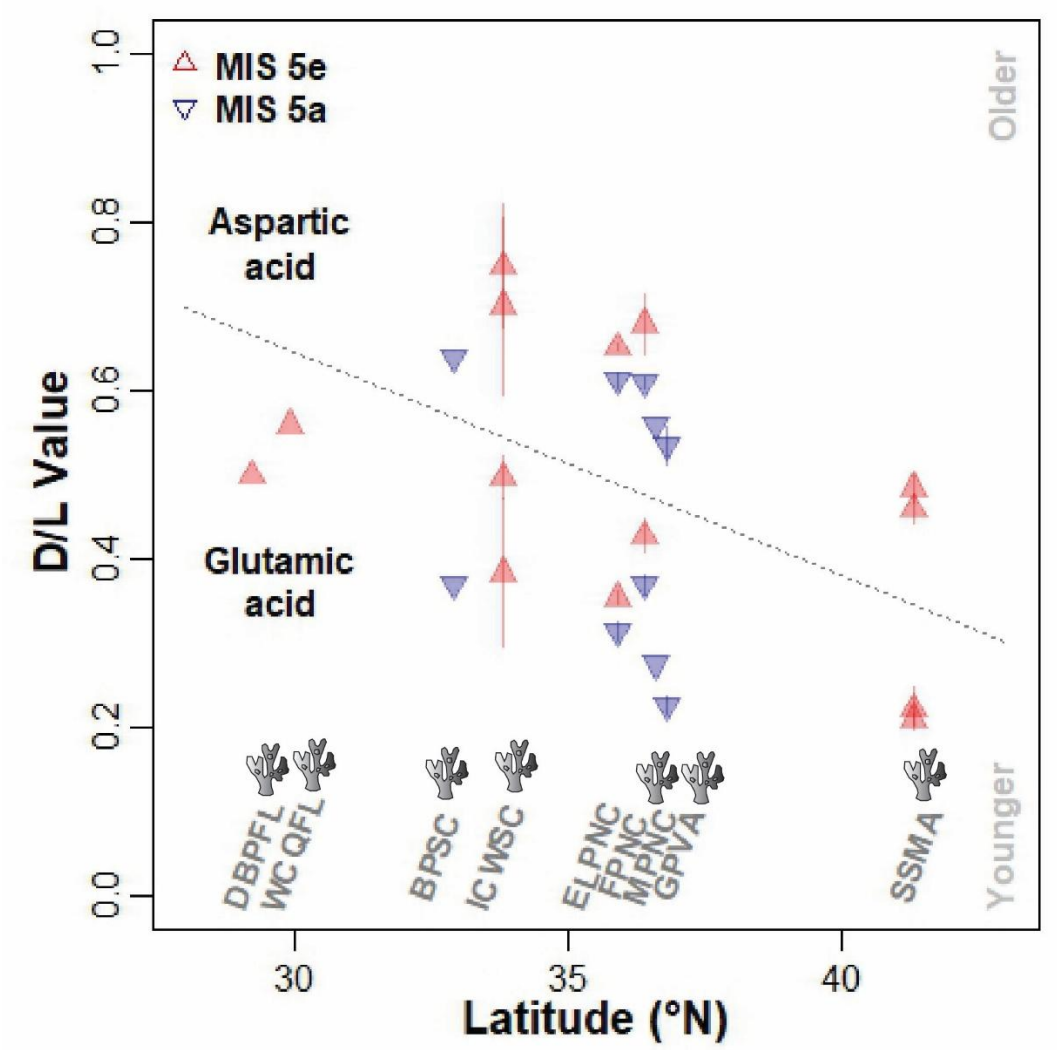

Figure 5.2. Layer-averaged AAR data for *Mercenaria* sp. analyzed in this study.

Points represent layer averages; error bars represent 95% confidence intervals. AAR data from sites Sankaty Sand, MA (SSMA) have been previously reported in Quizon et al., in prep. The values reported from ICWSC come from the middle and uppermost layers of the outcrop. The Glu values for the WCQFL and DBPFL samples come from gas chromatography as opposed to reverse-phase liquid chromatography. The coral symbology indicates sites anchored in absolute age estimates from U-Th geochronology.

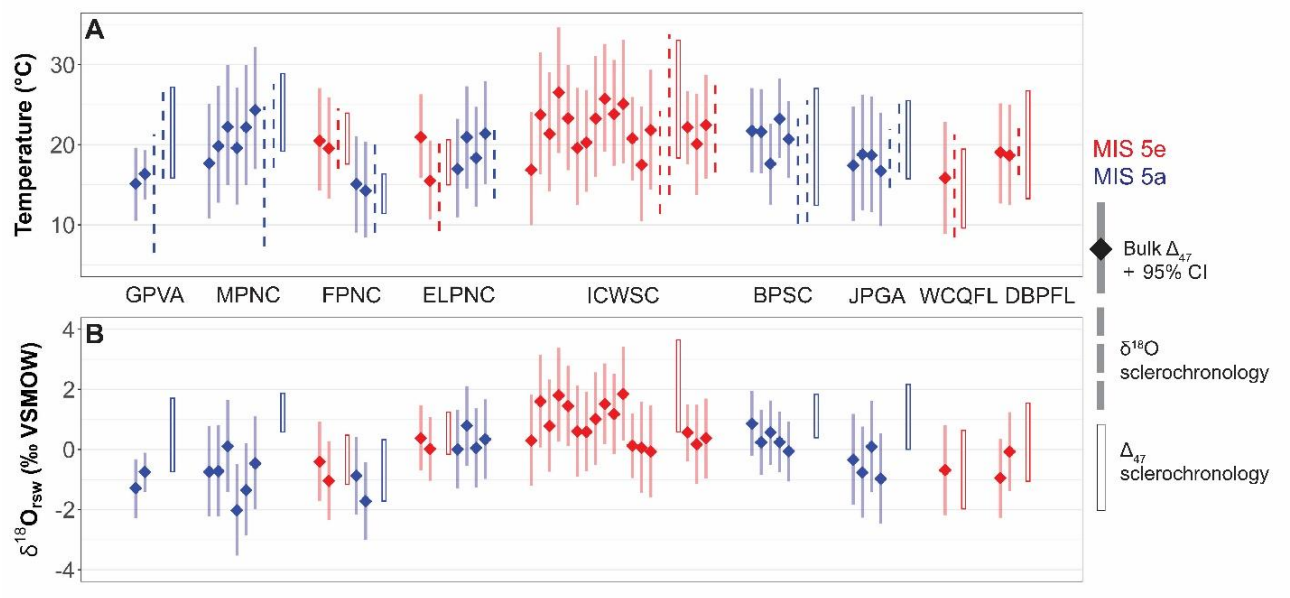

Figure 5.3. Reconstructed isotopic temperatures and $\delta^{18}O_w$ values for all samples analyzed in this study

See Table S5.3 for data summary.

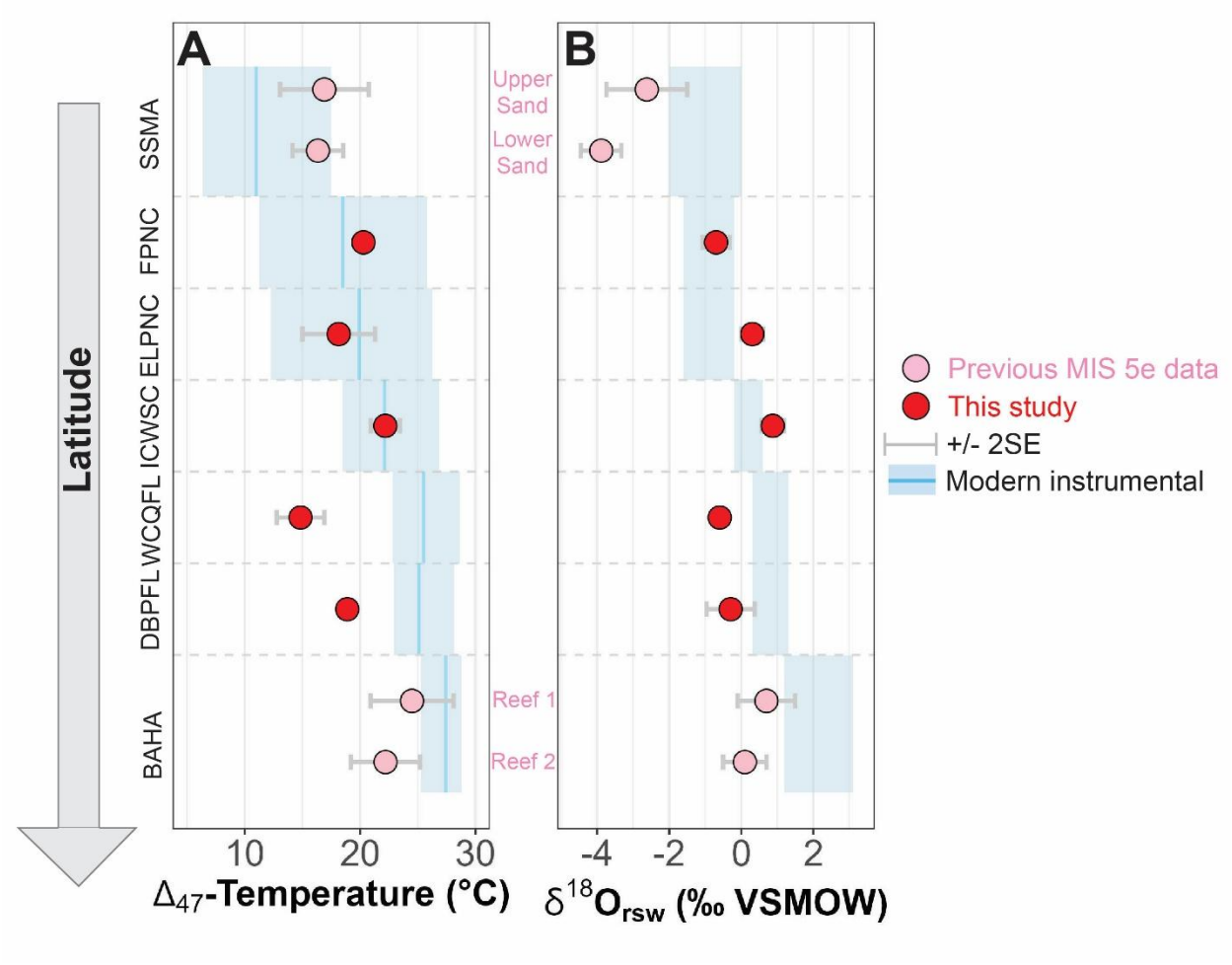

Figure 5.4. Reconstructed isotopic temperatures and $\delta^{18}O_w$ values for MIS5e-dated fossils in this study.

Average temperatures for each unit were calculated by taking the mean of (a) bulk Δ_{47}-temperatures, and (b) the mean temperature from Δ_{47} sclerochronology (if applicable). The grey error bars indicate +/- 2SE from averaging samples of each layer. Modern instrumental temperatures were obtained from the World Ocean Atlas database (Locarnini et al., 2019; see Methods); modern $\delta^{18}O_w$ values were obtained from the SeaSOx dataset (Quizon et al., in prep). Previous MIS 5e data from this figure have been reported in Quizon et al., in prep (Sankaty Sand, MA – 'SSMA') and Winkelstern et al., 2025 (Bahamas – 'BAHA').

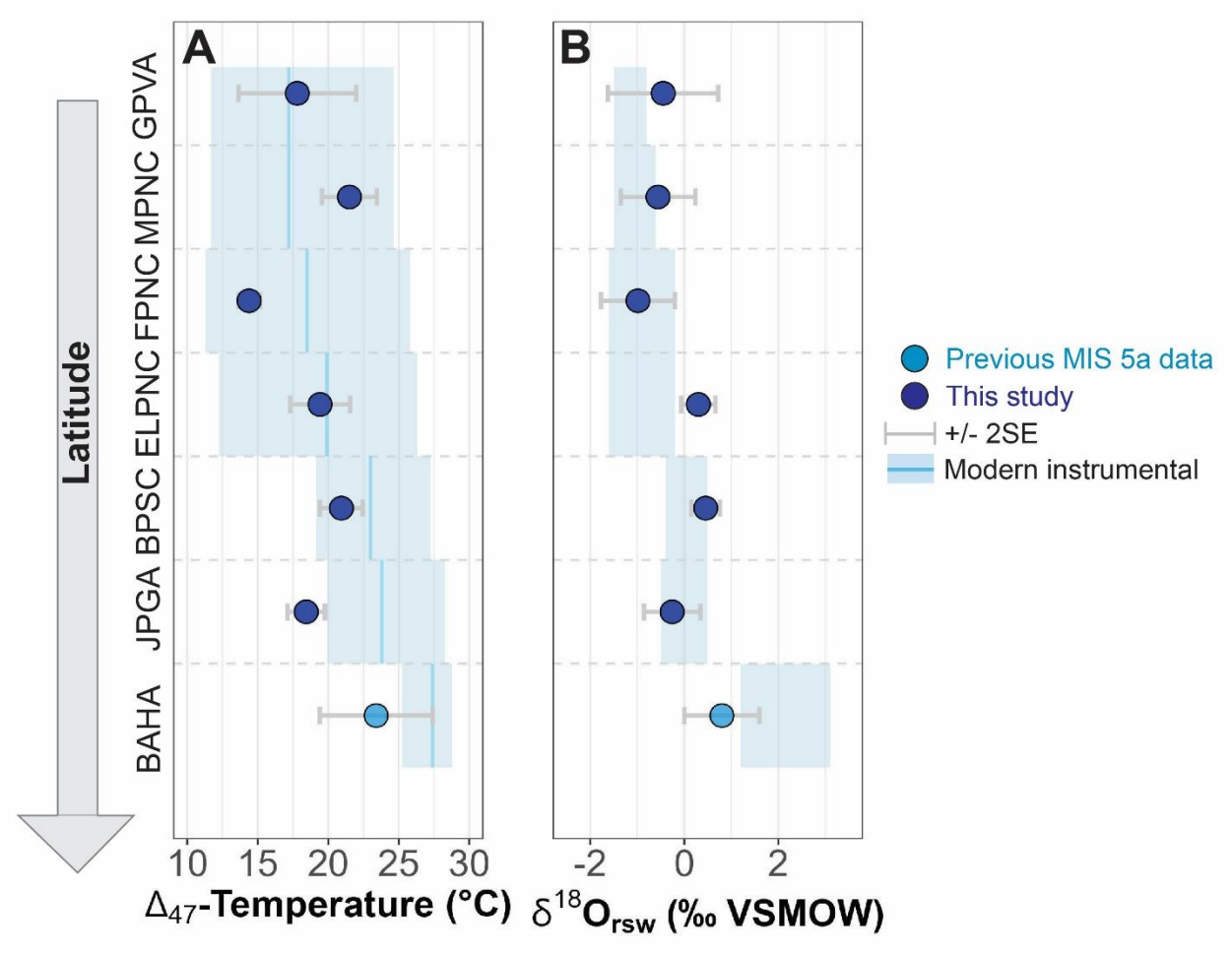

Figure 5.5. Reconstructed isotopic temperatures and $\delta^{18}O_w$ values for MIS5e-dated fossils in this study.

See Figure 5.4 for details about calculating unit average values and modern climatology/hydrology.

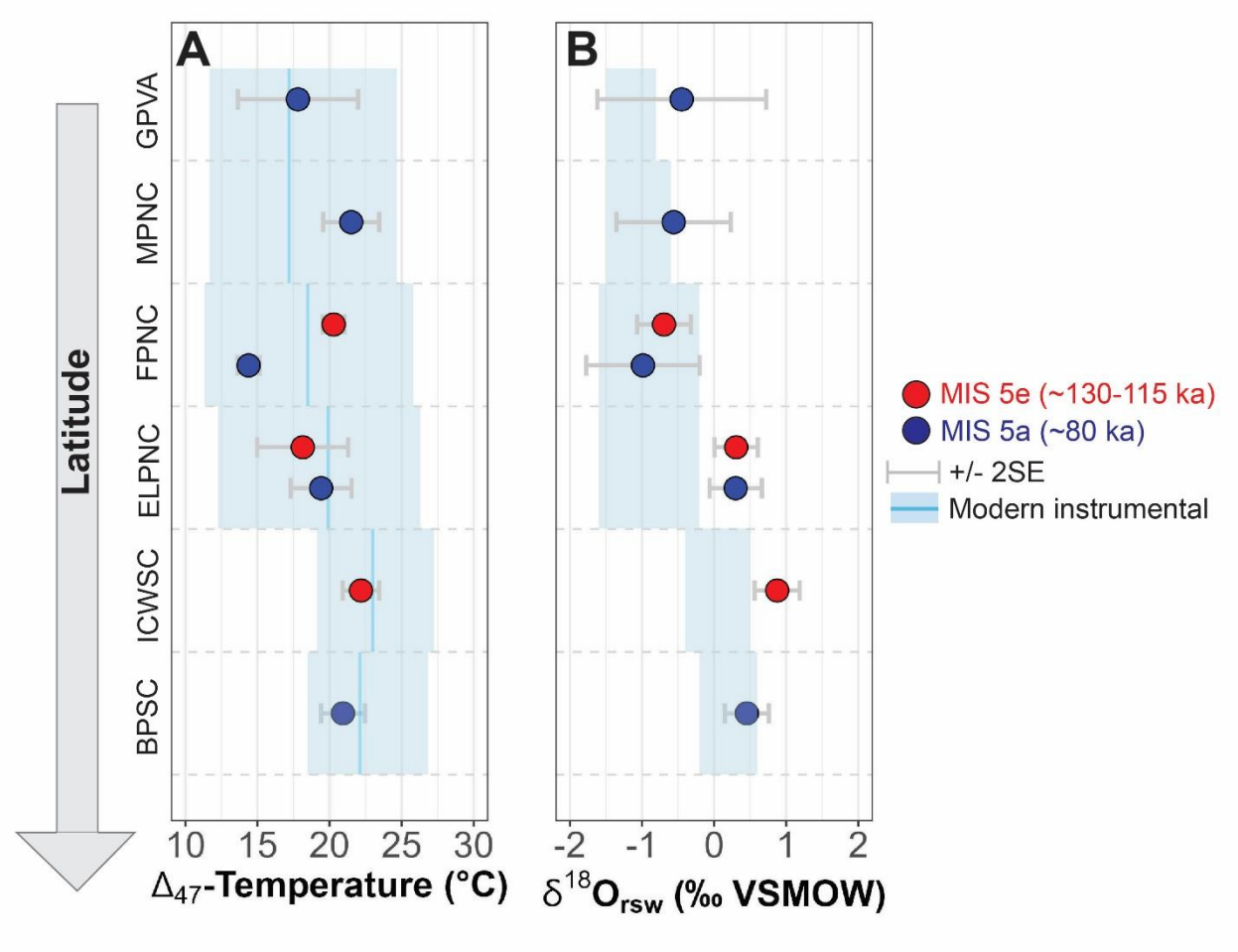

Figure 5.6. Reconstructed isotopic temperatures and $\delta^{18}O_w$ values for MIS5e- and MIS5a-dated fossils from the mid-coastal region (i.e., Virginia to South Carolina).

See Figure 5.4 for details about calculating unit average values and modern climatology/hydrology.

Site Name	Approximate Latitude (°N)	Approximate Longitude (°W)	Apparent ages of deposits?	Geochronology methods applied	Reference(s)
Gomez Pit, VA (GPVA)	36.78	76.20	MIS 5a	U-Th, OSL, ESR, AAR (new *Mercenaria* data in this study)	*Cronin et al., 1981; Szabo, 1985; Skinner, 1989; Mirecki et al., 1995; Lamothe et al., 1998; Wehmiller et al., 2004; Wehmiller et al., 2010; Wehmiller et al., 2021*
Moyock Pit, NC (MPNC)	36.51	76.15	MIS 5a	U-Th (unpublished), OSL, AAR (this study)	*Cronin et al., 1981; Szabo, 1985; Wehmiller et al., 2010; Parham et al., 2013; Wehmiller et al., 2021; D. Mallinson, pers. comm. to J. Wehmiller, 2026*
Forbes Pit, NC (FPNC)	36.32	76.02	MIS 5e & MIS 5a	OSL, AAR (this study)	*Parham et al., 2013*
East Lake Pit, NC (ELPNC)	35.89	75.96	MIS 5e & MIS 5a	U-Th, OSL, AAR (previously from *Mulinia*, new *Mercenaria* data in this study)	*Wehmiller et al., 2010; Parham et al., 2013; Wehmiller et al., 2021*
RP3 Site (ICWSC)	33.81	78.73	MIS 5e (and MIS 5c/5a?)	U-Th (unpublished), AAR (this study)	*McCartan et al., 1982; Wehmiller et al., 1988; Hollin and Hearty, 1990; Poirier, pers. comm.*
Berkeley Pit, SC (BPSC)	32.86	79.78	MIS 5a	U-Th, AAR (this study – RPLC, GC data in prior publications)	*Cronin et al., 1981; McCartan et al., 1982; Szabo, 1985; Wehmiller et al., 2004; Wehmiller et al., 2010*
Jones Pit, GA (JPGA)	31.92	81.07	MIS 5a	U-Th (this study – RPLC, GC data in prior publications)	*Hulbert and Pratt, 1988; Wehmiller et al., 2004; Wehmiller et al., 2010; W. Thompson, pers. comm. to J. Wehmiller, 2012*

WCQ Site (WCQFL)	29.88	81.35	MIS 5e	U-Th, OSL, AAR (this study – from GC, only Glu reported)	*Osmond et al., 1970; Burdette et al., 2009*
Daytona Beach Site (DBPFL)	29.16	81.02	MIS 5e	U-Th, AAR (this study – from GC, only Glu reported)	*W. Thompson, pers. comm. to J. Wehmiller, 2012*

Table 5.1. Summary of sample sites and brief descriptions of previous geochronology efforts.

GC = gas chromatography; RPLC = reverse-phase liquid chromatography; Glu = glutamic acid.

Site Name	# of shells measured for Δ_{47} sclerochronology	# of shells measured for $\delta^{18}O$ sclerochronology	# of shells measured for bulk Δ_{47}	# of shells measured for AAR
GPVA	1	2	2	2
MPNC	1	2	6	1
FPNC	2	4	4	4
ELPNC	1	2	6	4
ICWSC	1	3	17	6
BPSC	1	2	5	1
JPGA	1	2	4	0
WCQFL	1	1	1	1
DBPFL	1	1	2	1

Table 5.2. Summary of shell samples across sites, with descriptions of sampling strategies employed.

Note that $\delta^{18}O$ sclerochronology measurements are simultaneously collected alongside all Δ_{47} sclerochronology measurements. Full names of the abbreviated site names can be found in Table 5.1.

Site name	Unit age	Mean Δ_{47}-T +/- 2SE (°C)	Mean $\delta^{18}O_w$ +/- 2SE (‰ VSMOW)	n
GPVA	MIS 5a	17.8 +/- 4.2	-0.5 +/- 1.2	3
MPNC	MIS 5a	21.5 +/- 2.0	-0.6 +/- 0.8	7
FPNC	MIS 5e	20.3 +/- 0.8	-0.7 +/- 0.4	3
FPNC	MIS 5a	14.4 +/- 0.8	-1.0 +/- 0.8	3
ELPNC	MIS 5e	18.1 +/- 3.2	0.3 +/- 0.3	3
ELPNC	MIS 5a	19.4 +/- 2.2	0.3 +/- 0.4	4
ICWSC	MIS 5e	22.2 +/- 1.2	0.9 +/- 0.4	18
BPSC	MIS 5a	20.9 +/- 1.6	0.5 +/- 0.4	6
JPGA	MIS 5a	18.4 +/- 1.4	-0.3 +/- 0.6	5
WCQFL	MIS 5e	14.8 +/- 2.0	-0.6 +/- 0.2	2
DPBFL	MIS 5e	18.9 +/- 0.2	-0.3 +/- 0.6	3

Table 5.3. Unit-averaged Δ_{47}-temperature and reconstructed $\delta^{18}O_w$ data for each sample locality in this study.

For each unit, the average value was calculated as the mean from bulk Δ_{47} samples combined with the mean value from Δ_{47} sclerochronology.

Site	Winter (DJF) Temperature (°C)	Summer (JJA) Temperature (°C)	Mean Annual Temperature (°C)
GPVA	11.7	24.6	17.2
MPNC	11.7	24.6	17.2
FPNC	11.3	25.8	18.5
ELPNC	12.3	26.3	19.9
ICWSC	18.6	26.8	22.1
BPSC	19.1	27.2	23.0
JPGA	19.9	28.3	23.8
WCQFL	22.8	28.6	25.5
DBPFL	22.9	28.1	25.1

Table S5.1. Modern temperature data for sample sites in this study obtained from the World Ocean Atlas database (Locarnini et al., 2019).

Site	Min. instrumental $\delta^{18}O_w$ (‰ VSMOW)	Max. instrumental $\delta^{18}O_w$ (‰ VSMOW)
GPVA	-1.5	-0.8
MPNC	-1.5	-0.6
FPNC	-1.6	-0.2
ELPNC	-1.6	-0.2
ICWSC	-0.2	0.6
BPSC	-0.4	0.5
JPGA	-0.5	0.5
WCQFL	0.3	1.3
DBPFL	0.3	1.3

Table S5.2. Proximal instrumental $\delta^{18}O_w$ values for the sample sites in this study.

Site	Sample Name	Mean bulk T +/- 95% CI (°C)	Mean bulk $\delta^{18}O_w$ +/- 95% CI (‰)	n	Min. T from HR $\delta^{18}O$ (°C)	Max. T from HR $\delta^{18}O$ (°C)	Min. T from HR Δ_{47} (°C)	Max. T from HR Δ_{47} (°C)	Min. $\delta^{18}O_w$ from HR Δ_{47} (‰)	Max. $\delta^{18}O_w$ from HR Δ_{47} (‰)
GPVA	JW89-139	15.1 +/- 4.6	-1.3 +/- 1.0	7	6.5	21.3	-	-	-	-
	JW89-141	16.4 +/- 3.0	-0.8 +/- 0.7	16	15.7	26.6	15.9	21.2	-0.7	1.7
MPNC	JEM-83-MP108	17.7 +/- 7.4	-0.7 +/- 1.5	3	17.1	27.6	19.2	28.9	0.6	1.9
	JW-92-13	19.8 +/- 7.6	-0.7 +/- 1.5	3	-	-	-	-	-	-
	JW-92-15	22.2 +/- 7.7	0.1 +/- 1.6	3	-	-	-	-	-	-
	JW-92-16	19.6 +/- 7.5	-2.0 +/- 1.5	3	-	-	-	-	-	-
	JW-92-22	22.2 +/- 7.8	-1.4 +/- 1.6	3	7.3	24.8	-	-	-	-
	JW-92-23	24.3 +/- 7.9	-0.5 +/- 1.6	3	-	-	-	-	-	-
FPNC	JW2008-041-003	15.1 +/- 6.0	-0.9 +/- 1.3	4	-	-	-	-	-	-
	JW2008-041-004	14.3 +/- 6.1	-1.7 +/- 1.3	4	9.1	21.1	11.4	16.4	-1.7	0.3
	JW2008-042-002	20.5 +/- 6.6	-0.4 +/- 1.3	4	17.0	24.6	17.6	24.0	-1.2	0.5
	JW2008-042-012	19.6 +/- 6.4	-1.0 +/- 1.3	4	-	-	-	-	-	-
ELPNC	JW2004-161-001	17.0 +/- 6.3	0.0 +/- 1.3	4	-	-	-	-	-	-
	JW2004-161-002	21.0 +/- 6.4	0.8 +/- 1.3	4	-	-	-	-	-	-
	JW2004-161-003	18.4 +/- 6.4	0.1 +/- 1.3	4	13.3	22.1	-	-	-	-
	JW2004-161-004	21.4 +/- 6.5	0.3 +/- 1.3	4	-	-	-	-	-	-
	JW2004-164-001	21.0 +/- 5.3	0.4 +/- 1.1	6	7.2	20.7	15	20.6	-0.2	1.2
	JW2004-164-002	15.5 +/- 5.1	0.0 +/- 1.1	6	-	-	-	-	-	-
ICWSC	RP3-TopA-Merc-1	22.2 +/- 4.6	0.6 +/- 0.9	8	16.6	27.4	-	-	-	-

	RP3-TopA-Merc-2	20.1 +/- 6.4	0.2 +/- 1.3	4	-	-	-	-	-	-
	RP3-TopA-Merc-3	22.5 +/- 6.4	0.4 +/- 1.3	4	-	-	-	-	-	-
	RP3-Mid-Merc-1	20.8 +/- 5.2	0.1 +/- 1.1	6	11.4	24.2	-	-	-	-
	RP3-Mid-Merc-2	17.5 +/- 7.2	0.1 +/- 1.5	3	13.7	33.8	18.4	33.0	0.6	3.7
	RP3-Mid-Merc-3	21.8 +/- 7.5	-0.1 +/- 1.5	3	-	-	-	-	-	-
	IWOYS-5	16.9 +/- 7.2	0.3 +/- 1.5	3	-	-	-	-	-	-
	IWOYS-7	23.7 +/- 7.8	1.6 +/- 1.6	3	-	-	-	-	-	-
	IWOYS-9	21.4 +/- 7.6	0.8 +/- 1.5	3	-	-	-	-	-	-
	IWOYS-12	26.5 +/- 8.1	1.8 +/- 1.6	3	-	-	-	-	-	-
	IWOYS-14	23.3 +/- 6.6	1.4 +/- 1.4	4	-	-	-	-	-	-
	IWOYS-19	19.6 +/- 7.5	0.6 +/- 1.5	3	-	-	-	-	-	-
	IWOYS-24	20.3 +/- 6.6	0.6 +/- 1.3	4	-	-	-	-	-	-
	IWOYS-26	23.3 +/- 7.8	1.0 +/- 1.6	3	-	-	-	-	-	-
	IWOYS-30	25.7 +/- 6.9	1.5 +/- 1.4	4	-	-	-	-	-	-
	IWOYS-36	23.9 +/- 6.7	1.2 +/- 1.3	4	-	-	-	-	-	-
	IWOYS-38	25.1 +/- 8.0	1.8 +/- 1.6	3	-	-	-	-	-	-
BPSC	JW-92-120	21.7 +/- 5.3	0.9 +/- 1.1	6	-	-	-	-	-	-
	JW-92-121	23.2 +/- 5.0	0.3 +/- 1.0	7	-	-	-	-	-	-
	JW-92-122	21.6 +/- 5.3	0.2 +/- 1.1	6	10.1	23.3	-	-	-	-
	JW-92-123	20.7 +/- 4.8	-0.06 +/- 1.0	7	-	-	-	-	-	-
	JW-92-124	17.6 +/- 5.1	0.57 +/- 1.06	6	10.4	25.6	12.4	27.0	0.4	1.8

JPGA	JW95-059(-2)	17.4 +/- 7.4	-0.3 +/- 1.5	3	14.6	22.0	-	-	-	-
	JW95-060	18.8 +/- 7.5	-0.8 +/- 1.5	3	-	-	-	-	-	-
	JW97-004	18.7 +/- 7.3	0.1 +/- 1.5	3	-	-	-	-	-	-
	JW2000-009	16.7 +/- 7.3	-1.0 +/- 1.5	3	16.6	25.8	15.8	25.5	0.0	2.2
WCQFL	JW2009-096	15.9 +/- 7.0	-0.7 +/- 1.5	3	8.5	21.3	9.6	19.5	-2.0	0.6
DBPFL	JW2010-011	19.1 +/- 6.4	-1.0 +/- 1.4	4	16.2	22.0	13.3	26.7	-1.1	1.6
	JW99-034-01	18.7 +/- 6.3	-0.1 +/- 1.3	4	-	-	-	-	-	-

Table S5.3. Summary of reconstructed isotopic temperatures and $\delta^{18}O_w$ values for all samples analyzed in this study.

"HR" stands for high-resolution (i.e., sclerochronology). Note that all samples are *Mercenaria* sp., excluding the oyster samples from the lowermost layer at ICWSC.

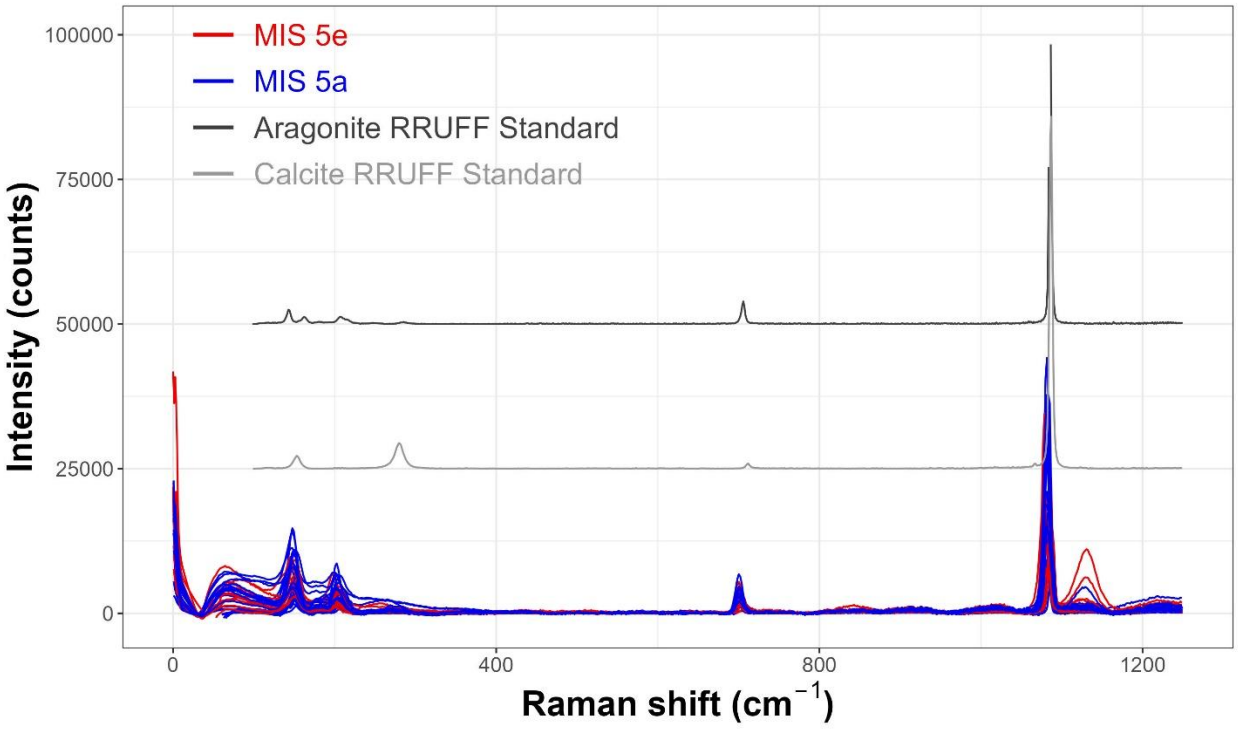

Figure S5.1. Raman spectra for all seven shells measured in this study and calcite and aragonite RRUFF standards.

Note the absence of clear calcite peaks at ~290cm^{-1}, indicating no substantial presence of secondary calcite precipitation or recrystallization. Not included above are the ICWSC oysters and the following *Mercenaria* samples: JW97-004 (JPGA), JW2009-096 (WCQFL), JW2010-011 (DBPFL), JW99-034-01 (DPBFL).

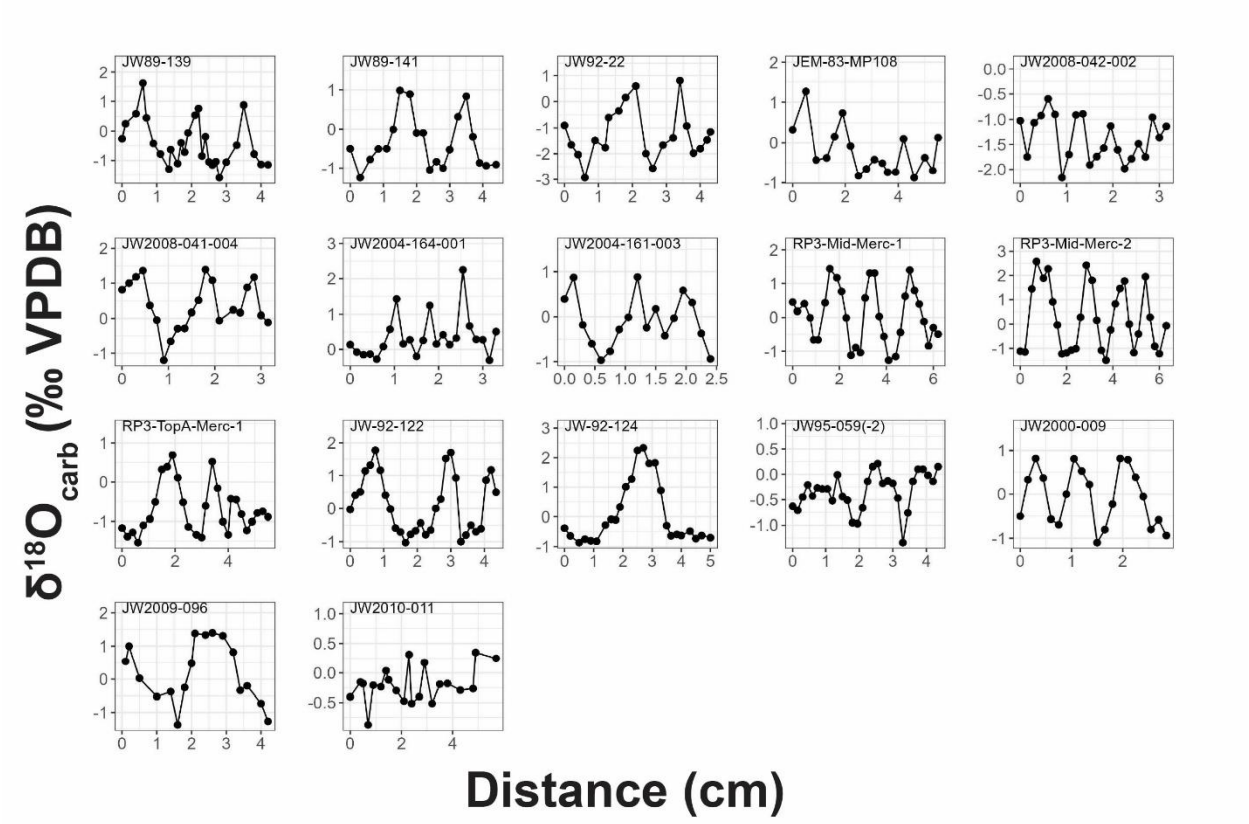

Figure S5.2. $\delta^{18}O$ sclerochronology profiles for select *Mercenaria* sp. in this study.

Note that $\delta^{18}O$ measurements are collected along the way when samples are measured for Δ_{47} sclerochronology.

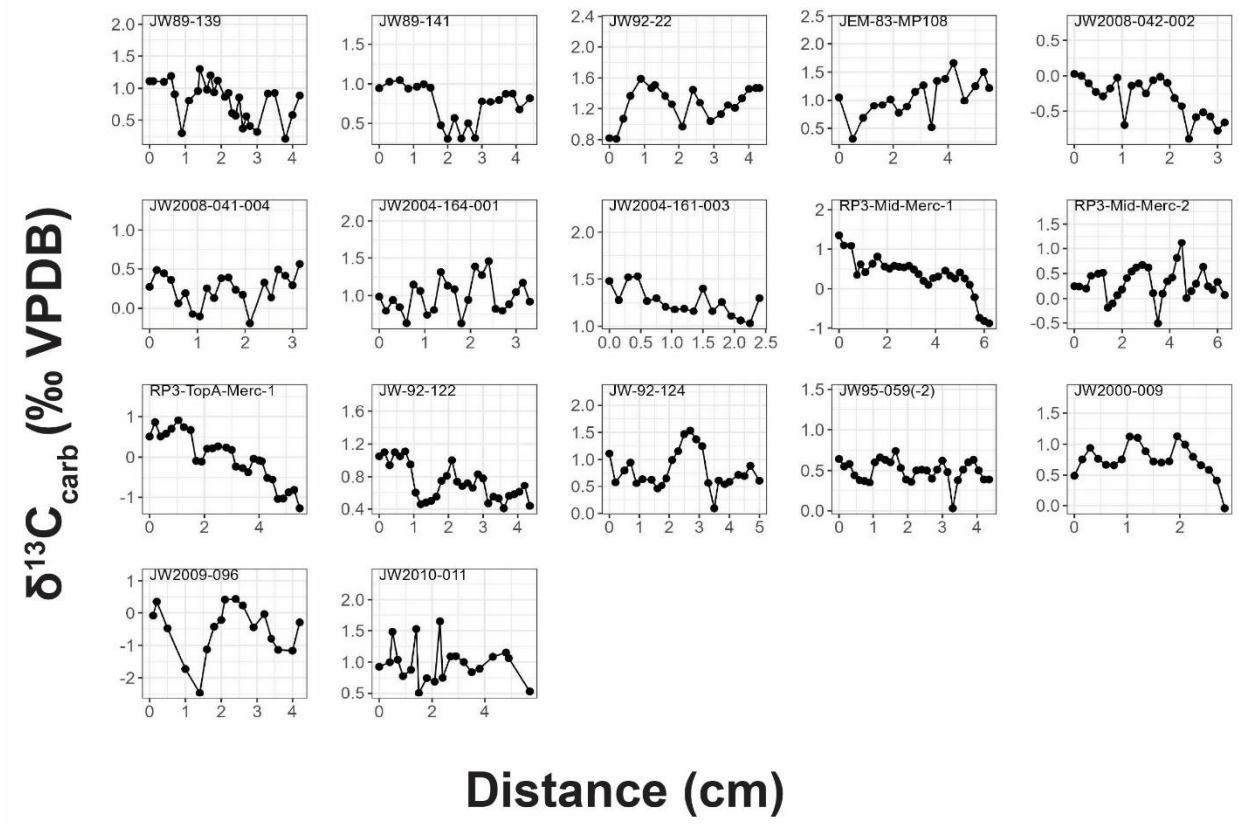

Figure S5.3. $\delta^{13}C$ sclerochronology profiles for select *Mercenaria* sp. in this study.

Note that $\delta^{13}C$ measurements are collected along the way when samples are measured for Δ_{47} sclerochronology.

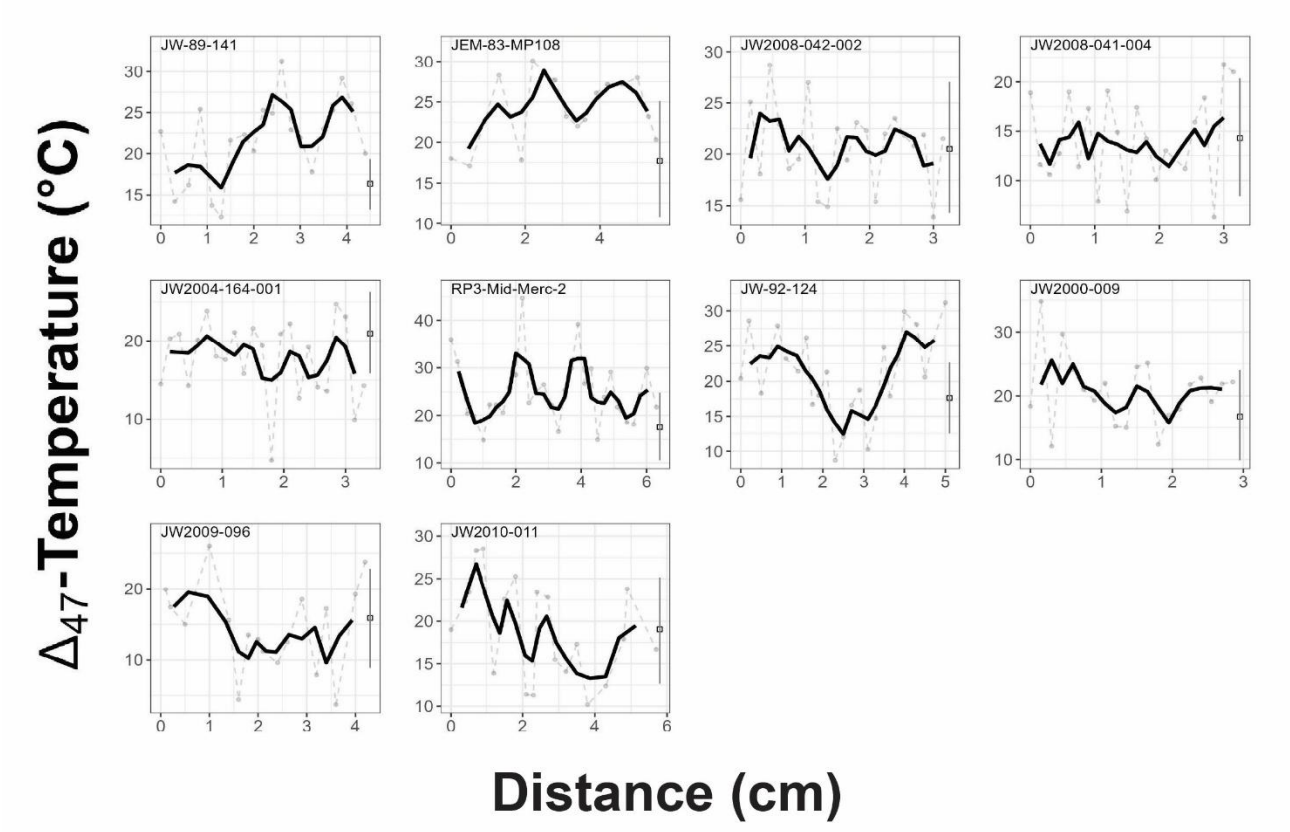

Figure S5.4. Δ_{47} sclerochronology profiles for select *Mercenaria* sp. in this study.

Dark lines represent 3-point smoothed profiles; dashed grey lines and circles represent individual replicates. Square data points and error bars represent bulk Δ_{47}-temperatures and 95% confidence intervals for these corresponding samples.

5.10 References

Adkins, J.F., McIntyre, K., & Schrag, D.P. (2002). The Salinity, Temperature, and $\delta^{18}O$ of the Glacial Deep Ocean. *Science* **298**(5599), 1769-1773.

Algeo, T.J., Wei, W., Liu, Z., Song, Y, & Song, H. (2025). Are Elemental Salinity Proxies Worth Their Salt? *Journal of Earth Science* **36**(4), 1848-1852. https://doi.org/10.1007/s12583-025-0197-2

Andrews, J.T., Piper, D.J.W., Jennings, A.E., & Miller, G.H. (2024). Growth of the Laurentide and Innuitian ice sheets during MIS 5 recorded in distal marine sediment. *Quaternary Science Reviews* **328**, 108532. https://doi.org/10.1016/j.quascirev.2024.108532

Bahr, A., Nürnberg, D., Karas, C., & Grützner, J. (2013). Millennial-scale versus long-term dynamics in the surface and subsurface of the western North Atlantic Subtropical Gyre during Marine Isotope Stage 5. *Global and Planetary Change* **111**, 77-87. https://doi.org/10.1016/j.gloplacha.2013.08.013

Bashirova, L.D., Kandiano, E.S., Sivkov, V.V., & Bauch, H.A. (2014). Migrations of the North Atlantic Polar front during the last 300 ka: Evidence from planktic foraminifera. *Oceanology* **54**(6), 798-807. https://doi.org/10.1134/S0001437014060010

Berger, A. (1989). Pleistocene climatic variability at astronomical frequencies. *Quaternary International* **2**, 1-14. https://doi.org/10.1016/1040-6182(89)90016-5

Boyle, E.A. (1988). Cadmium: Chemical tracer of deepwater paleoceanography. *Paleoceanography and Paleoclimatology* **3**(4), 471-489. https://doi.org/10.1029/PA003i004p00471

Braniecki, G.F.N., Surge, D., Hyland, E.G., Goodwin, & D.H. (2024). Reconstructed seasonality during the Mid Piacenzian Warm Interval and early Pleistocene cooling as recorded by growth temperatures from *Mercenaria* shells. *Quaternary Science Reviews* **328**, 108524. https://doi.org/10.1016/j.quascirev.2024.108524

Braniecki, G.F.N., Surge, D., & Hyland, E.G. (2025). Seasonal Sea Surface Temperatures from *Mercenaria* spp. During the Plio-Pleistocene: Oxygen Isotope Versus Clumped Isotope Paleothermometers. *Geosciences* **15**(8), 295. https://doi.org/10.3390/geosciences15080295

Burdette, K.E., Rink, J.W., Means, G.H., & Portell, R.W. (2009). Optical dating of the Anastasia Formation, Northeastern Florida, USA. *Southeastern Geology* **46**(4), 173-185.

Caldarescu, D.E., Sadatzki, H., Andersson, C., Schäfer, P., Fortunato, H., & Meckler, A.N. (2021). Clumped isotope thermometry in bivalve shells: A tool for reconstructing seasonal upwelling. *Geochimica et Cosmochimica Acta* **294**, 174-191. https://doi.org/10.1016/j.gca.2020.11.019

Chadwick, M., Allen, C.S., Sime, L.C., Crosta, X., & Hillenbrand, C-D. (2022). Reconstructing Antarctic winter sea-ice extent during Marine Isotope Stage 5e. *Climate of the Past* **18**(1), 129-146. https://doi.org/10.5194/cp-18-129-2022

Chapman, M.R., Shackleton, N.J., & Duplessy, J-C. (2000). Sea surface temperature variability during the last glacial-interglacial cycle: assessing the magnitude and pattern of climate change in the North Atlantic. *Palaeogeography, Palaeoclimatology, Palaeoecology* **157**(1-2), 1-25. https://doi.org/10.1016/S0031-0182(99)00168-6

Clark, P.U., Shakun, J.D., Rosenthal, Y., Zhu, C., Bartlein, P.J., Gregory, J.M., Köhler, P., Liu, Z., & Schrag, D.P. (2025). Mean ocean temperature change and decomposition of the benthic $\delta^{18}O$ record over the past 4.5 million years. *Climate of the Past* **21**(6), 973-1000. https://doi.org/10.5194/cp-21-973-2025

Cortijo, E., Lehman, S., Keigwin, L., Chapman, M., Paillard, D., & Labeyrie, L. (1999). Changes in Meridional Temperature and Salinity Gradients in the North Atlantic Ocean (30°-72°N) during the Last Interglacial Period. *Paleoceanography and Paleoclimatology* **14**(1), 23-33. https://doi.org/10.1029/1998PA900004

Craig, H., & Gordon, L.I. Deuterium and Oxygen 18 Variations in the Ocean and the Marine Atmosphere. *Stable Isotopes in Oceanographic Studies* 9-130 (1965).

Creveling, J.R., Mitrovica, J.X., Clark, P.U., Waelbroeck, C., & Pico, T. (2017). Predicted bounds on peak global mean sea level during marine isotope stages 5a and 5c. *Quaternary Science Reviews* **163**, 193-208. https://doi.org/10.1016/j.quascirev.2017.03.003

Cronin, T.M., Szabo, B.J., Ager, T.A., Hazel, J.E., & Owens, J.P. (1981). Quaternary Climates and Sea Levels of the U.S. Atlantic Coastal Plain. *Science* **211**(4479), 233-240. https://doi.org/10.1126/science.211.4479.233

Curley, A.N., Petersen, S.V., Fricke, H., & Gleason, J. (2025). Insight into climate and hydrology of the late cretaceous western interior basin from clumped isotope Paleothermometry and strontium isotopes. *Earth and Planetary Science Letters* **651**, 119180. https://doi.org/10.1016/j.epsl.2024.119180

Curry, W.B., Duplessy, J.C., Labeyrie, L.D., & Shackleton, N.J. (1988). Changes in the distribution of $\delta^{13}C$ of deep water ΣCO_2 between the Last Glaciation and the Holocene. *Paleoceanography and Paleoclimatology* **3**(3), 317-341. https://doi.org/10.1029/PA003i003p00317

Dean, S., Georgiou, N., Poirier, R., Doar III, W.R., Brill, D., Chauveau, D., Cerrone, C., Austermann, J., & Rovere, A. (2026). Last interglacial relative sea-level changes at Myrtle Beach, South Carolina. *Quaternary Science Reviews* **375**, 109769. https://doi.org/10.1016/j.quascirev.2025.109769

de Winter, N.J., Müller, I.A., Kocken, I.J., Thibault, N., Ullmann, C.V., Farnsworth, A., Lunt, D.J., Claeys, P., & Ziegler, M. (2021). Absolute seasonal temperature estimates from clumped isotopes in bivalve shells suggest warm and variable greenhouse climate. *Communications Earth & Environment* **2**(121). https://doi.org/10.1038/s43247-021-00193-9

de Winter, N.J., al Fudhaili, N., Arndt, I., Claeys, P., Fraaije, R., Goderis, S., Jagt, J., López Correa, M., Munnecke, A., Stolarski, J., & Ziegler, M. (2025). Living on the edge: Response of Late Cretaceous rudist bivalves (Hippuritida) to hot and highly seasonal climate in the low-latitude Saiwan site, Oman. *Climate of the Past* **21**(11), 2361-2387. https://doi.org/10.5194/cp-21-2361-2025

Dumitru, O.A., Dyer, B., Austermann, J., Sandstrom, M.R., Goldstein, S.L., D'Andrea, W.J., Cashman, M., Creel, R., Bolge, L., & Raymo, M.E. (2023). Last interglacial global mean sea level from high-precision U-series ages of Bahamian fossil coral reefs. *Quaternary Science Reviews* **318**, 108287. https://doi.org/10.1016/j.quascirev.2023.108287

Duplessy, J.C., Shackleton, N.J., Fairbanks, R.G., Labeyrie, L., Oppo, D., & Kallel, N. (1988). Deepwater source variations during the last climatic cycle and their impact on the global deepwater circulation. *Paleoceanography and Paleoclimatology* **3**(3), 343-360. https://doi.org/10.1029/PA003i003p00343

Dutton, A., & Lambeck, K. (2012). Ice Volume and Sea Level During the Last Interglacial. *Science* **337**(6091), 216-219. https://doi.org/10.1126/science.1205749

Eiler, J.M. (2007). "Clumped-isotope" geochemistry – The study of naturally-occurring, multiply-substituted isotopologues. *Earth and Planetary Science Letters* **262**(3-4), 309-327. https://doi.org/10.1016/j.epsl.2007.08.020

Elderfield, H., & Rickaby, R.E.M. (2000). Oceanic Cd/P ratio and nutrient utilization in the glacial Southern Ocean. *Nature* **405**, 305-310.

Fouke, K.W., & Kerans, C. (2024). Evidence for a Sea Level Fall During the Last Interglacial Highstand on West Caicos, Turks and Caicos Islands. *Paleoceanography and Paleoclimatology* **39**(8), e2024PA004879. https://doi.org/10.1029/2024PA004879

Ghosh, P., Adkins, J., Affek, H., Balta, B., Guo, W., Schauble, E.A., Schrag, D., & Eiler, J.M. ^{13}C-^{18}O bonds in carbonate minerals: A new kind of paleothermometer. *Geochimica et Cosmochimica Acta* **70**(6), 1439-1456. https://doi.org/10.1016/j.gca.2005.11.014

Grant, K.M., Rohling, E.J., Bar-Matthews, M., Ayalon, A., Medina-Elizalde, M., Bronk Ramsey, C., Satow, C., & Roberts, A.P. Rapid coupling between ice volume and polar temperature over the past 150,000 years. *Nature* **491**, 744-747. https://doi.org/10.1038/nature11593

Henkes, G.A., Passey, B.H., Wanamaker Jr., A.D., Grossman, E.L., Ambrose Jr., W.G., & Carroll, M.L. (2013). Carbonate clumped isotope compositions of modern marine mollusk and brachiopod shells. *Geochimica et Cosmochimica Acta* **106**, 307-325. https://doi.org/10.1016/j.gca.2012.12.020

Hoffman, J.J., Petersen, S.V., & Jones, M.M. (2025). Traditional and clumped isotope oyster sclerochronology: Implications for sub-annual temperature and water chemistry variation in the Western Interior Seaway during the mid-Cretaceous Thermal Maximum. *Palaeogeography, Palaeoclimatology, Palaeoecology* **664**, 112778. https://doi.org/10.1016/j.palaeo.2025.112778

Huyghe, D., Daëron, M., de Rafelis, M., Blamart, D., Sébilo, M., Paulet, Y-M., Lartaud, F. (2022). Clumped isotopes in modern marine bivalves. *Geochimica et Cosmochimica Acta* **316**, 41-58. https://doi.org/10.1016/j.gca.2021.09.019

Hsia, S., Toth, L.T., Mortlock, R., & Kerans, C. (2024). Re-evaluating Marine Isotope Stage 5a paleo-sea-level trends from across the Florida Keys reef tract. *Quaternary Science Advances* **15**, 100222. https://doi.org/10.1016/j.qsa.2024.100222

Hulbert, R.C., & Pratt, A.E. (1988). New Pleistocene (Rancholabrean) vertebrate faunas from coastal Georgia. *Journal of Vertebrate Paleontology* **18**(2), 412-429. https://doi.org/10.1080/02724634.1998.10011069

Irvali, N., Ninnemann, U.S., Galaasen, E.V., Rosenthal, Y., Kroon, D., Oppo, D.W., Kleiven, H.F., Darling, K.F., & Kissel, C. (2012). Rapid switches in subpolar North Atlantic hydrography and climate during the Last Interglacial (MIS 5e). *Paleoceanography and Paleoclimatology* **27**(2), PA2207. https://doi.org/10.1029/2011PA002244

Irvali, N., Ninnemann, U.S., Kleiven, H.F., Galaasen, E.V., Morley, A., & Rosenthal, Y. (2016). Evidence for regional cooling, frontal advances, and East Greenland Ice Sheet changes during the demise of the last interglacial. *Quaternary Science Reviews* **150**, 184-199. https://doi.org/10.1016/j.quascirev.2016.08.029

Jeandel, C., Arsouze, T., Lacan, F., Téchiné, P., & Dutay, J-C. (2007). Isotopic Nd compositions and concentrations of the lithogenic inputs into the ocean: A compilation, with an emphasis on the margins. *Chemical Geology* **239**(1-2), 156-164. https://doi.org/10.1016/j.chemgeo.2006.11.013

Johnson, A.L.A., Valentine, A., Leng, M.J., Sloane, H.J., Schöne, B.R., & Balson, P.S. (2017). Isotopic temperatures from the early and mid-Pliocene of the US Middle Atlantic Coastal Plain, and their implications for the cause of regional marine climate change. *PALAIOS* **32**(4), 250-269. https://doi.org/10.2110/palo.2016.080

Johnson, A.L.A., Valentine, A.M., Schöne, B.R., Leng, M.H., & Goolaerts, S. (2022). Sclerochronological evidence of pronounced seasonality from the late Pliocene of the

southern North Sea basin and its implications. *Climate of the Past* **18**(5), 1203-1229. https://doi.org/10.5194/cp-18-1203-2022

Johnson, A.L.A., Schöne, B.R., Leng, M.J., Bhattacharya, T., Moss, D.K., Ivany, L.C., & Duff, R.P. (2024). Sclerochronological evidence of life history and ambient temperature from modern and early Pleistocene *Glycymeris americana* (Mollusk:Bivalvia) of the U.S. Eastern Seaboard. *PALAIOS* **39**(6), 175-193. https://doi.org/10.2110/palo.2023.034

Jones, M.M., Petersen, S.V., & Curley, A.N. (2022). A tropically hot mid-Cretaceous North American Western Interior Seaway. *Geology* **50**(8), 954-958. https://doi.org/10.1130/G49998.1

Khim, B-K., & Krantz, D.E. (1996). Oxygen isotopic identity of the Delaware Coastal Current. *Journal of Geophysical Research* **101**(C7), 16509-16514. https://doi.org/10.1029/96JC00201

Kim, S-T., O'Neil, J.R., Hillaire-Marcel, C., & Mucci, A. (2007). Oxygen isotope fractionation between synthetic aragonite and water: Influence of temperature and Mg^{2+} concentration. *Geochimica et Cosmochimica Acta* **71**(19), 4704-4715. https://doi.org/10.1016/j.gca.2007.04.019

Kniest, J.F., Davies, A.J., Brugger, J., Fiebig, J., Bernecker, M., Todd, J.A., Hickler, T., Voigt, S., Woodland, A., & Raddatz, J. (2024). Dual clumped isotopes from Mid-Eocene bivalve shell reveal a hot and summer wet climate of the Paris Basin. *Communications Earth & Environment* **5**, 330. https://doi.org/10.1038/s43247-024-01491-8

Kukla, G., McManus, J.F., Rousseau, D-D., & Chuine, I. (1997). How long and how stable was the last interglacial? *Quaternary Science Reviews* **16**(6), 605-612. https://doi.org/10.1016/S0277-3791(96)00114-X

Lamothe, M., Wehmiller, J.F., & Noller, J.S. (1998). Comparison of approaches to dating Atlantic coastal plain sediments, Virginia Beach, Virginia. Dating and Earthquakes: Reivew of Quaternary Geochronology and its Application to Paleoseismology, U.S. Nucl. Reg. Com. NUREG/CR-5562.

Lisiecki, L.E., & Raymo, M.E. (2005). A Pliocene-Pleistocene stack of 57 globally distributed benthic $\delta^{18}O$ records. *Paleoceanography and Paleoclimatology* **20**(1), PA1003. https://doi.org/10.1029/2004PA001071

Locarnini, R.A., Mishonov, A.V., Baranova, O.K., et al. (2019). World Ocean Atlas 2018, Volume 1: Temperature. Mishonov, A.V. (Ed.), NOAA Atlas NESDIS 81, 52 pp.

Loutre, M.F., & Berger, A. (2003). Marine Isotope Stage 11 as an analogue for the present interglacial. *Global and Planetary Change* **36**(3), 209-217. https://doi.org/10.1016/S0921-8181(02)00186-8

Marchal, O., François, R., Stocker, T.F., & Joos, F. (2000). Ocean thermohaline circulation and sedimentary $^{231}Pa/^{230Th}$ ratio. *Paleoceanography and Paleoclimatology* **15**(6), 625-641. https://doi.org/10.1029/200PA000496

Martrat, B., Grimalt, J.O., Shackleton, N.J., de Abreu, L., Hutterli, M.A., & Stocker, T.F. (2007). Four Climate Cycles of Recurring Deep and Surface Water Destabilizations on the Iberian Margin. *Science* **317**(5837), 502-507. https://doi.org/10.1126/science.1139994

Martrat, B., Jimenez-Amat, P., Zahn, R., & Grimalt, J.O. (2014). Similarities and dissimilarities between the last two deglaciations and interglaciations in the North Atlantic region. *Quaternary Science Reviews* **99**, 122-134. https://doi.org/10.1016/j.quascirev.2014.06.016

Matsumoto, K. (2007). Radiocarbon-based circulation age of the world oceans. *Journal of Geophysical Research* **112**(C9), C09004. https://doi.org/10.1029/2007JC004095

McCartan, L., Owens, J.P., Blackwelder, B.W., Szabo, B.J., Belknap, D.F., Kriausakul, N., Mitterer, R.M., & Wehmiller, J.W. (1982). Comparison of amino acid racemization geochronometry with lithostratigraphy, biostratigraphy, uranium-series coral dating, and magnetostratigraphy in the Atlantic Coastal Plain of the southeastern United States. *Quaternary Research* **18**(3), 337-359. https://doi.org/10.1016/0033-5894(82)90078-3

McKay, N.P., Overpeck, J.T., & Otto-Bliesner, B.L. (2011). The role of ocean thermal expansion in Last Interglacial sea level rise. *Geophysical Research Letters* **38**(14), L14605. https://doi.org/10.1029/2011GL048280

Meckler, A.N., Sexton, P.F., Piasecki, A.M., Leutert, T.J., Marquardt, J., Ziegler, M., Agterhuis, T., Lourens, L.J., Rae, J.W.B., Barnet, J., Tripati, A., & Bernasconi, S.M. (2022). Cenozoic evolution of deep ocean temperature from clumped isotope thermometry. *Science* **377**(6601), 86-90. https://doi.org/10.1126/science.abk0604

Miller, G.H., Kaufman, D.S., & Clarke, S.J. (2013). Amino Acid Dating: Encyclopedia of Quaternary Science (Second Edition), p. 37-48.

Minnebo, L., Winkelstern, I., Zhang, J., & Petersen, S. (2024). Last Interglacial coastal hydroclimate variability in Bermuda revealed by clumped isotope oyster sclerochronology. *Palaeogeography, Palaeoclimatology, Palaeoecology* **643**, 112195. https://doi.org/10.1016/j.palaeo.2024.112195

Mirecki, J.E., Wehmiller, J.F., & Skinner, A.F. (1995). Geochronology of Quaternary Coastal Plain Deposits, Southeastern Virginia, U.S.A. *Journal of Coastal Research* **11**(4), 1135-1144.

Mixon, R.B., Szabo, B.J., & Owens, J.P. (1982). Uranium-series dating of mollusks and corals, and age of Pleistocene deposits, Chesapeake Bay area, Virginia and Maryland. *Professional Paper* 1067. https://doi.org/10.3133/pp1067E

Muhs, D.R., Pandolfi, J.M., Simmons, K.R., & Schumann, R.R. (2012). Sea-level history of past interglacial periods from uranium-series dating of corals, Curaçao, Leeward Antilles islands. *Quaternary Research* **78**(2), 157-169. https://doi.org/10.1016/j.yqres.2012.05.008

O'Hora, H.E., Petersen, S.V., Vellekoop, J., Jones, M.M., & Scholz, S.R. (2022). Clumped-isotope-derived climate trends leading up to the end-Cretaceous mass extinction in northwestern Europe. *Climate of the Past* **18**, 1963-1982. https://doi.org/10.5194/cp-18-1963-2022

Oppo, D.W., McManus, J.F., & Cullen, J.L. (2006). Evolution and demise of the Last Interglacial warmth in the subpolar North Atlantic. *Quaternary Science Reviews* **25**(23-24), 3268-3277. https://doi.org/10.1016/j.quascirev.2006.07.006

Osmond, J.K., May, J.P., & Tanner, W.F. (1970). Age of the Cape Kennedy Barrier-and-Lagoon Complex. *Journal of Geophysical Research* **75**(2), 469-479. https://doi.org/10.1029/JB075i002p00469

Otto-Bliesner, B.L., Rosenbloom, N., Stone, E.J., McKay, N.P., Lunt, D.J., Brady, E.C., & Overpeck, J.T. (2013). How warm was the last interglacial? New model-data comparisons. *Philosophical Transactions A Math Phys. Eng. Sci.* **371**, 20130097. https://doi.org/10.1098/rsta.2013.0097

Parham, P.R., Riggs, S.R., Culver, S.J., Mallinson, D.J., Rink, W.J., & Burdette, K. (2013). Quaternary coastal lithofacies, sequence development and stratigraphy in a passive margin setting, North Carolina and Virginia, USA. *Sedimentology* **60**(2), 503-547. https://doi.org/10.1111/j.1365-3091.2012.01349.x

Potter, E-K., Esat, T.M., Schellmann, G., Radtke, U., Lambeck, K,. & McCulloch, M.T. (2004). Suborbital-period sea-level oscillations during marine isotope substages 5a and 5c. *Earth and Planetary Science Letters* **225**(1-2), 191-204. https://doi.org/10.1016/j.epsl.2004.05.034

Schauble, E.A., Ghosh, P., & Eiler, J.M. (2006). Preferential formation of ^{13}C-^{18}O bonds in carbonate minerals, estimated using first-principles lattice dynamics. *Geochimica et Cosmochimica Acta* **70**(10), 2510-2529. https://doi.org/10.1016/j.gca.2006.02.011

Schlidt, V., Evans, D., de Winter, N.J., Bernecker, M., Arndt, I., Staudigel, P.T., Davies, A.J., Brand, U., Müller, W., & Fiebig, J. (2025). Most bivalves and gastropods calcify indistinguishably from dual clumped isotope equilibrium. *Geochimica et Cosmochimica Acta* **410**, 174-187. https://doi.org/10.1016/j.gca.2025.10.008

Schneider, R., Schmitt, J., Köhler, P., Joos, F., & Fischer, H. (2013). A reconstruction of atmospheric carbon dioxide and its stable carbon isotopic composition from the

penultimate glacial maximum to the last glacial inception. *Climate of the Past* **9**, 2507-2523. https://doi.org/10.5194/cp-9-2507-2013

Schmidt, G.A., Bigg, G.R., & Rohling, E.J. (1999). "Global Seawater Oxygen-18 Database – v1.22". https://data.giss.nasa.gov/o18data/

Schrag, D.P., Hampt, G., & Murray, D.W. (1996). Pore Fluid Constraints on the Temperature and Oxygen Isotopic Composition of the Glacial Ocean. *Science* **272**(5270), 1930-1932. https://doi.org/10.1126/science.272.5270.1930

Sellards, E.H. (1912). The soils and other surface residual materials of Florida, their origin, character, and the formations from which derived; a study in agrogeology. *Florida Geological Survey Annual Report* **4**, 1-79.

Shackleton, N.J. (1986). Paleogene stable isotope events. *Palaeogeography, Palaeoclimatology, Palaeoecology* **57**(1), 91-102. https://doi.org/10.1016/0031-0182(86)90008-8

Simms, A.R., DeWitt, R., Rodriguez, A.B., Lambeck, K., & Anderson, J.B. (2009). Revisiting marine isotope stage 3 and 5a (MIS3-5a) sea levels within the northwestern Gulf of Mexico. *Global and Planetary Change* **66**(1-2), 100-111. https://doi.org/10.1016/j.gloplacha.2008.03.014

Skinner, A.F. (1989). ESR dosimetry and dating in aragonitic mollusks. *International Journal of Radiation Applications and Instrumentation. Part A. Applied Radiation and Isotopes* **40**(10-12), 1081-1085. https://doi.org/10.1016/0883-2889(89)90044-0

Steinsland, K., Grant, D.M., Ninnemann, U.S., Fahl, K., Stein, R., & De Schepper, S. (2023). Sea ice variability in the North Atlantic subpolar gyre throughout the Last Interglacial. *Quaternary Science Reviews* **313**, 108198. https://doi.org/10.1016/j.quascirev.2023.108198

Stocker, T.F., & Wright, D.G. (1996). Rapid changes in ocean circulation and atmospheric radiocarbon. *Paleoceanography* **11**(6), 773-795. https://doi.org/10.1029/96PA02640

Stone, E.J., Capron, E., Lunt, D.J., Payne, A.J., Singarayer, J.S., Valdes, P.J., & Wolff, E.W. (2016). Impact of meltwater on high-latitude early Last Interglacial climate. *Climate of the Past* **12**(9), 1919-1932. https://doi.org/10.5194/cp-12-1919-2016

Szabo, B.J. (1985). Uranium-series dating of fossil corals from marine sediments of southeastern United States Atlantic Coastal Plain. *GSA Bulletin* **96**(3), 398-406.

Tawil-Morsink, K., Austermann, J., Dyer, B., Dumitru, O.A., Precht, W.F., Cashman, M., Goldstein, S.L., & Raymo, M.E. (2022). Probabilistic investigation of global mean sea level during MIS 5a based on observations from Cave Hill, Barbados. *Quaternary Science Reviews* **295**, 107783. https://doi.org/10.1016/j.quascirev.2022.107783

Thompson, S.B., & Creveling, J.R. (2021). A global database of marine isotope substage 5a and 5c marine terraces and paleoshoreline indicators. *Earth System Science Data* **13**(7), 3467-3490. https://doi.org/10.5194/essd-13-3467-2021

Thompson, S.B., Creveling, J.R., Latychev, K., & Mitrovica, J.X. (2023). Three-dimensional glacial isostatic adjustment modeling reconciles conflicting geographic trends in North American marine isotope stage 5a relative sea level observations. *Geology* **51**(9), 808-812. https://doi.org/10.1130/G51257.1

Turney, C.S.M., Jones, R.T., McKay, N.P., van Sebille, E., Thomas, Z.A., Hillenbrand, C-D., & Fogwill, C.J. (2020). A global mean sea surface temperature dataset for the Last Interglacial (129-116 ka) and contribution of thermal expansion to sea level change. *Earth System Science Data* **12**(4), 3341-3356. https://doi.org/10.5194/essd-12-3341-2020

Turney, C.S.M., & Jones, R.T. (2010). Does the Agulhas Current amplify global temperatures during super-interglacials? *Journal of Quaternary Science* **25**(6), 839-843. https://doi.org/10.1002/jqs.1423

Waelbroeck, C., Labeyrie, L., Michel, E., Duplessy, J.C., McManus, J.F., Lambeck, K., Balbon, E., & Labracherie, M. (2002). Sea-level and deep water temperature changes derived from benthic foraminifera isotopic records. *Quaternary Science Reviews* **21**(1-3), 295-305. https://doi.org/10.1016/S0277-3791(01)00101-9

Wehmiller, J.F., Belknap, D.F., Boutin, B.S., Mirecki, J.E., Rahaim, S.D., & York, L.L. (1988). A review of the aminostratigraphy of Quaternary mollusks from United States Atlantic Coastal Plain sites. *Geological Society of America Special Papers* **227**, 69-110. https://doi.org/10.1130/SPE227-p69

Wehmiller, J.F., Simmons, K.R., Cheng, H., Lawrence Edwards, R., Martin-McNaughton, J., York, L.L., Krantz, D.E., & Shen, C-C. (2004). Uranium-series coral ages from the US Atlantic Coastal Plain-the "80ka problem" revisited. *Quaternary International* **120**(1), 3-14. https://doi.org/10.1016/j.quaint.2004.01.002

Wehmiller, J.F., Thieler, E.R., Miller, D., Pellerito, V., Bakeman Keeney, V., Riggs, S.R., Culver, S., Mallinson, D., Farrell, K.M., York, L.L., Pierson, J., & Parham, P.R. (2010). Aminostratigraphy of surface and subsurface Quaternary sediments, North Carolina coastal plain, USA. *Quaternary Geochronology* **5**(4), 459-492. https://doi.org/10.1016/j.quageo.2009.10.005

Wehmiller, J.F. (2013). Interlaboratory comparison of amino acid enantiomeric ratios in Pleistocene fossils. *Quaternary Geochronology* **16**, 173-182. https://doi.org/10.1016/j.quageo.2012.08.007

Wehmiller, J.F., & Pellerito, V. (2015). An evolving database for Quaternary aminostratigraphy. *GeoResJ* **6**, 115-123. https://doi.org/10.1016/j.grj.2015.02.009

Wehmiller, J.F., Brothers, L.L., Ramsey, K.W., Foster, D.S., Mattheus, C.R., Hein, C.J., & Shawler, J.L. (2021). Molluscan aminostratigraphy of the US Mid-Atlantic Quaternary coastal system: Implications for onshore-offshore correlation, paleochannel and barrier island evolution, and local late Quaternary sea-level history. *Quaternary Geochronology* **66**, 101177. https://doi.org/10.1016/j.quageo.2021.101177

Weiss, T.L., Linsley, B.K., Gordon, A.L., Rosenthal, Y., & Dannenmann-Di Palma, S. (2022). Constraints on Marine Isotope Stage 3 and 5 Sea Level From the Flooding History of the Karimata Strait in Indonesia. *Paleoceanography and Paleoclimatology* **37**(9), e2021PA004361. https://doi.org/10.1029/2021PA004361

Winkelstern, I., Surge, D., & Hudley, J.W. (2013). Multiproxy sclerochronological evidence for Plio-Pleistocene regional warmth: United States Mid-Atlantic Coastal Plain. *PALAIOS* **28**(9), 649-660. https://doi.org/10.2110/palo.2013.p13-010r

Winkelstern, I.Z,. Rowe, M.P., Lohmann, K.C., Defliese, W.F., Petersen, S.V., & Brewer, A.W. (2017). Meltwater pulse recorded in Last Interglacial mollusk shells from Bermuda. *Paleoceanography* **32**(2), 132-145. https://doi.org/10.1002/2016PA003014

Winkelstern, I., Petersen, S., Curran, H.A., Phillips, C., Quizon, A., Glumac, B., & Griffing, D. (2025). Cooling climate across last interglacial high stands on San Salvador and Great Inagua, The Bahamas. *The Depositional Record* **12**(1), e70038. https://doi.org/10.1002/dep2.70038

Yin, Q., & Berger, A. (2015). Interglacial analogues of the Holocene and its natural near future. *Quaternary Science Reviews* **120**, 28-46. https://doi.org/10.1016/j.quascirev.2015.04.008

Zeng, M., Rashid, H., Lodestro, S., & Gruetzner, J. (2025). Millennial-scale surface water mass changes between the North Atlantic subpolar and subtropical gyre since the last glacial-interglacial cycle. *Global and Planetary Change* **253**, 104921. https://doi.org/10.1016/j.gloplacha.2025.104921

Zhang, J.Z., Petersen, S.V., Winkelstern, I.Z., & Lohmann, K.C. (2021). Seasonally Variable Aquifer Discharge and Cooler Climate in Bermuda During the Last Interglacial Revealed by Subannual Clumped Isotope Analysis. *Paleoceanography and Paleoclimatology* **36**(6), e2020PA004145. https://doi.org/10.1029/2020PA004145

Zhang, J.Z., & Petersen, S.V. (2023). Clumped and oxygen isotope sclerochronology methods tested in the bivalve *Lucina pensylvanica*. *Chemical Geology* **620**, 121346. https://doi.org/10.1016/j.chemgeo.2023.121346

Zhang, J.Z., Petersen, S.V., Lavis, S., & Williams, B. (2024). Quantifying variations in $\delta^{18}O_w$ and salinity in modern Bermudan waters on hourly to monthly timescales. *Frontiers in Marine Science* **11**, 1441113. https://doi.org/10.3389/fmars.2024.1441113

Zinke, J., Watanabe, T.K., Rühs, S., Pfeiffer, M., Grab, S., Garbe-Schönberg, D., & Biastoch, A. (2022). A 334-year coral record of surface temperature and salinity variability in the greater Agulhas Current region. *Climate of the Past* **18**(6), 1453-1474. https://doi.org/10.5194/cp-18-1453-2022

Chapter 6 End-Last Interglacial Transition and Substantial Ice Sheet Melt Detected at Sankaty Sand, Massachusetts

6.1 Abstract

The Sankaty Head Cliff deposits of Nantucket Island, MA include two fossiliferous marine units between two glacial drifts. These shelly units have been proposed to reflect the transition from peak Last Interglacial (~130-125 ka) to late Last Interglacial (<120 ka) conditions based on faunal interpretations and some previous dating efforts. In this study, we test this previous interpretation with new amino acid racemization (AAR) dating combined with traditional stable ($\delta^{18}O_{carb}$, $\delta^{13}C_{carb}$) and clumped (Δ_{47}) isotope measurements of seven *Mercenaria* sp. fossils. AAR data are consistent with deposition of both units within the Last Interglacial (MIS 5e), but isotopic data suggest deposition in different environmental settings. Δ_{47}-temperatures from both units are similar and suggest MIS 5e conditions in Nantucket were warmer than today. However, trends in $\delta^{13}C_{carb}$ and reconstructed seawater $\delta^{18}O$ ($\delta^{18}O_{rsw}$) suggest a strong influence of glacial meltwater during deposition of the older unit, disappearing into the younger unit. This is consistent with more ice sheet melt occurring early in the interglacial, with ice sheet proximity to this site and influence to these coastal waters declining over time as ice sheets retreated. Methodologically, our new data demonstrate the power of Δ_{47} sclerochronology to accurately detect seasonal temperature changes in situations where $\delta^{18}O_{rsw}$ is uncertain and fluctuating, such as due to meltwater influence.

6.2 Introduction

The Last Interglacial (MIS 5e, ~130-115 ka) was the most recent time in Earth's history when global temperatures were as warm as they are today (e.g., Turney et al,. 2020). Paleoclimate and paleoceanographic reconstructions from the Last Interglacial and other past warm intervals can be informative about potential near-future climate dynamics, such as how the melting of ice sheets into the North Atlantic has been linked to the collapse of Atlantic Meridional Overturning Circulation (AMOC) (e.g., Ivanovic et al., 2018). However, most records from the Last Interglacial come from open-ocean sediment cores. Fewer records exist documenting how coastal temperatures or coastal waters evolved through the Last Interglacial. Due to a combination of sea level changes, coastal configurations, and ice sheets scraping sediments away during the Last Glacial Maximum, very few sites containing Last Interglacial sediments exist between 43°N and 26°N on the east coast.

The only known Last Interglacial site on the entire northern East Coast is the Sankaty Head Cliff in Massachusetts, which exposes Late Pleistocene sediments and fossils on the southeastern end of Nantucket Island (Fig. 6.1). The earliest descriptions of this site date back to the 1800s (e.g., Desor and Cabot, 1849; Verrill, 1875), and great attention has been called to this site's position at the terminal moraine of the Laurentide ice sheet; Wilson (1906) describes this site as having "perhaps some of the best-developed morainal features to be found in any part of the world". Oldale et al. (1982) stated that investigation of this site is "critical for relating North American glacial and interglacial history to North Atlantic oceanography". Overall, Sankaty Head Cliff is geographically well-positioned for studying Last Interglacial climate and ice sheet dynamics as it is an ice-proximal, mid-latitude site susceptible to changes in North Atlantic circulation.

Two marine units outcrop at Sankaty Head, sandwiched between underlying (Illinoian, ~191-130 ka) and overlying (Wisconsin, ~75-11ka) glacial "drifts", with ages of these drifts inferred from a U-Th based age estimate of MIS 5e for the marine units (Oldale et al., 1982). Paleoclimatic and paleoceanographic reconstruction from the marine units is possible through isotopic paleothermometry of marine macrofossils contained therein. While $\delta^{18}O_{carb}$ paleothermometry is a well-tested method that has been used for decades (although never at this site), it has the disadvantage of relying on prior knowledge or assumption of the isotopic composition of surrounding seawater ($\delta^{18}O_{sw}$). Δ_{47} paleothermometry is a newer method that relates the abundances of 'clumped' ^{13}C-^{18}O bonds in a carbonate as a Δ_{47} value to its formation temperature, independent of $\delta^{18}O_{sw}$ (e.g., Eiler, 2011). When used in conjunction with $\delta^{18}O_{carb}$ paleothermometry, Δ_{47} can be used to reconstruct $\delta^{18}O_{sw}$ ($\delta^{18}O_{rsw}$). When applied at subannual resolution along the growth axis of a mollusk, this method can simultaneously reconstruct seasonal variations in paleotemperatures and paleo-$\delta^{18}O_{rsw}$ (Zhang and Petersen, 2023).

Given the proximitiy of the Laurentide Ice Sheet (LIS) to Sankaty Head and the unknown magnitude of its influence on coastal $\delta^{18}O_{sw}$ (e.g., Clark et al., 1993; Parker et al., 2022), it is necessary to use Δ_{47} with $\delta^{18}O_{carb}$ to correctly reconstruct temperature and $\delta^{18}O_{sw}$. Further, by reconstructing $\delta^{18}O_{rsw}$ at the same time, this method can detect changes in the influence of meltwater from the LIS. $\delta^{18}O_{sw}$ influenced by meltwater would be isotopically depleted relative to surrounding seawater (0 +/- 2‰) because the oxygen isotopic composition of the glacial ice is much lower (-20 to -35‰ – e.g., Hillaire-Marcel and Causse, 1989; Ferguson and Jasechko, 2015; Vetter et al., 2017) due to Rayleigh distillation.

Unfortunately, uncertainties in the ages of the Sankaty Sand marine deposits preclude a complete understanding of Last Interglacial climate at this site. The lower and upper marine units

– referred to as the "Lower Sand" and "Upper Sand" by Oldale et al. (1982) – are fossiliferous, containing a fauna of mostly marine bivalves such as *Mercenaria mercenaria* (quahog clam), *Crassostrea virginica* (Eastern oyster), and *Mytilus edulis* (blue mussel), and are interpreted to reflect deposition during a sea level highstand. Faunal evidence based on bryozoa, ostracodes, and crustaceans suggests that Lower Sand conditions were warmer than Upper Sand conditions by up to 10°C (Verrill, 1875; Cushman, 1904; Gustavson, 1976). This led previous workers to suggest that the Lower Sand reflects the peak Last Interglacial (MIS 5e) while the Upper Sand was deposited during the Wisconsin glaciation (post-MIS 5e, <100 ka) (Gustavson, 1976).

Later work dated a coral fragment (*Astrangia* sp.) from the Upper Sand and determined a U-Th age of 133 ± 7 ka, suggesting both the Lower and Upper Sand may have been deposited during MIS 5e (Oldale et al., 1982). This was supported by amino acid racemization (AAR) geochronology conducted on *M. mercenaria* and extrapolations of gradients from the mid-Atlantic (see Materials and Methods) (Belknap, 1979; Belknap and Wehmiller, 1980; Oldale et al., 1982). Quantitative paleotemperature and paleo-$\delta^{18}O_{sw}$ reconstructions from both units could help resolve the disagreement between previous studies by determining whether environmental conditions were similar or different between the two units. If conditions changed dramatically, this would suggest a larger difference in depositional age. Temperatures similar to modern would be consistent with peak interglacial conditions (MIS 5e), whereas temperatures significantly cooler than modern would be expected for an age younger than MIS 5e.

In this study, we present brand-new $\delta^{18}O_{carb}$ and Δ_{47} measurements and use these to reconstruct temperature and $\delta^{18}O_{rsw}$ from both marine units at Sankaty Head Cliffs. We also present new AAR measurements using updated laboratory techniques to verify previous age

constraints. In doing this work, we also investigate the utility of subannual $\delta^{18}O_{carb}$ and Δ_{47} sampling strategies in unraveling past climate in ice-proximal environments.

6.3 Materials & Methods

6.3.1 Dating (AAR)

Seven fossil *Mercenaria mercenaria* shells were sampled for AAR – four from the Lower Sand and three from the Upper Sand (Fig. S6.1). Samples were analyzed at Northern Arizona University's Amino Acid Geochronology Lab on an Agilent series 1100/1200 reverse phase chromatograph (see Appendices for details). These data were directly compared to the AAR results from Oldale et al. (1982).

6.3.2 Isotopic Measurements ($\delta^{18}O$, $\delta^{13}C$, Δ_{47})

Isotopic measurements were conducted on the seven *Mercenaria* shells to reconstruct paleotemperatures and paleo-$\delta^{18}O_{rsw}$ values. These consisted of: (1) bulk Δ_{47} measurements; (2) Δ_{47} sclerochronology measurements; and (3) $\delta^{18}O$ (and $\delta^{13}C$) sclerochronology measurements (see Appendices for details). All seven *Mercenaria* shells were sampled for bulk Δ_{47}, two were sampled for $\delta^{18}O$ sclerochronology (one from each unit), and two were sampled for Δ_{47} sclerochronology (one from each unit) (Fig. S6.2). Δ_{47}-derived $\delta^{18}O_{rsw}$ values for all samples were calculated via the aragonite-water fractionation from Kim et al. (2007).

6.4 Results

6.4.1 Dating (AAR)

Our AAR data demonstrate that averaged D/L values for all measured amino acids from the Lower and Upper Sands are within error of each other (Fig. 6.2). Averaged leucine D/L data from both units are within error of the previous averaged leucine D/L values reported in Oldale

et al. (1982). These data reconfirm a minimal age difference between the two units based on the ~10ka age resolution capabilities of AAR (Miller and Brigham-Grette, 1989).

6.4.2 Sclerochronology

$\delta^{18}O$ sclerochronology from all four shells exhibit seasonal variability and reflect between 1-3 years of growth (Fig. 6.3A), although the shapes and ranges of the profiles between the Lower and Upper Sands differ greatly. The sclerochronology profiles from the Lower Sand are quite variable. Mean shell $\delta^{18}O_{carb}$ values in the Lower Sand are lower than those from the Upper Sand by ~1-2‰ on average. In contrast, Upper Sand profiles exhibit larger, slower changes. $\delta^{13}C_{carb}$ sclerochronology data (Fig. S6.3B) also exhibit several years of growth and reveal a clear difference between the units, with values from the Lower Sand generally ~1-2‰ depleted relative to those from the Upper Sand.

Climate seasonality is apparent in subannual Δ_{47}-temperature data from both units (Fig. S6.5B). These variations more clearly reveal temperature seasonality relative to $\delta^{18}O$ sclerochronology (Fig. S6.5A) and show that $\delta^{18}O_{sw}$ varies throughout the year by >1‰ (Fig. S6.5C), thereby confounding the seasonal $\delta^{18}O_{carb}$ signal.

6.4.3 Temperature & $\delta^{18}O_{sw}$

Peak Δ_{47}-temperatures from both units are warmer than modern (Fig. 6.4A) and bulk Δ_{47}-temperatures from both units fall above modern mean annual temperature (MAT). Δ_{47} sclerochronology temperature ranges from the Lower and Upper Sands are ~17–24°C and ~14–24°C respectively, and $\delta^{18}O$ sclerochronology temperature ranges from these respective shells are ~16-24°C and ~11-25°C. $\delta^{18}O$ sclerochronology temperature profiles from the Upper Sand align with Δ_{47}-temperatures from this unit, while one $\delta^{18}O$ sclerochronology profile from the Lower Sand does not align with the other isotopic temperatures from this unit (Fig. S6.6).

$\delta^{18}O_{rsw}$ values in the Lower Sand are isotopically depleted relative to values from the Upper Sand, while values from the Lower Sand (and some from the Upper Sand) are depleted relative to modern ocean waters in the region (Fig. 6.4B). Bulk and Δ_{47} sclerochronology $\delta^{18}O_{rsw}$ values in the Lower Sand range between -5 to -2‰, while values increase in the Upper Sand to values between -4 to 0‰. All Lower Sand values and bulk Upper Sand values are much lower than the modern instrumental range of 0 to -2‰.

6.5 Discussion

6.5.1 Age Interpretations

Our AAR data corroborate the previous conclusion from Oldale et al. (1982) that both marine units were deposited within ~15 ka of MIS 5e. However, the isotopic data suggest different climate states and hydrologic regimes within MIS 5e. Similar to or slightly warmer than modern temperatures and substantially depleted $\delta^{18}O_{rsw}$ values suggest that the Lower Sand was likely deposited during peak Last Interglacial warmth (~130-125 ka), coincident with substantial ice sheet melt that lowered local $\delta^{18}O_{rsw}$. In contrast, slightly lower temperatures on average and relatively enriched $\delta^{18}O_{rsw}$ values from the Upper Sand suggest that it was likely deposited during the transition into the subglacial episode following the Last Interglacial (i.e., end-MIS 5e into MIS 5d, <120 ka).

6.5.2 Paleoenvironment Interpretations

Cumulative isotopic data suggest that the Lower Sand reflects peak Last Interglacial conditions. Peak Lower Sand summer Δ_{47}-temperatures were ~6°C warmer than modern summer temperatures and average (bulk) Δ_{47}-temperatures were warmer than modern MAT by ~3-5°C. $\delta^{18}O_{rsw}$ values are significantly depleted (<-3‰) relative to modern instrumental values, likely

due to the influx of isotopically depleted meltwater from proximal ice sheets during peak warmth. This is consistent with previous studies reporting large amounts of ice rafting and southward expansions of polar meltwater in the North Atlantic water during peak MIS 5e conditions (e.g., Galaasen et al., 2014) but is among the first direct observations of freshening of coastal waters. This meltwater may have also carried terrestrial organic carbon (e.g., Sharp, 2007), leading to slightly depleted $\delta^{13}C$ values (<0‰) relative to those from the Upper Sand (~+1‰).

Meanwhile, cumulative isotopic data suggest that the Upper Sand reflects late Last Interglacial conditions. Peak Δ_{47}-temperatures also fall above modern summer temperatures by ~6°C, though winter Δ_{47}-temperatures and $\delta^{18}O$-temperatures are lower than those from the Lower Sand. $\delta^{18}O_{rsw}$ values are generally enriched relative to Lower Sand values, with some falling within the modern instrumental range. Although these Upper Sand shells were also likely influenced by glacial meltwater, these relatively enriched $\delta^{18}O_{rsw}$ values are consistent with a more saline precipitating reservoir later during MIS 5e following a main episode of ice sheet retreat and peak warmth.

Three-point smoothed Δ_{47} sclerochronology data from both units demonstrate the method's potential for reconstructing seasonal temperatures with more certainty and interpreting $\delta^{18}O_{sw}$ variability throughout the year. Although $\delta^{18}O_{carb}$ sclerochronology can be useful for approximating seasonal temperature variability, $\delta^{18}O_{sw}$ variability of >1‰ throughout the year (Fig. 6.4B) biases $\delta^{18}O$-temperature reconstructions, making it difficult to refine absolute temperature $\delta^{18}O$-temperature estimates. Many studies assume a constant, year-round $\delta^{18}O_{sw}$ value to calculate $\delta^{18}O$-temperatures, but our Δ_{47} sclerochronology data show why this should not be the case. Further, bulk shell Δ_{47} data on their own can provide snapshot estimates of mean

annual temperatures and $\delta^{18}O_{sw}$ values but cannot capture seasonality. Δ_{47} sclerochronology resolves all these issues.

This seasonal-scale $\delta^{18}O_{rsw}$ variability derived from Δ_{47} sclerochronology can shed light on seasonal-scale hydrological processes. For instance, in both units the Δ_{47}-temperature increases after apparent winter extrema align with the lowest $\delta^{18}O_{rsw}$ (Fig. S6.5), which is consistent with spring ice melt. Separately, seasonal-scale $\delta^{18}O_{rsw}$ variations are relatively smaller in the Lower Sand (i.e., constant influx of glacial meltwater) and larger in the Upper Sand (i.e., larger seasonal signal due to greater distance from ice sheets).

6.5.3 Comparison to Previous MIS5e Findings

Our finding that peak SSTs were on average warmer than modern are consistent with the previously reported broad biostratigraphic estimates (Verrill, 1875; Cushman, 1904; Gustavson, 1976; Oldale et al., 1982). They are also consistent with global proxy and model work showing that average Last Interglacial temperatures were similar to or slightly warmer (0-2°C) than today (e.g., Turney et al,. 2020), though our data suggest peak local temperatures up to ~6°C warmer than modern. However, the LIG climatic optimum may only have lasted 2-3ka (e.g., Oppo et al., 2006), and the proxy data suggest LIG warm anomalies in this region to varying degrees. It is therefore likely that these proxy data, like those demonstrated in this study, span several time intervals within the Last Interglacial and not just peak warmth. Recent studies have suggested the occurrence of multiple sea level highstands in places like Bermuda (Winkelstern et al., 2017; Zhang et al., 2021; Minnebo et al., 2024), the Bahamas (Winkelstern et al., 2025), and the Turks and Caicos Islands (Fouke and Kerans, 2024), and it is likely that proxy archives were deposited during different intra-MIS 5e highstands.

6.6 Conclusions

Our AAR data align with previously published data suggesting that both marine units were deposited during MIS 5e, and our isotopic data suggest that peak temperatures were warmer than modern across both units, consistent with other findings in the North Atlantic. $\delta^{18}O_{rsw}$ values across both units are generally depleted relative to modern, thus indicative of proximal glacial meltwater input. Furthermore, these data suggest a distinct paleoenvironmental shift across units, as $\delta^{18}O_{sw}$ values increased by ~1-2‰ on average; this is consistent with ice sheet retreat following peak Last Interglacial conditions. Finally, our methodology demonstrates that $\delta^{18}O$ sclerochronology may not accurately capture seasonality. $\delta^{18}O_{rsw}$ values from Δ_{47} sclerochronology vary by >1‰ throughout the year, effectively biasing $\delta^{18}O$-seasonality estimates when using a year-averaged assumed $\delta^{18}O_{rsw}$ value. As an alternative, 3-point smoothed Δ_{47} sclerochronology shows the clearest seasonality signal, demonstrating its potential for more accurate paleoseasonality reconstructions and seasonal-scale paleohydrology interpretations.

6.7 Acknowledgments

We would like to thank Ashling Neary for her help with Δ_{47} measurements; Justin VanDeVelde for his help with Δ_{47} and instrumental measurements of $\delta^{18}O_{sw}$; Cecilie Phillips for her help with drilling shells for $\delta^{18}O$ sclerochronology sampling; KC Lohmann for his help with $\delta^{18}O$ measurements; the members of Northern Arizona University's Amino Acid Geochronology Lab (Jordon Bright, Darrell Kaufman) for AAR measurements; and the NSF-GRFP, NSF grant 1903237, and the University of Michigan Department of Earth and Environmental Science's Turner Grants provided to AAQ.

6.8 Appendices

6.8.1 Specimens & sampling methods

Clumped isotope measurements were measured on a NuCarb automated sample preparation device connected to a Nu Perspective mass spectrometer in the University of Michigan Stable Isotope Lab. Full procedures for this setup can be found in O'Hora et al. (2022), Jones et al. (2022), and Quizon et al. (2025). 3-4 mg aliquots of sample powder were reacted with phosphoric acid in individual vials at 70°C to produce CO_2; this gas was purified for Δ_{47} analysis through two water traps and a Porapak-filled trap containing silver wool. Δ_{47} data were collected in 'bellows mode' at a major ion beam current of 80nA, consistently maintained for 80 sample-reference cycles by continuous bellows adjustment. The shot noise limit for Δ_{47} is 0.0074‰ under this instrumental setup.

Throughout the entire study interval, five in-house carbonate standards and four community carbonate standards were analyzed alongside samples. The in-house carbonate standards include our Carrara Marble (CM), Bahamian Ooids (OO), a fully-crushed *Arctica islandica* bivalve from Iceland (Ice), a synthetic carbonate (GU1), and a fully-crushed *Cittarium pica* gastropod from Bermuda (Pica) as described previously (O'Hora et al., 2022). The community carbonate standards referenced are the ETH1-4 standards (Bernasconi et al., 2021). To adjust for drift in the I-CDES90 reference frame over time, we apply a window-specific fixed offset to all Δ_{47} data using two low temperature standards (Ice, OO), leaving our third low temperature standard (Pica) as a check standard. The long-term standard deviation in Δ_{47} from all standards over the measurement interval (excluding Pica) is 0.022‰. Measured Δ_{47} values were calculated from raw voltages through an R-code script (RDevelopment CORE TEAM, 2008) using updated IUPAC parameters following Petersen et al. (2019).

Bulk Δ_{47} measurements from each shell (n=6 replicates) capture several years of mean annual temperature (MAT) across each shell's lifespan. Using a low-speed dental drill, we extracted >6mg of powder ~1cm deep from the outer layer of each shell, typically on the ventral margin. Δ_{47}-temperatures were calculated from the mean Δ_{47} value using the calibration equation from Anderson et al. (2021). Sample mean Δ_{47}-temperatures and $\delta^{18}O_{carb}$ values were used to reconstruct Δ_{47}-derived $\delta^{18}O_{sw}$ for each powder via aragonite-water fractionation from Kim et al. (2007).

Sequential >3mg powders were drilled per shell: 22 powders for the shell measured from the Lower Sand (JW-83-88), 24 powders for the shell measured from the Upper Sand (JW-83-69). Powders were collected every 2.5-5mm along the surface of each shell's growth axis using a low-speed dental drill with care taken not to penetrate to interior layers. The same procedures described above to obtain bulk Δ_{47} measurements were used to obtain Δ_{47} sclerochronology measurements, convert to temperatures, and calculate $\delta^{18}O_{rsw}$ values. However, since each powder was measured as a single replicate, 3-point averaging was applied to these Δ_{47} measurements to 'smooth' the sclerochronology profiles (see Fig. S6.5B).

~50ug of powder was collected every 2.5-5mm along each shell's growth axis using a low-speed dental drill, again making sure not to penetrate interior layers. Sample powders only analyzed for $\delta^{18}O$ and $\delta^{13}C$ sclerochronology (i.e., JW-83-59 and JW-83-96) were measured using a Kiel IV automated carbonate device attached to a Thermo-Finnegan MAT 253 dual inlet mass spectrometer at the University of Michigan Stable Isotope Lab. Data were standardized against the NBS-18 and NBS-19 standards, with units reported in per mille (‰) relative to the VPDB standard. Uncertainty was routinely better than 0.1‰ for both oxygen and carbon isotopes. Temperatures for Fig. S6.6 were calculated using the aragonite-water fractionation

equation from Kim et al. (2007) using shell-averaged $\delta^{18}O_{rsw}$ from Δ_{47} sclerochronology (JW-83-88, JW-83-69) or bulk $\delta^{18}O_{rsw}$ (JW-83-96, JW-83-59).

6.8.2 Screening for preservation

We obtained Raman spectra from the inner and outer layers of each shell to assess mineralogy and thus preservation (Fig. S6.3). These spectra from all seven shells indicate the preservation of original aragonite with trace amounts of calcite and no evidence of diagenetic alterations (i.e., recrystallization, secondary calcite precipitation). We therefore infer that isotopic signatures measured in these shells preserve information about their inhabited environments without alterations.

6.8.3 Amino acid racemization (AAR)

AAR is a relative dating technique which relates the abundances of the L- and D-enantiomer forms of an amino acid in an organism to that organism's age (Miller et al., 2013; Wehmiller et al., 2013). Once the organism dies, all the L-enantiomers of an amino acid racemize into their respective D-enantiomers, resulting in older samples yielding higher ratios of D- to L-enantiomers ("D/L"). Two lines of evidence support a Last Interglacial age estimate for the marine units at Sankaty Head Cliff. The first is a U-Th absolute age estimate of 133+/-7 ka from a coral fragment found in the Upper Sand (Oldale et al., 1982). The second is an amino acid racemization (AAR) based age estimate between 120-140 ka from *Mercenaria* sp. clams obtained from both units. As D/L values are also temperature-dependent (Miller et al., 2013; Wehmiller, 2013) and thus latitude-dependent (i.e., higher temperature histories yield higher D/L values), the 120-140 ka estimate is calculated from an extrapolated latitudinal gradient that includes other U-Th age-constrained sites along the Atlantic Coastal Plain (ACP) (Belknap, 1979; Belknap and Wehmiller, 1980).

We used a diamond wheel Dremel to cut off >50mg fragments from one half of each shell. These samples were measured at Northern Arizona University's Amino Acid Geochronology Lab. After a series of cleaning and purification steps, the fragments were measured for D/L ratios of eight amino acids on an Agilent series 1100/1200 reverse phase chromatograph. Previous studies (e.g., Wehmiller et al., 2021) recommend using D/L ratios of glutamic and aspartic acid from these samples for age interpretation due to their high abundances in mollusk shells.

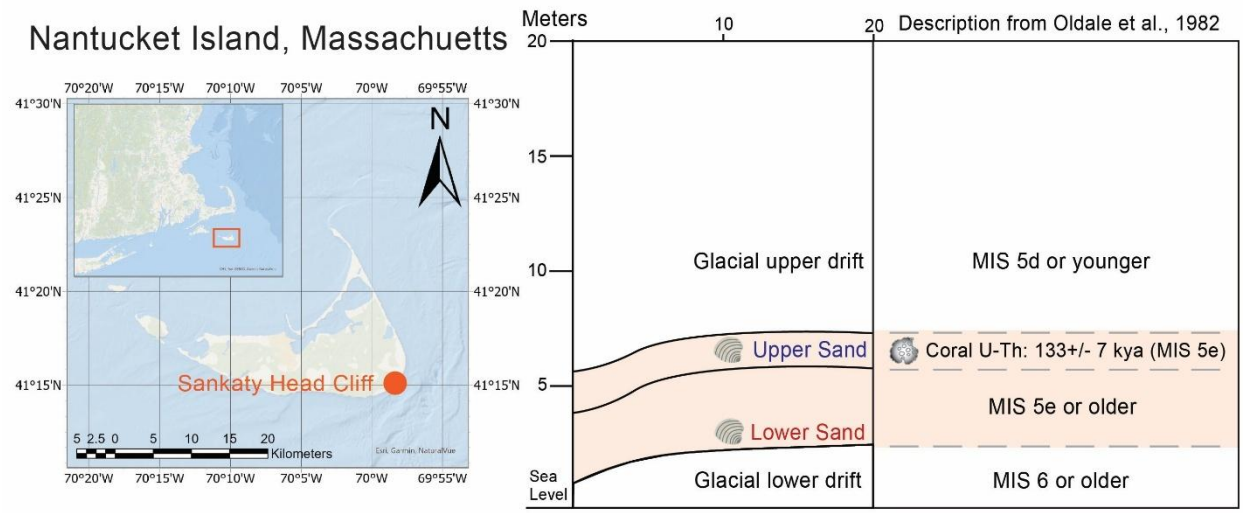

Figure 6.1. Map and simplified cross-section of the Sankaty Head Cliff deposits at Nantucket Island, Massachusetts (41.28°N, 69.96°W), adapted from Oldale et al. (1982).

Ages were determined based on one coral U-Th absolute age estimate and relative aminostratigraphy (Oldale et al., 1982).

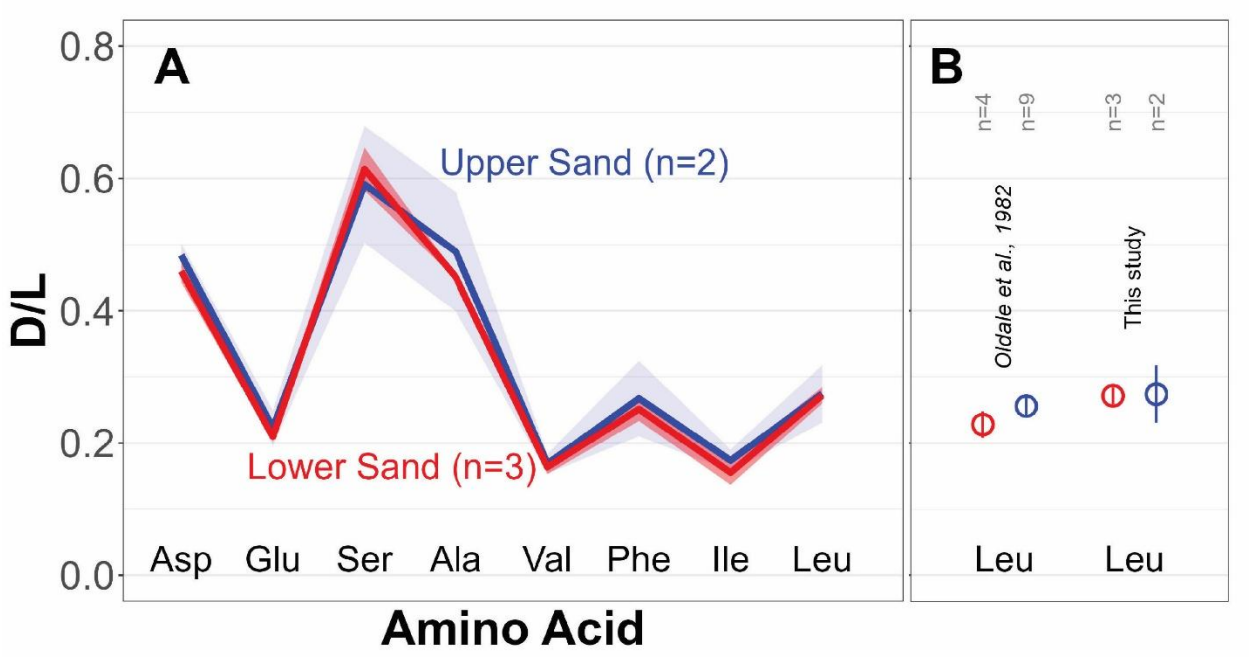

Figure 6.2. Average amino acid racemization (AAR) data from *Mercenaria mercenaria* from the Upper (blue) and Lower (red) Sands analyzed in this study.

Lines and error envelopes in (A) represent D/L average values and 95% CI from each unit; Points and error bars in (B) represents leucine average values and 95% CI from each unit. Asp = aspartic acid; Glu = glutamic acid; Ser = serine; Ala = alanine; Val = valine; Phe = phenylalanine; Ile = isoleucine; Leu = leucine. Note: the shells analyzed in this study for AAR measurements are different than those measured in Oldale et al. (1982).

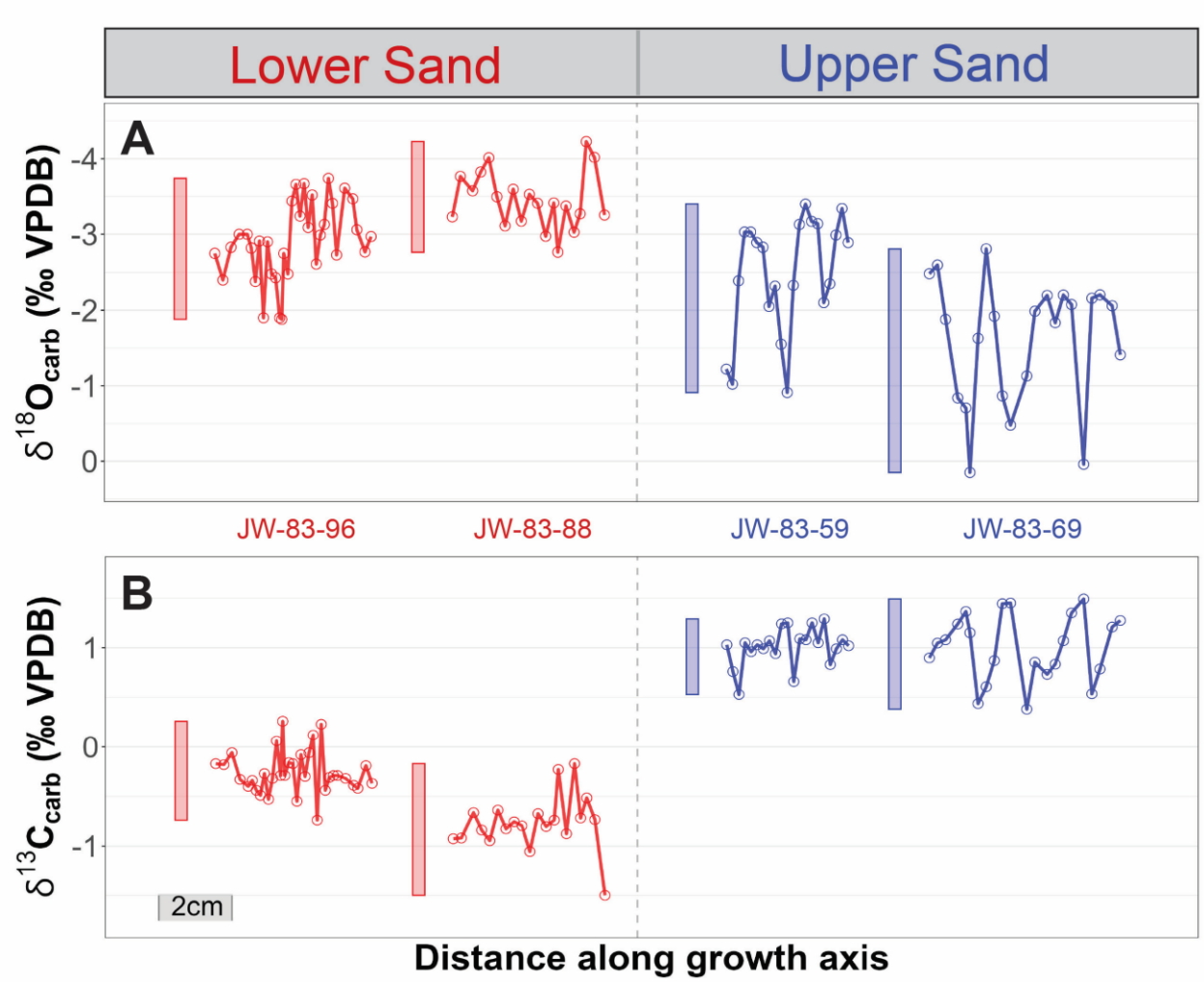

Figure 6.3. $\delta^{18}O_{carb}$ (A) and $\delta^{13}C_{carb}$ (B) sclerochronology data for four shells: two from the Lower Sand, and two from the Upper Sand.

Bars represent absolute ranges for each sclerochronology profile.

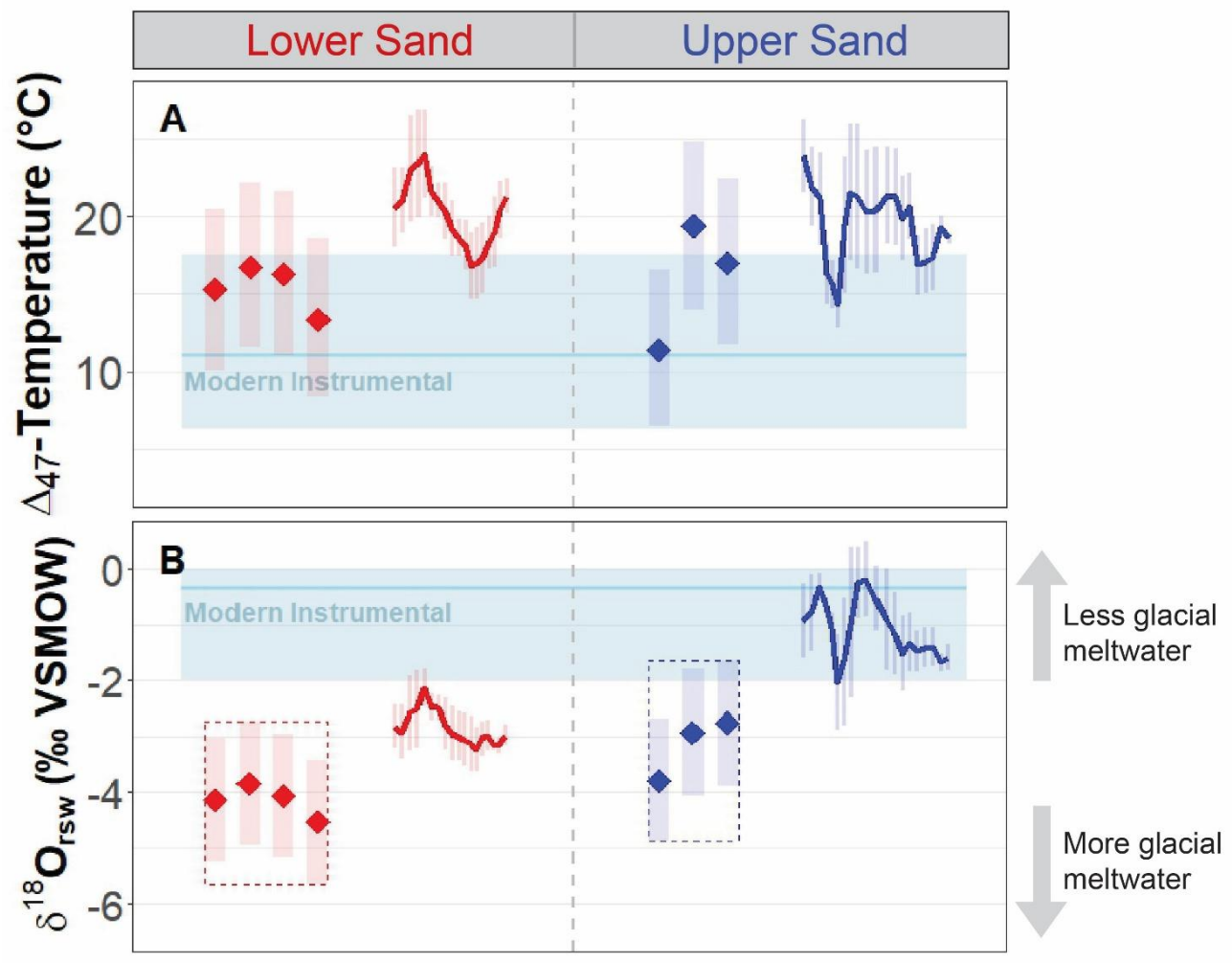

Figure 6.4. Bulk Δ_{47} and high-resolution (HR) Δ_{47} sclerochronology temperature (A) and reconstructed seawater $\delta^{18}O$ ('$\delta^{18}O_{rsw}$') (B) data from both the Lower and Upper Sands of the Sankaty Head Cliff deposits.

Error bars on bulk measurements represent 95% confidence intervals (n=6) based on the long-term standard deviation in Δ_{47} from our carbonate standards. Error envelopes for Δ_{47} sclerochronology measurements represent +/- 1SE from 3-point averaging. The horizontal blue lines in the modern instrumental ranges correspond to World Ocean Atlas mean annual temperature (11°C) and NASA GISS modeled $\delta^{18}O_{sw}$ (-0.35‰) respectively.

Sample Latitude & Longitude	Instrumental Mean Annual Temperature	Instrumental Summer (JJA) Temperature	Instrumental Winter (DJF) Temperature
41.28°N, 69.96°W	**11.0°C +/- 0.5°C**	**17.5°C +/- 0.5°C**	**6.3°C +/- 0.5°C**

Table S6.1. Instrumental temperature data for the latitude/longitude information corresponding to Sankaty Head Cliff on Nantucket Island, Massachusetts.

Temperatures were gathered from the World Ocean Atlas (WOA) 2018 dataset (2005-2017 period, 1/4° resolution, monthly means) for comparison the reconstructed isotopic temperatures (Locarnini et al., 2019). To account for depth, these temperatures were determined by averaging temperatures over the known depth range of *Mercenaria* sp. (~20m) in the grid cell nearest the collection site.

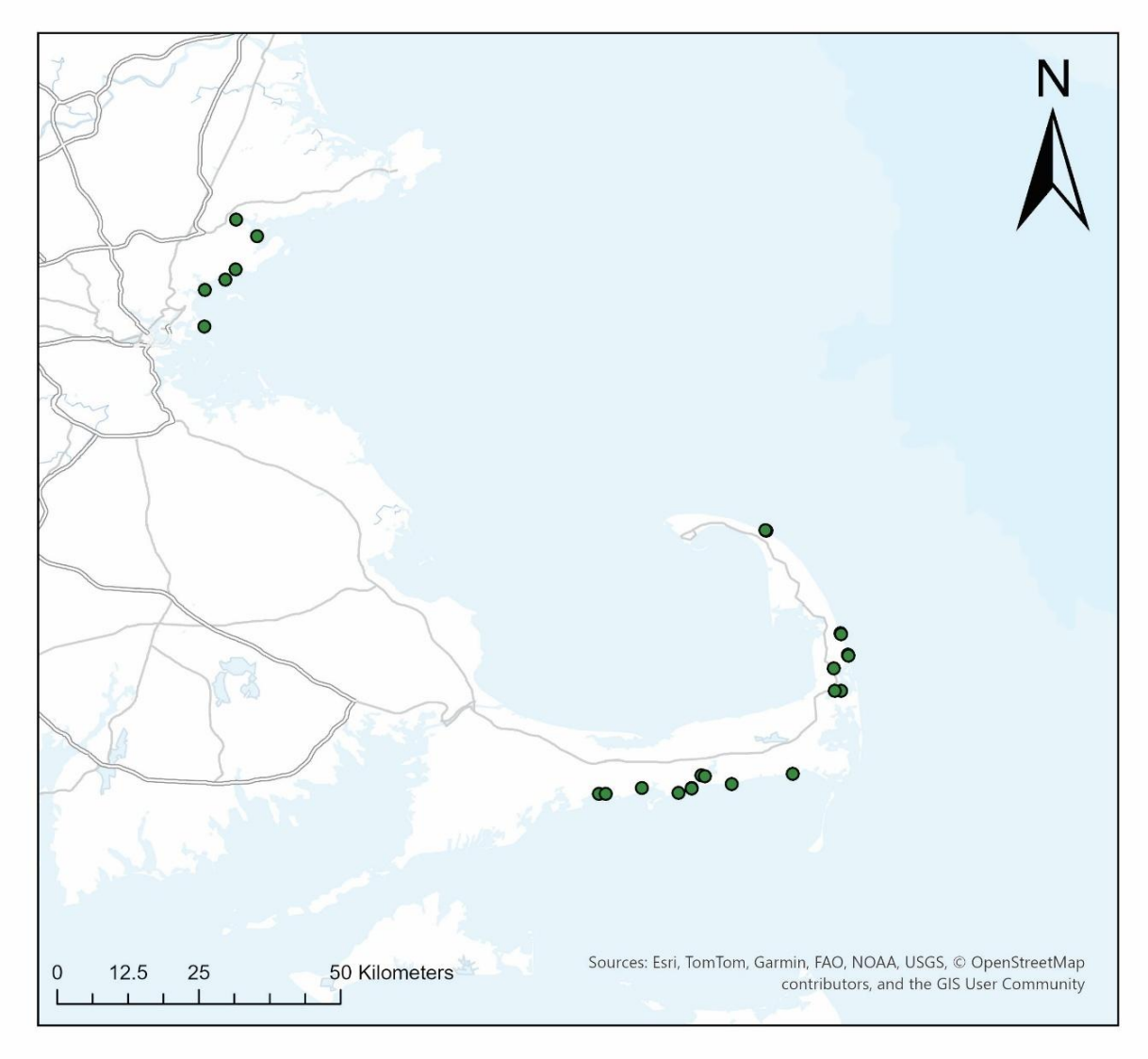

Figure S6.1. Map of water samples measured for salinity and $\delta^{18}O_{sw}$ measurements collected from the Boston and Cape Cod regions in Massachusetts in the SeaSOx dataset (Quizon et al., in prep).

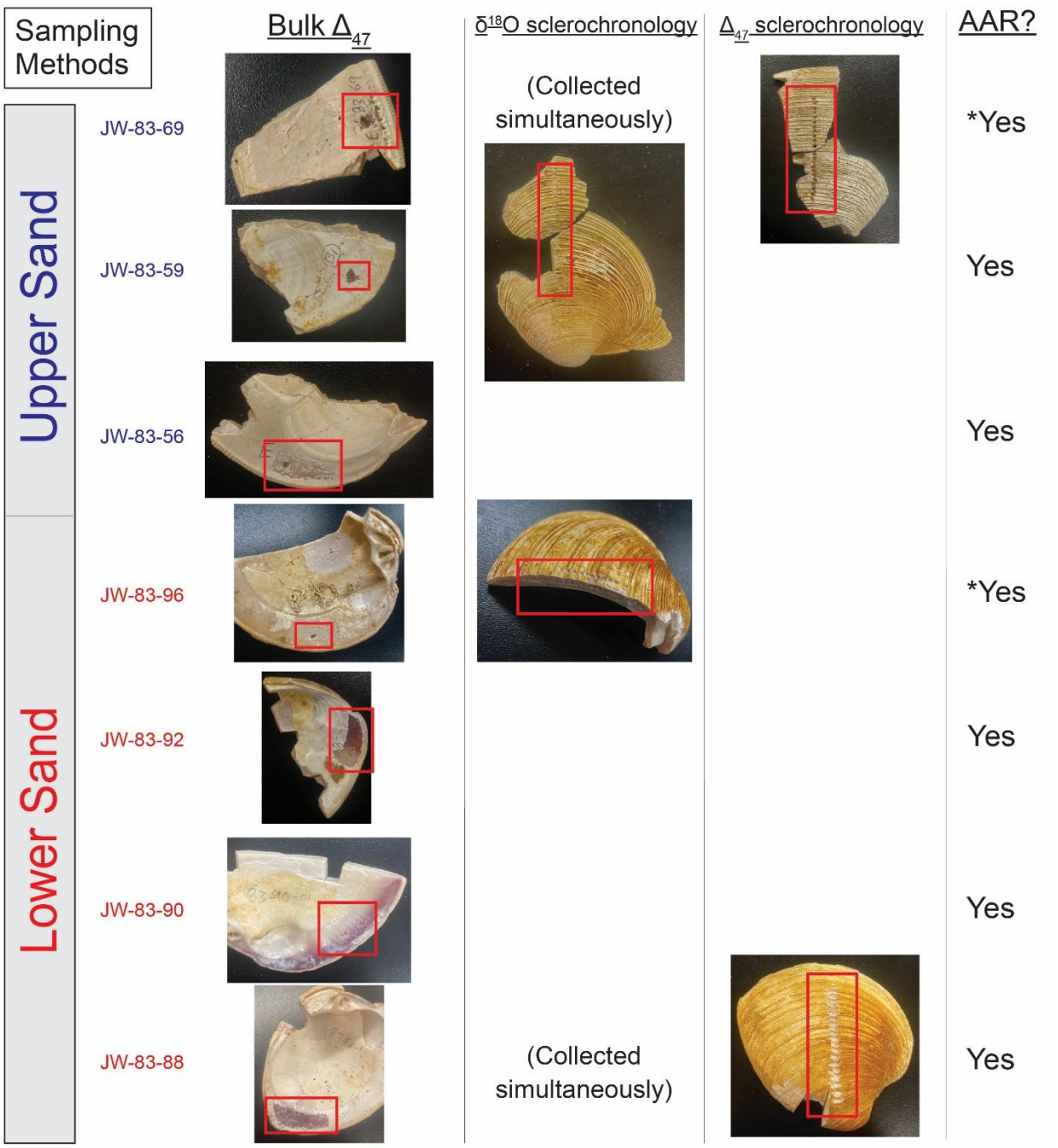

Figure S6.2. Pictures of all seven shells measured in this study and corresponding sampling methods applied to each shell.

Asterisks are marked for shells measured for AAR but not included for unit average calculations due to contamination (see Fig. S6.4).

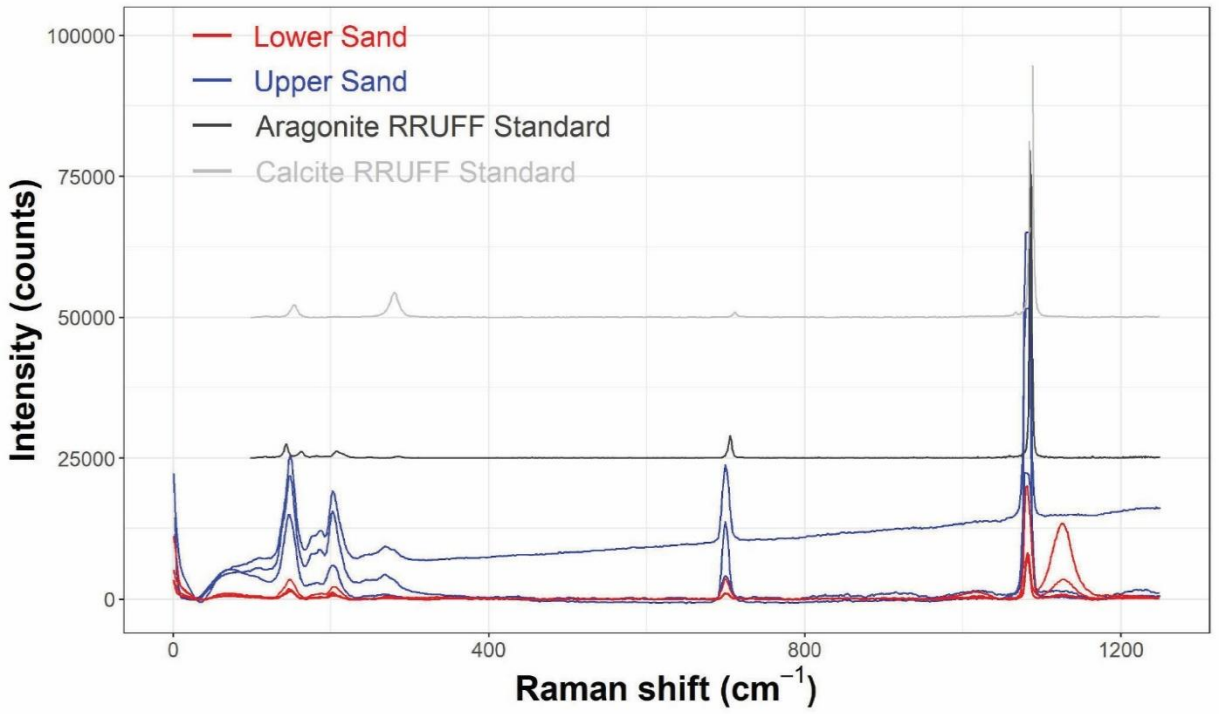

Figure S6.3. Raman spectra for all seven shells measured in this study and calcite and aragonite RRUFF standards.

Note the absence of clear calcite peaks at ~290cm^{-1}, indicating no substantial presence of secondary calcite precipitation or recrystallization.

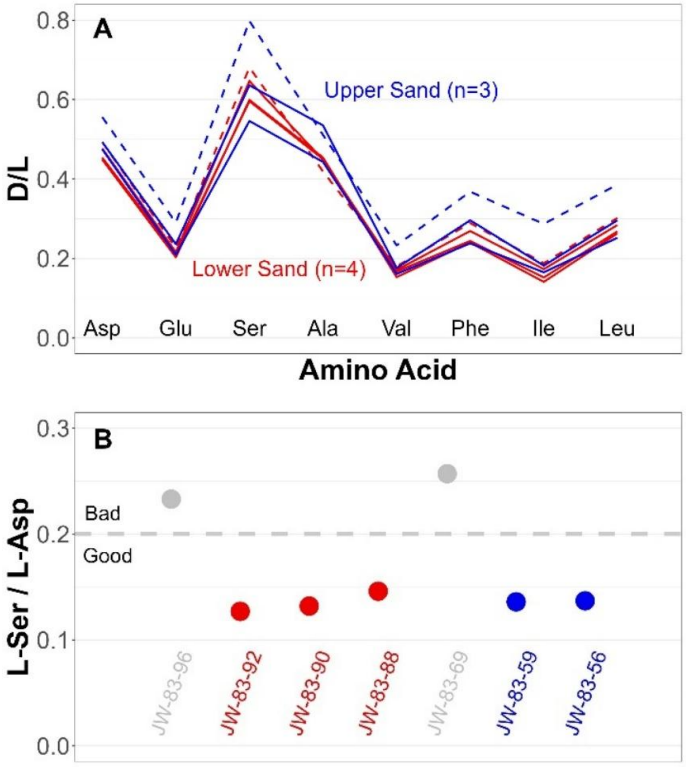

Sample Name	Unit	D/L Asp	D/L Glu	D/L Ser	D/L Ala	D/L Val	D/L Phe	D/L Ile	D/L Leu	L-Ser / L-Asp
JW-83-96	Lower	0.493	0.227	0.681	0.419	0.180	0.289	0.188	0.302	0.233
JW-83-92	Lower	0.449	0.203	0.599	0.454	0.153	0.240	0.141	0.263	0.127
JW-83-90	Lower	0.454	0.210	0.596	0.450	0.167	0.244	0.152	0.268	0.132
JW-83-88	Lower	0.477	0.216	0.647	0.448	0.171	0.269	0.173	0.284	0.146
JW-83-69	Upper	0.556	0.290	0.798	0.511	0.233	0.368	0.287	0.386	0.257
JW-83-59	Upper	0.493	0.236	0.636	0.535	0.176	0.296	0.182	0.296	0.136
JW-83-56	Upper	0.475	0.209	0.546	0.443	0.161	0.238	0.165	0.252	0.137

Figure S6.4. Amino acid racemization (AAR) data and corresponding table from all *Mercenaria* sp. samples analyzed in this study (A), including the JW-83-69 (Upper Sand) and JW-83-96 (Lower Sand) colored in grey which are likely contaminated as evident in higher than expected L-Ser/L-Asp values (>0.2) (B).

Asp = aspartic acid; Glu = glutamic acid; Ser = serine; Ala = alanine; Val = valine; Phe = phenylalanine; Ile = isoleucine; Leu = leucine. Dotted colored lines represent Lower and Upper Sand averages from all shells within each unit.

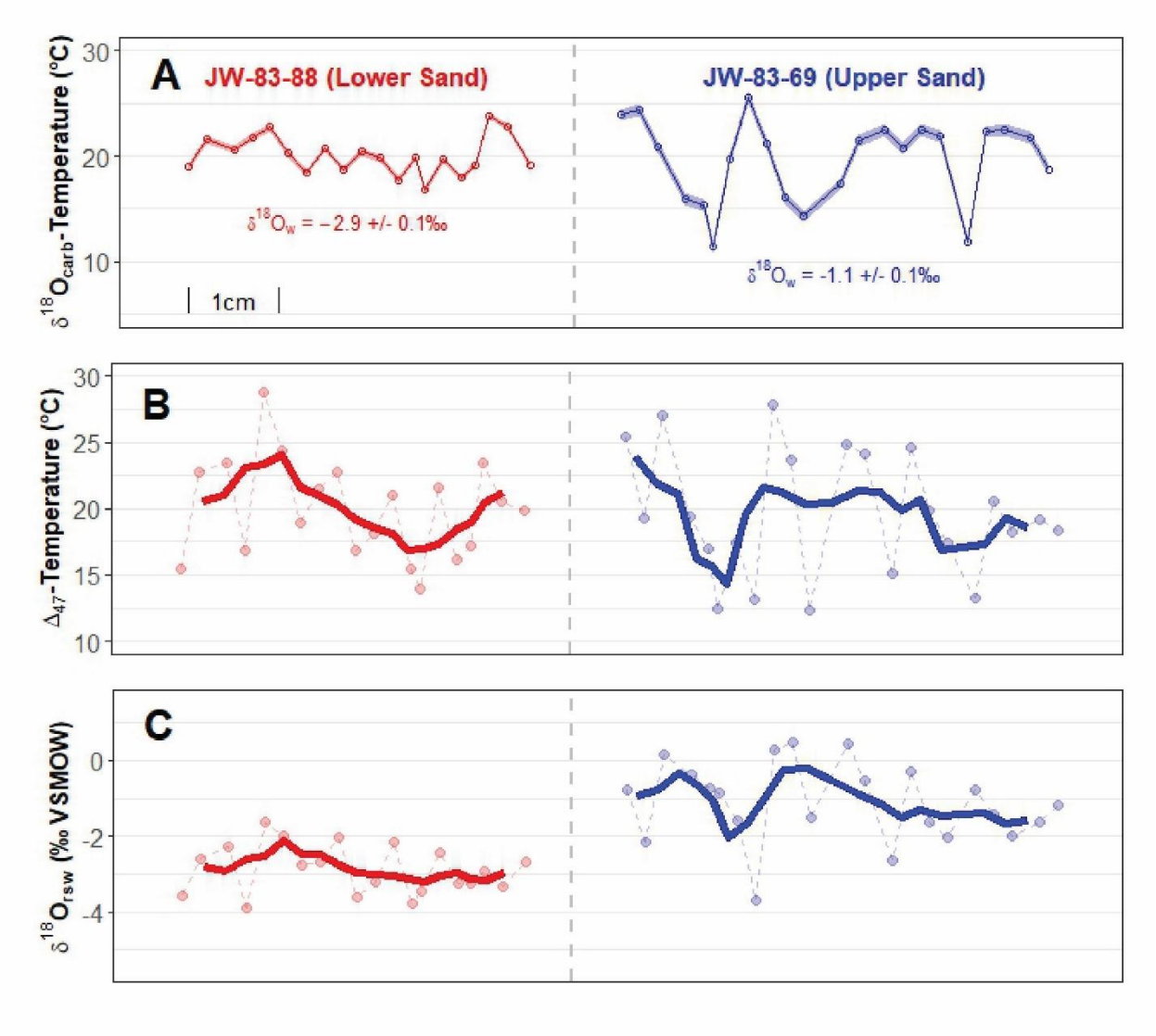

Figure S6.5. $\delta^{18}O_{carb}$ -temperature data (A), 3-point averaged Δ_{47}-temperature data (B), and 3-point averaged reconstructed $\delta^{18}O_{sw}$ ($\delta^{18}O_{rsw}$) data (C) for samples JW-83-88 and JW-83-69.

Error bars for $\delta^{18}O_{carb}$-temperature represent +/- 1SE from sample-averaged $\delta^{18}O_{rsw}$. Background points and dashed lines for Δ_{47}-temperature and $\delta^{18}O_{rsw}$ represent replicate measurements used for 3-point averaging.

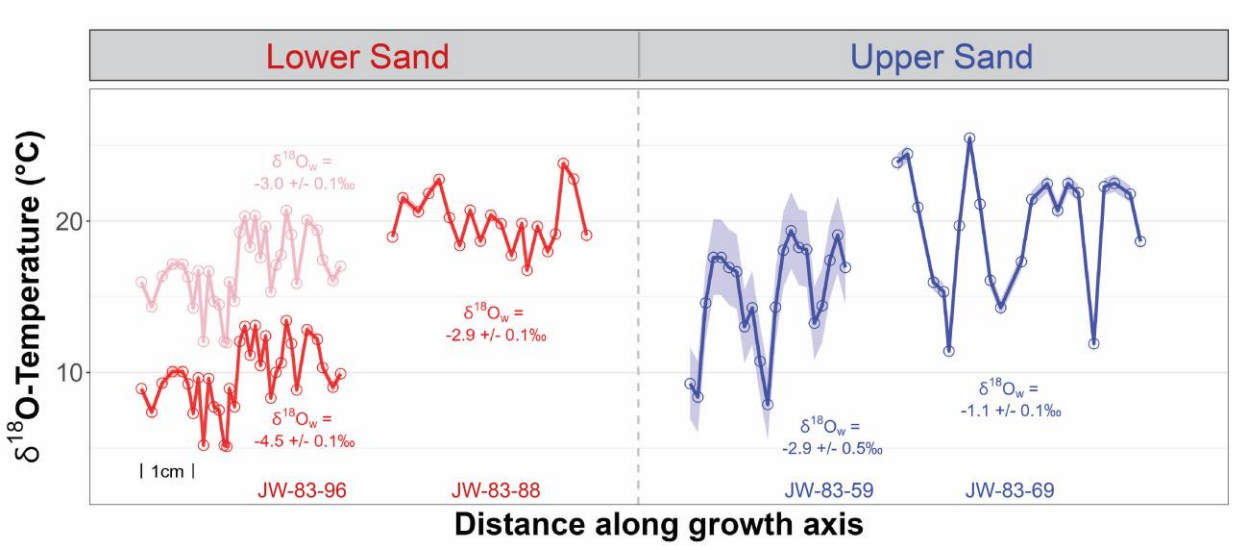

Figure S6.6. $\delta^{18}O$-temperature sclerochronology data for four shells: two from the Lower Sand and two from the Upper Sand.

Temperatures were calculated using the aragonite-water fractionation equation from Kim et al. (2007) using shell-averaged $\delta^{18}O_{rsw}$ from Δ_{47} sclerochronology (JW-83-88, JW-83-69) or bulk $\delta^{18}O_{rsw}$ (JW-83-96, JW-83-59). Error envelopes represent +/- 1SE in $\delta^{18}O_{rsw}$. The faded red $\delta^{18}O$-temperature profile for JW-83-96 was calculated using an upper $\delta^{18}O_{rsw}$ estimate of -3.0‰.

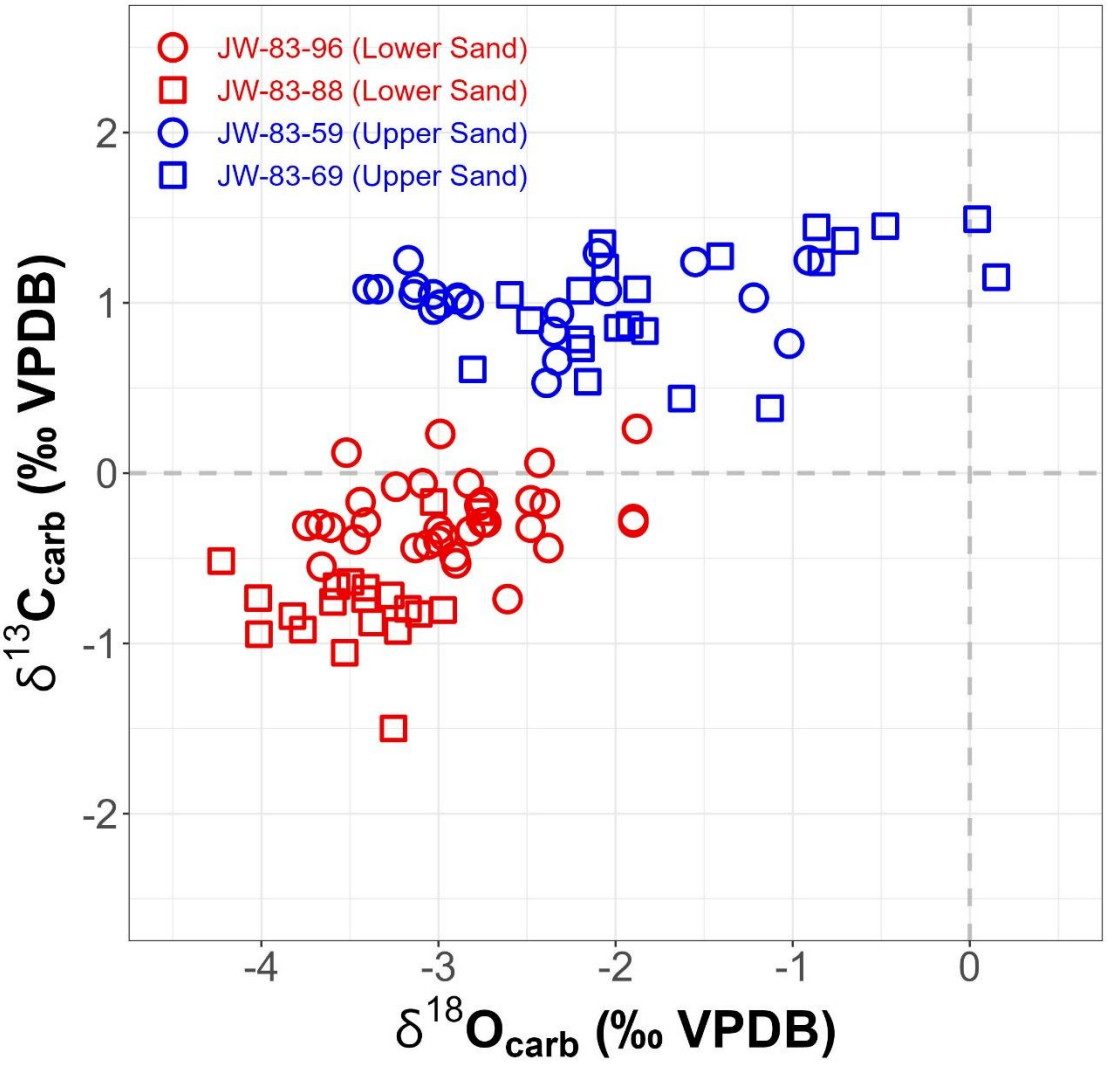

Figure S6.7. $\delta^{13}C_{carb}$ versus $\delta^{18}O_{carb}$ data for samples measured for $\delta^{18}O$ and Δ_{47} sclerochronology.

Circles represent measurements collected from $\delta^{18}O$ sclerochronology; squares represent measurements collected from Δ_{47} sclerochronology.

6.9 References

Anderson, N.T. et al., 2021, A Unified Clumped Isotope Thermometer Calibration (0.5-1,100°C) Using Carbonate-Based Standardization: Geophysical Research Letters, v. 48, p. e2020GL092069, doi: 10.1029/2020GL092069.

Belknap, D.F., 1979, Application of Amino Acid Geochronology To Stratigraphy of Late Cenozoic Marine Units of the Atlantic Coastal Plain [Ph.D. thesis]

Belknap, D.F., and Wehmiller, J.F., 1980, Amino acid racemization in Quaternary molluscs: Examples from Delaware, Maryland, and Virginia: Biogeochemistry of Amino Acids, p. 401-414.

Bernasconi, S. M., Daëron, M., Bergmann, K. D., Bonifacie, M., Meckler, A. N., Affek, H. P., Anderson, N., Bajnai, D., Barkan, E., Beverly, E., Blamart, D., Burgener, L., Calmels, D., Chaduteau, C., Clog, M., Davidheiser-Kroll, B., Davies, A., Dux, F., Eiler, J., Elliott, B., Fetrow, A. C., Fiebig, J., Goldberg, S., Hermoso, M., Huntington, K. W., Hyland, E., Ingalls, M., Jaggi, M., John, C. M., Jost, A. B., Katz, S., Kelson, J., Kluge, T., Kocken, I. J., Laskar, A., Leutert, T. J., Liang, D., Lucarelli, J., Mackey, T. J., Mangenot, X., Meinicke, N., Modestou, S. E., Müller, I. A., Murray, S., Neary, A., Packard, N., Passey, B. H., Pelletier, E., Petersen, S., Piasecki, A., Schauer, A., Snell, K. E., Swart, P. K., Tripati, A., Upadhyay, D., Vennemann, T., Winkelstern, I., Yarian, D., Yoshida, N., Zhang, N., Ziegler, M., 2021, InterCarb: A Community Effort to Improve Interlaboratory Standardization of the Carbonate Clumped Isotope Thermometer Using Carbonate Standards: Geochem. Geophys. Geosystems v. 22, e2020GC009588.

Clark, P.U., Clague, J.J., Curry, B.B., Dreimanis, A., Hicock, S.R., Miller, G.H., Berger, G.W., Eyles, N., Lamothe, M., Miller, B.B., Mott, R.J., Oldale, R.N., Stea, R.R., Szabo, J.P., Thorleifson, L.H., and Vincent, J.-S., 1993, Initiation and development of the Laurentide and Cordilleran Ice Sheets following the last interglaciation: Quaternary Science Reviews, v. 12, no. 2, p. 79-114.

Cushman, J.A., 1904, Notes on the Pleistocene fauna of Sankaty Head, Nantucket, Mass.: American Geologist, v. 34, no. 3, p. 169-174.

Desor, M.E., and Cabot, E.C., 1849, On the Tertiary and more recent Deposits in the Island of Nantucket: Geological Society of London Quarterly Journal, v. 5, p. 340-344.

Eiler, J.M., 2011, Paleoclimate reconstruction using carbonate clumped isotope thermometry: Quaternary Science Reviews, v. 20, no. 25-26, p. 3575-3588.

Epstein, S., and Mayeda, T., 1953, Variation of O18 content of waters from natural sources: Geochimica et Cosmochimica Acta, v. 4, p. 213-224, doi:10.1016/0016-7037(53)90051-9.

Ferguson, G., and Jasechko, S., 2015, The isotopic composition of the Laurentide Ice Sheet and fossil groundwater: Geophysical Research Letters, v. 42, no. 12, p. 4856-4861, doi:10.1002/2015GL064106.

Fouke, K.W., and Kerans, C., 2024, Evidence for a Sea Level Fall During the Last Interglacial Highstand on West Caicos, Turks and Caicos Islands: Paleoceanography and Paleoclimatology, v. 39, no. 8, e2024PA004879.

Galaasen, E.V., Ninneman, U.S., Irvali, N., Kleiven, H.F., Rosenthal, Y., Kissel, C., and Hodell, D.A., 2014, Rapid Reductions in North Atlantic Deep Water During the Peak of the Last Interglacial Period: Science, v. 343(6175), p. 1129-1132., doi:10.1126/science.1248667.

Grossman, E.L., and Ku, T-L., 1986, Oxygen and carbon isotope fractionation in biogenic aragonite: Temperature effects: Chemical Geology: Isotope Geoscience section, v. 59, p 59-74, doi:10.1016/0168-9622(86)90057-6.

Gustavson, T.C., 1976, Paleotemperature analysis of the marine Pleistocene of Long Island, New York, and Nantucket Island, Massachusetts: Geological Society of America Bulletin, v. 87, p. 1-8.

Hillaire-Marcel, C., and Causse, C., 1989, The late Pleistocene Laurentide glacier: Th/U dating of its major fluctuations and ^{18}O range of the ice: Quaternary Research, v. 32, p. 125-135.

Ivanovic, R.F., Gregoire, L.J., Burke, A., Wickert, A.D., Valdes, P.J., Ng, H.C., Robinson, L.F., McManus, J.F., Mitrovica, J.X., Lee, L., and Dentith, J.E., 2018, Acceleration of Northern Ice Sheet Melt Induces AMOC Slowdown and Northern Cooling in Simulations of the Early Last Deglaciation: Paleoceanography and Paleoclimatology, v. 33, no. 7, p. 807-824, doi:10.1029/2017PA003308.

Jones, M.M., Petersen, S.V., and Curley, A.N., 2022, A tropically hot mid-Cretaceous North American Western Interior Seaway: Geology, v. 50, p. 954-958, doi:10.1130/G49998.1.

Kim, S-T., O'Neil, J.R., Hillaire-Marcel, C., and Mucci, A., 2007, Oxygen isotope fractionation between synthetic aragonite and water: Influence of temperature and Mg^{2+}concentration: Geochmica et Cosmochimica Acta, v. 71, p. 4704-4715, doi:10.1016/j.gca.2007.04.019.

Locarnini, R.A., Mishonov, A.V., Baranova, O.K., et al, 2019: World Ocean Atlas 2018, Volume 1: Temperature. Mishonov, A.V. (Ed.), NOAA Atlas NESDIS 81, 52 pp.

Miller, G.H., and Brigham-Grette, J., 1989, Amino acid geochronology: Resolution and precision in carbonate fossils: Quaternary International, v. 1, p. 111-128, doi:10.1016/1040-6182(89)90011-6.

Miller, G.H., Kaufman, D.S., and Clarke, S.J., 2013, Amino Acid Dating: Encyclopedia of Quaternary Science (Second Edition), p. 37-48.

Minnebo, L., Winkelstern, I., Zhang, J., and Petersen, S., 2024, Last Interglacial coastal hydroclimate variability in Bermuda revealed by clumped isotope oyster sclerochronology: Palaeogeography, Palaeoclimatology, Palaeoecology, v. 643, doi:10.1016/j.palaeo.2024.112195.

O'Hora, H.E., Petersen, S.V., Vellekoop, J., Jones, M.M., and Scholz, S.R., 2022, Clumped-isotope-derived climate trends leading up to the end-Cretaceous mass extinction in northwestern Europe: Climate of the Past, v. 18, p. 1963-1982, doi:10.5194/cp-18-1963-2022.

Oldale, R.N., Valentine, P.C., Cronin, T.M., Spiker, E.C., Blackwelder, B.W., Belknap, D.F., Wehmiller, J.F., and Szabo, B.J., 1982, Stratigraphy, structure, absolute age, and paleontology of the upper Pleistocene deposits at Sankaty Head, Nantucket Island, Massachusetts: Geology, v. 10, p. 246-252.

Oppo, D.W., McManus, J.F., and Cullen J.L., 2006, Evolution and demise of the Last Interglacial warmth in the subpolar North Atlantic: Quaternary Science Reviews, v. 25, p. 3268-3277, doi:10.1016/j.quascirev.2006.07.006.

Parham, P.R., Riggs, S.R., Culver, S.J., Mallinson, D.J., Rink, W.J., and Burdette K., 2013, Quaternary coastal lithofacies, sequence development and stratigraphy in a passive margin setting, North Carolina and Virginia, USA: Sedimentology, v. 60, p. 503-547, doi:10.1111/j.1365-3091.2012.01349.x.

Parker, R.L., Foster, G.L., Gutjahr, M., Wilson, P.A., Littler, K.L., Cooper, M.J., Michalik, A., Milton, J.A., Crocket, K.C., and Bailey, I., 2022, Laurentide Ice Sheet extent over the last 130 thousand years traced by the Pb isotope signature of weathering inputs to the Labrador Sea: Quaternary Science Reviews, v. 287, 107564, doi:10.1016/j.quascirev.2022.107564.

Quizon, A.A., Petersen, S.V., de Winter, N.J., and Vellekoop, J., 2025, Clumped isotope thermometry (Δ_{47}) measurements in marine gastropods suggest equilibrium precipitation: Geochimica et Cosmochimica Acta, v. 410, p. 234-249, doi:10.1016/j.gca.2025.10.023

Sharp, Z., 2017, Principles of Stable Isotope Geochemistry, 2nd Edition, doi:10.25844/h9q1-0p82.

Turney, C.S.M., Jones, R.T., McKay, N.P., van Sebille, E., Thomas, Z.A., Hillenbrand, C-D., and Fogwill, C.J., 2020, A global mean sea surface temperature dataset for the Last Interglacial (129-116 ka) and contribution of thermal expansion to sea level change: Earth System Science Data, v. 12, p. 3341-3356, doi:10.5194/essd-12-3341-2020.

Verrill, A.E., 1875, On the post-Pliocene fossils of Sankaty Head, Nantucket Island, with a note on the geology by S.H. Scudder: American Journal of Science, v. 10, p. 364-375.

Vetter, L., Spero, H.J., Eggins, S.M., Williams, C., and Flower, B.P., 2017, Oxygen isotope geochemistry of Laurentide ice-sheet meltwater across Termination I: Quaternary Science Reviews, v. 178, p. 102-117, doi:10.1016/j.quascirev.2017.10.007.

Wehmiller, J.F., 2013, United States Quaternary coastal sequences and molluscan racemization geochronology - What have they meant for each other over the past 45 years? Quaternary Geochronology, v. 16, p. 3-20.

Wehmiller, J.F., Brothers, L.L., Ramsey, K.W., Foster, D.S., Mattheus, C.R., Hein, C.J., and Shawler, J.L., 2021, Molluscan aminostratigraphy of the US Mid-Atlantic Quaternary coastal system: Implications for onshore-offshore correlation, paleochannel and barrier island evolution, and local late Quaternary sea-level history: Quaternary Geochronology, v. 66, p. 101177, doi:10.1016/j.quageo.2021.101177.

Wilson, J.H., 1906, The glacial history of Nantucket and Cape Cod with an argument for a fourth center of glacial dispersion in North America: New York, Columbia University Press, 90p.

Winkelstern, I.Z., Rowe, M.P., Lohmann, K.C., Defliese, W.F., Petersen, S.V., and Brewer, A.W., 2017, Meltwater pulse recorded in Last Interglacial mollusk shells from Bermuda: Paleoceanography, v. 32, no. 2, p. 132-145, doi:10.1002/2016PA003014.

Winkelstern, I.Z., Petersen, S., Curran, H.A., Phillips, C., Quizon, A., Glumac, B., and Griffing, D., 2025, Cooling Climate Across Last Interglacial High Stands on San Salvador and Great Inagua, The Bahamas: The Depositional Record, v. 12, no. 1, e70038, doi:10.1002/dep2.70038.

Zhang, J.Z., Petersen, S.V., Winkelstern, I.Z., and Lohmann, K.C., 2021, Seasonally Variable Aquifer Discharge and Cooler Climate in Bermuda During the Last Interglacial Revealed by Subannual Clumped Isotope Analysis: Paleoceanography and Paleoclimatology, v. 36, doi:10.1029/2020PA004145.

Zhang, J.Z., and Petersen, S.V., 2023, Clumped and oxygen isotope sclerochronology methods tested in the bivalve *Lucina pensylvania*: Chemical Geology, v. 620, p. 121346, doi:10.1016/j.chemgeo.2023.121346.

Chapter 7 Conclusions

This dissertation consists of five content chapters that explore innovations in the applications of traditional stable oxygen and clumped isotope methods in the fields of paleoclimate and paleoceanography. This concluding chapter highlights the key findings from each of these chapters and discusses the future implications of this work.

7.1 Do marine gastropods precipitate in 'clumped' isotope equilibrium and faithfully record environmental temperatures (Chapter 2)?

In Chapter 2, we assessed whether marine gastropods – an archive largely unexplored for Δ_{47} thermometry – generally tend to precipitate their shells in or out of Δ_{47} equilibrium and thus if they faithfully record environmental temperatures. To do this, we measured Δ_{47} in various modern marine gastropods across the phylogenetic tree that span localities around the globe. We found that many gastropods do precipitate their shells in Δ_{47} (and Δ_{48}) equilibrium, and we therefore deem these species viable for Δ_{47}-paleotemperature reconstruction. However, a few taxa that are abundant in the fossil record – i.e., *Campanile*, *Turritella*/*Caviturritella* – do not precipitate in Δ_{47} equilibrium, and we therefore recommend using caution before looking to these taxa as accurate recorders of paleoclimate.

This study supports the assumption that the isotope geochemistry of carbonate precipitation in marine gastropods is similar to that in bivalve mollusks. Many studies have already utilized Δ_{47} measurements in bivalve mollusks for paleotemperature reconstructions, and

this study sets the groundwork for future works that incorporate Δ_{47} measurements from gastropod mollusks. However, we also encourage future study into taxa such as *Campanile* and *Turritella*/*Caviturritella* to delve into a more precise explanation of why their isotopic behavior deviates from other marine gastropods. This work could also help address broader questions across various disciplines, answering outstandings questions about gastropod phylogeny (i.e., linking differing gastropod precipitation mechanisms to divergent evolutionary pathways) and carbonate chemistry in biogenic calcifiers (i.e., defining new types of biologically mediated carbonate precipitation mechanisms).

7.2 Do all turritellid gastropods exhibit vital (disequilibrium) effects, and can these biases be corrected for in the fossil record (Chapter 3)?

In Chapter 3, we assessed whether turritellids collectively exhibit vital (disequilibrium) effects and whether the biases observed in Chapter 3 can be corrected for in the fossil record. To do so, we analyzed Δ_{47} measurements from modern and fossil (Mid-Miocene, ~18-14 Ma) turritellids collected from the Guajira Peninsula in Colombia. We found that the modern turritellids also exhibit the same direction and average magnitude of the turritellid vital effect signature (i.e., offset from Δ_{47} equilibrium) reported in Chapter 2. After applying a correction to the fossil turritellid Δ_{47}-tempeatures based on this offset, we found that corrected temperatures align with previously reported paleotemperature estimates in the region from other proxies, highlighting the potential of this vital effect-based adjustment to obtain more accurate paleotemperatures.

This study builds on the turritellid Δ_{47} dataset from Chapter 2 and helps us better understand isotopic behavior in turritellid gastropods more broadly. These new data also help set the framework for future studies that may utilize fossil turritellid Δ_{47}-temperatures for

paleoclimatic (and paleoceanographic) interpretations. However, several unanswered questions about turritellids still remain including, crucially, how turritellids precipitate their shells differently from other gastropods and how this mechanism is linked to disequilibrium signatures. We encourage future interdisciplinary paleontological and geochemical studies of turritellids, ideally in-situ, to address these questions.

7.3 Is there a latitudinal $\delta^{18}O_w$ gradient that aligns with the latitudinal salinity gradient along the U.S. Eastern Seaboard, and can $\delta^{18}O_w$ signatures distinguish the Labrador Current and Gulf Stream (Chapter 4)?

In Chapter 4, we assessed whether modern $\delta^{18}O_w$ data exhibit a latitudinal gradient that aligns with the modern salinity gradient observed along the U.S. Eastern Seaboard and whether these data can be used to distinguish the Labrador and Gulf Stream boundary currents. We tested this by collecting 358 brand-new $\delta^{18}O_w$ (and salinity) measurements along the Eastern Seaboard, effectively doubling the number of existing data in the broader North Atlantic region. These data suggest that $\delta^{18}O_w$ and salinity are correlated in this region and demonstrate that the Labrador Current and Gulf Stream appear to exhibit distinct $\delta^{18}O_w$-salinity signatures.

This study expands on the number of existing modern instrumental $\delta^{18}O_w$ data in this region, which was relatively sparse before the collection of these measurements. This alone can assist with efforts to better understand modern hydrology and oceanography through the lens of isotope geochemistry, and we encourage future use of these data for such endeavors. Furthermore, the trends identified from this dataset have considerable implications for paleoclimatic and paleoceanographic interpretations. Firstly, this dataset exhibits significant $\delta^{18}O_w$ variability site by site and along the coast; this suggests that paleo-$\delta^{18}O_w$ values varied quite a bit along the coastline, thus creating uncertainties in $\delta^{18}O$-based paleotemperature

reconstructions that make assumptions about $\delta^{18}O_w$ in the past. Collection of these measurements as reference points for $\delta^{18}O_w$ assumptions reduces these uncertainties for studies centered around the North Atlantic. Secondly, this dataset demonstrates that the Labrador Current and Gulf Stream possess distinct $\delta^{18}O_w$ signatures, underlining the potential for paleo-$\delta^{18}O_w$ values along the Eastern Seaboard to be used to track these boundary currents in the past (as further discussed in Chapter 5).

7.4 What were paleoclimate and paleoceanographic conditions along the Atlantic Coastal Plain during Marine Isotope Stage 5, and can we use Δ_{47}-derived paleo- $\delta^{18}O_w$ values to distinguish the Labrador Current and Gulf Stream (Chapter 5)?

In Chapter 5, we reconstructed paleoclimate and paleoceanographic conditions along the Atlantic Coastal Plain during two substages of the Marine Isotope Stage 5 interglacial period (MIS 5e, ~130-115 ka; MIS 5a, ~80 ka) and determined whether we can use Δ_{47}-derived paleo-$\delta^{18}O_w$ to distinguish between the Labrador Current and Gulf Stream. To do this, we obtained Δ_{47}-derived paleotemperatures and paleo-$\delta^{18}O_w$ values from MIS 5e- and MIS 5a-dated fossil mollusks collected from nine sites along the Eastern Seaboard. Reconstructed temperature data suggest that MIS 5a temperatures were generally similar to modern while MIS 5e temperatures were similar to modern, although the degree of variability within the MIS 5e samples suggest the likely occurrence of multiple depositional episodes (i.e., local highstands) within MIS 5e. Meanwhile, reconstructed $\delta^{18}O_w$ values align with modern instrumental $\delta^{18}O_w$ values and thus track with modern-day Labrador Current and Gulf Stream signatures, illustrating the potential of paleo-$\delta^{18}O_w$ to be used as a water mass tracer.

This study adds to the existing sparse MIS 5e and (especially sparse) MIS 5a proxy paleotemperature dataset from the broader North Atlantic region, which can inform future MIS

5e and potentially MIS 5a climate model simulations. Furthermore, the likely occurrence of multiple depositional episodes within MIS 5e has substantial implications for how we interpret paleotemperature data and incorporate them into climate models for not only the Last Interglacial but also other warm intervals. For example – what different time slices within the Last Interglacial are recorded from proxy data used to calculate globally averaged temperature anomalies? These data encourage us to think critically about the geochronological constraints behind regional paleoclimate comparisons and how we interpret proxy data moving forward.

Meanwhile, the paleo-$\delta^{18}O_w$ data in this study can be used to continue to develop the framework for using Δ_{47}-derived paleo-$\delta^{18}O_w$ as a water mass tracer. Previous studies have set up this framework by combining $\delta^{18}O_{carb}$ measurements with other paleotemperature proxy measurements (e.g., Sr/Ca) and have used back-calculated paleo-$\delta^{18}O_w$ to infer changes in regional circulation patterns. However, Δ_{47} thermometry allows us to simultaneously collect Δ_{47} and $\delta^{18}O_{carb}$ on an isotope ratio mass spectrometer from a single powder, simplifying sampling procedures and subsequent data processing. We encourage future Δ_{47}-centered paleoceanography studies to consider water mass movement and ocean circulation changes as an explanation for paleo-$\delta^{18}O_w$ variability throughout the geologic past.

7.5 How did paleoclimate and paleoceanographic conditions evolve over the Last Interglacial at Nantucket, Massachusetts (Chapter 6)?

In Chapter 6, we reconstructed paleoclimate and paleoceanographic conditions at Nantucket, Massachusetts (Sankaty Sand) over the Last Interglacial (MIS 5e). To do this, we collected Δ_{47}-derived paleotemperatures and paleo-$\delta^{18}O_w$ values from 7 fossil mollusks across the two units at the Sankaty Sand outcrop. We determined that temperatures across both units were warmer than modern on average, which is consistent with global trends. However, paleo-

$\delta^{18}O_w$ values from both units are substantially depleted (i.e., fresher) relative to modern which suggests the presence of substantial ice sheet meltwater, with increasing mean paleo-$\delta^{18}O_w$ values from the lower to upper unit consistent with ice sheet retreat over time.

Like the previous chapter, this study adds to the existing MIS 5e proxy paleotemperature dataset from the North Atlantic, supporting the previous reported warm temperature anomaly (relative to present-day) in this region. However, the paleo-$\delta^{18}O_w$ values tell a regional story not told before, providing insights into local ice sheet dynamics and how they evolved over time. As with the previous chapter, we encourage future Δ_{47}-centered paleoceanography studies to consider this newer interpretation of Δ_{47}-derived paleo-$\delta^{18}O_w$ variability – i.e., melting ice sheets – in addition to previous interpretations of hydrological variability.

7.6 Future Directions

The conclusions from these chapters set up the framework for future studies utilizing Δ_{47}-paleothermometry measurements in marine gastropods and Δ_{47}-derived paleo-$\delta^{18}O_w$ for reconstructions of past ocean circulation and ice sheet melt. Altogether, these chapters expand our knowledge of these isotope proxies and document innovations in their use as forensic tools in investigations of paleoclimate and paleoceanography.

Moving forward, we are excited to see the direction that future studies take based on the findings from this dissertation, especially across disciplines. Firstly, the marine gastropod findings can help inform future studies of the phylogeny and evolution of gastropods (and other biogenic calcifiers), which is becoming increasingly relevant amidst the modern-day biodiversity crisis. Secondly, the geochemical findings regarding marine gastropod carbonate precipitation can help refine our understanding of the role that these taxa (and biogenic calcifiers, broadly) play in the marine carbon cycle, especially as oceanographers become increasingly interested in

the role that our oceans play in regulating global climate through carbon sequestration. And finally, the paleo-$\delta^{18}O_w$ findings naturally lend themselves towards investigations of past (and future) ocean and climate conditions, enabling investigations of the following example topics: how past currents influenced regional coastal climate during warm periods, how the position of these currents shifted in the past and may shift in the future with sea level rise, how current behavior may have impacted ecosystem dynamics and influenced regional extinction events, and how North Atlantic ice sheet dynamics are tied to a warm climate state. As a next step, I plan to continue to assist with carbonate chemistry and carbon sequestration efforts moving forward, apply my knowledge across the aforementioned disciplines to these fields.